STUDIA

UNIVERSITATIS BABEŞ-BOLYAI

Chemia

CLUJ-NAPOCA 2005

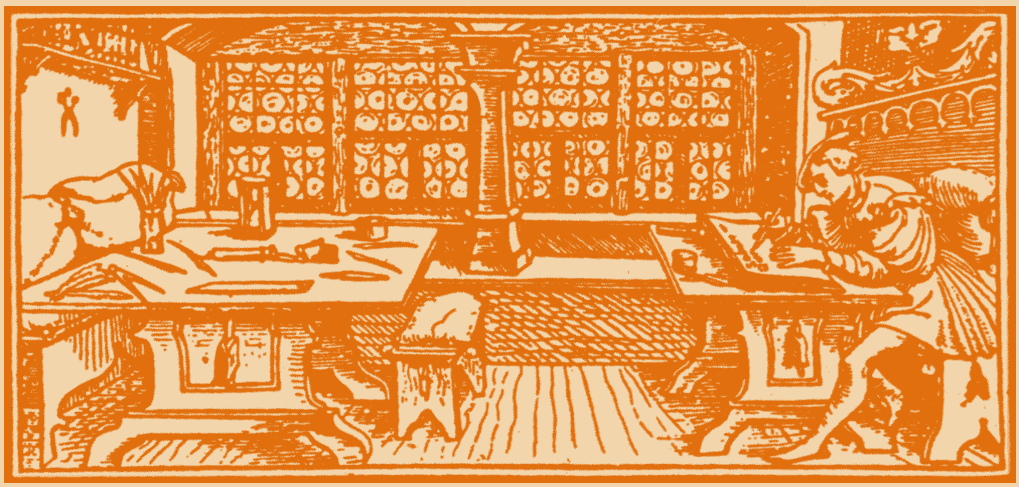

2

ANUL L **2005**

S T U D I A
UNIVERSITATIS BABEŞ-BOLYAI
CHEMIA
2

EDITORIAL OFFICE: Republicii no. 24, 400015 Cluj-Napoca ♦ Phone 0264-40.53.52

CUPRINS - CONTENTS - SOMMAIRE

STUDIA UNIVERSITATIS BABEŞ-BOLYAI

CHEMIA

Special Issue

Dedicated to the papers presented at

CAPE Forum 2005

Cluj-Napoca, February 25-26, 2005

This special issue of STUDIA UNIVERSITATIS BABEŞ-BOLYAI, CHEMIA is dedicated to the papers presented at the CAPE FORUM 2005 organized by the "BABEŞ-BOLYAI" University of Cluj-Napoca, Department of Chemical Engineering lead by Prof.Dr.Ing. Şerban Paul AGACHI and by the University POLITEHNICA of Bucharest, Department of Chemical Engineering, Center of Technology Transfer in the Process Industry lead by Prof.Dr.Ing. Valentin PLEŞU.

The CAPE FORUM annual series of international meetings is a major scientific event for all those interested and active in the field of **CAPE** (***C****omputer* ***A****ided* ***P****rocess* ***E****ngineering*). Started in the early '90 under the coordination of **CAPE-WP** which is a working party of the European Federation of Chemical Engineers (**EFCE**) on the topic of CAPE, this event was held in the past by major European universities located in France, Spain, United Kingdom, Belgium, The Netherlands, Denmark and Hungary.

The 2005 forum brought together more than 100 participants from: Belgium, Denmark, Finland, Germany, Hungary, Italy, The Netherlands, Poland, Spain, Switzerland, U.S.A. and Romania.

All papers presented in this special issue were selected after an international peer review.

The Organizers of CAPE FORUM 2005

STUDIA UNIVERSITATIS BABEŞ-BOLYAI, CHEMIA, L, 2, 2005

IMPLEMENTATION OF BIVARIATE POPULATION BALANCE EQUATIONS IN CFD CODES FOR MODELLING NANOPARTICLE FORMATION IN TURBULENT FLAMES

ALESSANDRO ZUCCA, DANIELE L. MARCHISIO, ANTONELLO A. BARRESI

Dipartimento di Scienza dei Materiali ed Ingegneria Chimica Politecnico di Torino
Corso Duca degli Abruzzi, 24 10129 Torino – Italy

ABSTRACT. In recent years the problem of studying particle formation and dynamics in turbulent flames has become more and more important, for both environmental and technological reasons. Information on size and morphology of the particulate matter is often required, since these characteristics largely influence the effects of particles on human health and global climate (in the case of soot), and the features of the produced material (in the case of combustion synthesis). The solution of the population balance equation has to be integrated with Computational Fluid Dynamics (CFD), which needs to be employed for the simulation of temperature, composition and velocity fields of the flame. In this work, the recently proposed Direct Quadrature Method of Moments (DQMOM), which allows the solution of the bivariate population balance equation with low additional computational effort, is applied to the study of soot formation in turbulent non-premixed flames. The model takes into account nucleation, molecular growth, oxidation and aggregation of particles; simplified kinetic rates are employed, while velocity and scalar fields are computed by simulations based on the solution of the Reynolds Averaged Navier Stokes (RANS) equations. The bivariate formulation of the DQMOM (in terms of particle volume and surface area) is implemented and compared with the monovariate formulation (in terms of particle volume). Simulation results show that the DQMOM is a suitable tool for the solution of the considered problem both in the monovariate and in the bivariate case, and evidence the importance of a proper treatment of particle fractal dimension to obtain accurate predictions of the morphological properties of soot aggregates.

1. INTRODUCTION

The interest of the scientific community in combustion formed particulate is twofold. On the one hand, in fact, toxicological and environmental studies have focused the attention of the combustion community on the accurate modelling of the formation of carbonaceous nano- and microparticle (soot) in turbulent flames [1]; on the other hand, combustion sintesized nanoparticles are gaining growing importance in a wide range of applications. In the former case, the particulate matter is an undesired by-product, while in the latter case particles constitute a tailored material, with particular features, which is the main product of the process.

In this work, we will focus in particular on the problem of soot formation, which is caused by incomplete oxidation of the species that constitute the fuel, with the production of benzene molecules, which grow to give polycyclic aromatic hydrocarbons (PAH), considered key compounds in the reactions involved in the first stages of the process [2]. Further growth of these high molecular weight compounds leads to the inception of solid particles that in turn grow by surface reaction and aggregate.

The use of Computational Fluid Dynamics (CFD) for studying turbulent combustion is nowadays quite common, and much progress has been done in the last decades for the prediction of flame temperature and composition. Moreover, the capability of predicting a number of pollutants is an important tool in design and optimization of low-emission burners.

In the case of soot formation, the study of gas-phase reactions leading to nucleation of the first solid particles has to be coupled with the study of the evolution of the particle distribution by solving a population balance equation (PBE), which is a balance equation in terms of the distribution of one or more particle state variables, or internal coordinates. When the mixing time scale is large with respect to the characteristic times of the processes affecting the evolution of the population, which strongly depends on flame temperature and composition profiles, the solution of the PBE must be integrated in a CFD code.

The efficient coupling of the population balance with fluid dynamics computation is still the subject of current research. For homogeneous systems with only one internal coordinate, the population balance can be solved by using one of the many available discretization methods [3]. This implies the solution of a large number of equations (20-40) that makes this approach unsuitable for many CFD applications. An alternative approach is the solution of the transport equations of the moments of the size distribution, using a quadrature formula for the closure of unknown terms. Nodes and weights of the quadrature approximation can be evaluated from the moments of the distribution by using a very efficient algorithm [4, 5]. The method has been recently presented in a direct formulation (Direct Quadrature Method of Moments or DQMOM) [6] that allows one to solve the population balance equation with more than one internal coordinate without intolerable increase in the complexity of the algorithm.

In this work the DQMOM has been applied for the solution of the population balance equation for the prediction of soot formation in turbulent flames. A detailed treatment of this method can be found in the next section. The solution of the bivariate population balance equation will be discussed in detail, and the applicability of the method to the problem of soot formation will be assessed. The test case investigated in this work is an ethylene-air turbulent flame (A) studied by Kent and Honnery [7], for which some experimental data are available. In this flame a turbulent jet of ethylene is burned in still air. The use of this fuel, which assures that a relevant amount of soot is formed, is very common in experimental works on soot formation. Once the model has been validated, it will be applied to the study of soot formation in methane/air lean combustion.

2. MATHEMATICAL MODEL

2.1 Computational Fluid Dynamics (CFD)

CFD is based on the solution of the continuity and Navier-Stokes equations. To take into account the highly irregular nature of turbulence, the components of the velocity vector are usually decomposed in the summation of a mean value and fluctuations; therefore, applying Favre averaging (valid for flows with variable density), the continuity, Navier-Stokes and scalar transport equations become respectively:

$$\frac{\partial \bar{\rho}}{\partial t} + \frac{\partial}{\partial x_i}\left(\bar{\rho}\tilde{U}_i\right) = 0\,, \tag{1}$$

$$\frac{\partial}{\partial t}\bar{\rho}\tilde{U}_i + \frac{\partial}{\partial x_i}\bar{\rho}\tilde{U}_i\tilde{U}_j + \frac{\partial}{\partial x_i}\bar{\rho}\widetilde{u_i u_j} = -\frac{\partial \bar{p}}{\partial x_i} + \nu\frac{\partial^2 \bar{\rho}\tilde{U}_i}{\partial x_j \partial x_j}\,, \tag{2}$$

$$\frac{\partial}{\partial t}\bar{\rho}\tilde{\Phi}_\alpha + \frac{\partial}{\partial x_i}\bar{\rho}\tilde{\Phi}_\alpha\tilde{U}_i + \frac{\partial}{\partial x_i}\bar{\rho}\overline{\phi_\alpha u_i} = (\Gamma + \Gamma_t)\frac{\partial^2\bar{\rho}\tilde{\Phi}_\alpha}{\partial x_i \partial x_i} + \overline{S}(\mathbf{\Phi}) \tag{3}$$

where $\bar{\rho}$ and $\bar{p}$ are the mean density and pressure respectively, ν is the kinematic viscosity, $\tilde{U}_i$ is the Favre-averaged value of the *i*-th component of the fluid mean velocity (we are using Einstein's notation, so that repeated indices imply summation), u_i is the same component of the fluctuation of velocity, Φ_α and ϕ_α are the mean and fluctuating concentration of the α-th scalar, Γ is the molecular diffusivity, Γ_t is the turbulent diffusivity $(\Gamma_t = \nu_t / Sc_t)$, and $\overline{S}(\mathbf{\Phi})$ is the Favre-averaged chemical source term. The third term on the left-hand side of equation (2), the so-called Reynolds stress tensor, is generated by the decomposition and needs to be closed. As far as the solution of this closure problem is concerned, the standard [8], RNG [9] and 'realizable' [10] *k-ε* models are relatively simple approaches based on the eddy-viscosity concept, where the Reynolds stresses are expressed in terms of mean velocity gradients and of the so-called turbulent viscosity ν_t. If the Reynolds Stress Model (RSM) is employed, the problem is closed by solving transport equations for the turbulent stresses [11,12].

The closure of the chemical source term $\overline{S}(\mathbf{\Phi})$ is another major issue in the modelling of turbulent reacting flows. Some of the most widely used modelling approaches are the Eddy dissipation model [13], the Transported Probability Density Function (PDF) method [14], the Presumed PDF method [15,16] and the laminar flamelet model [17]. A complete and detailed description of these methods can be found in the selected references, and in the book by Fox [18]. We will briefly present the beta-PDF approach, that has been employed in the present work for the description of turbulence-chemistry interaction. The global composition of the system is represented via the *mixture fraction*, which is a conservative scalar defined as follows:

$$\xi = \frac{\Phi_\alpha - \Phi_{\alpha,o}}{\Phi_{\alpha,f} - \Phi_{\alpha,o}}, \tag{4}$$

where Φ_α is the concentration of a generic scalar α, and the subscripts *f* and *o* refer to the fuel and the oxidizer stream respectively (and in general to two different inlet streams trough which the reactants are fed separately). It is clear that, according to the definition in (4), the mixture fraction lays within the range [0,1] ($\xi = 1$ for the 'fuel' stream, and $\xi = 0$ for the 'oxidizer' stream). In a turbulent flow, the mixture fraction is of course a fluctuating quantity; its mean value identifies the global composition of the system, while its variance (ξ'^2) is a measure of the extent of mixedness at the molecular level, and is dissipated during the mixing process.

The method requires to solve the transport equations for the mean mixture fraction and the mixture fraction variance:

$$\frac{\partial}{\partial t}\left(\bar{\rho}\tilde{\xi}\right) + \frac{\partial}{\partial x_i}\left(\bar{\rho}\tilde{U}_i\tilde{\xi}\right) = \frac{\partial}{\partial x_i}\left(\frac{\mu_t}{\sigma_t}\frac{\partial\tilde{\xi}}{\partial x_i}\right), \tag{5}$$

$$\frac{\partial}{\partial t}\left(\bar{\rho}\overline{\xi'^2}\right)+\frac{\partial}{\partial x_i}\left(\bar{\rho}\tilde{U}_i\overline{\xi'^2}\right)=\frac{\partial}{\partial x_i}\left(\frac{\mu_t}{Sc_t}\frac{\partial\overline{\xi'^2}}{\partial x_i}\right)+2\frac{\mu_t}{Sc_t}\left(\frac{\partial\tilde{\xi}}{\partial x_i}\right)^2-C_\Phi\bar{\rho}\frac{\tilde{\varepsilon}}{\tilde{k}}\overline{\xi'^2}\,, \tag{6}$$

where the last two terms in (6) are the generation and the dissipation term respectively. The constant C_Φ appearing in the dissipation term is usually set equal to 2.

The temperature and composition fields are calculated evaluating the temperature and composition corresponding to each value of mean mixture fraction $\tilde{\xi}$, mixture fraction variance $\overline{\xi'^2}$, and of enthalpy $\tilde{H}$ for non-adiabatic systems; for non-adiabatic systems, the average value of the scalar Φ_α can be evaluated by the following integral:

$$\tilde{\Phi}_\alpha=\int_0^1 f_\zeta\left(\xi\right)\Phi_\alpha\left(\xi,\tilde{H}\right)d\xi\,, \tag{7}$$

where $f_\zeta(\xi)$ is the mixture fraction PDF, and $\Phi_\alpha\left(\xi,\tilde{H}\right)$ is the relationship that links mixture fraction, mixture fraction variance and enthalpy to the scalar concentration Φ_α.

Several presumed shapes of PDF have been employed for the mixture fraction, such as the beta-PDF and the double-delta-PDF. By using the beta-PDF approach, the mixture fraction PDF is described as follows [15]:

$$f_\zeta\left(\xi\right)=\frac{\xi^{\alpha-1}\left(1-\xi\right)^{\beta-1}}{\int_0^1\xi^{\alpha-1}\left(1-\xi\right)^{\beta-1}d\xi}\,, \tag{8}$$

where

$$\alpha=\tilde{\xi}\left[\frac{\tilde{\xi}\left(1-\tilde{\xi}\right)}{\overline{\xi'^2}}-1\right], \tag{9}$$

$$\beta=\left(1-\tilde{\xi}\right)\left[\frac{\tilde{\xi}\left(1-\tilde{\xi}\right)}{\overline{\xi'^2}}-1\right]. \tag{10}$$

For a number of possible values of mean mixture fraction and mixture fraction variance, the values of temperature and chemical species involved in the reaction are computed (through Eq. (7)) and stored in a look-up table. In this way the turbulent-chemistry interactions are pre-processed and calculations do not need to be repeated at each iteration, thus resulting in a relevant saving of computational resources.

The treatment of chemistry is hidden in the function $\Phi_\alpha(\xi$ which can be evaluated by different options. An option which is widely used for combustion computations is the *equilibrium assumption*. In this case the equilibrium composition and temperature are evaluated for each value of mixture fraction, variance and enthalpy (if it is the case) by minimization of the Gibbs free energy of the mixture. No detailed kinetic data are required (the reactions are assumed infinitely fast but reversible), and only the species present in the system have to be specified.

Once the mixture fraction PDF is evaluated in the whole domain by solving Eqs. (5) and (6), the temperature and composition profiles are obtained by reading the appropriate value in the look-up table. The mean value of scalars in each computational cell is calculated by interpolation between the neighbouring stored values.

2.2 The Direct Quadrature Method of Moments (DQMOM)

As already stated, the solution of the population balance, which is necessary when the prediction of the evolution of a population of particles is of interest, has to be coupled, in the case of combustion-formed particulate, with the simulation of temperature and composition fields of the flame within a CFD code.

Among the possible solution techniques, we present in this section the DQMOM, which requires low additional computational cost and is therefore suitable for this kind of application.

Let us consider the population balance equation:

$$\frac{\partial \tilde{n}(\boldsymbol{\xi};\mathbf{x},t)}{\partial t} + \frac{\partial}{\partial x_i}\tilde{U}_i \tilde{n}(\boldsymbol{\xi};\mathbf{x},t) - \frac{\partial}{\partial x_i}\left[\Gamma_t \frac{\partial \tilde{n}(\boldsymbol{\xi};\mathbf{x},t)}{\partial x_i}\right] = S(\boldsymbol{\xi};\mathbf{x},t), \tag{11}$$

where $\tilde{n}$ is the Favre averaged number density function, $\boldsymbol{\xi}$ is the internal coordinate vector (i.e., the vector of particle state variables), $\mathbf{x}$ is the spatial coordinate vector, and $S(\boldsymbol{\xi};\mathbf{x},t)$ is the source term, which takes into account continuous and discontinuous changes in the internal coordinates vector, due to, e.g., molecular surface growth, oxidation, aggregation and breakage. The method is based on the moments approach, so that Eq. (11) is solved in terms of the mixed moments of the distribution which, for a generic multivariate number density function, are defined as follows:

$$m_{k_1,k_2,\ldots,k_M} = \int_{-\infty}^{\infty} \xi_1^{k_1} \int_{-\infty}^{\infty} \xi_2^{k_2} \cdots \int_{-\infty}^{\infty} \xi_n^{k_M} \tilde{n}(\boldsymbol{\xi};\mathbf{x},t)\, d\xi_1 d\xi_2 \cdots d\xi_M \tag{12}$$

where k_i is the order of the moment with respect to ξ_i.

In this case, the source terms for the moments need to be closed; the main idea behind the approach is the use of a quadrature approximation of the number density function [4, 5]. This corresponds to the approximation of the PSD as follows:

$$\tilde{n}(\boldsymbol{\xi};\mathbf{x},t) \approx \sum_{\alpha=1}^{N} w_\alpha(\mathbf{x},t) \prod_{i=1}^{M} \delta\left[\xi_i - \xi_{i\alpha}(\mathbf{x},t)\right], \tag{13}$$

where $w_\alpha(\mathbf{x},t)$ are the 'weights' and $\xi_{i\alpha}(\mathbf{x},t)$ are the 'abscissas' of the quadrature approximation, M is the number of internal coordinates, and δ indicates the Dirac delta function. Therefore, the mixed moments of the distribution can be written as:

$$m_{k_1,k_2,\ldots,k_M} = \sum_{\alpha=1}^{N} w_\alpha \prod_{i=1}^{M} \xi_{i\alpha}^{k_i}. \tag{14}$$

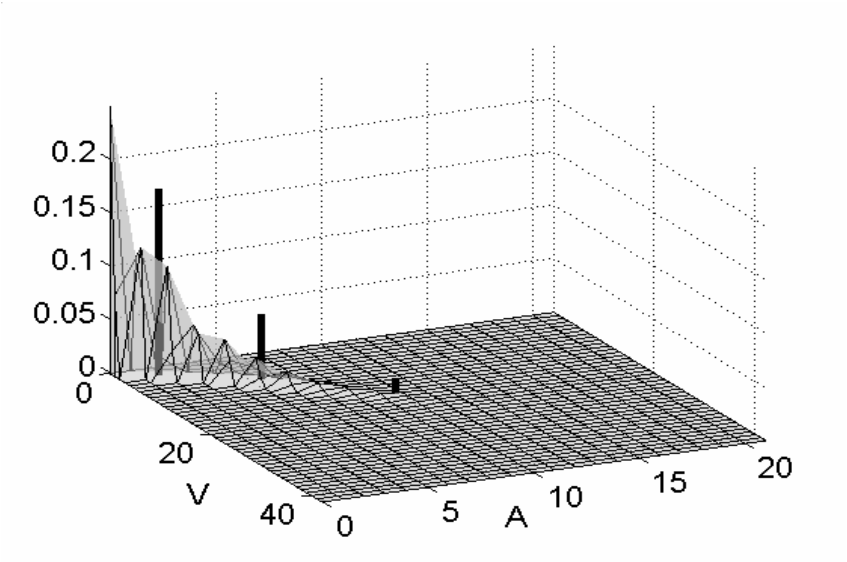

Figure 1. Comparison between a bivariate number density function with respect to surface area and volume (pure coalescence of droplets), and its quadrature approximation with three nodes (black peaks).

It is possible to show that weights and abscissas of the quadrature approximation can be computed forcing them to yield known values of the moments; this can be done either resorting to the Product-Difference (PD) algorithm and solving an eigenvalue-eigenvector problem [19] (but in this case the problem becomes extremely complex when we need to deal with more than one internal coordinate), or directly solving the transport equation of weights and abscissas, as explained by Marchisio and Fox [6]. The DQMOM is based on the latter approach. Let us consider the bivariate case, which has been investigated in the present work: we need to solve the following equations:

$$\frac{\partial w_\alpha}{\partial t} + \frac{\partial}{\partial x_i}\left(\bar{U}_i w_\alpha\right) - \frac{\partial}{\partial x_i}\left[\Gamma_t \frac{\partial w_\alpha}{\partial x_i}\right] = a_\alpha , \tag{15}$$

$$\frac{\partial \varsigma_{1,\alpha}}{\partial t} + \frac{\partial}{\partial x_i}\left(\bar{U}_i \varsigma_{1,\alpha}\right) - \frac{\partial}{\partial x_i}\left[\Gamma_t \frac{\partial \varsigma_{1,\alpha}}{\partial x_i}\right] = b_{1,\alpha} , \tag{16}$$

$$\frac{\partial \varsigma_{2,\alpha}}{\partial t} + \frac{\partial}{\partial x_i}\left(\bar{U}_i \varsigma_{2,\alpha}\right) - \frac{\partial}{\partial x_i}\left[\Gamma_t \frac{\partial \varsigma_{2,\alpha}}{\partial x_i}\right] = b_{2,\alpha} \tag{17}$$

where $\varsigma_{i,\alpha} = w_\alpha \xi_{i,\alpha}$ indicates the □-th 'weighted abscissa', and $a_□$, and $b_{i,□}$ are the source terms. It is possible to show that such source terms can be easily evaluated solving a linear algebraic system, obtained from the population balance equation after the application of the quadrature approximation and forcing the moments to be tracked with high accuracy [6].In principle, if *N* nodes are employed to follow the evolution of *M*

internal coordinates, the method requires the solution of balance equations for $N(M+1)$ scalars, and therefore the solution of a linear system of correspondent rank. We will focus our attention on the bivariate case, which is of interest in the case of soot formation; in this case the number density function is approximated by the following expression:

$$\tilde{n}\left(\xi_1,\xi_2;\mathbf{x},t\right)=\sum_{\alpha=1}^{N} w_\alpha\left(\mathbf{x},t\right)\cdot\delta\left[\xi_1-\xi_{1,\alpha}\left(\mathbf{x},t\right)\right]\cdot\delta\left[\xi_2-\xi_{2,\alpha}\left(\mathbf{x},t\right)\right] \tag{18}$$

and we need to solve for $3N$ scalars (N weights and $2N$ abscissas). A graphical representation of the bivariate quadrature approximation on which the DQMOM is based is depicted in Fig. 1, where a bivariate number density function and its DQMOM representation are compared. If we substitute Eq. (18) into Eq.(11), and rewrite the population balance in terms of the moments of the distribution, we obtain the following linear system:

$$\sum_{\alpha=1}^{N}\left[\left(1-k-l\right)\xi_{1,\alpha}^{k}\xi_{2,\alpha}^{l}a_\alpha+k\xi_{1,\alpha}^{k-1}\xi_{2,\alpha}^{l}b_{1,\alpha}+l\xi_{1,\alpha}^{k}\xi_{2,\alpha}^{l-1}b_{2,\alpha}\right]=\bar{C}_{k,l}+S_{k,l}^{(N)} \tag{19}$$

where $S_{k,l}^{(N)}$ is quadrature approximation with N nodes of the source term for the mixed moment of order k with respect to the first internal coordinate (the volume V in our case), and of order l with respect to the second internal coordinate (the surface area A), and $\bar{C}_{k,l}$ is a correction term which is needed due to the finite-mode representation of the distribution, and is effective only for moments of order two or higher. It is a function of the gradients of internal coordinates, and is evaluated as follows:

$$\bar{C}_{k,l}=\left(\Gamma+\Gamma_t\right)\sum_{\alpha=1}^{N} w_\alpha\left[k\left(k-1\right)V_\alpha^{k-2}A_\alpha^{l}\frac{\partial V_\alpha}{\partial x_i}\frac{\partial V_\alpha}{\partial x_i}+2klV_\alpha^{k-1}A_\alpha^{l-1}\frac{\partial V_\alpha}{\partial x_i}\frac{\partial A_\alpha}{\partial x_i}+\right.$$
$$\left.+l\left(l-1\right)V_\alpha^{k}A_\alpha^{l-2}\frac{\partial A_\alpha}{\partial x_i}\frac{\partial A_\alpha}{\partial x_i}\right]. \tag{20}$$

Let us consider, for the sake of simplicity, the case of two nodes; we need to track 6 mixed moments of the distribution. If, for example, we choose the following 6 pure integer moments: m_{00}, m_{10}, m_{01}, m_{20}, m_{02}, m_{30}, considering particle volume (V) and surface area (A) as the two internal coordinates, the linear system (19) becomes:

$$\begin{pmatrix} 1 & 1 & 0 & 0 & 0 & 0 \\ 0 & 0 & 1 & 1 & 0 & 0 \\ 0 & 0 & 0 & 0 & 1 & 1 \\ -V_1^2 & -V_2^2 & 2V_1 & 2V_2 & 0 & 0 \\ -A_1^2 & -A_2^2 & 0 & 0 & 2A_1 & 2A_2 \\ -2V_1^3 & -2V_2^3 & 3V_1^2 & 3V_2^2 & 0 & 0 \end{pmatrix}\begin{pmatrix} a_1 \\ a_2 \\ b_{V1} \\ b_{V2} \\ b_{A1} \\ b_{A2} \end{pmatrix}=\begin{pmatrix} \overline{S_{00}}^{(2)} \\ \overline{S_{10}}^{(2)} \\ \overline{S_{01}}^{(2)} \\ \overline{S_{20}}^{(2)}+\overline{C_{20}} \\ \overline{S_{02}}^{(2)}+\overline{C_{02}} \\ \overline{S_{30}}^{(2)}+\overline{C_{30}} \end{pmatrix}, \tag{21}$$

We can evaluate the quadrature approximations of the source terms, $\overline{S}_{k,l}^{(N)}$, as described in the following of this section.

Nucleation

For numerical reasons, it is convenient to assume the nucleation of a uniform distribution of nuclei of volume $0 \le v_0 \le \varepsilon_V$ and surface area $0 \le a_0 \le \varepsilon_A$; in this case we obtain the following expression for the nucleation source term:

$$\bar{S}_{k,l}^{(N)} = J(\mathbf{x},t)\frac{\varepsilon_V^k \varepsilon_A^l}{(k+1)(l+1)}, \tag{22}$$

where $J(\mathbf{x},t)$ is the nucleation rate.

In this way, we can compute by the PD algorithm the values of the distinct abscissas corresponding to the nuclei distribution, and use these values to initialize the DQMOM in the regions where particle number density is null, and the matrix of system (19) would be otherwise singular.

Aggregation

If the result of aggregation is a fractal cluster with fractal dimension D_f, and if we assume the following scaling relationship between surface area and volume:

$$\frac{A}{a_0} = \left(\frac{V}{v_0}\right)^{\frac{2}{D_f}}, \tag{23}$$

where a_0 and v_0 are the area and volume of primary particles, then the source term of moments due to aggregation becomes:

$$\bar{S}_{k,l} = \frac{1}{2}\iiint\int_0^\infty \left[(V_1+V_2)^k \left(A_\alpha^{\frac{D_f}{2}} + A_\gamma^{\frac{D_f}{2}} \right)^{\frac{2l}{D_f}} - V_1^k A_2^l - V_1^k A_2^l \right] \cdot \\ \cdot \beta(V_1,V_2,A_1,A_2)\, n(V_1,A_1)\, n(V_2,A_2)\, dV_1 dV_2 dA_1 dA_2, \tag{24}$$

and, after the application of the quadrature approximation:

$$S_{k,l}^{(N)} = \frac{1}{2}\sum_{\alpha=1}^{N}\sum_{\gamma=1}^{N} \left\{ (V_\alpha + V_\gamma)^k \left(A_\alpha^{\frac{D_f}{2}} + A_\gamma^{\frac{D_f}{2}} \right)^{\frac{2l}{D_f}} - V_\alpha^k A_\alpha^l - V_\gamma^k A_\gamma^l \right\} \beta_{\alpha,\gamma} w_\alpha w_\gamma ; \tag{25}$$

we can observe that the terms in curly brackets represent the contributions (positive) of the aggregate and (negative) of the parent particles to the moment $m_{k,l}$

Molecular growth

When considering continuous changes, in general we can account for the drift term for each coordinate independently. If we denote with $G_V(V,A)$ and $G_A(V,A)$ the rate of continuous change of volume and surface area respectively, the source term of the moments is:

$$\bar{S}_{k,l}^{(N)} = \sum_{\alpha=1}^{N} w_\alpha \left[k V_\alpha^{k-1} A_\alpha^l G_V(V_\alpha, A_\alpha) + l V_\alpha^k A_\alpha^{l-1} G_A(V_\alpha, A_\alpha) \right]. \tag{26}$$

Usually, a variation of volume results in a corresponding variation of surface area according to the appropriate volume/area scaling relationship. On the contrary, a change in surface area can be due not to a net mass flux between the particle and

the environment, but to changes in particle structure, as a consequence of external forces; in this case only the surface area is varied, while volume is not affected by the process ($G_V(V,A)=0$).

2.3 Fractal dimension

When solving the population balance in terms of only one internal coordinate, e.g. particle diameter or volume, (monovariate case) the value of the fractal dimension has to be assumed or evaluated independently. The simplest choice is to fix a unique constant value for all the particles; this is quite a rough approximation, since it is known that aged soot aggregates undergo some restructuring processes that compact the aggregates increasing their fractal dimension [20, 21]. An alternative approach, recently proposed by Artelt *et al.* [22], relates the fractal dimension to the ratio $\tau = t_c / t_r$ of the characteristic collision time $t_c = \left(\bar{\beta} \cdot m_0\right)^{-1}$, where $\bar{\beta}$ is the mean aggregation kernel and m_0 is the number concentration of particles (i.e., the zero-th moment of the distribution), to the characteristic restructuring time t_r. If it is assumed that the restructuring of soot particles is due to an elastic-mechanical strain effect, the characteristic time t_r can be considered equal to a turbulence time micro-scale $\left(t_r = \sqrt{15\nu/\varepsilon}\right)$, so that the rate of the restructuring process is assumed proportional to the shear rate inside the turbulent eddy.

According to Artelt *et al.* [22], the evolution of the fractal dimension can be modelled as:

$$D_f = \begin{cases} D_{f,\min} + \left(D_{f,0} - D_{f,\min}\right)^{1/\tau^s} & \tau \le 1 \\ D_{f,\max} + \left(D_{f,\max} - D_{f,0}\right)^{\tau^s} & \tau > 1 \end{cases}. \tag{27}$$

In Eq.(27), $D_{f,\min} \ge 1$ and $D_{f,\max} \le 3$ are the minimum and maximum value of the fractal dimension, corresponding to the limiting cases for $t_c \ll t_r$ and $t_c \gg t_r$ respectively, $D_{f,0}$ is the fractal dimension at which the characteristic times of the two processes are equal, which is assumed to be the arithmetic average value between the limiting cases, and *s* is a parameter that defines the slope of fractal dimension variation. A detailed discussion of these approaches can be found in [23], where the solution of the monovariate population balance equation was extensively treated. A more rigorous treatment of the fractal properties of aggregates requires the solution of a bivariate population balance equation, which has been implemented and compared with the monovariate simulation in the present work.

2.4 Kinetic models for soot formation

The model takes into account nucleation of particles, molecular growth, aggregation and oxidation of soot particles. Since the main objective of this work is to assess the performance of the bivariate DQMOM for this kind of application, simplified kinetic models were employed, in order to avoid unnecessary CPU load required for the implementation of detailed kinetics. Several models available in the

related literature were tested, and the rate expressions that gave the best agreement with experimental data are reported in Tab. 1. Acetylene is chosen as the key compound for nucleation and molecular growth. The aggregation kernel, which depends on the Knudsen number (the ratio between the mean-free-path of gas molecules, λ, and the particle radius: $Kn = 2\lambda/L$), was evaluated by the Fuchs interpolation formula [27], which is valid in the transition regime between the free molecule ($Kn \ll 1$) and the continuum ($Kn \gg 1$) regime. All the rate expressions were adapted to take into account the fractal dimension D_f of the particle.

The radiative transfer due to soot particles was taken into account by introducing an additional source term for the energy equation:

$$\dot{Q}_{rad} = -\sigma \cdot a_S \cdot \left(T^4 - T_\infty^4\right), \tag{28}$$

where σ is the Stefan-Boltzmann constant, a_S is the soot absorption coefficient, and T_∞ is the radiative environment temperature (set to 300 K).

The absorption coefficient was evaluated by the expression recently proposed by Widmann [28]:

$$a_S = 2370 \cdot T \cdot f_V \tag{29}$$

where f_V is the soot volume fraction.

2.5 Numerical details

Process	Rate expression	Ref.
Nucleation ($m^{-3}s^{-1}$)	$J = N_A \cdot \rho^2 \cdot T^{\frac{1}{2}} \cdot 6 \cdot 10^6 \cdot \exp\left(-\frac{46100}{T}\right) X_{C_2H_2}$	[24]
Molecular Growth ($m\ s^{-1}$)	$G_{mg} = \frac{6}{D_f \rho_s}\left(\frac{R_c}{R_{c0}}\right)^{3-D_f} \cdot 2 \cdot M_s \cdot \exp\left(-\frac{6038}{T}\right)[C_2H_2]$	[25]
Oxidation ($m\ s^{-1}$)	$G_{ox} = -\frac{P}{D_f \rho_s} \cdot T^{-\frac{1}{2}} \cdot 6.5 \cdot \exp\left(-\frac{26500}{T}\right) \cdot Y_{O_2}$	[26]
Aggregation (m^3s^{-1})	$\beta_{12} = 4\pi(D_1+D_2)(R_{c1}+R_{c2})\left[\frac{R_{c1}+R_{c2}}{R_{c1}+R_{c2}+\left(g_1^2+g_2^2\right)^{1/2}} + \frac{4(D_1+D_2)}{(R_{c1}+R_{c2})\left(c_1^2+c_2^2\right)^{1/2}}\right]^{-1}$ $c_i = \sqrt{\frac{8k_bT}{\pi m_i}} \qquad D_i = \frac{k_bT}{6\pi\mu R_{ci}}\left[\frac{5+4Kn_i+6Kn_i^2+18Kn_i^3}{5-Kn_i+(8+\pi)Kn_i^2}\right] \qquad l_i = \frac{8D_i}{\pi c_i}$ $g_i = \frac{\left(2R_{ci}+l_i\right)^3-\left(4R_{ci}^2+l_i^2\right)^{3/2}}{6R_{ci}l_i} - 2R_{ci}$	[27]

Legend		
k_b : Boltzmann constant	m : particle mass	
M_s : soot molecular weight	μ .:gas viscosity	
N_A : Avogadro's Number	ρ .:gas density	
X : mole fraction	ρ_σ.:soot density	
Y : mass fraction		

The DQMOM was implemented via user-defined functions within the commercial finite-volume CFD code FLUENT 6.0, which computes the velocity, temperature and composition fields. The standard k-ε model was employed for the turbulence closure, while the mixture-fraction beta-PDF approach with the chemical equilibrium assumption (considering 19 species) was used for modelling micro-mixing and reaction. The particles have been assumed small enough as to have a negligible effect on the global flow-field of the flame, so that the simulation can be monophase. The simulations were carried out with a two-dimensional conformal grid with 10500 rectangular cells.

3. RESULTS AND DISCUSSION

As it has been shown in our work on the solution of the monovariate population balance [23], the agreement with experimental data of temperature and soot volume fraction is quite good for the flame under investigation, even if quite simple modelling approaches have been employed to model turbulence-chemistry interaction and kinetics of soot formation. If we accept the assumption that particle morphology has no effect on the radiative properties of soot and on kinetics of soot formation, the profiles of velocity, temperature and volume fraction shouldn't change passing from the monovariate to the bivariate population balance. The first hypothesis is quite strong, but it is coherent with the model employed for the treatment of radiation, which assumes the absorption effect of soot only proportional to soot volume fraction. The models employed for the kinetics of surface growth and oxidation are instead function of fractal dimension (and therefore particle morphology), but results of the bivariate simulation showed that the profiles of soot volume fractions (reported in Fig. 2) are not significantly different from those obtained in the monovariate case. Therefore, for the bivariate simulations, the velocity, temperature and gas phase composition fields were not updated during the computation, but the profiles computed during monovariate simulations (see [23]) were held constant. In this way, only the transport equations of the six scalars required for the solution of the population balance with the two nodes DQMOM ($w_1, w_2, V_1, V_2, A_1, A_2$) were solved, with significant saving of computational resources.

For the simulations, the choice of only pure moments discussed in the previous section and leading to the linear system in Eq.(21) was implemented. The choice of only pure moments is maybe not the best one, especially if accurate information on the shape of the bivariate particle size distribution is required, since the correlation between internal coordinates is not accounted for properly; however, this choice guarantees both good numerical stability, and good accuracy in the predictions of lower order moments. A more complete discussion of the choice of moments to be tracked, and a validation of the method by comparison with Monte Carlo simulations, can be found in [29].

Aggregation is supposed to lead to particles with the lowest fractal dimension (D_f = 1.8), while the restructuring process is modelled by the following expression, similar to that proposed by Koch and Friedlander [30] for sintering of aggregates formed by primary spherical particles:

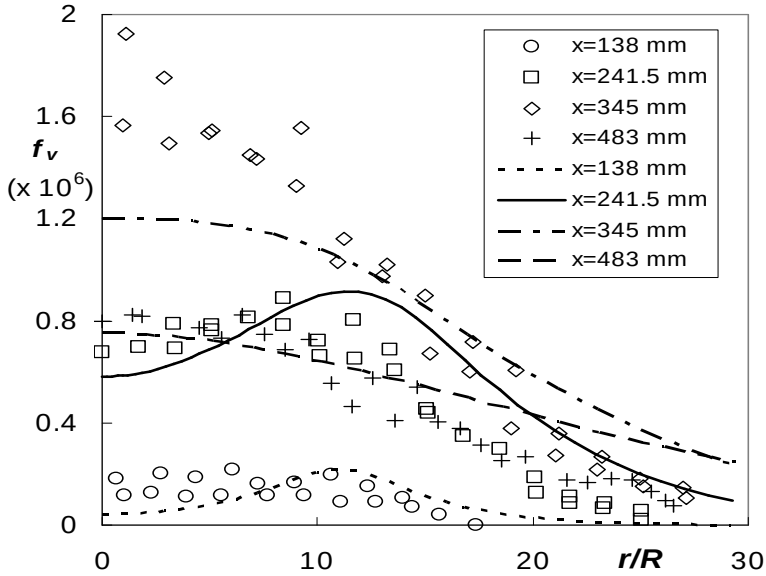

Figure 2. Comparison between experimental (symbols) and simulated (lines) soot volume fraction from bivariate simulations at several heights above the burner.

$$\frac{dA}{dt} = -\frac{1}{t_r}\left(A - A_{\min}\right), \tag{30}$$

where $A_{\min}$ is the surface area of a sphere with the same volume as the restructured particle. The local fractal dimension, which is needed to compute the collision radius and the kinetic expressions for aggregation, oxidation and molecular growth, is computed from the local volume and surface areas through the following equation, derived from Eq. (23):

$$D_f = 2\frac{\ln\left(\frac{V}{v_o}\right)}{\ln\left(\frac{A}{a_0}\right)} \tag{31}$$

The use of a larger number of nodes would result in more accurate predictions, but numerical problems concerning the conditioning of the linear system can hinder convergence.

In Fig. 3 the evolution along the axis of the flame of the fractal dimension (a) and the mean particle size (b) obtained from the bivariate simulation is shown and compared to profiles obtained from the algebraic equation (Artelt's model). As expected, in the first part of the flame aggregation is dominant, and the mean fractal dimension decreases; when, further downstream, aggregation becomes too slow, the restructuring process keeps on increasing fractal dimension and reducing surface area and collision radius. It is possible to see that when Eq. (27) is employed, although the qualitative behaviour is well reproduced, the restructuring rate (and the final fractal

dimension of the aggregates) is overestimated, and the simulated collision radius is lower than in the case of bivariate simulations.

In Fig. 4 the same results reported in Fig. 3 are reported in the area-volume phase plane. In this plot the evolution of the mean particle volume and mean particle surface area (defined as the area of the sphere of radius R_c) is reported. In the same figure, some contour lines at constant fractal dimension are plotted; the trajectories obtained by imposing a constant value of D_f overlap these contour lines. It is clear that the choice of a constant value of fractal dimension is a strong modelling limitation and could represent also a poor approximation if the process under study is characterized by marked morphology changes (as it is for soot formation in turbulent flames).

The agreement between the bivariate and the monovariate simulations is quite good as far as the restructuring rate is not significant, while evident differences are observed in the last part of the flame, where aggregation becomes much less important and the restructuring process makes aggregates more compact, reducing the value of particle surface area.

Even if a validation of the bivariate DQMOM for the prediction of particle morphology still needs to be done, since the bivariate formulation describes with more detail the processes occurring in the flame its prediction will likely be more accurate. However, this study has highlighted the importance of modelling the evolution of particle morphology with the maximum possible detail.

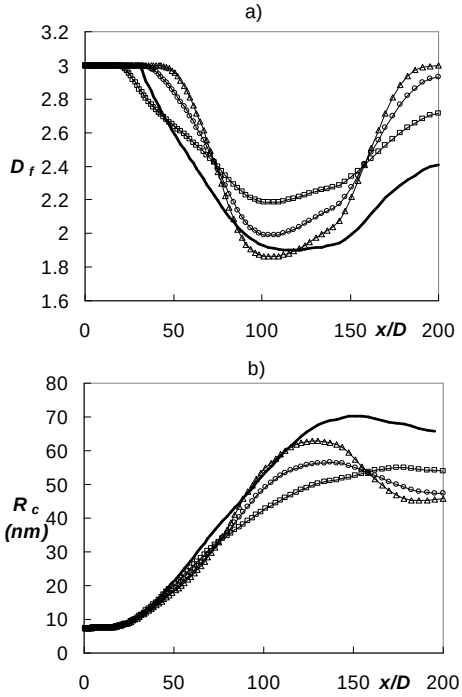

Figure 3: Axial profiles of fractal dimension (a) and collision radius (b). Solid line: bi-variate simulation; symbols: mono-variate simulation with algebraic equation for variation of D_f. Squares: s=0.5; Circles: s=1.0; Triangles: s=1.5.

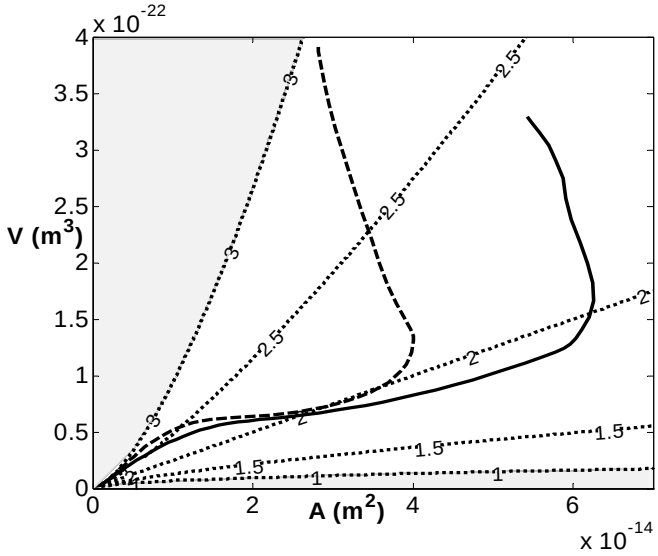

Figure 4. Evolution of particle volume and surface area in the phase plane: comparison between monovariate and bivariate simulations. Dashed line: monovariate simulation (Artelt's model, *s*=1); Dotted lines: contour levels of constant fractal dimension; Solid line: bivariate simulation.

4. CONCLUSIONS

In this work the population balance equation was implemented in a commercial CFD code for modelling soot formation in turbulent diffusion flames. The problem was solved by the DQMOM, which is a novel formulation of the well-known QMOM and presents important advantages for treating multi-variate population balances. Simulation results have shown that the method is a suitable tool for the solution of the considered problem in the mono-variate case, and can be easily extended to the bi-variate case to take into account more rigorously the fractal properties of soot particles.

Acknowledgements

Partial financial support to this research by the Italian Ministry of University and Research (M.I.U.R.) is gratefully acknowledged (PRIN Project 2003: *Combustion formed particulate: mechanisms of formation, low-emission technologies, health and climate effects.*).

Nomenclature

A particle surface area
a source term for weights
a_s absorption coefficient
b source term for abscissas
C correction term

d particle diameter
D_f fractal dimension
f_v soot volume fraction
J nucleation rate
k order of the moments
Kn *K*nudsen number
L abscissa of the quadrature approximation
L *w*eighted abscissa
t time
M n° of internal coordinates
m moment of the distribution
N *n*° of nodes of the quadrature approximation
P pressure
R radius
S source term
T temperature
U mean value of velocity
u fluctuation of velocity
V particle volume
w weight of the quadrature approximation
x spatial coordinate

Greek letters

β aggregation kernel
Γ diffusivity
ε maximum size of nuclei/turbulent dissipation rate
λ mean free path of gas molecules
ν kinematic viscosity
$\boldsymbol{\xi}$ internal coordinate vector
ρ density
σ Stefan-Boltzmann constant
$\boldsymbol{\Phi}$ scalar vector
ϕ fluctuation of scalar concentration

Subscripts

0 primary particle
c coagulation
g gyration
r restructurisation
t turbulent

REFERENCES

1. A. D'Anna, A. Violi, A. D'Alessio, A. F. Sarofim, *Combustion and Flame,* **2001**, *127*, 1995-2003.
2. H. Richter, J. B. Howard, *Progress in Energy and Combustion Science*, **2000**, *26*, 565-608.
3. M. Vanni, *Journal of Colloid and Interface Science,* **2000**, *221*, 143-160.
4. R. McGraw, *Aerosol Science & Technology*, **1997**, *27*, 255-265.
5. D. L. Marchisio, J. T. Pikturna, R. O. Fox, R. D. Vigil, A.A. Barresi, *A.I.Ch.E. Journal*, **2003**, *49*, 1266-1276.

6. D. L. Marchisio, R. O. Fox, *Journal of Aerosol Scence,* **2005**, *36*, 43-73.
7. J. H. Kent, D. Honnery, *Combustion Science and Technology*, **1987**, *54*, 383-397.
8. B. E. Launder, D. B. Spalding, "Lectures in Mathematical Models of Turbulence", Academic Press, London, England, 1972.
9. V. Yakhot, S. A. Orszag, *Journal of Scientific Computing*, **1986**, *1*, 1-51
10. T. H. Shih, W. W. Liou, A. Shabbir, J. Zhu, *Computers and Fluids*, **1995**, *24*, 227-238.
11. B. E. Launder, G. J. Reece, W. Rodi, *Journal of Fluid Mechanics*, **1975**, *68*, 537-566.
12. B. E. Launder, *International Journal of Heat and Fluid Flow*, **1989**, *10*, 282-300.
13. B. F. Magnussen, B. H. Hjertager, *Proceedings of the 16th International Symposium on Combustion*, **1976**, The Combustion Institute, 719-729.
14. S. B. Pope, *Progress in Energy and Combustion Science*, **1985**, *11*, 119-192.
15. J. Baldyga, *Chemical Engineering Science*, **1994**, *49*, 1985-2003.
16. R. O. Fox, *Chemical Engineering and Processing*, **1998**, *37*, 521-535.
17. K. N. Bray, N. Peters, In P. A. Libby and F. A. Williams (eds.), "Chemically Reacting Flows", Academic Press, 1994.
18. R. O. Fox, "Computational models for turbulent reacting flows", Cambridge University Press, Cambridge, UK, 2003.
19. R.G. Gordon, *Journal of Mathematical Physics,* **1968**, *9*, 655.
20. S. Di Stasio, *Journal of Aerosol Science*, **2001**, *32*, 509-524.
21. S. Di Stasio, A.G. Kostandopoulos, M. Kostoglou, *Journal of Colloid and Interface Science*, **2002**, *247*, 33-46.
22. C. Artelt, H. J. Schmid, W. Peukert, *Journal of Aerosol Science*, **2003**, *34*, 511-534.
23. A. Zucca, D. L. Marchisio, A. A. Barresi, R. O. Fox, *Chemical Engineering Science*, **2005**, to appear.
24. J. B. Moss, C. D. Stewart, K. J. Young, *Combustion and Flame*, **1995**, *101*, 491-500.
25. F. Liu, H. Guo, G. J. Smallwood, O. Gulder, *Combustion Theory and Modelling*, **2003**, *7*, 301-315.
26. R. Said, A. Garo, R. Borghi, *Combustion and Flame*, **1997**, *108***,** 71-86.
27. N. A. Fuchs, "Mechanics of Aerosols", Pergamon, New York, U.S.A., 1964.
28. J. F. Widmann, *Combustion Science and Technology,* **2003**,*175*, 2299-2308.
29. A. Zucca, "Modelling of turbulence-chemistry interaction and soot formation in turbulent flames.", Ph.D. Thesis, Politecnico di Torino, Torino, 2005.
30. W. Koch, S. K. Friedlander, *Journal of Colloid and Interface Science,* **1990**, *140*, 419-427.

STUDIA UNIVERSITATIS BABES-BOLYAI, CHEMIA, L, 2, 2005

SCHEDULING BATCH PROCESSING: GENETIC ALGORITHMS VERSUS MATHEMATICAL PROGRAMMING

JERKER BJÖRKQVIST

Åbo Akademi University, Turku, Finland

ABSTRACT. Genetic algorithms have during the recent years gained popularity also in the domain of chemical engineering, among other applications for scheduling purposes. A genetic algorithm builds new sequences by combining and mutating previous sequences of genes, i.e. chromosomes, into a new set of chromosomes. In this new set, only the fittest survive, and the procedure is repeated. As a schedule in chemical batch plant can be seen as a sequence of starting points for the batches, the methodology of genetic algorithms can be applied also to batch scheduling.

In this work, the genetic algorithm approach is used combined with a Discrete Event Simulation (DES) approach. Here the genetic algorithm determines the order of the batches, whereas the DES-approaches insert the batches in the actual schedule. Using this two-stage optimization and some tuning of the DES procedures, schedules with similar objective function values as with mathematical optimization can be achieved, but usually much faster, which is essential for industrial scheduling systems.

INTRODUCTION

Genetic algorithms are a straightforward way of generating sequences that can be used for different purposes. Even if the implementation is rather trivial, applying genetic algorithms to actual problems are seldom as easy. This is also the case with batch scheduling. First of all, the question is how to represent the batches using the genes in the chromosome. One solution is to let the chromosome, i.e. the sequence of genes, represent the feed-order in which the batches are “entered” into the plant. As we now know the order of the batches, we have to somehow determine the real starting times of the batches. Only then we can give a goodness of the schedule, which is needed for the genetic algorithm. One method used for determining starting times for batches is Discrete Event Simulation (DES), used by e.g. Azzarello-Pantel et. al. (1998) [1]. This they call a two-stage methodology, the genetic algorithm determine the relative order of the batches, whereas DES determine the real starting times. Löhl et. al. (1998) [4] use a somewhat similar approach but use an analogue term “schedule builder” for the operations of DES.

One typical issue is that the DES operation has to use some particular heuristics for building the schedule. This heuristics might for instance be to insert the following run as early as possible on any available machine. This heuristics may however yield schedules that are not optimal in some other context. Schedules also often render infeasible, if batches are inserted one by one and internal batch relationships at some point are impossible to fulfill.

The two-stage methodology can also be adopted so that the gene represents for instance the start of a series of batches that are tightly coupled. Here, *tightly coupled* means that intermediates between the batches have limited storage time. This decreases the search space and hence erases candidates for optimal solutions. However, an open question is if these erases candidates truly contain optimal solution to the schedule problem.

In this work, the basic two-stage methodology of a genetic part and a DES part is used. In this approach, three different ways for connecting the genetic algorithm and the DES part is used. The first version is individual insertion of batches; the second is where complete chains of batches are inserted. A chain of batches here corresponds to that part of the production chain where intermediate products have limited storage time. The third version is where batches are inserted one by one, but now the gene represents from which chain the batch should be inserted into the schedule.

This resembles the work simultaneously performed by Berning et. al. (2004) [2], in which the GA schedule-builder approach is augmented by chain building procedures.

In this work, the methodology is tested using both some more theoretical job-shop-type scheduling and with some real-life scheduling problem taken from a pharmaceutical plant. In the plant in question typical conditions for the scheduling arises, such as different type of storage of the intermediates, sequence dependent cleaning and other issues that limits the sequencing possibilities of equipment used.

Similar schedules have earlier been optimized by Roslöf et. al. (2001) [5] and Björkqvist et. al. (2002) [3] using mathematical programming methods. In this work, the schedules are built using the GA/DES-methodology, and the tests shown that GA/DES perform very well. Here this mean that an objective functions of similar quality will usually be reached much faster using GA/DES methodology compared to the mathematical programming approach used in earlier works.

PROBLEM FORMULATION

In a batch processing plant, final products are produced using a set of operations in the plant. A recipe denotes the operations needed for producing some amount of a final product. The recipe also denotes the internal relation between the operations, which typically is precedence constrains, i.e. which operations produces respectively consumes the intermediates. We here call operations that are instantiated “runs”. A run can be performed on a set of suitable equipment *Ui*. Now, the scheduling problem is to find starting times *ti* and selected unit *ui* for all runs, according the selected objective function. The objective function can vary, often minimizing the total make-span is used, but other might be important, e.g. minimizing the setup-time needed between operations or minimizing the number of late orders. In this paper, we use the total make-span as the objective function.

SCHEDULING USING MATHEMATICAL PROGRAMMING

A mathematical programming approach can be used for scheduling. Here, we use a Mixed Integer Linear Programming (MILP) formulation for specifying the optimization problem. The basic approach is to compare relative orders of the runs and build inequalities accordingly:

$$t_j + t^p{}_j < t_j \ \vee \ t_j + t^p{}_j < t_j$$

which using a ”Big-M” reformulation is transferred into a MILP expression

$$t_i + t^p{}_i < t_j + y_{i,j} M$$

$$t_j + t^p{}_j < t_i + (1 - y_{i,j}) M$$

where $y_{i,j}$ is a binary variable specifying if run *i* will precede run *j*. In the case of more general batch scheduling, this notation is not enough, but these formulation are not given here, but can be found in Björkqvist et. al. (2002) [3].

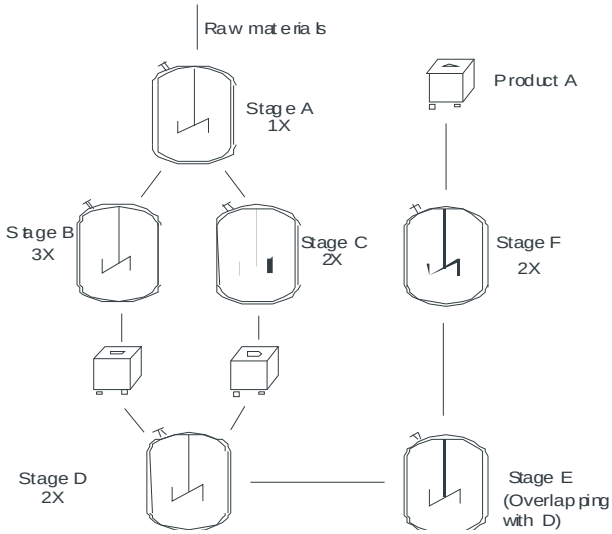

Figure 1. Example of a recipe

The basic MILP formulation presented above works fine for small problems, and optimal solutions to the scheduling problem will be provided. Practical problem can however seldom be solved using direct MILP formulations, the methodology used here is instead a iterative procedure, which is basically contains the following steps:

1. Solve a subset of the original scheduling problem to optimality
2. Fix the relative order of the runs in the previously solved problem, enlarge the subset of the problem and resolve until completely solved

This procedure is moreover called Sequential Updating Procedure (SUP). If we start reinserting runs in the schedule, we call this procedure Post Processing (PP).

SCHEDULING USING GENETIC ALGORITHMS

The proposed Genetic Algorithm approach is actually a combined Genetic Algorithm and Discrete Event Simulation (DES) approach. The Discrete Event Simulation is used for simulating systems where discrete events change the otherwise continuous simulations. Here, the discrete events are when operations are started and stopped in the plant. Now, we let the Genetic Algorithm provide the order in which the events are taking place, whereas the DES-simulation provides the timing information. The DES here use the logic:

* For the given run, selected the machine where it first can be started, and derive the starting time for this run

Now, when the procedure is repeated for each run, a schedule is generated. From this schedule, the metrics of the schedule can be calculated. Some selected metrics (e.g. the total make-span) of the schedule is now providing the fitness-value.

In a genetic algorithm, a chromosome represents a solution candidate to an optimization problem. In our scheduling case, the chromosome represents in which order DES will insert runs to the schedule. We let the genes in the chromosome specify which run the DES should insert next.

However, many times this lead to infeasible situations, as the production process also requires some particular run precedence. If the chromosome specifies a run order that that contradicts to this precedence, the schedule cannot be build. Hence, we let the gene specify which groups of runs to be scheduled next, inside this group the runs are ordered according to internal precedence. This is the approach used here.

The GA is implemented the standard way using a crossover, mutation and elitism.

TEST USING JOB-SHOP-PROBLEMS

In order to validate the general quality of the schedules achieved with the two approaches, some standard job-shop scheduling problems were solved. In a job-shop problem, a job is a collection of operations (runs), each of which shall be performed once on each machine. In the job-shop problem, the order in which the runs shall be performed on the machines are given. Here, we test with two different sizes of job-shop-problems, which are built according to the OR Library of test problems. The job-shop instances where 6x6, 10x10, 20x5, 15x15. The objective function used here is to minimize the make-span.

Table 1

Objective function value (minimizing make-span) and processing times for some job-shop problems

JSP size	SUP	SUP+PP	GA
6x6	58 (0 s)	55 (0,1 s)	55 (14 s)
10x10	1401 (0,9 s)	994 (450 s)	1018 (11 s)
20x5	1259 (90 s)	1206 (260 s)	1207 (16 s)
15x15	1503 (6 s)	1191 (75 s)	1243 (86 s)

Additionally, we can compare how the objective function value is developed over time for the methods SUP+PP versus GA. In figure 2 the typical trends are shown. GA drops rapidly to an asymptotical level, where as the mathematical programming approach slowly moves towards the same level, and by time if will be better than the GA approach. This has been observed as the general trend.

SOLVING A PRODUCTION PLANNING PROBLEM

Next, the two methodologies are applied to the actual problem, a scheduling problem for batch operations. What here is different from the pure job-shop problem is that the schedulers also have to handle some new sequencing constrains, such as limited shelf life of intermediate products. Other new issues are for instance that one run may wait on several runs before it can be started. Intermediate storage is also an important issue, as the production equipment itself often is used as storage for intermediates. Now the question is if we can draw similar conclusions for the more general scheduling problem in the chemical industry.

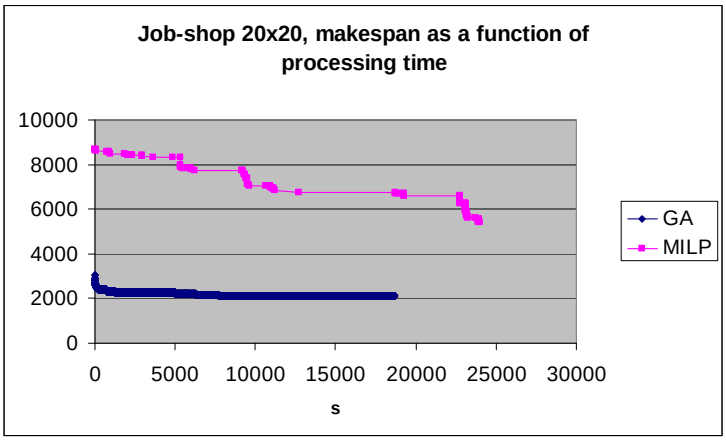

Figure 2. Objective function value for SUP+PP / GA

As an example, a fictive product P is produced at a plant. This product P is produced according to the recipe given in figure 3.

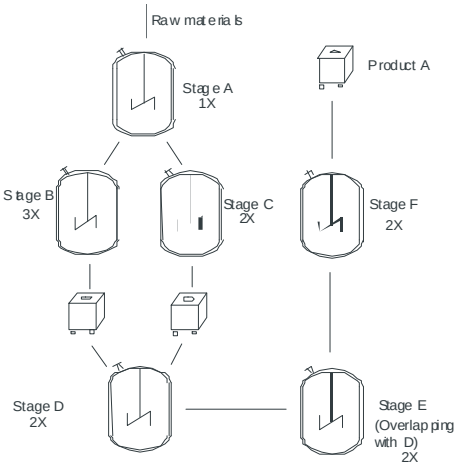

Figure 3. Production recipe for A

In the figure we note that the production of one batch of final product A is started by stage A, where after intermediates products are used by stage B and stage C. After this we store the intermediates temporally and feed them to stage D. So it continues until we finally get product A. Each stage of production has a production time, cleaning time and available units according to table 2.

The basic batch is for production of 150 kg final product A. Now the scheduling problem is solved by both the mathematical approach and the GA approach. The results are given in table 3, here has also the total make-span been used as the objective function.

Table 2

Stages for production of A

Stage	Units	Def. cleaning	Processing	Shelf-life
A	U1, U2	4	7	48
B	U3, U4	2	4	60
C	U3, U4	2	7	60
D	U1, U2	4	10	24
E	U5	4	8	24
F	U6	0	1	48

Table 3

Optimization results for production of A

Case	Amount	SUP+PP	GA1	GA2
1	300	2160 (0s)	2160 (0s)	2460 (0s)
2	600	3360 (3s)	3300 (1s)	3600 (1s)
3	900	4440 (198 s)	4440 (24s)	4740 (4s)
4	1200	5760 (171s)	5580 (1s)	6060 (1s)
5	2400	13740 (407s)	10440 (18s)	10380 (38s)

In the table GA1 and GA2 denotes slightly different DES inserting strategies, where GA1 is a single run inserting strategy and GA2 is a strategy of always inserting runs in the precedence order. Here we see that the GA optimization method is rather competitive, and produce good results very fast. However, the trend is also here like the trend in job-shop problem that in the long run SUP+PP produces better results.

The corresponding comparison of objective value development during the optimization is shown in figure 4. In the beginning, the GA approach rapidly drops to the level that remains almost constant. SUP+PP (MILP in the figure) in this case also seems to be remain on a higher level than the GA approach, but would eventually reach the optimal objective function value.

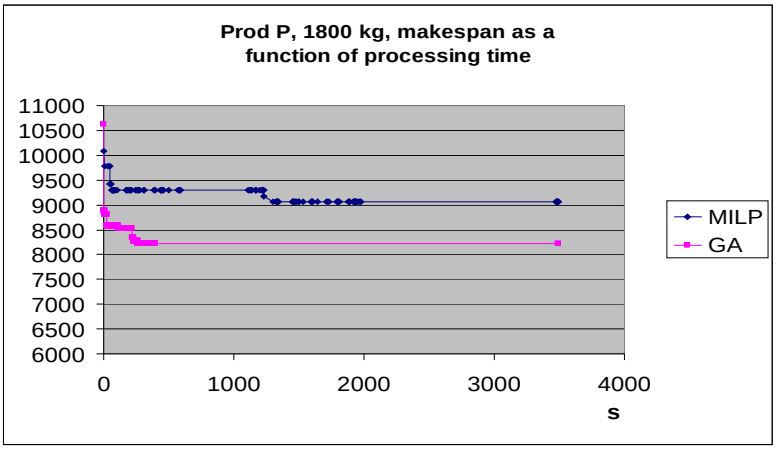

Figure 4. Objective function as a function of optimization time

SUMMARY

In the paper, we have shown two different ways of optimizing batch scheduling. We have shown that both mathematical programming and genetic algorithms can be applied, and it was shown that scheduling results using both approaches are comparable. However, the general trend seems to be that genetic algorithms more rapidly produce good results, hence genetic algorithms should be a good choice for interactive systems, where the need for fast response times of the scheduling subsystem is essential. However, the mathematical programming approach can still be important for getting information on the quality of the solution.

REFERENCES

1. Azzaro-Pantel, C., Bernal-Haro, L., Baudet, P., Domenech, S., Pibouleau, L., 1998. A two-stage methodology for short-term batch plant scheduling: discrete-event simulation and genetic algorithm. Comput. Chem. Eng. 22 (10), 807-825.
2. Berning, G., Brandenburg, M., Gürsoy, K., Kussi, J.S., Mehta, V., Tölle, F-J., 2004. Integrating collaborative planning and supply chain optimization for the chemical process industry (I) methodology. Comput. Chem. Eng. 28 (6-7) 913-927.
3. Björkqvist, J., Roslöf, J., Rönnback, R., Westerlund, T., 2002. Evaluation of an iterative mathematical optimization approach for industrial size batch scheduling. In: Pierucci, S. (Ed.), Selected Papers of The Fifth Italian Conference on Chemical and Process Engineering. Vol. 5, 33-40.
4. Löhl, T., Schulz, C., Engell, S., 1998. Sequencing of Batch Operations for a Highly Coupled Production Process: Genetic Algorithms Versus Mathematical Programming. Comput. Chem. Eng. 22 (Suppl) S579-S585.
5. Roslöf, J., Harjunkoski, I., Björkqvist J., Karlsson S., Westerlund T., 2001. An MILP-based reordering algorithm for complex industrial scheduling and rescheduling, Comput. Chem. Eng 25 (4-6), 821-828.

STUDIA UNIVERSITATIS BABEŞ-BOLYAI, CHEMIA, L, 2, 2005

SELECTIVE CATALYTIC REDUCTION OF NO_X WITH NH_3 IN UNSTEADY-STATE REACTORS

CLAUDIU CRISTIAN BOTAR-JID*, PAUL SERBAN AGACHI*, DAVIDE FISSORE*, ANTONELLO A. BARRESI**

* *Faculty of Chemistry and Chemical Engineering, University "Babes-Bolyai" of Cluj, Str. Arany Janos nr. 11, 3400 Cluj-Napoca (Romania)*

** *Dipartimento di Scienza dei Materiali ed Ingegneria Chimica, Politecnico di Torino, corso Duca degli Abruzzi 24, 10129 Torino (Italy)*

ABSTRACT. The paper surveys the perspective of de-NO*x* Selective Catalytic Reduction (SCR) with ammonia in forced unsteady-state reactors. Two types of reactor configuration were investigated by means of numerical simulation: the well known reverse-flow reactor (RFR) and, as an alternative, a reactors network (RN) with periodical change of feeding position. While in the first device the unsteady-state operation results from periodical reversal of the flow direction, in the second one this is a consequence of modifying the reactor sequence in the network, the flow direction remaining the same; by this way ammonia emissions, which occur in RFR at every switch of flow direction and whose level is subject to stricter limits than for NO_x, is avoided. The influence of the switching time and of the switching strategy in the RN on the mean concentration of NH_3 and NO_x in the reactor outlet flow was also investigated.

Keywords: Reverse-flow reactor, Reactors Network, Chromatographic reactor, Selective Catalytic Reduction, Pollutant destruction

INTRODUCTION

Forced unsteady-state catalytic reactors have been a subject of intensive investigation by means of experiments and numerical simulations in the past several years. The unsteady-state operation may provide significant efficiency enhancement, increased selectivity, high productivity and low operating costs in a number of catalytic processes.

Unsteady-state operation may arise from variations (periodical or not) in the inlet flow rate, feed composition, temperature or pressure, as well as from the periodical reversal of the feed direction.

Reverse-flow operation has two main advantages: first, it allows for trapping the moving heat/concentration wave inside the catalytic bed when exothermic reactions take place, giving the possibility of exploiting the thermal storage capacity of the catalytic bed, which acts as a regenerative heat exchanger, allowing for auto-thermal behaviour even when the adiabatic temperature rise of the feed is low. Second, when exothermic equilibrium-limited reactions are carried out, the reversal of the flow allows for approaching the temperature distribution corresponding to maximum product generation. The Reverse-Flow Reactor (RFR) operation was suggested firstly by Cottrell (1938) as an efficient way to treat dilute pollutant mixtures.

The idea of using a RFR for destruction of a pollutant A with a reactant B, for which the maximum allowable emission is much lower than that of the first one, was firstly given by Agar and Ruppel (1988). They suggested to carry out the selective catalytic reduction (SCR) of NOx with ammonia in a RFR with a catalyst that strongly adsorbs the ammonia. This operation method is referred to as reverse flow chromatographic reactor (RFCR) and allows not only the trapping of the hot wave but also the trapping of ammonia in the bed minimizing its emissions and providing an effective response to reactant fluctuations in the feed rate.

Successful operation of a RFCR requires finding of a catalyst which strongly adsorbs the ammonia: the higher the adsorptivity, the more efficient is the operation.

Nevertheless the RFR exhibits the problem of wash out, i.e. the emission of unconverted reactants occurring when the flow direction is reversed.

The problem of wash out in the RFR was addressed by Brinkmann et al. (1999) in catalytic after-burners, by Velardi & Barresi (2002) in low pressure methanol synthesis and by Fissore, Barresi & Baldi (2003) in synthesis gas production. In all these papers an alternative reactor configuration was studied to avoid the occurrence of wash out, namely a Reactors Network (RN) made of two or three reactors connected in a closed sequence (Figure 1).

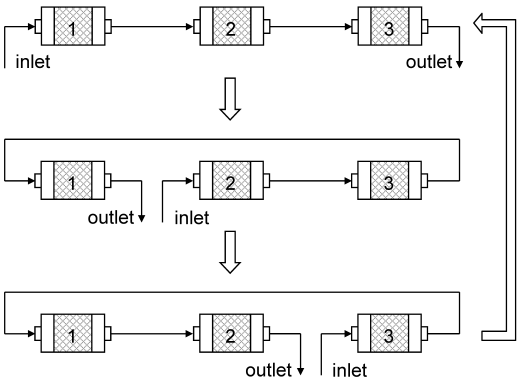

Figure 1. Exemple of Reactor Network operation

A set of valves enables to change the feed position, thus varying the sequence of reactors, simulating the behaviour of a moving bed, and achieving a sustained dynamic behaviour. Contrary to the RFR, the flow direction is maintained in this way, ensuring a uniform catalyst exploitation and avoiding wash out. One of the aim of this paper is thus to study the possibility of carrying out the SCR of NO_x with ammonia using the RN in order to overcome the problems aroused with the RFR.

The assumption of negligible temperature rise in the RFCR and isothermal condition is present in all the works concerning the SCR with NH_3. This allowed to simplify the analysis, enabling to focus on the impact of the operation strategy on the dynamic features caused by the trapping of one reactant in the reactor.

The adiabatic rise in NO_x removal is usually of the order of 10-20 K, but the temperature rise in a RFR can be a multiple of this value, thus allowing, for example, autothermal operation when low temperature gas is fed to the reactor. In this conditions, as it was stressed in the conclusion of the paper of Yong & Luss (2003), the choice of the switching time will be affected also by the dynamics of the heat wave, as too long switching time will lead to reaction extinction, due to the heat removal from the catalyst.

To study the possibility of improving the reactor operation we also have taken into account, beside the storage of the adsorbed ammonia on the catalyst bed, different chemical activities and adsorptive capacities of the catalyst.

The influence of reaction kinetics and catalyst characteristics will be stressed, as well as the influence of the switching time in both reactor configurations: this analysis is important not only as it allows to compare the two devices and to optimise the operation, but also as the switching time is the main operating parameter that can be changed to fulfil the operation constraints.

THE MODEL

An Eley-Rideal mechanism is used to describe the reaction between NO_x (A) in the gas phase and the ammonia (B) adsorbed on the catalyst:

$$A + B_S \rightarrow C\,; \tag{1}$$

$$B + S \rightarrow B_S\,. \tag{2}$$

The reduction reaction is considered to be of first order with respect to each reactant:

$$r_{red} = -k_{red} c_{A,i} \theta_B\,; \tag{3}$$

where θ_B is the ammonia surface coverage and $c_{A,i}$ is the nondimensional concentration of reactant A at the gas-solid interface. The adsorption rate of ammonia on the catalyst surface is assumed to be proportional to the ammonia concentration in the gas phase and to the fraction of free surface sites:

$$r_{ads} = k_{ads} c_{B,i} \left(1 - \theta_B\right); \tag{4}$$

while the rate of desorption is assumed to be proportional to the concentration of the adsorbed species:

$$r_{des} = k_{des} \theta_B\,. \tag{5}$$

An Arrhenius type dependence of the kinetic constants k_{red}, k_{ads} and k_{des} from the temperature is assumed:

$$\begin{aligned} k_{red} &= k_{0,red} e^{-\frac{E_{a,red}}{RT_S}} \\ k_{ads} &= k_{0,ads} e^{-\frac{E_{a,ads}}{RT_S}} \\ k_{des} &= k_{0,des} e^{-\frac{E_{a,des}}{RT_S}} \end{aligned}\,. \tag{6}$$

A Temkin-type adsorption isotherm, where the activation energy for desorption is a function of the surface coverage, is assumed:

$$E_{a,des} = E^0_{a,des}\left(1-\beta\theta_B{}^{\sigma}\right); \tag{7}$$

A surface coverage of this type was used in previous studies and was verified experimentally by Tronconi et al. (1996).

A monolith is considered for the SCR reaction. Solid catalytic surface is considered in pseudo-steady state conditions, pressure loss inside the reactor was neglected.

The system of non-dimensional partial differential equations that describes the process dynamics is the following:

1. Gas phase mass balance:

$$\frac{\partial c^*_A}{\partial t^*} = -v^* \frac{\partial c^*_A}{\partial x^*} + Pe_A(c^*_{A,i} - c^*_A); \tag{8}$$

$$\frac{\partial c^*_B}{\partial t^*} = -v^* \frac{\partial c^*_B}{\partial x^*} + Pe_B(c^*_{B,i} - c^*_B); \tag{9}$$

where $C_A{}^*$ and $C_B{}^*$ are the non-dimensional gas concentration at the interface.

2. Solid phase mass balance:

$$\frac{\partial \theta_B}{\partial t^*} = Da_{ads} e^{-\gamma_{ads}\left(\frac{1}{T_S^*}-1\right)} c^*_{B,i}(1-\theta_B) - Da_{des} e^{-\gamma_{des}\left(\frac{1}{T_S^*}-1\right)} e^{\gamma_{des}\frac{\beta\theta_B^{\sigma}}{T_S^*}} \theta_B - Da_{red} e^{-\gamma_{red}\left(\frac{1}{T_S^*}-1\right)} c^*_{A.i}\theta_B \tag{10}$$

where:

$$x^* = \frac{x}{L},\ v^* = \frac{v}{v_0},\ t^* = t\frac{v_0}{L},\ c^*_A = \frac{c_A}{c^f_A},\ c^*_{A,i} = \frac{c_{A.i}}{c^f_A},\ c^*_B = \frac{c_B}{c^f_A},\ c^*_{B,i} = \frac{c_{B.i}}{c^f_A},\ Pe_A = \frac{h_A a_v L}{v_0},$$

$$Pe_B = \frac{h_B a_v L}{v_0},\ \gamma_{ads} = \frac{E_{a,ads}}{RT^f},\ \gamma_{des} = \frac{E^0{}_{a,des}}{RT^f},\ \gamma_{red} = \frac{E_{a,red}}{RT^f},\ Da_{ads} = \frac{k_{0,ads} e^{-\gamma_{ads}} L c^f_A}{v_0},$$

$$Da_{des} = \frac{k_{0,des} e^{-\gamma_{des}} L}{v_0}, \qquad Da = \frac{k_{0,red} e^{-\gamma_{red}} L c^f_A}{v_0} \tag{11}$$

Conventional Danckwerts boundary conditions are assumed at the inlet of the RFR and RN and the continuity of the gas concentration and temperature profiles are imposed between the reactors of the network.

Reactants are supposed to be feed at the same part of the reactor, inlet concentration of the gases are considered constant and equal to the feeding value, and the initial concentration of ammonia adsorbed on the catalyst surface is equal to zero in all the reactor configurations considered.

The system of Partial Differential Equations has been solved by discretizing the domain of spatial variable into a grid of 100 points, equally spaced, obtaining a grid-independent solution. The MatLAB solver ode15s was used to solve the system.

The influence of reaction kinetics and catalyst activity on NO_x selective catalytic reduction with ammonia in isothermal conditions system, both in the RFR and RN was investigated; process conditions used in sensitivity analysis are given in Table 1. Firstly, the values of *Da*, Da_{ads} and Da_{des} were varied, to point out the influence of kinetic activity and adsorption/desorption kinetic on the performance of the system. The results that can be obtained in the system with a commercial catalyst will be also shown: to this purpose the kinetic model proposed by Tronconi at al. (1996) for a V_2O_5/TiO_2 catalyst (with V_2O_5 loading of 1.47%) was used.

Table 1.

Values of the main operating parameters used in the simulations.

c_{NOx}	560 ppmV
c_{NH3}	450 ppmV
c_m	210 mol m^{-3}
L	0.45 m
v	0.27 m s^{-1}
a_v	200 m^{-1}

THE RESULTS

In order to investigate the influence of the unsteady-state operation mode on the adsorption-desorption of ammonia and on the reaction between ammonia and NO_x in the gas phase, the reactor was considered to operate in isothermal condition. Two different devices were considered, namely the RFR and a RN made of three reactors with variable position of the feed: the feeding position is moved from one reactor to the following one in the direct sequence, i.e. the system is fed through reactor number 1 and the order of the reactors is 1-2-3 and after a time period, the feed position is shifted, acting on a set of valves, so that the first reactor of the sequence becomes the third one, thus changing the order to 2-3-1.

When isothermal operation is assumed, as in this case, the switching time is the main operating parameter, particularly for control purposes. The influence of this parameter was investigated for different values of *Da* (Figure 2), of Da_{ads} (Figure 3) and of Da_{des} (Figure 4).

The inlet concentration of NO_x was fixed to 560 ppmV; a slightly lower concentration of ammonia (450 ppmV) was considered to be fed to the reactor.The performance of the devices were evaluated after the transient, when the periodic steady-state was reached, in terms of mean outlet concentrations of NO_x and of NH_3; the mean values were calculated over the entire length of a period.

The first evidence is that when either the catalyst activity or the adsorption kinetic are enhanced the emissions of both NO_x and NH_3 decrease, as it is expected; the same behaviour is obtained when the desorption kinetic is decreased. The influence of the switching time on the mean outlet concentration of NO_x and NH_3 in the RFR and in the RN is similar. At high switching time the performance of the RFR and that of the RN is the same both from the point of view of NO_x and NH_3 emissions. As far as lower values of the switching time are considered the emissions of NO_x and of NH_3 in the RFR are decreased when the switching time is increased as a consequence of the higher amount of ammonia which is stored in the catalyst. The performance of the RN is different: there is a first range of switching time where

the outlet ammonia concentration is almost zero and the outlet NO_x concentration decreases almost linearly; after this range, the outlet pollutant concentrations start increasing up to a certain value, before decreasing and approaching the behaviour of the RFR. This different behaviour can be explained considering the dynamics of the concentration profiles in the reactor: while in the RFR a bell shaped profiles is obtained as a consequence of the reversal of the flow direction, in the RN more complex profiles may be obtained and, as a consequence of the switching strategy, the ammonia profile may exit from one of the reactors of the network, thus giving rise to higher reactants emissions. This behaviour is similar to that observed for the temperature profile in the RN by Brinkmann et al. (1999).

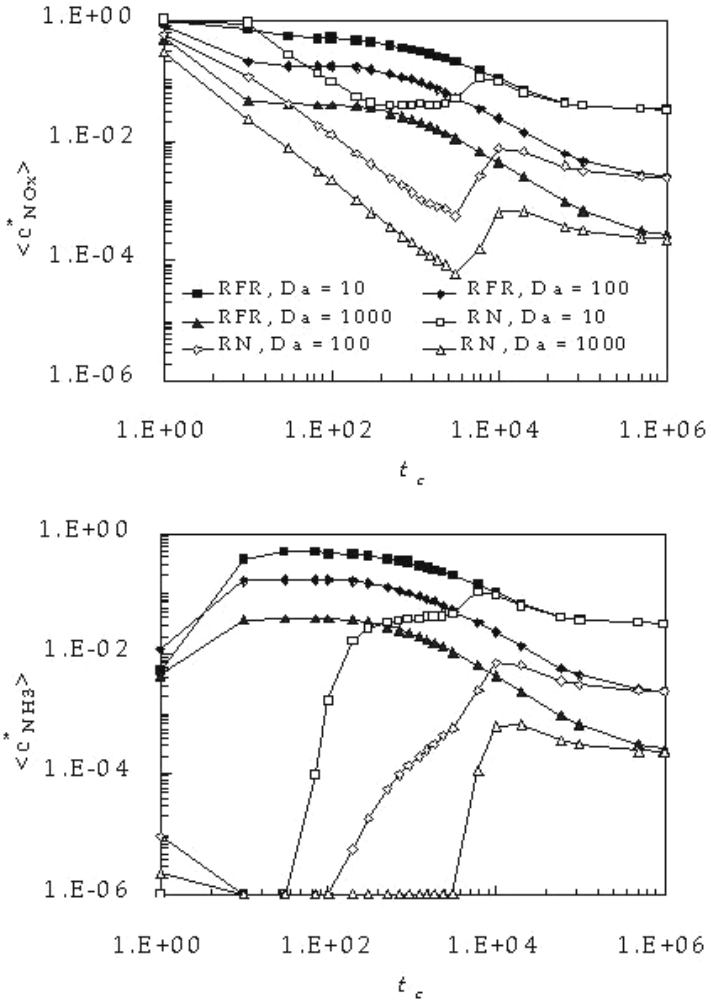

Figure 2. Influence of the switching time on the mean outlet non-dimensional concentration of NO_x (upper graph) and of ammonia (lower graph) for various values of *Da* in the RFR and in the RN (isothermal system).

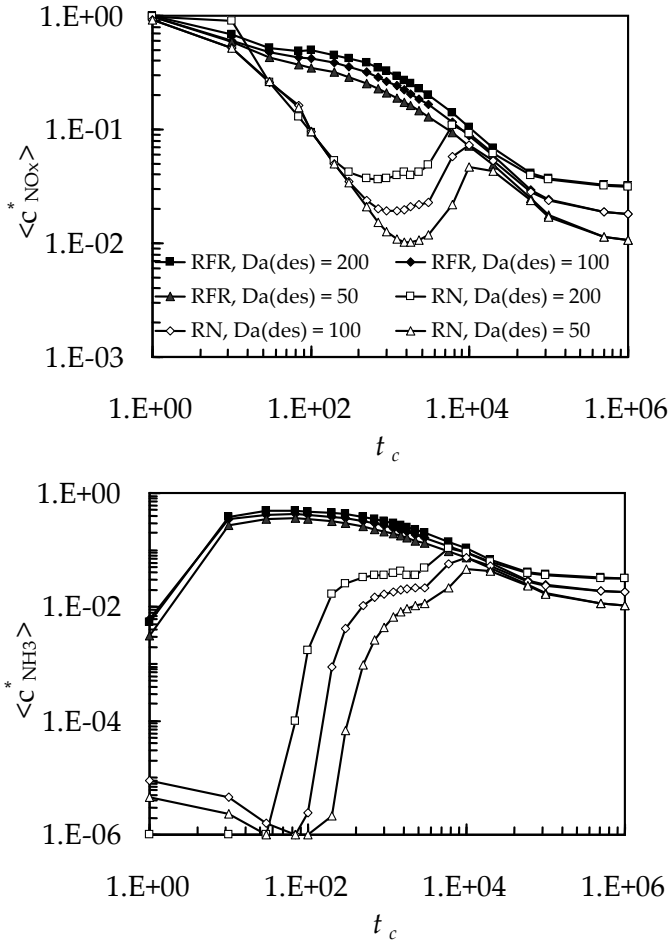

Figure 3. Influence of the switching time on the mean outlet non-dimensional concentration of NO_x (upper graph) and of ammonia (lower graph) for various values of $Da_{(des)}$ in the RFR and in the RN (isothermal system).

In conclusion, there is a wide range of switching time where the RN exhibits no ammonia emissions and NO_x emissions lower than those obtainable in the RFR; this is a consequence of the absence of wash out, as discussed previously; the extent of this "optimal" range is a function of the parameter of the system, namely Da, Da_{ads}, Da_{des}.

Finally, the performance obtainable with a commercially available catalyst are considered. In this case several different design configurations are investigated. The kinetic model of Tronconi et al. (1996) was used for the simulations. The influence of the switching time was analysed in various configurations, namely the RFR and the RN made up of two and three reactors (with different switching strategy). The

influence of the switching time on the mean outlet concentration of NO_x and NH_3 is very different from that previously obtained: a maximum value of switching time is found beyond which conversion decreases both in the RFR and in the RN. As far as the ammonia outlet concentration is concerned, the value decreases when the switching time is increased in the RFR, while in the various RN considered a minimum appears. It is important to notice that it is mandatory that no ammonia is present in the product stream, thus only the three reactors network with switching strategy 1-2-3 -> 3-1-2 can be used, even if this results is achieved in a narrow range of switching times. On the contrary, the RFR can be operated with switching time between 600 and 3000 in order to avoid NO_x emissions, even if a certain amount of NH_3 is released from the reactor.

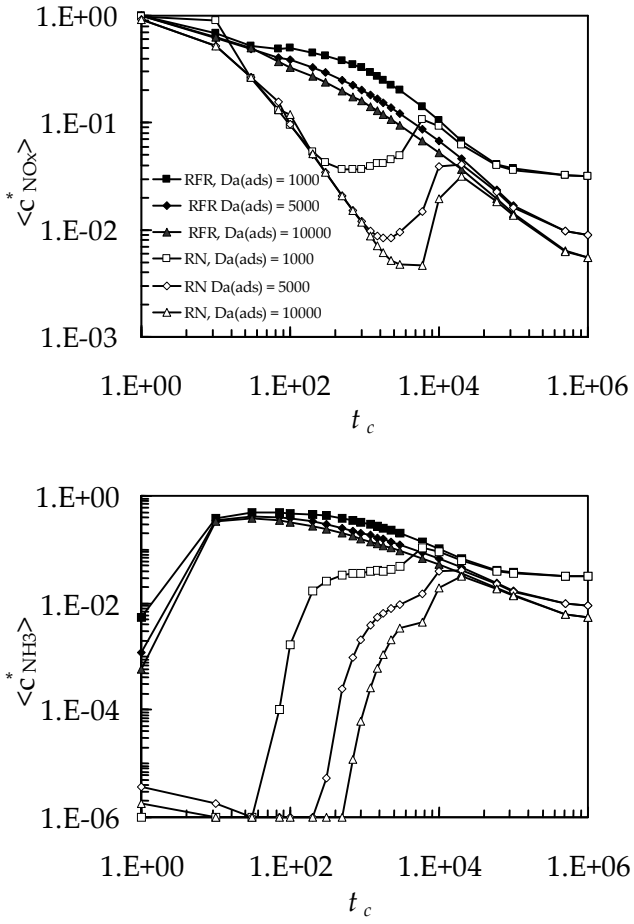

Figure 4. Influence of the switching time on the mean outlet non-dimensional concentration of NO_x (upper graph) and of ammonia (lower graph) for various values of $Da_{(ads)}$ in the RFR and in the RN (isothermal system).

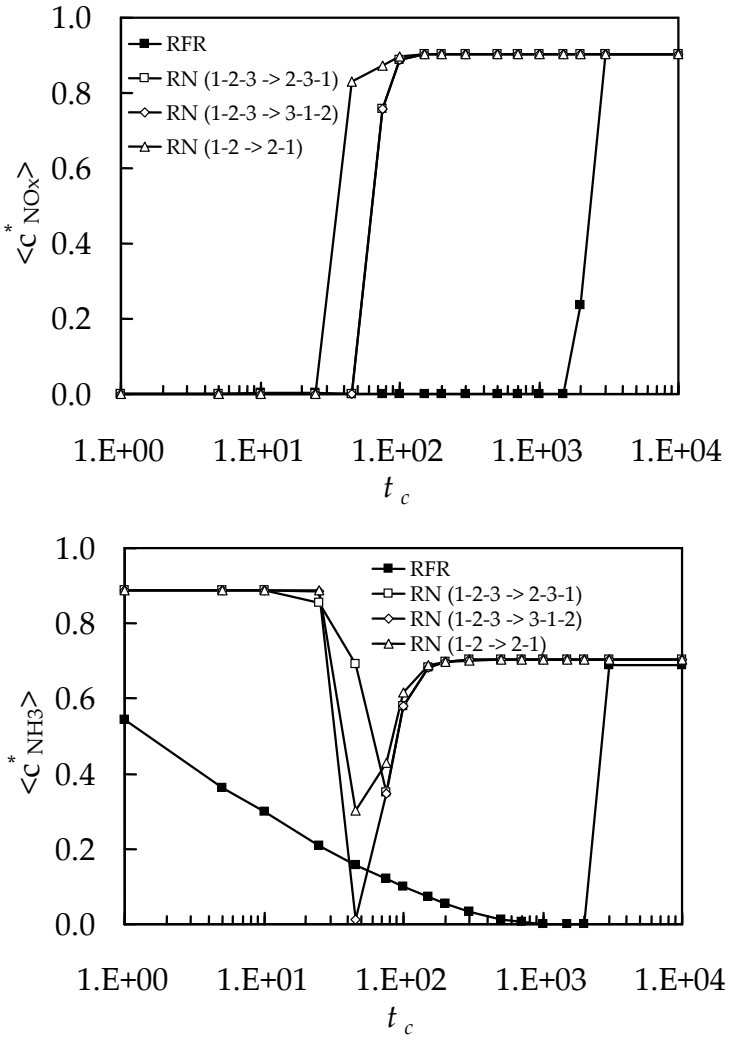

Figure 5. Influence of the switching time on the mean outlet non-dimensional concentration of NO_x (upper graph) and of ammonia (lower graph) in the RFR and in various configurations of the RN for the operating parameters of Table 1 (isothermal system).

This behaviour, which is different from that shown in Figures 2-4, can be explained if the values of *Da*, $Da_{(ads)}$, $Da_{(des)}$ are calculated for the commercial catalyst considered in the paper of Tronconi et al. (1996): for example *Da* is very high, about 10^5, thus altering the dynamic of the system in comparison to the values previously considered and masking the wash out phenomena.

CONCLUSIONS

The feasibility of SCR of NO_x with ammonia in unsteady-state reactors was studied for various reactors configurations by means of numerical simulations, using a heterogeneous mathematical model and an Eley-Rideal kinetic mechanism. Isothermal system, in which the problem of the heat storage in the system is neglected, was simulated. The results are strongly influenced by the system parameter, namely *Da* (kinetic constant of the reduction reaction), $Da_{(ads)}$ (kinetic constant of the adsorption reaction) and $Da_{(des)}$ (kinetic constant of the desorption reaction). In particular, when the adsorption and the reaction rate are not very high, the RN, which does not exhibits the wash out phenomena, is the only device which ensures the fulfilment on the emissions limits for the two reactants, while when the adsorption and the reaction rate are very high, as in the case of the system of Tronconi et al. (1996), the results are different, and the RFR has to be preferred as the problem of wash out is bypassed by the high adsorption and reaction rate.

ACKNOWLEDGEMENTS

Claudiu Cristian Botar-Jid is grateful to the European Commission for a Marie Curie Training Site Fellowship that supported him during his stage at Politecnico di Torino (SICOFOR Contract Nr. HPMT-CT-2001-00343). Thanks are due to the Italian Ministry of University and Research (PRIN - 2002 2094284) for the financial support to this work.

NOTATION

C^*	non-dimensional concentration
c	concentration, mol m^{-3}
c_A^f	concentration of reactant A in the feed, mol m^{-3}
Da	Damkohler number
E_a	activation energy, J mol^{-1}
h_A, h_B	mass transfer coefficients
k	reduction kinetic constant, m^3 mol^{-1} s^{-1}
k_0	pre-exponential factor of the reduction kinetic constant, m^3 mol^{-1} s^{-1}
k_{ads}	adsorption kinetic constant, m^3 mol^{-1} s^{-1}
$k_{0,ads}$	pre-exponential factor of the adsorption kinetic constant, m^3 mol^{-1} s^{-1}
k_{des}	desorption kinetic constant, s^{-1}
$k_{0,des}$	pre-exponential factor of the desorption kinetic constant, s^{-1}
L	total reactor length, m
Pe	Peclet number for mass transport
R	ideal gas constant, J mol^{-1} K^{-1}
r	reaction rate, mol m^{-3} s^{-1}
T	temperature, K
t	temporal coordinate, s
t^*	non-dimensional temporal coordinate
t_c	non-dimensional switching time
T^f	inlet gas temperature, K
v	gas velocity, m s^{-1}
v_0	superficial velocity

*v**	non-dimensional gas velocity
x	axial coordinate, m
*x**	non-dimensional spatial coordinate

Greeks

β	parameter for surface coverage dependence
γ	non-dimensional activation energy
θ	surface coverage
σ	parameter for the surface coverage dependence

Subscripts and superscripts

ads	adsorption process
A	identifies NO_X
B	identifies NH_3
B_S	identifies NH_3 adsorbed
des	desorption process
i	interface
S	solid

Abbreviations

RFCR	Reverse-flow Chromatographic Reactor
RF	Reverse-flow Reactor
RN	Reactors Network
SCR	Selective Catalytic Reduction

REFERENCES

Agar, D. W, & Ruppel, W. (1988). Extended reactor concept for dynamic DeNOx design. *Chemical Engineering Science*, *43*, 2073-2078.

Brinkmann, M., Barresi, A. A., Vanni, M., & Baldi, G. (1999). Unsteady-state treatment of very lean waste gases in a network of catalytic burners. *Catalysis Today*, *47*, 263-277.

Cottrell, F. G. (1938). Purifying gases and apparatus therefore, U. S. Patent 2, 171, 733.

Fissore, D., Barresi, A. A., & Baldi, G. (2003). Synthesis gas production in a forced unsteady state reactor network. *Industrial & Engineering Chemistry Research*, *42*, 2489-2495.

Tronconi, E., Lietti, L., Forzatti, P., & Malloggi, S. (1996). Experimental and theoretical investigation of the dynamics of the SCR-DeNOx reaction. *Chemical Engineering Science*, *51*, 2965-2970.

Yong, J., & Luss, D. (2003). Pollutant destruction in a reverse-flow chromatographic reactor. *Chemical Engineering Science*, *58*, 1095-1102.

Velardi, S. A., & Barresi, A. A. (2002). Methanol synthesis in forced unsteady-state reactor network. *Chemical Engineering Science*, *57*, 2995-3004.

STUDIA UNIVERSITATIS BABEŞ-BOLYAI, CHEMIA, L, 2, 2005

NAMING POLYHEX TUBULAR OBJECTS ORIGINATING IN SQUARE TILED LATTICES

MIRCEA V. DIUDEA and SIMONA S. CIGHER

Faculty of Chemistry and Chemical Engineering,
Babeş-Bolyai University, 400028 Cluj, Romania

ABSTRACT. Tiling of a tubular nanostructure can be modified, from the tetragonal (4,4) to hexagonal (6,3) by cutting procedures. As implemented in the Torus software program, these provide tubular/toroidal objects of various size, embedding and covering. Naming polyhex tubular objects is given both in Diudea and Hamada terms. Topological description by α-spiral code was adapted for polyhex tubular and toroidal nets.

1. INTRODUCTION

Covering a local planar surface by various polygonal or curved regions is an ancient human activity. It occurred in house building, particularly in floor, windows and ceiling decoration. There were well known three regular Platonic tessellations: (4,4), (6,3) and (3,6). The Greek and Roman mosaics were very appreciated in this respect.

Covering is nowadays a mathematically founded science.[1] It makes use of the Graph and Set Theory and often inspires from the Arts and Architecture.

Covering transformation is one of the ways in understanding chemical reactions occurring in nanostructures.[2-4]

Among the carbon allotropes, intensively studied in the last decade,[5-9] the only orientable closed surface *S* entirely coverable by a benzenoid lattice is the torus. A polyhedral cage obeys the Euler theorem[10].

$$N - E + F = 2(1 - g) \qquad (1)$$

where *N, E, F,* and *g* are respectively the number of vertices, edges, faces, and genus – zero for the sphere and unity, in case of the torus.

The article is organised as follows. The second section introduces to some cutting procedures performed on the chessboard tessellation embedded in torus and cylinder. A third section deals with the perfect Clar structures and the perfect Corannulenic systems. The last two sections provide conclusions and references.

2. CUTTING PROCEDURES ON (4,4) TESSELLATION

Embedding[5] (*i.e.*, drawing of a graph on a (closed) surface with no crossing lines) of the hexagonal trivalent (6,3) net (cf. the Schäfli notation) in the torus or the cylinder is achieved mainly by the well-known graphite zone-folding.[11,13,14,19-21]

The method finds an equivalent planar parallelogram, tiled with the graphitic polyhex lattice. When two opposite edges are identified, a tube is formed, which is completely defined by two integer parameters (*k*,*l*), according to Hamada *et al.*[22] The two parameters quantify (in terms of the primitive lattice vectors of graphene) the *chiral* vector *R* on which the tube is rolled up. In case: *armchair* A, (*k*,*k*) and *zigzag* Z, (*k*,0), the tube is achiral. The translation vector *T* follows the tube axis and is orthogonal to *R*

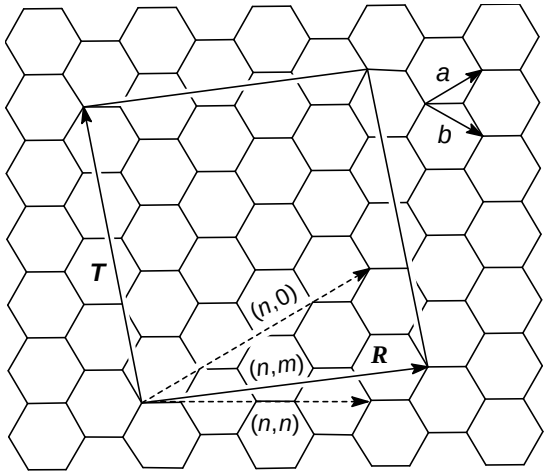

Figure 1. The rolled up area delimited by *T* and *R* corresponds to the *repeat unit* of an (*n*,*m*) *chiral tube*, ((3,2) in Figure; the achiral limit cases (n,0) and (n,n) are (4,0) and (2,2), respectively.

When the two remaining edges are further identified (*cf.*, the *translation* or twisting vector *T*) the torus thus obtained is completely defined by four integers (*e.g.*, (*k,l,p,q*)), reducible to three parameters, according to Kirby *et al.*[12,14]

An alternative to the parallelogram procedure uses the topological coordinates, extracted from the adjacency matrix eigenvectors.[15-18]

2.1. Basic Polyhex Constructions

Our construction starts with embedding of the tetragonal (4,4) net on either the cylinder or torus.[23-28]

A cylindrical surface is covered by a square net as follows:

- take the cross section of a *c* -fold polygon and move it along the cylinder axis;
- join the *n* subsequent images of the polygon, to form a tube.

The parameters are calculated by the cylindrical coordinates as:

$$P(x, y, z) \tag{2}$$
$$x = r\cos\theta$$
$$y = r\sin\theta$$
$$z = z$$
$$\theta_i = \frac{2\pi}{c} i \quad ; \quad i = 0,...,c-1$$
$$z_i = \frac{z}{n} i \quad ; \quad i = 0,...,n-1$$

Toroidal parameters

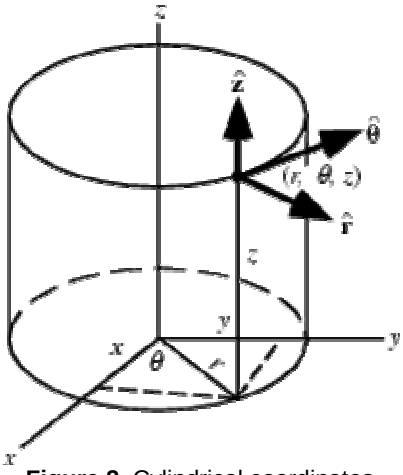

Figure 2. Cylindrical coordinates

The embedding of the (4,4) net on the torus is made by circulating a *c*-fold cycle, circumscribed to the toroidal tube cross-section of radius *r*, around the large hollow of the torus, of radius $R > r$ (Figure 3). Its subsequent *n images*, equally spaced and joined with edges, point by point, form a polyhedral torus tiled by a tetragonal pattern. The position of each of the *n* images of the "circulant" around the central hollow is characterized by angle θ while angle φ locates the *c* points across the tube. In all, *c* x *n* points are generated. The parameters *R* and *r* are not directly involved in the topological characterization of the lattice.

Toroidal parameters A (4,4) square tiled torus

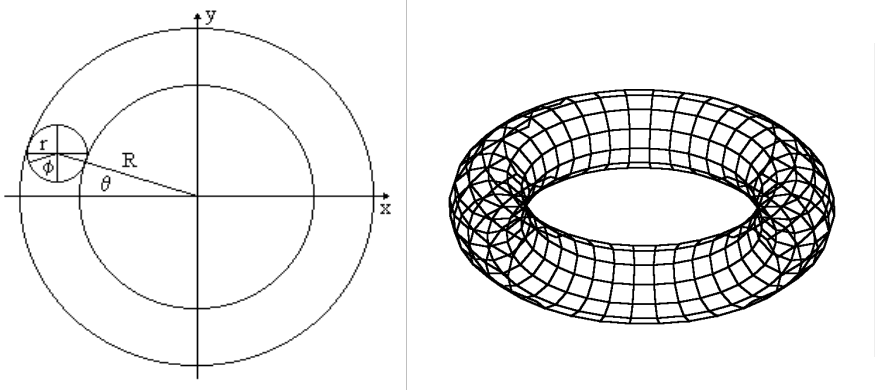

Figure 3. Embedding of the (4,4) net in the torus.

The parameters are calculated by the following formulas:

$$P(x, y, z): \tag{3}$$

$$x = \cos(\theta)(R + r\cos\varphi)$$

$$y = \sin(\theta)(R + r\cos\varphi)$$

$$z = r\sin\varphi$$

$$\theta_i = \frac{2\pi}{n} i \quad ; \quad i = 0,...,n-1$$

$$\varphi_j = \frac{2\pi}{c} j \quad ; \quad j = 0,...,c-1$$

The tetragonal objects thus obtained are named by a string specifying the tiling and dimensions of the net: (4,4)[*c*,*n*] (for tubes, Tu is added in the front of), with the (integer) parameters in the square brackets being the number of atoms in the tube cross-section and the number of cross-sections around the torus (or along the tube), respectively. The objects consist of $c \times n$ vertices, $c \times n$ squares and $4 \times c \times n/2$ edges, 4 being the vertex degree of the net (which is a regular graph). This covering appears in some metal clusters and silicon nanotubes.[29,30]

Next, the tetragonal (4,4) net is modified to give, most often, a hexagonal (6,3) net or other patterns, of chemical interest. Several cutting procedures we have developed in this respect.[24-28,31,32]

A cutting operation consists of deleting appropriate edges in a tetragonal (4,4) lattice in order to produce some larger polygonal faces. By deleting each second *horizontal* edge and alternating edges and cuts in each second row it results in a standard (6,3)H/Z pattern (Figure 4,a). A *vertical* action of the above algorithm leads to a standard (6,3)V/A pattern (Figure 4,b). The specifications Z (zigzag) and A (armchair) come from the shape of the tube cross-section.

(a) (6,3)H/Z pattern (b) (6,3)V/A pattern

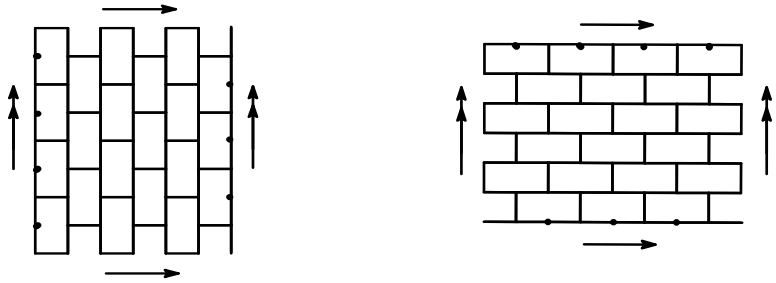

Figure 4. The (6,3) covering by H- (a) and V- (b) cutting of the (4,4) net. Note that each hexagon consumes exactly two squares of the (4,4) lattice.

By construction, the number of hexagons in the H/Z-objects is half the number of squares on dimension *c* while, in V/A-objects, the reduced number of hexagons appears on dimension *n*. Thus, (6,3)Z[2*c*,*n*] has the same number of hexes as its embedding isomer (6,3)A[*c*,2*n*]. Recall that, the above cutting procedure leaves unchanged the number of vertices in the original (4,4) lattice.

After optimizing, *e.g.*, by a Molecular Mechanics procedure, (6,3) lattices appear like in Figure 5.

(a) Tu(6,3)A[12,12]; N = 144 (b) (6,3)H/Z[12,50]; N = 600

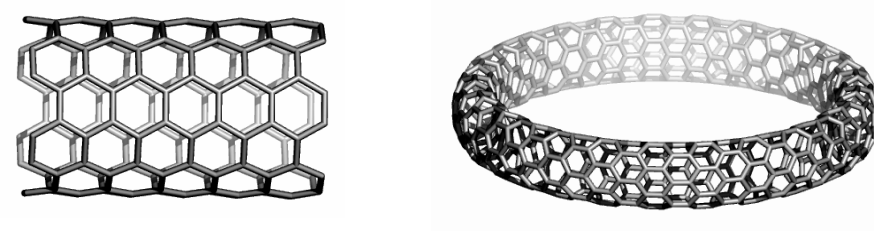

Figure 5. The (6,3) covering in the cylindrical and toroidal embedding, respectively.

2.2. Twisted/Chiral Polyhex Structures

Twisted, chiral, patterns can be generated by the following two procedures: (1) horizontal twisting of a layer of connections (Figure 6a) and (2) vertical twisting (offset) of the end connections (not shown). In cylindrical embedding, only one twisting type (namely the one parallel to the cylinder generator) will work, because of the open ends. Edge cutting is further needed to change squares into hexagons (Figure 6b). Twisting an even number of layers is needed to obtain a hexagonal net. The type of cutting will dictate the type of embedding and, ultimately, the shape of objects.

(a) (4,4) net (b) (6,3) net

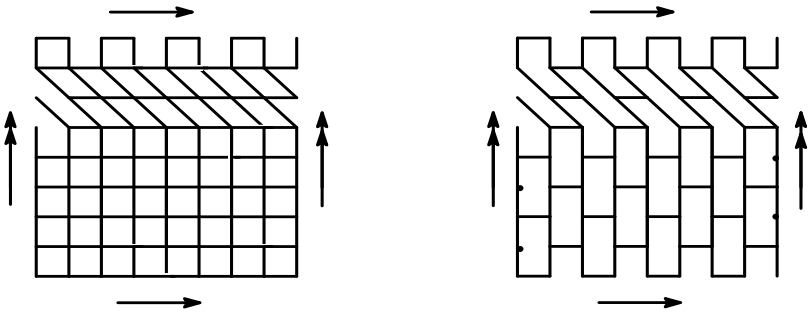

Figure 6. Twisted (4,4) pattern (a) and its (6,3) derivative (b).

The twisting parameter *t* takes integer values in the range [0,*c*]. It is just the deviation (in number of hexagons) of the chiral (*i.e.*, rolling-up) vector to the zigzag line, in the graphite sheet representation.[11-14,20,21]

In case of tubes, Tu(6,3)HH*t*[*c*,*n*], the number of atoms on the *c*-dimension increases as *t* increases, concomitant with the shortening of *n*-dimension (in general, non-integer values, having a statistical meaning).[33] The twisting preserves the type of net (Z, in this case) and the total number of hexagons as well (*i.e*., (*c*/2) × (*n*-1)), the same as in the non-twisted tube). Correspondingly, the number of "zigzags" (*i.e*., the number of end-hexagons) increases, from *c*/2 up to twice the initial value. The final object will be Tu(6,3)HH*c*[*c*,*n*] = Tu(6,3)Z[2*c*,*n*/2]. Note that diameter doubling of single walled nanotubes has been observed experimentally [34,35] and termed "tube coalescence".

In case of Tu(6,3)HV*t*[*c*,*n*], the twisting keeps the *c*, *n* dimensions but stepwise adds the Z-character (*i.e*., adds zigzag hexagons), finishing in a pure Z-net, particularly Tu(6,3)Z[2*c*,*n*/2]. The crenel and zigzag tips coexist, as can be seen from Figure 7 (the right column). The two embeddings, HH and HV can be named by two integer parameters, according to Hamada *et al*.[22]

Clearly, both local covering and embedding (*i.e*., global covering) contribute to the structural (and electronic) properties of the tubular nanostructures.

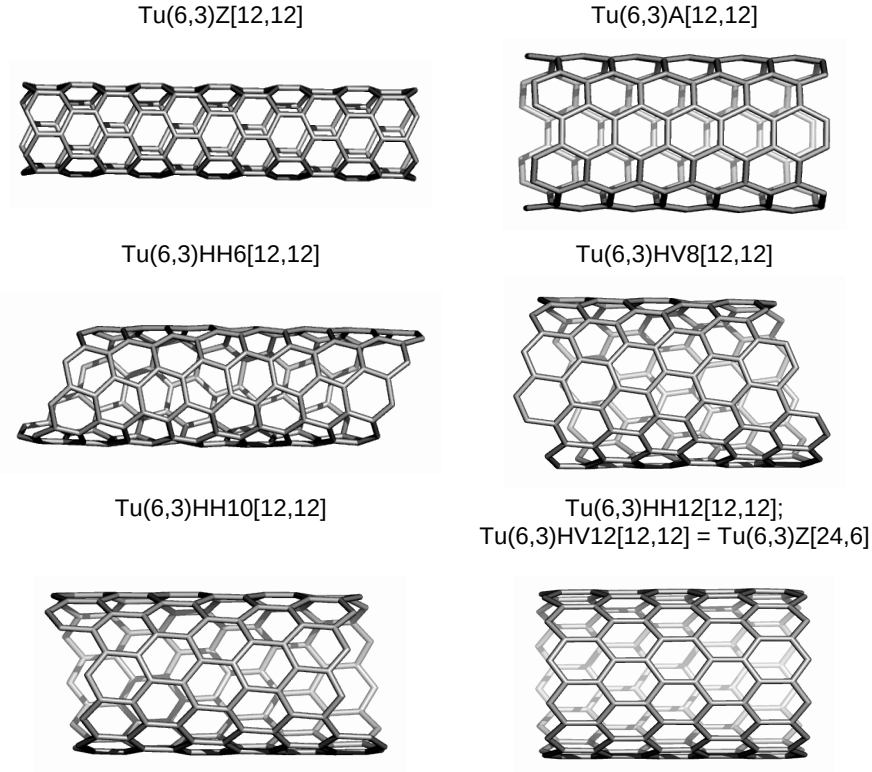

Figure 7. Nanotube twisting; diameter doubling at *t* = *c* is evident by comparing the top left corner tube with the bottom right one.

Correspondence between the name of polyhex tubes in our approach and the two integer parameter (*k*,*l*) notation is given below:

$$\mathrm{TUH/Z}[c,n]: \quad c=2k; \quad t=0; \quad \mathrm{Z}(c/2,0) \tag{4}$$

$$\mathrm{TUHH}t[c,n]: \quad c=2k+l; \quad t=|c-2k|; \quad k=(c-t)/2; \quad l=t \tag{5}$$

$$\mathrm{TUHV}t[c,n]: \quad c=k+l; \quad t=|k-l|; \quad k=(c+t)/2; \quad l=(c-t)/2 \tag{6}$$

$$\mathrm{TUV/A}[c,n]: \quad c=2k; \quad t=0; \quad \mathrm{A}(c/2,c/2) \tag{7}$$

$$t_{hh}=\frac{|c_{hv}\text{-}t_{hv}|}{2}; \quad c_{hh}=\frac{3c_{hv}+t_{hv}}{2} \tag{8}$$

$$t_{hv}=\frac{|c_{hh}\text{-}3t_{hh}|}{2}; \quad c_{hv}=\frac{c_{hh}+t_{hh}}{2} \tag{9}$$

with *n* remaining indefinite.

In case of tori, each of the above twistings superimpose on the two basic cuttings, thus resulting four classes of twisted tori: (i) H-twist, H-cut HH*t*[*c*,*n*]; (ii) V-twist, H-cut, VH*t*[*c*,*n*]; (iii) H-twist, V-cut, HV*t*[*c*,*n*] and (iv) V-twist, V-cut, VV*t*[*c*,*n*].[36]

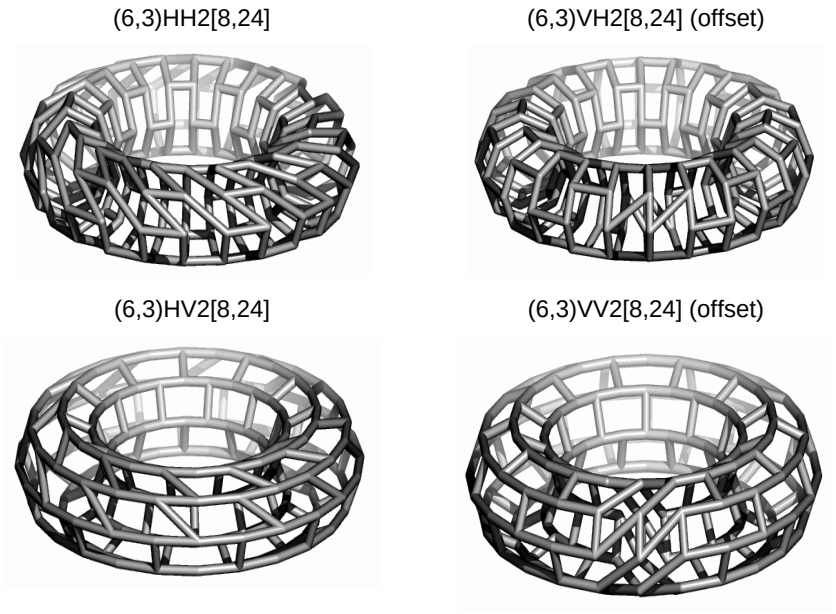

Figure 8. The four classes of twisted polyhex tori (non-optimized geometry).

Figures 9 and 10 illustrate some optimized twisted polyhex tori.

(6,3)HH2[10,100]; N = 1000 (6,3)VH2[10,50]; N = 500

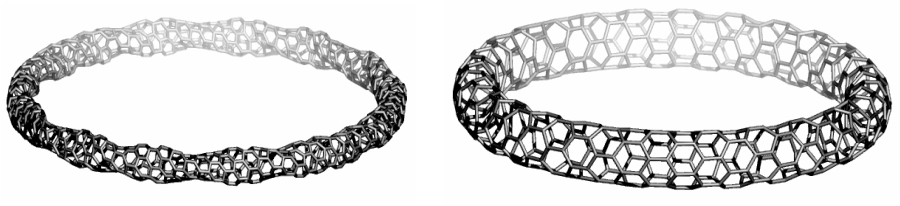

Figure 9. A twisted (6,3) covering in horizontal H-cutting (optimized) toroids.

A toroidal object is drawn as an equivalent planar parallelogram that needs the specification (in two integer parameter notation[22]) of the two involved tubes (Figure 11).

(6,3)VV2[10,100]; N = 1000 (6,3)HV2[10,50]; N = 500

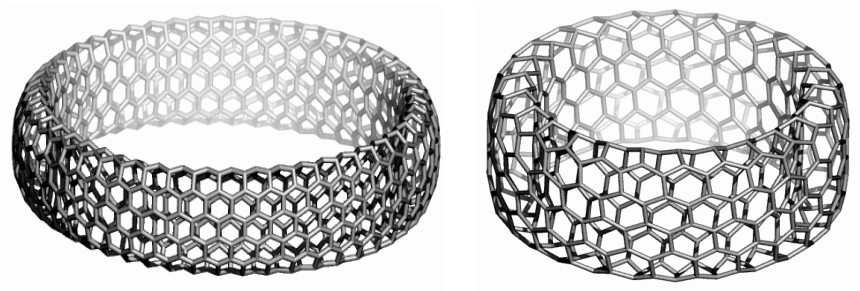

Figure 10. A twisted (6,3) covering in vertical V-cutting (optimized) toroids.

One tube is built up by taking as circumference the rolling-up vector *R*, given in terms of the primitive lattice vectors of graphene:

$$R = ka_1 + la_2 \tag{10}$$

The second tube is formally defined on the translating (or twisting) vector *T*:

$$T = pa_1 + qa_2 \tag{11}$$

Going from a torus, generated as above, to its composing vectors, the first tube can be identified by cutting the object across the tube while the second one results by cutting it around the large hollow. Anyway, a four integer parameter description (*k*,*l*,*p*,*q*) is obtained. Correspondence between the name of tori in our approach X*t*[*c*,*n*] and the four integer parameter (*k*,*l*,*p*,*q*) notation is detailed in Table 1.

The coordinates for the HH4[14,6] torus depicted in Figure 11 are: (5, -4, 3, 3). Note that this representation is not unique and is reducible to three parameter notation, theorized by Kirby *et al*.[12,14]

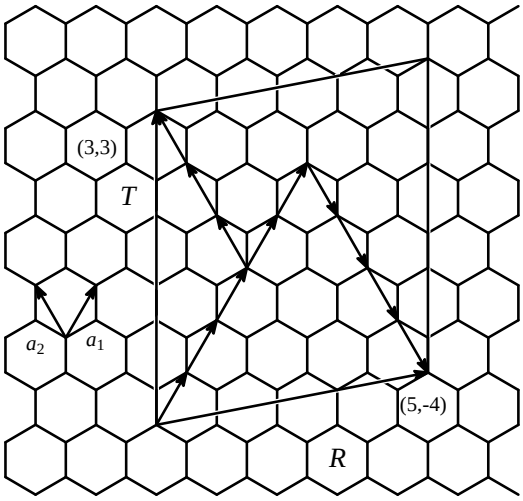

Figure 11. Representation of the torus HH4[14,6] by an equivalent parallelogram involves specification of two tubes: one defined on the rolling-up vector *R* (with integer coordinates (*k*,*l*)) and the other on the translating vector *T* (given by pair (*p*,*q*)). The four parameter specification of the depicted torus is (5, -4, 3, 3).

Table 1

Correspondence between the X*t*[*c*,*n*] and (*k*,*l*,*p*,*q*) notations.

	Torus [*c*,*n*]	Tube *R*	Tube *T*	Torus (*k*,*l*,*p*,*q*)*	*N*
1	H	H/Z	V/A	$(c/2,-c/2,n/2,n/2)$	$2(kq-lp)=cn$
2	V	V/A	H/Z	$(c/2,c/2,n/2,-n/2)$	$2(lp-kq)=cn$
3	HH*t*	HH (tw)	V/A	$[(c-t)/2,-t,n/2,n/2]$	$2(2kq-lp)=cn$
4	HV*t*	HV (tw)	H/Z	$[(c+t)/2,(c-t)/2,n/2,-n/2]$	$2(lp-kq)=cn$
5	VH*t* (offset)	H/Z	HV (tw)	$[c/2,-c/2,(n+t)/2,(n-t)/2]$	$2(kq-lp)=cn$
6	VV*t* (offset)	V/A	HH (tw)	$[c/2,c/2,(n-t)/2,-t)]$	$2(2lp-kq)=cn$

*First pair (*k*,*l*) denotes the rolling-up vector *R* while last pair (*p*,*q*) specifies the translating/twisting vector *T*; (*m*,-*m*) = (*m*,0), is a Z-tube; (*m*,*m*) is an A-tube (see Figure 7).

In our procedure, H-twisting involves an intrinsic chiral (HH or HV) *R*-based tube and a non-twisted *T*-based one (Table 1, entries 3 and 4). Conversely, in V-twisting, the *R*-based tube is a non-chiral (H/Z or V/A) one while the second *T*-based tube is twisted (leading to “offset” closed toroids - Table 1, entries 5 and 6). The resulting

tori are all different, at least as 3D structures, because of distinct embedding. Note that the HV lattice is essentially a HH one, the objects differing, however, as embedding and electronic structure. In generating chiral tori, the above procedure leaves untwisted one of the two constitutive vectors (see above).

We stress that there exist three approchs for generating/naming toroidal lattices non-unique and non-equivalent: Kirby's[11,12], Klein and Zhu[37] and Diudea[26,27]. In this respect several errors have been reported in the literature [38].

Encoding the type of tessellation can be done, for example, by the spiral code.[39-41] It was first proposed for coding and constructing spherical fullerenes. We adapted the spiral code for tubular structures.[42] In a periodic tubular net, the spiral code brings information on size and sequence of faces and embedding the actual object on the parent (4,4)[*c*,*n*] lattice. The α-spiral code for the polyhex tubes is given in Table 2 and for the polyhex toroids is given in Table 3.

Table 2

Ring spiral code of tubes.

	Series	Ring spiral code
1	H/Z[*c*,*n*]	$n \cdot [6^{c/2}]$
2	HHt[*c*,*n*]	$n(1-t/2c)\cdot[6^{c/(1-t/2c))/2}]$
3	HVt[*c*,*n*]	$n/2\cdot[6^{c}]$
4	V/A[*c*,*n*]	$n/2\cdot[6^{c}]$

Table 3

Ring spiral code of tori.

	Series	Ring spiral code
1	H/Z[*c*,*n*]	$[6^{c/2}]^{n}$
2	HH[*c*,*n*]	$[(6^{c/2})^{t}]^{n/t}$
3	HV[*c*,*n*]	$[(6^{c})^{t}]^{n/2t}$
4	VH[*c*,*n*]	$[(6^{n})^{t}]^{c/2t}$
5	VV[*c*,*n*]	$[(6^{n/2})^{t}]^{c/t}$
6	V/A[*c*,*n*]	$[6^{c}]^{n/2}$

The number *t* inside the brackets equals the helicity[43] while the number out the brackets gives the steps of a helix. Note that the helicity could be less than *t*, if an integer number of steps appear.

3. Perfect Clar and Perfect Corannulenic Structures

A perfect Clar structure[44,45] PCS (Figure 12a) is a vertex disjoint set of faces whose boundaries form a 2-factor. A *k*-factor is a regular *k*-valent spanning subgraph. A PCS will include each vertex of *G* once and only once. It is associated

with a Fries structure,[46] which is a Kekulé structure drawn over the maximum possible number of benzenoid (alternating single-double edge) hexagonal faces. A Kekulé structure is a set of pairwise disjoint edges of *G* (covering all its vertices) that coincides with a perfect matching and a 1-factor in Graph Theory.[47] A trivalent polyhedral graph has a PCS if and only if it has a Fries structure.

By extension, a perfect corannulenic system PCorS can be imagined.[36] The operation[48] sequence *Leapfrog-Quadrupling*, applied on trivalent maps, provides a perfect Clar-like corannulenic structure PCorS, with the associated Fries-like structure defined on all the vertices of graph, excepting the corannulenic core ones (Figure 12b, in black).

(a) (6,3)H[24,36] PCS (b) (6,3)H[24,36]) PCorS

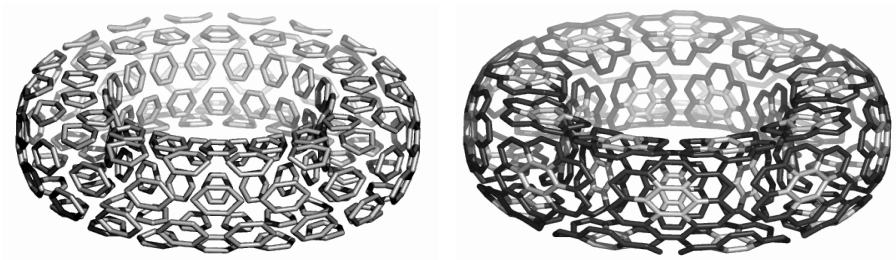

Figure 12. The perfect Clar and Cor structures of a H/Z polyhex torus (see text).

Table 4 gives the criteria for the perfect Clar structures PCS in tori: divisibility by 6 of the net dimensions (see also[49-52]). These criteria superimpose over the metallic (open-shell) character ones. In the opposite, Clar fullerenes (available by Leapfrog operation) show closed-shell structure.[49,50]

The last column in Table 4 gives the criteria for the perfect corannulenic structure PCorS. Any PCorS is necessarily a PCS. The supplementary condition is divisibility by four of the net dimensions.

Table 4

Covering criteria for perfect Clar and perfect Corannulenic structure in polyhex tori originating in square tiled tori

No	Torus	Criterion for perfect Clar structure PCS	Criterion for perfect Corannulenic structure PCorS
	Non-Twisted		
1	H/Z[*c*,*n*]	0 mod (*c*,6)	0 mod (*c*,12); 0 mod (*n*,4)
2	V/A[*c*,*n*]	0 mod (*n*,6)	0 mod (*c*,4); 0 mod (*n*,12)
	H-Twisted		
3	HH*t*[*c*,*n*]	0 mod (*c*,6)	0 mod (*c*,12); 0 mod (*n*,4); 0 mod (*t*,4)

No	Torus	Criterion for perfect Clar structure PCS	Criterion for perfect Corannulenic structure PCorS
4	HV*t*[*c*,*n*]	0 mod (*n*,6) & 0 mod(*t*,6)	0 mod (*c*,4); 0 mod (*n*,12) 0 mod (*t*,12)
	V-Twisted		
5	VH*t*[*c*,*n*]	0 mod (*c*,6) & 0 mod (*t*,6)	0 mod (*c*,12); 0 mod (*n*,4); 0 mod (*t*,12)
6	VV*t*[*c*,*n*]	0 mod (*n*,6)	0 mod (*c*,4); 0 mod (*n*,12); 0 mod (*t*,4)

4. CONCLUSIONS

We have presented a way for modifying the tiling of a nanostructure by cutting the tetragonal (4,4) lattice, embedded in the torus or cylinder, to give the hexagonal (6,3) covering. The topology of polyhex tubes and tori was described by the α-spiral code, adapted for tubular objects.

A perfect corannulenic system PCorS was proposed, by analogy to the well-known perfect Clar system, to give account for some supra-organized fully-resonant π-electronic aromatic systems in fullerenes, nanotubes and nanotori.

It is worthy to note the recent interest in the field of toroidal nanostructures after the publication of results on magnetic behaviour by Terrones *et al* [53]. The authors have shown that corrugated tori, constructed from C_{60} connected along the 3-fold axis, show ring currents of 3 orders of magnitude larger than that of benzene.

REFERENCES

1. B. Grünbaum and G. C. Shephard, *Tilings and Patterns*, Freeman, New York, 1985.
2. D. J. Klein and H. Zhu, in: A. T. Balaban, (Ed.), *From Chemical Topology to Three - Dimensional Geometry*, Plenum Press, New York, 1997, pp. 297-341.
3. B. de La Vaissière, P. W. Fowler, and M. Deza, *J. Chem. Inf. Comput. Sci.*, **2001**, *41*, 376-386.
4. M. Deza, P. W. Fowler, M. Shtorgin, and K. Vietze, *J. Chem. Inf. Comput. Sci.*, **2000**, *40*, 1325-1332.
5. M. Endo, S. Iijima, and M. S. Dresselhaus, *Carbon Nanotubes*, Pergamon, **1996**.
6. P. W. Fowler and D. E. Manolopolous, *An atlas of fullerenes*, Oxford University Press, London, **1994**.
7. M. S. Dresselhaus, G. Dresselhaus, and P. C. Eklund, *Science of fullerenes and carbon nanotubes*, Acad. Press, San Diego, **1996**.
8. K. Tanaka, T. Yamabe, and K. Fukui, *The science and technology of carbon nanotubes*, Elsevier, **1999**.
9. A. T. Balaban, (Ed.), *From Chemical Topology to Three - Dimensional Geometry*, Plenum Press, New York, **1997**.

10. L. Euler, *Novi Comment*. *Acad*. *Sci*. *I*. *Petropolitanae*, **1758**, *4*, 109-160.
11. E. C. Kirby, *Croat*. *Chem*. *Acta*, **1993**, *66*, 13-26.
12. E. C. Kirby, R. B. Mallion, and P. Pollak, *J. Chem*. *Soc*. *Faraday Trans*., **1993**, *89*, 1945-1953.
13. D. J. Klein, *J*. *Chem*. *Inf*. *Comput*. *Sci*., **1994**, *34*, 453-459.
14. E. C. Kirby and P. Pollak, *J*. *Chem*. *Inf*. *Comput*. *Sci*., **1998**, *38*, 66-70.
15. T. Pisanski and J. Shawe-Taylor, *J*. *Chem*. *Inf*. *Comput*. *Sci*., **2000**, *40*, 567-571.
16. A. Graovac, D. Plavšić, M. Kaufman, T. Pisanski, and E. C. Kirby, *J*. *Chem*. *Phys*., **2000**, *113*, 1925-1931.
17. I. Laszlo, A. Rassat, P. W. Fowler, and A. Graovac, *Chem*. *Phys*. *Lett*., **2001**, *342*, 369-374.
18. I. Laszlo and A. Rassat, *J*. *Chem*. *Inf*. *Comput*. *Sci*., **2003**, *43*, 519-524.
19. E. C. Kirby, R. B. Mallion, and P. Pollak, *J*. *Chem*. *Soc*. *Faraday Trans*., **1993**, *89*, 1945- 1953.
20. A. Ceulemans, L. F. Chibotaru, S. A. Bovin, and P. W. Fowler, *J*. *Chem*. *Phys*., **2000**, *112*, 4271-4278.
21. A. L. Ivanovskii, *Russ*. *Chem*. *Rev*.,**1999**, *68*, 103-118.
22. N. Hamada, S. Sawada, and A. Oshiyama, *Phys*. *Rev*. *Lett*., **1992**, *68*, 1579-1581.
23. M. V. Diudea, B. Parv, and O. Ursu, *Torus* 1.1 software program, Babes-Bolyai University, 2001.
24. M. V. Diudea, I. Silaghi-Dumitrescu, and B. Parv, *MATCH*, *Commun*. *Math*. *Comput*. *Chem*., **2001**, *44*, 117-133.
25. M. V. Diudea and E. C. Kirby, *Fullerene Sci*. *Technol*., **2001**, *9*, 445-465.
26. M. V. Diudea, *Bull*. *Chem*. *Soc*. *Japan*, **2002**, *75*, 487-492.
27. M. V. Diudea, B. Parv, and O. Ursu, O., *Studia Univ*. *"Babes-Bolyai"*, **2003,** *48*, 3-10.
28. M. V. Diudea, O. Ursu, and B. Parv, *Studia Univ*. *"Babes-Bolyai"*, **2003,** *48*, 11-20.
29. A. K. Singh, T. M. Briere, V. Kumar, and Y. Kawazoe, *Phys*. *Rev*. *Lett*., **2003**, *91*, 146802-1 - 146802-4.
30. A. K. Singh, V. Kumar, and Y. Kawazoe, *J*. *Mater*. *Chem*., **2004**, *14*, 555-563.
31. M. V. Diudea, *Fullerenes*, *Nanotubes Carbon Nanostruct*., **2002**, *10*, 273-292.
32. M. V. Diudea, *Phys*. *Chem*. *Chem*. *Phys*., **2002**, *4*, 4740-4746.
33. M. V. Diudea, T. S. Balaban, E. C. Kirby, and A. Graovac, *Phys*. *Chem*.,*Chem*. *Phys*., **2003**, *5*, 4210 – 4214.
34. S. L. Fang, A. M. Rao, P. C. Eklund, P. Nikolaev, A. G. Rinzler and R. E. Smalley, *J*. *Mater*. *Res*., **1998**, *13*, 2405-2411.
35. M. Terrones, H. Terrones, F. Banhart, J-C. Charlier, and P. M. Ajayan, *Science*, **2000**, *288*, 1226-1229.
36. M. V. Diudea, in: M. V. Diudea, Ed., *Nanostructures-Novel Architecture*, NOVA, New York, 2004 (in press).
37. D. J. Klein, H. Zhu, *From Chemical Topology to Three-Dimensional Geometry,* A.T. Balaban Ed., Plenum: New York, **1997**, Chapter 9, 297-341
38. G. Cash, *J*. *Chem*. *Inf*. *Comput*. *Sci*., **1998**, *38*, 58-61
39. D. E. Manolopoulos, J. C. May and S. E. Down, *Chem*. *Phys*. *Lett*., **1991**, *181*, 105-111.
40. G. Brinkmann and P. W. Fowler, *J*. *Chem*. *Inf*. *Comput*. *Sci*., **1998**, *38*, 463-468.
41. P. W. Fowler, T. Pisanski, A. Graovac, and J. Žerovnik, *DIMACS Ser*. *Discrete Maths*. *Theor*. *Comput*. *Sci*., **2000**, *51*, 175-187
42. M. V. Diudea, *Phys*. *Chem*., *Chem*. *Phys*., **2002**, *4*, 4740-4746
43. D. J. Klein, W. A. Seitz, and T. G. Schmalz, *J*. *Phys*. *Chem*., **1993**, *97*, 1231-1236
44. E. Clar, *Polycyclic Hydrocarbons*, Acad. Press, London, **1964**.
45. E. Clar, *The Aromatic Sextet*, Wiley, New York, **1972**.
46. K. Fries, *J*. *Liebigs Ann*. *Chem*., **1927**, *454*, 121-324.
47. W-Ch. Shiu, P. Ch. B. Lam, and H. Zhang, *Theochem*4, **2000**, p 0210.

48. M. V. Diudea, P. E. John, A. Graovac, M. Primorac, and T. Pisanski, *Croat*. *Chem*. *Acta*, **2003**, *76*, 153-159
49. M. Yoshida, M. Fujita, P. W. Fowler, and E. C. Kirby, *J*. *Chem*. *Soc*., *Faraday Trans*., **1997**, *93*, 1037-1043
50. P. W. Fowler and T. Pisanski, *J*. *Chem*. *Soc*., *Faraday Trans*., **1994**, *90*, 2865-2871
51. J. R. Dias, *J*. *Chem*. *Inf*. *Comput*. *Sci*., **1999**, *39*, 144-150
52. P. W. Fowler, *Chem*. *Phys*. *Lett*., **1986**, *131*, 444-450
53. J. A. Rodriguez-Manzo, F. Lopez-Urias, M. Terrones and H. Terrones, *Nanolett*, **2004**, *4*, 2179-2183

STUDIA UNIVERSITATIS BABES-BOLYAI, CHEMIA, 2005

MODELING AND SIMULATION OF THE LIMESTONE THERMAL DECOMPOSTION IN THE VERTICAL LIMEKILN

ANA-MARIA CORMOS, CALIN CORMOS, SERBAN AGACHI

Babes – Bolyai University, Faculty of Chemistry and Chemical Engineering,
11 Arany Janos Street, RO-400028, Cluj-Napoca, Romania, Tel: +40264593833,
Fax: +40264590818, E-mail: cani@chem.ubbcluj.ro, cormos@chem.ubbcluj.ro,
sagachi@chem.ubbcluj.ro

ABSTRACT. A mathematical model of the limestone thermal decomposition process has been developed in order to determine the evolutions of temperature, solid and gaseous products distribution in the vertical limekiln.

The modeling approach considers the kiln divided into four different subsystems: the gas phase, two solid phases (limestone and coke) and the kiln wall. The model incorporates a detailed mathematical description for the two phases presented into the system, also taking into account the heat transfer through the kiln wall. The gas phase, solid phases and kiln wall have been modeled using mass and heat balance equations for counter-current flow systems. Both time and spatial distribution for gaseous and solid components are described revealing the interactions between different subsystems considered.

A variability study has been used to point out the main process variables and material properties included in the dynamic model. The dynamic model has been compared and fitted with process data collected from an industrial limekiln resulting in a dynamic simulator able to show the evolution of the main process variables versus time and space.

1. INTRODUCTION

Calcium oxide (lime) is one of the most used raw materials for different industries: constructions, steel manufacture, chemical processes, environmental protection etc. In soda ash manufacture, both process products are needed: gaseous flow (carbon dioxide) and solid flow (lime). The lime manufacture process is performed in vertical kilns.

The decrease of energy consumption and efficient use of raw materials for the decomposition process of the limestone in the vertical lime kiln may result in important economic benefits.

Mathematical modeling and simulation in dynamic conditions of the vertical lime kiln represent a valuable tool for studying different construction design approaches, operating strategies and control system design configurations.

2. MATHEMATICAL MODEL

The vertical lime kiln is divided in three zones. The first zone is the heating zone for the solid phase (a mixture of limestone and coke) and at the same time the cooling zone for the gaseous phase. The second zone is the thermal decomposition zone of the limestone and coke combustion. The third zone is the cooling zone for the solid phase (lime) and the heating zone for the gaseous phase (air) that enters into the kiln.

The kinetics of the endothermic decomposition reaction of calcium carbonate decomposition:

$$CaCO_3 \rightarrow CaO + CO_2$$

is considered to follow first order Arrhenius' law.

The coke combustion was modeled using the overall reaction scheme of Amundson in which both CO and CO_2 are recognized as primary products:

$$2\frac{\eta+1}{\eta+2}\mathrm{C}+\mathrm{O}_2 \xrightarrow{k_c} 2\frac{\eta}{\eta+2}\mathrm{CO}+\frac{2}{\eta+2}\mathrm{CO}_2$$

where η-is the primary production ratio $\eta = 70 \cdot e^{-3070/T}$ [1].

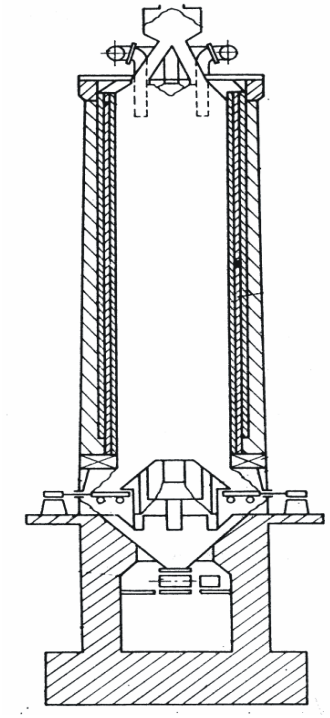

Figure 1. Limekiln

Assumptions:

- Model parameters are constant in the radial cross section of the kiln;
- Limestone is uniformly distributed across the kiln section;
- Flowing regime is ideal for both phases (plug flow);
- Both gas and solids velocity is considered constant.

The modeling approach considers the lime kiln divided into four different subsystems: the gas phase, two solid phases (limestone and coke) and the kiln wall.

The model incorporates a detailed mathematical description for the different phases describing also the heat transfer through the kiln wall.

The gas phase, solid phases and kiln wall, have been modeled using mass and heat balance equations for counter-current flow systems. The mathematical equations of the model are presented below [2-5].

The mathematical equations for heating and cooling zones:

$$\frac{Q_i c_{p_i}}{v_i}\cdot\frac{\partial T_i}{\partial t} = -Q_i c_{p_i}\frac{\partial T_i}{\partial z} + S_{energ}$$

$$M_p \cdot c_{p_p} \cdot \frac{\partial T_p}{\partial t} = S_{energ}$$

where:

c_p - specific heat, [kcal/(kg K)]
M - mass per unit height of vertical kiln, [kg/m]
Q - flow rate, [kg/h]
T - temperature [K]
v - gas and solids velocity, [m/h]
i - gas, limestone and respective coke
S_{energ} – energy source terms.

The source terms in the heat balance equation include: heat fluxes from gas to solids and wall and from solids to wall.

The mathematical equations for reaction zone:

- Total Mass Balance Equation:

$$\frac{1}{v_i}\cdot\frac{\partial Q_i}{\partial t} = -\frac{\partial Q_i}{\partial z} + S_{mass}$$

- Components Mass Balance Equations:

$$\frac{1}{v_s}\cdot\frac{\partial\left(Q_m x_j\right)}{\partial t} = -\frac{\partial\left(Q_m x_j\right)}{\partial z} + S_{comp\,j}$$

$$\frac{1}{v_g}\cdot\frac{\partial\left(Q_g x_k\right)}{\partial t} = -\frac{\partial\left(Q_g x_k\right)}{\partial z} + S_{comp\,k}$$

- Heat Transfer Equations:

$$\frac{Q_i c_{p_i}}{v_i}\cdot\frac{\partial T_i}{\partial t} = -Q_i c_{p_i}\frac{\partial T_i}{\partial z} + S_{energ}$$

$$M_p \cdot c_{p_p}\cdot\frac{\partial T_p}{\partial t} = S_{energ}$$

where:

c_p - specific heat, [kcal/(kg K)]
M - mass per unit height of vertical kiln, [kg/m]
Q - flow rate, [kg/h]
T - temperature [K]
v - gas and solids velocity, [m/h]
x - component concentration
Indices:
i - gas, limestone and respective coke
j - $CaCO_3$ and CaO
k - O_2, CO_2, CO and N_2
S_{mass}, S_{comp}, S_{energ} - source terms.

Extra source for mass (S_{mass}) are due to limestone thermal decomposition reaction and coke combustion.

Carbon dioxide and carbon monoxide are transferred from the solids phases to gas phase (S_{comp}).

S_{energ} terms include: reactions heat (endothermic limestone decomposition reaction and exothermic coke combustion), heat fluxes from gas to solids and wall and from solids to wall.

For the simulation the thermal decomposition process of the limestone in a vertical limekiln, the parameters presented in the table 1 were used.

Table 1.

Parameters of the model

Limekiln parameter:	
Height	H = 16 m
Diameter	D = 4.5 m
Input flows:	
Air flow	Q_g = 9676 kg/h
Limestone flow	Q_m = 10500 kg/h
Coke flow	Q_c = 1000 kg/h
Feed composition:	
Air	X_{O2} = 0.233; X_{N2} = 0.767;
Limestone	X_{CaCO3} = 0.98
Coke	X_C = 0.8
Input feed temperature	T_0 = 20 + 273K
Velocity:	
Solid phases	v_s = 0.4062 m/h
Gas phase	v_g = 1.5 m/s

3. RESULTS AND DISCUSSIONS

The mathematical model of the limestone decomposition process was simulated using MATLAB software package (version 7).

The simulation of the mathematical model of the limestone thermal decomposition process reveals the evolutions (both in time and space) of temperature, solid and gaseous products distribution in a vertical lime kiln.

Some of the most representative simulation results are presented in the figures below. The limestone is the principal raw material of the process, the feed of limestone is on the top of lime kiln, so that in the figures below the bench mark "0" is the top of lime kiln.

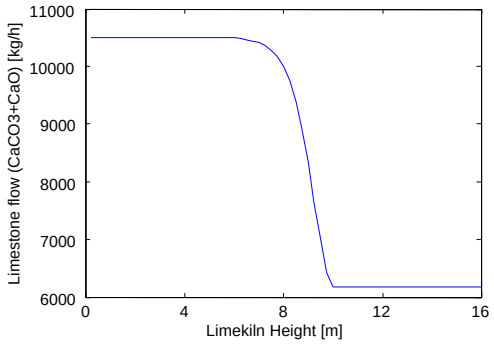

Figure 2. Limestone flow profile along the kiln height

In the figures 2, 3 and 4 the limestone, gas and coke flow profiles along the kiln height are presented. The flows are constant in the heating and cooling zones of the kiln. The decompositon of calcium carbonate and coke burning processes

lead to decreased of solid flows in the reaction zone. Also, the gas flow is increased along the reaction zone because of carbon dioxide and carbon monoxide formation in those two processes.

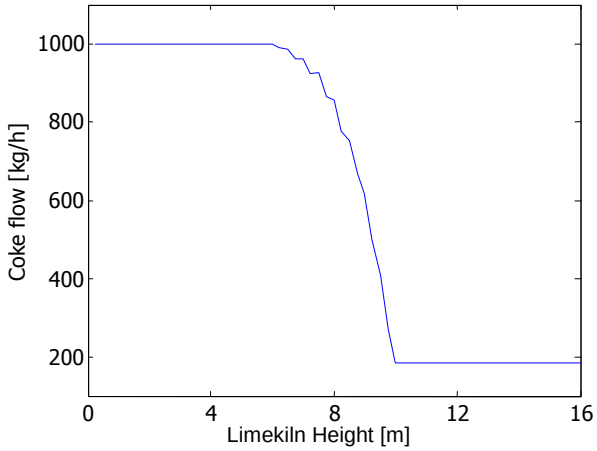

Figure 3. Coke flow profile along the kiln height

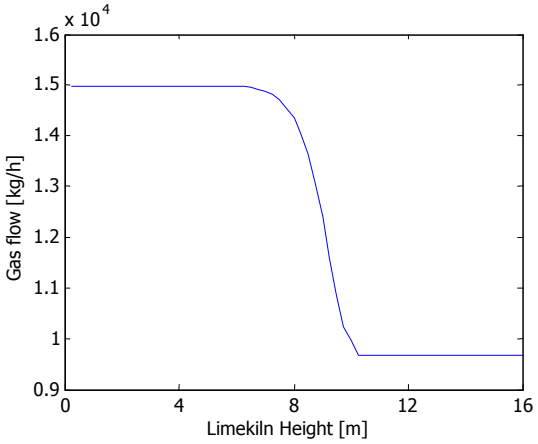

Figure 4. Gas flow profile along the kiln height

The figure 5 shows that the calcium oxide concentration increases along the reaction zone (from top to bottom of the limekiln) at value 89.43 % [weight %] what is corresponded to 95.7 % conversion of limestone.

In figure 6, the carbon dioxide concentration profile on the vertical limekiln is presented. The concentration of the carbon dioxide on the top of the limekiln obtained by simulation has value 38.2% [volume %] and is comparable with the one obtained in the real plant (38-41% [volume %]).

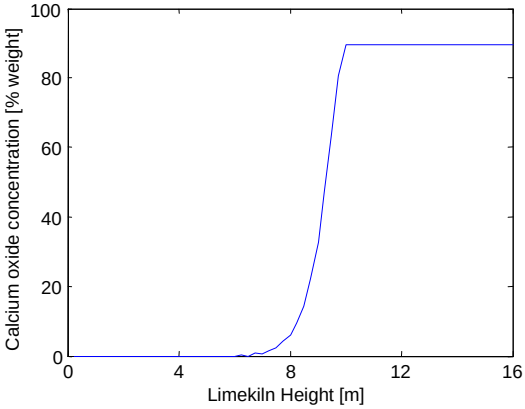

Figure 5. Calcium oxide concentration profile along the kiln height

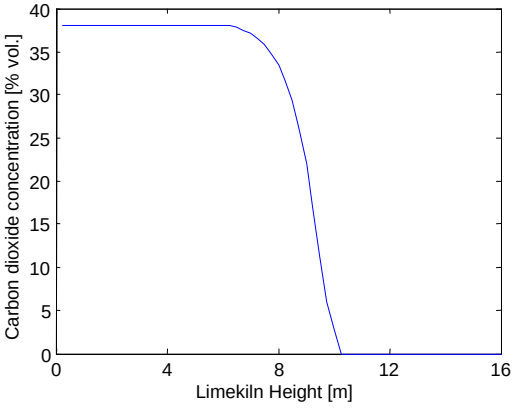

Figure 6. Carbon dioxide concentration profile along the kiln height

The limestone ($CaCO_3$ + CaO) T_m, coke T_c, gas T_g and inside kiln wall T_p temperatures profiles are presented in the figure 7.

The figure 7 shows that the solids temperatures increase in the heating zone. The limestone and coke introduced on the top of the kiln are heated by the warm gaseous phase, leaving the reaction zone, up to the point when limestone thermal decomposition and cook burning begin. The lime resulted in the decomposition zone is cooled in the third zone with the gaseous phase (air) introduced at the bottom of the kiln. The maximum of temperatures are in the second zone where the coke's burning reaction takes place in parallel with thermal decomposition of the limestone. The wall temperature profile follows the gaseous and solid phases profiles.

In the table 2, the simulation results of the limekiln are compared with real plant operation data in order to validate the application developed for simulation of the process.

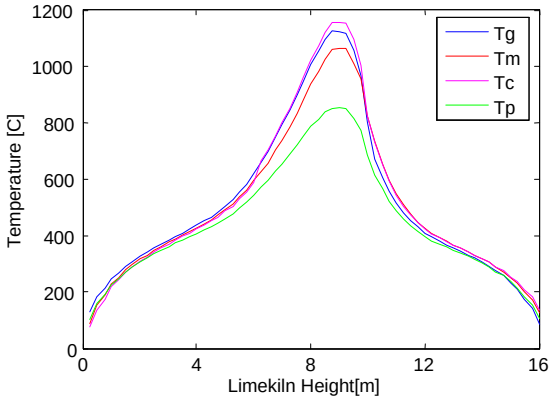

Figure 7. Temperatures profile along the kiln height

Tabel 2.

Comparison of simulation results with real plant data

Parameter	Real plant dataparameters	Process simulation results
Reaction zone temperature	1050 – 1200^{o}C	1159^{o}C
Output gas temperature	80 – 160^{o}C	130^{o}C
Gas composition [volume %]:		
CO_2	38 – 41%	38.2 %
O_2	0.4 – 1.5 %	1.12 %
CO	0.5 – 2.5 %	0.58 %
Output lime temperature	50 – 120^{o}C	120^{o}C
Lime composition [weight %]:		
$CaCO_3$	< 10 %	7.16 %
CaO	> 80 %	89.43 %
Efficiency of limestone decomposition	91 – 96 %	95.7 %
Thermal efficiency of limekiln	75 %	76 %

From the comparison of simulation results with data collected from the real plant a close similarity can be observed. This fact validates the mathematical model of the process and the simulation results obtained using MATLAB software package.

The dynamic behavior of the lime kiln was also investigated in the presence of the typical process disturbances (e.g. limestone flow variation). Some of the representative results are presented in the figures 8 and 9.

The process response at a step increase of ΔQm=+10% are characterized by the oscillation of parameters. The oscillation amplitude of parameters is decreasing in time, needing more than 20 hours to attend a new stationary phase.

The simulation results were compared with real plant operation data in order to validate the application developed for the process. From the comparison of the simulation results with data collected from real plant operation a close similarity can be noticed. This fact validates the mathematical model of limestone decomposition process in a vertical kiln.

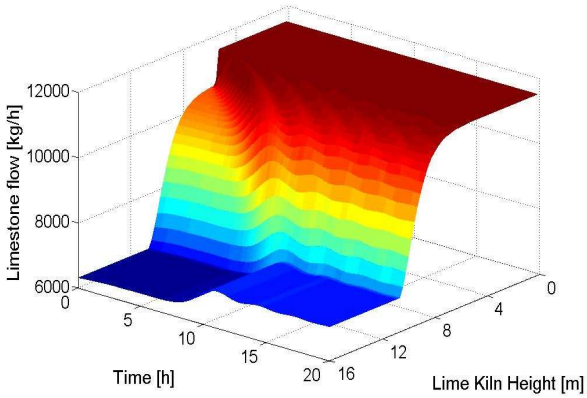

Figure 8. Dynamic response of limestone flow for a step increase of ΔQm=+10%

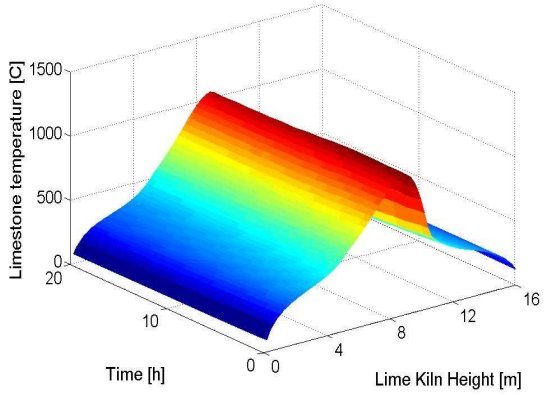

Figure 9. Dynamic response of limestone temperature for a step increase of ΔQm=+10%

4. CONCLUSIONS

Modeling and simulation of the thermal decomposition of limestone in the vertical limekiln was done using MATLAB software.

The evolutions in both time and space of the process parameters (solid and gaseous flows, composition of the streams, temperatures) were studied during the limestone decomposition process. The simulation results were compared with real plant operation data in order to validate the application developed for the process.

The mathematical model of the limestone thermal decomposition can be used to study the behavior of the process in changing operating conditions and the influence of different disturbances on the thermal decomposition of limestone. The process simulation results can be very useful to establish the optimal operation conditions and to design the control system for the plant.

REFERENCES

1. Biggs M.J., Agarwal P.K., The CO/CO2 product ratio for a porous char particle within an incipiently fluidized bed: a numerical study, Chem. Eng. Sci. 52(6), 941-952, 1997
2. Cristea M., Maniut C., Cormos A.M., Agachi S., Simulation of Calcium Carbonate Decomposition in the Rotary Calciner, 30th Conference SSCHE, Tatranske Matliare, Slovakia, 26-30 May, 2003
3. Cristea V.M., Agachi S.P., Control of an Industrial Rotary Calciner for Soda Ash Production, Proceeding of ESCAPE-12 Congress, Hague, The Netherlands, 463-468, 2002
4. Cormos A.M., Cristea M., Agachi S., Zaha G., Dynamic Simulation of the Calcium Carbonate Thermal Decomposition in Vertical Lime Kiln, CHISA 2000 Congress, 27-31 August, Praha, 2000
5. Le Blanc G.D., Seborg D.E., Holman K.L., Physically-Based, Dynamic Model of a Lime Kiln, AIChE Annual Meeting, Los Angeles, 18 November, 1997

STUDIA UNIVERSITATIS BABES-BOLYAI, CHEMIA, L, 2, 2005

NEURAL NETWORKS APPLICATIONS IN CHEMISTRY AND CHEMICAL ENGINEERING

VASILE-MIRCEA CRISTEA, PAUL ŞERBAN AGACHI

"Babeş-Bolyai" University, Faculty of Chemistry and Chemical Engineering, 11 Arany Janos, 400028 Cluj-Napoca, e-mail: mcristea@chem.ubbcluj.ro

ABSTRACT. The paper presents results of using artificial Neural Networks (NN) in chemistry and chemical engineering applications. Several incentives accomplished by NN are revealed and sustained by relevant examples: capability of predicting the behaviour of systems for which the first principle modelling is difficult or insufficiently known (Simulation of Electrochemical Impedance Diagrams), capacity of building reliable dynamic models subsequently used for model based control (Model Predictive Control of the Drying Process of Electric Insulators) and ability of ANN to perform classification tasks where the membership of individuals to specific groups is not obvious (Characterisation of Commercial Vinegar).

1. INTRODUCTION

The field of NN has a history of five decades but it has found solid application only in the last decade and the field is still developing rapidly. Founded on an idealised model of the biological neuron, the calculation paradigm of NN is able to represent information on complex systems. The main characteristics of the NN model are the inputting of information (signals) from exterior or other units of the network, feeding it to the given unit (neuron) that processes it and then sending it, as output, to other units or output of the network. The main benefits of the NN approach consist in its remarkable ability of learning, generalisation and robust behaviour in the presence of noise [1]. As a consequence, the NN may be successfully used for modelling systems in which detailed governing rules are unknown or are difficult to formalise, but the desired input-output set is known. The NN prediction capability of generating new values of outputs is usually highly appreciated.

The use of NN models for control purposes has gained considerable attention in the field of chemical process control, being the subject of several scientific reports, as they are increasingly applied for system identification and controller design [2]. The favourable opportunities offered by the NN also consist in important savings of computer resources, having direct effect over the on-line computation in control oriented applications. The results presented in the following, reveal the potential of NN for both simulation and control applications.

2.SIMULATION OF ELECTROCHEMICAL IMPEDANCE DIAGRAMS

The NN approach has been used to improve the electrochemical impedance spectroscopy (EIS) set of experimental data by NN simulation, for copper electro-deposition. The trained NN, with data obtained in different experimental conditions (electrode potential, and thiourea concentrations), were used: (i) to improve the estimation of two important electrochemical parameters (the double layer capacity of the interface and the electrolyte resistance) by generating supplementary output

data for new frequency values, both inside and outside the investigated domain; (ii) to generate impedance spectra for new electrode potential values within the investigated range of the potential [3].

The investigated system has been considered as having three input variables: the continuous amplitude component of the sinusoidal applied voltage, the signal frequency and the thiourea concentration. First, the NN has been trained using the bulk set of experimental data (90% of the original experimental set). Second, in order to test the NN generalization capability, the remained subset of experimental data (10% of the original experimental set) was operated. Results showing the comparison between the experimental and NN simulated data are presented in figures 1 to 3, for for all the three NN output variables: current amplitude, real part and imaginary part of the electrochemical impedance.

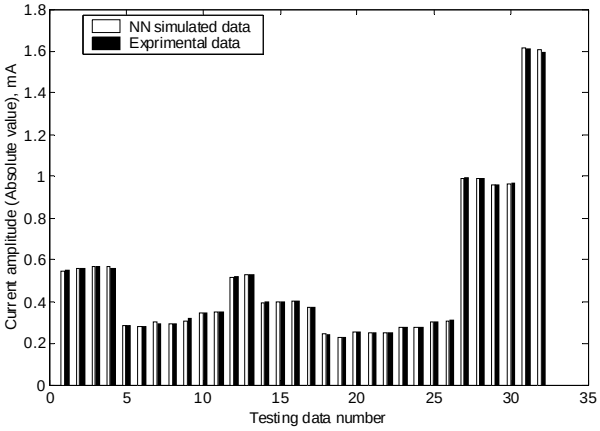

Figure 1. Comparison between NN simulated data and experimental data for current amplitude. Experimental conditions: sinusoidal frequency ranging from 2.2 Hz to 6.8 kHz; thiourea concentration c=10 mg/l.

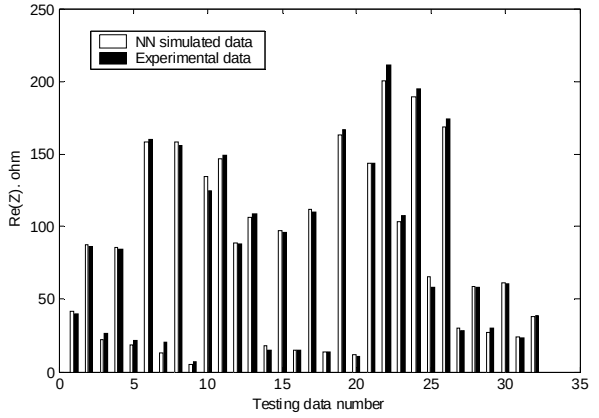

Figure 2. Comparison between NN simulated and experimental data for the real part Re(Z) of the electrochemical impedance. Experimental conditions: sinusoidal frequency ranging from 2.2 Hz to 6.8 kHz; thiourea concentration c=10 mg/l.

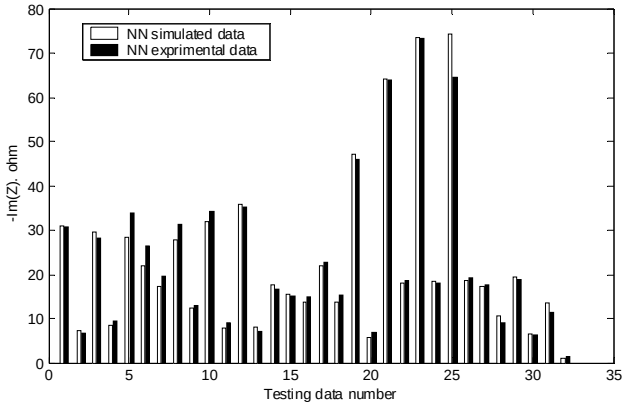

Figure 3. Comparison between NN simulated and experimental data, for the imaginary part Im(Z) of the electrochemical impedance. Experimental conditions: sinusoidal frequency ranging from 2.2 Hz to 6.8 kHz; thiourea concentration c=10 mg/l.

Results presented in figures 1 to 3 reveal a good prediction capability of the trained NN, with good results for the case of the presented frequency range: 2.2 Hz to 6.8 kHz.

Additional investigation has been performed to study the prediction capability of the trained NN for generating outputs of the electrochemical system for input variables having values situated between (different from) the experimental values used in the training or testing steps. Thus, different values for the amplitude and for the frequency of the input electrode potential have been supplied to the NN and the obtained results are presented in figure 4.

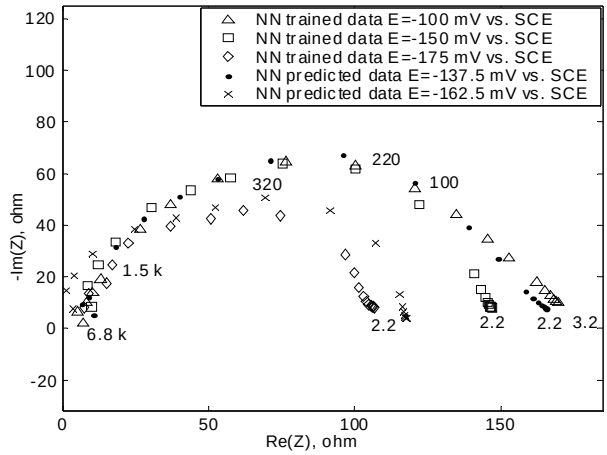

Figure 4. Nyquist plot presenting NN predicted values of the electrical impedance for different values of the input electrode potential. Experimental conditions: sinusoidal frequency ranging from 2.2 Hz to 6.8 kHz; thiourea concentration c=10 mg/l.

The obtained results fit to a shape that conforms with the expected form (qualitatively inferred by induction) for the electrochemical impedance. This agreement proves that the trained NN were able to predict well the electrochemical impedance of this complex system, otherwise difficult to be described using analytical models.

3. MODEL PREDICTIVE CONTROL OF THE DRYING PROCESS OF ELECTRIC INSULATORS

The high-voltage electric insulator production implies a first step batch drying process in order to reduce the moisture content of the drying product from 18-20% to 0.4%, performed in special gas-heated drying chambers. Gas and air flow rates are controlled according to a special program, during a period of about 100 hours, in order to obtain the desired moisture content and avoiding the risk of unsafe tensions in the drying products. Building a detailed first principle model, able to thoroughly describe the spatial and temporal evolution of properties inside the electric insulator body and needed in model based control, is complex and not yet reliable [4]. The NN-based control may overcome some of these problems.

The NN model of the dryer has been developed to serve two goals. The first one is to provide information on time evolution of target variables, inherently needed for prediction in the Model Predictive Control (MPC) algorithm. The second one is to infer the moisture content of the drying product, based on available measured variables, model that is later used for NN observer based MPC. The NN developed model has the complimentary property of requesting reduced computation effort, supplying the algorithm with speed necessary for real time implementation.

Taking into account that the target variable, i.e. the moisture content of the product, is not available for direct measurement, a NN based state observer is proposed for its estimation. The data provided by the NN state observer is used for feedback MPC of the product moisture content, as shown in figure 5, [5].

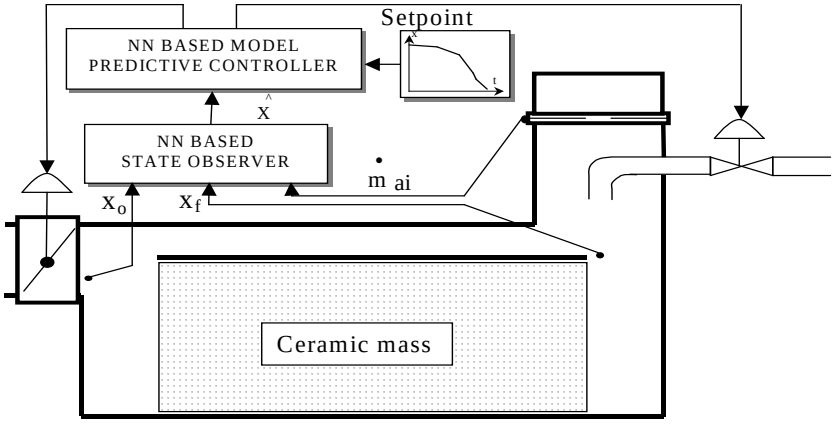

Figure 5. Structure of the control system for direct moisture content control using NN based state observer and NN based MPC controller.

The time dependent setpoint selection for the moisture content is based on practical and theoretical considerations concerning the time evolution of the product drying-rate. The conditions stated by the above mentioned considerations are best fulfilled by a seven-segment ramp function, which is actually used as setpoint. Simulations were conducted using this control structure and the results, for two *10%* heating power disturbances applied at both *t=3000 s* and *t=1250000 s*, are presented in figure 6.

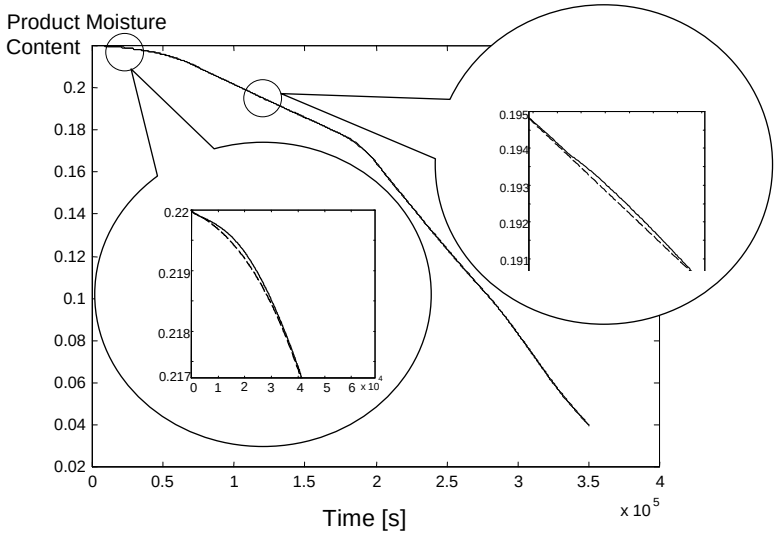

Figure 6. Setpoint (dashed line) following and disturbance rejection ability for direct moisture content control using NN based state observer and NN MPC (solid line).

The simulation results for this control structure show both good setpoint following and disturbance rejection capability. The applied model predictive algorithm has a few special features that makes it more effective: it operates with constraints on manipulated variables and controlled variables; in order to obtain the feasible and feasible control performance, a nonlinear form of the MPC algorithm was used; the MPC controller was tuned according to the dynamic sensitivity analysis. A significant reduction of the computation time (2:1 ratio) has been also observed as a consequence of NN model use that requires less computer power compared to the first principle model.

4. CHARACTERISATION OF COMMERCIAL VINEGAR BY NEURAL NETWORKS

The aim of this appication was to classify several vinegars using the Neural Networks approach [6]. The classification was based on the determination of eleven analytical parameters of commercial vinegars, divided into five categories according to the raw material: white wine vinegar (WWV), red wine vinegar (RWV), alcohol vinegar (ALV), apple vinegar (APV), and non-coloured industrial vinegar (NIV). The analytical parameters assessed were the usual employed for controlling and monitoring the quality of vinegar: total acidity ($g \cdot L^{-1}$) detached in volatile acidity ($g \cdot L^{-1}$) and fixed

acidity ($g \cdot L^{-1}$), pH, dry matter ($g \cdot L^{-1}$), ash content ($g \cdot L^{-1}$), sulphates ($g \cdot L^{-1}$), chlorides ($g \cdot L^{-1}$), glycerol ($g \cdot L^{-1}$), total polyphenol index (TPI, dimensionless), Folin-Ciocalteu index (FCI, dimensionless) and modified colour intensity (MCI, dimensionless). Ninety-four commercial vinegars were acquired in six supermarkets in Tarragona (Catalonia, Spain) during the year 2000. The markets selected cover most of the sales to consumers of food and beverages. Samples were taken directly from every meter of displayed product in the stand (i.e. those brand names with more rack space are represented with more samples). Using this sampling method a representative mix, directly related to the market share of each vendor, was achieved. As a result, the number of vinegars per categories was not homogeneous (WWV: 54 samples; RWV, 32 samples; ALV, 3 samples; APV, 4 samples; and NIV, 2 samples).

First, the NN has been trained to learn the vinegar categories based on the original set of data from which a randomly selected set of data (testing set) has been extracted. Second, the trained NN was used for testing the prediction capability using the testing set of not yet encountered data. For the testing set of 13 vinegar samples the NN succeeded to predict the right category, without any mismatch. The obtained results showed a good capability of the NN to classify the vinegar category.

Results of this NN based category classification, for the testing set of data, are presented in Table1.

Table 1

NN based category classification

Sample no.	Actual category	Predicted category				
		WWV	RWV	NIV	APV	ALV
4	WWV	✓	-	-	-	-
10	APV	-	-	-	✓	-
15	WWV	✓	-	-	-	-
25	ALV	-	-	-	-	✓
30	RWV	-	✓	-	-	-
34	RWV	-	✓	-	-	
44	RWV	-	✓	-	-	-
47	WWV	✓	-	-	-	-
56	WWV	✓	-	-	-	-
64	WWV	✓	-	-	-	-
72	RWV	-	✓	-	-	-
78	WWV	✓	-	-	-	-
82	WWV	✓	-	-	-	-

Another NN was trained to classify the producer. For the same set of 13 vinegar samples, this special trained NN succeeded to predict the producer (among the set of 9 producers), with small errors. For this case the classification errors vary, when picking different sets of training/testing data, from perfect match to one mismatch out of the 13 samples. A perfect match case is presented in Table 2.

The results show a good capability of the NN to classify the vinegar, according to both investigated criteria: category and producer. Results also demonstrate that NN succeed to capture the intrinsic relationship between vinegar properties and producer, thus stating that product characteristics are strongly dependent on the production techniques.

Table 2

NN based producer classification

Sample no.	Actual Producer	Predicted Producer								
		P1	P2	P3	P4	P5	P6	P7	P8	P9
4	P1	✓	-	-	-	-	-	-	-	-
9	P1	✓	-	-	-	-	-	-	-	-
14	P2	-	✓	-	-	-	-	-	-	-
26	P2	-	✓	-	-	-	-	-	-	-
30	P3	-	-	✓	-	-				
34	P3	-	-	✓	-	-	-	-	-	-
44	P4	-	-	-	✓	-	-	-	-	-
47	P4	-	-	-	✓	-	-	-	-	-
56	P5	-	-	-	-	✓	-	-	-	
64	P6	-	-	-	-	-	✓	-	-	-
72	P7	-	-	-	-	-	-	✓	-	-
78	P8	-	-	-	-	-	-	-	✓	-
82	P9	-	-	-	-	-	-	-	-	✓

5. CONCLUSIONS

Important incentives of the ANN approach are explored, such as modelling process for which detailed governing rules may be difficult to formalize as first principle models and reducing the computation time in the case of nonlinear model based control. Simulation results also reveal benefits for the NN based MPC using the NN based observer approach (control of inferred variables), compared with traditional direct feedback control methods.

For the simulation of electrochemical impedance diagrams the employed NN architecture was of the multilayer feed-forward structure with the backpropagation training algorithm used for computing the network biases and weights. Two layers of neurons have been considered, having the tan-sigmoid transfer function for the hidden layer and the purelin transfer function for the output layer. The quasi-Newton Levenberg-Marquardt algorithm was used for training the NN and an early stopping method was applied for preventing the NN overfitting and for improving generalisation.

For the dynamic NN based model of the drying process the NN inputs are the states of the system at current moment of time t together with the manipulated variables, and the NN-outputs are the three state variables considered at the next sampling time $t+\Delta t$. The trained NN is designed to predict one step into the future the behaviour of the state variables. Applied repeatedly, the dynamic NN predicts the time evolution of the state variables over a desired time horizon.

For the classification purposes the NN architecture had a radial basis layer and a competitive layer. The first one computed the distance between the input vector and the training input vectors, generating a vector with elements measuring the deviation with the training input vector. The second layer processed the deviation vector for each class of inputs creating a vector of probabilities from which the competitive transfer function selects the maximum of the probabilities.

Designing the network architecture, i.e. the number of layers and the number of neurons in each layer of the NN, is not a trivial task as there are no simple rules for setting them. Trial and error techniques still play an important role for setting a minimal but successful NN structure. Another important aspect is the pre-processing of the data used for training the NN. Expunging the outliers in the process of training and repeating the training procedure with the remaining set of data may be a good choice to filter the noisy or non-confident process data.

Although NN do not prove to be a panacea for all modelling or control purposes they present incentives for a large set of applications showing continuous open improving potential for further development.

REFERENCES

1. M. T. Hagan, H. B. Demuth, M. H. Beale, “Neural Networks Design”, MA: PWS Publishing, Boston, 1996.
2. S. Haykin, “Neural Networks A Comprehensive Foundation”, MacMillan Publishing Company, Englewood Cliffs, 1994.
3. M. V. Cristea, S. Varvara, L. Muresan, I. C. Popescu, *Indian Journal of Chemistry*, **2003** *42A*, 764-768.
4. O. Krischer, W. Kast, “Die wissenschaftlichen Grundlagen der Trocknungstechnik”, Springer-Verlag, 1992.
5. V. M. Cristea, R. Roman, S. P. Agachi, Neural Networks Based Model Predictive Control of the Drying Process, European Symposium on Computer Aided Process Engineering-13, Lappeenranta, Finland, 1-4 June, 2003, 389-394.
6. M. V. Cristea, L. Jimenez, J. M. Mateo, I. Achaeradino, C. Güell, F. Lopez, Characterization of Commercial Vinegar by Neural Networks, 9-th Mediterranean Congress of Chemical Engineering, 26-29 Nov., 2002, 509.

STUDIA UNIVERSITATIS BABEŞ-BOLYAI, CHEMIA, L, 2, 2005

GENETIC ALGORITHMS OPTIMISATION AND ITS USE IN CHEMICAL ENGINEERING

ROMAN BOCHENEK, JACEK JEŻOWSKI*, ALINA JEŻOWSKA

[*] *Rzeszów University of Technology, Department of Chemical and Process Engineering,*
35-959 Rzeszów, Al. Powstanców Warszawy 6, Poland,
* email: *ichjj@prz.rzeszow.pl*

ABSTRACT. The paper deals with applications of genetic algorithms (GA) optimisation in chemical and process engineering. A novel optimisation procedure has been developed that is aimed at reducing an effect of premature degeneration. The description of optimisation algorithm is given. Solutions of two chemical engineering problems are also presented. The results show that the developed GA optimisation subroutine is efficient tool for solving complex nonlinear problems of chemical and process engineering.

Keywords: optimisation, genetic algorithms, reaction equilibrium, batch plant

1. INTRODUCTION

Genetic algorithm is relatively modern stochastic optimisation strategy. Applications in chemical in process engineering range from structural and parametric optimisation of processes, apparatus and systems (see e.g. [1]) via process modelling (e.g. [2]) to expert systems (for instance [3]).

GA strategy has an opinion of efficient optimisation technique for global optimisation of combinatorial problems, such as, for instance, scheduling of batch processes. The application to problems with only continuous variables is possible though rare. Deterministic approaches are expected to be more reliable tools for such problems. However, one should take into account such difficulties with deterministic methods as e.g. discontinuities of functions.

Similarly to other stochastic optimisation methods such as adaptive random search (ARS) or simulated annealing (SA) there are many versions of GA. In fact, only few common rules are applied in majority of GA optimisation techniques published in the literature, such as:

- fixed number of members in generated populations,
- given number of generated populations applied commonly as stopping criterion,
- crossover operator is the basic mean for genetic changes (though there exist many types of such operator) while mutation is treated as auxiliary operator.

Some procedures developed in the literature are quite complex while others simple. It is difficult to assess effectiveness of some versions suggested in the literature since insufficient tests had been carried out. More sophisticated versions usually ensure higher probability of locating global optimum. Such approaches need, however, more control parameters which have to be tuned by the user for specific problem. This requires a lot of trials and, also, user's experience.

In this work we present a GA-based optimisation method that is designed for general nonlinear mixed-integer optimisation problem (MINLP). We have attempted to reach a compromise between reliability of locating global optimum (that usually requires complex algorithm, many operators and numerous control parameters) and easiness of application (that requires a simple algorithm and a small number of control parameters).

In the following we present a description of the developed method. Then, examples of applications from chemical and process engineering are given.

2. GENETIC ALGORITHMS

The developed approach is aimed at solving general problem as follows:

$$\min FC(\boldsymbol{x},\boldsymbol{y}) \tag{1}$$

s.t.

$$h_k(\boldsymbol{x},\boldsymbol{y}) = 0\ , \qquad k=1,\ \ldots,\ K \tag{2}$$

$$g_l(\boldsymbol{x},\boldsymbol{y}) \le 0\ , \qquad l=1,\ \ldots,\ L \tag{3}$$

$$x_i^L \le x_i \le x_i^U\ , \qquad i=1,\ \ldots,\ I \tag{4}$$

$$y_j^L \le y_j \le y_j^U\ , \quad y_j \in \boldsymbol{D}_j, \qquad j=1,\ \ldots,\ J \tag{5}$$

where: $\boldsymbol{x}$ is vector of continuous variables and $\boldsymbol{y}$ is vector of discrete variables.

In contrast to early GA methods our algorithm does not use traditional chromosome code. We have applied easy and "natural" for technical problems representation where chromosome is defined by a vector of decision parameters. To cope with inequality constraints a well known penalty function approach was adapted, i.e. the original goal function was augmented by penalty terms.

Equality constraints are dealt for in two ways:

1) by replacing each equality by a pair of inequalities:

$$h_k(\boldsymbol{x},\boldsymbol{y})=0 \quad \rightarrow \quad h_k(\boldsymbol{x},\boldsymbol{y}) \ge -\varepsilon \ \text{ and } \ h_k(\boldsymbol{x},\boldsymbol{y}) \le \varepsilon \tag{6}$$

where: ε is a sufficiently small number

2) by determining values of some variables sequentially from equations or by solving simultaneous equations set.

The latter approach is more efficient since it reduces number of degrees of freedom. However, it is necessary to find such independent variables (i.e. the variables that are generated by optimisation algorithm) that linear equations are created in regards to the dependent variables. This is greatly facilitated by a possibility of applying sequential calculations in frame of GA.

In order to increase chances of survival of the best fitted individuals and to decrease an effect of "premature degeneration" we applied the so called "genetically modified sub-population". Members of this sub-population are created by using genetic operators to randomly chosen members of the parent population. Next, we form an intermediate population that is the superset of the parent population and genetically modified sub-population. The selection mechanism chooses the individuals that create the parent population of next generation. It is worthwhile noting that the sub-population has less number of members than the parent population and the number of its members is determined by a control parameter called modification ratio *u_mod*.

The procedure of genetic algorithm optimisation is given in the following. Figure 1 illustrates the main steps.

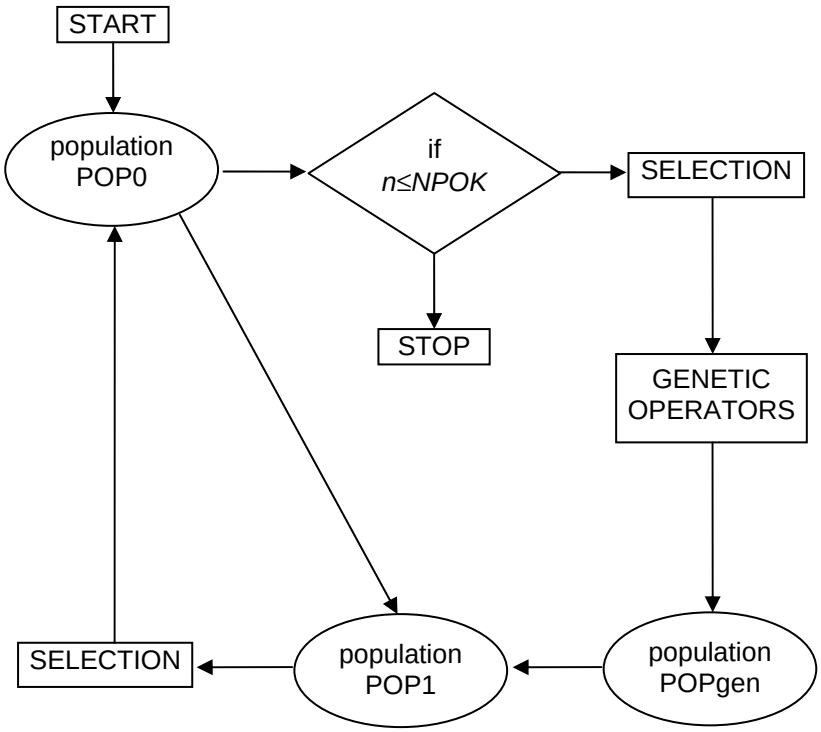

Figure 1. Flow sheet of optimisation algorithm

1) input values of control parameters
- population size *NPOP*,
- total number of populations generated in optimisation *NPOK*,
- number of genetic operators *NOPER*,
- modification ratio *u_mod*,
- probabilities of using the operators p_gen_i (i=1,..., *NOPER*)

[As in many others GA optimisation methods the population size is kept constant during optimisation. Also, given total number of generated populations is used as the stopping criterion.]

2) Calculation of parameters for fitness function.

Fitness function with penalty terms is calculated from:
- for minimisation: $FP=C_{max}-FC-CK$ (7)
- for maximisation: $FP=C_{min}+FC-CK$ (8)

Parameters C_{max}, C_{min} are calculated as follows. A set of many individuals (e.g. 10.000) is randomly generated and parameters C_{max}, C_{min} are determined from:

- for minimisation: C_{max}= abs(max{*FC*+*CK*}) (9)
- for maximisation: C_{min}=abs(min{*FC*-*CK*}) (10)

where abs () is the operator transforming negative into positive value

3) calculation of genetically modified population size
NPOPgen=int (*u_mod***NPOP*)
where int () is the operator that transforms real number into integer one

4) creation of initial population *POP0*

5) calculation of fitness function for members of population *POP0* from (7) for minimisation or from (8) for maximisation.

6) calculation of probabilities $p0_i$ (*i*=1, ...,*NPOP*) for selecting individuals from population *POP0*.

7) creation of genetically modified sub-population
a. selection of genetic operator *i* with probability p_gen_i
b. selection of individual (individuals) *i* for genetic modifications with probability $p0_i$
c. creation of modified individual (individuals) *i* by using selected operator
d. points a) and b) are performed until given size of sub-population *NPOPgen* is reached

8) calculation of fitness function for members of sub-population *POPgen*.

9) calculation of probabilities $p1_i$ (*i*=1,...,*NPOP*+*NPOPgen*) for selecting individuals from the superset consisting of sub-population and parent population

10) creation of offspring population having *NPOP* members by choosing members from the superset consisting of parent population and sub-population with probability $p1_i$ (the superset is intermediate population)

11) the population from previous step is copied into parent population of next generation

12) points (5) to (11) are performed until generation number is greater than *NPOK*

In the present version of the algorithm we applied the following genetic operators:

1. Simple crossover. Two parents exchange information by interchanging parts of their chromosomes. For selected parents and randomly chosen cutting position "*k*" in chromosomes the operation is given by:

$$\{x_1,x_2, ...,x_n\} + \{y_1,y_2, ...,y_n\} \rightarrow \{x_1,x_2,...,x_k,y_{k+1},...,y_n\} + \{y_1,y_2,...,y_k,x_{k+1}, ...,x_n\}$$

2. Arithmetic crossover. This operation though operates on two parents gives only one offspring that is linear combination of parents as follows:

$$\{x_1,x_2, ...,x_n\} + \{y_1,y_2, ...,y_n\} \rightarrow \{r*x_1+(1-r)*y_1,r*x_2+(1-r)*y_n,..., r*x_n+(1-r)*y_n\}$$

3. Heuristic crossover. Similarly to the arithmetic crossover also one offspring is produced from two parents. However, offspring's chromosome depends on fitness functions of parents according to:

$\{x_1,x_2, ...,x_n\} + \{y_1,y_2, ...,y_n\} \rightarrow P$

$P=\{x_1+r(x_1- y_1), x_2+r(x_2- y_2),...,x_n+r(x_n- y_n)\}$, if $FP(X)>FP(Y)$

or

$P=\{y_1+r(y_1- x_1), y_2+r(y_2- x_2),...,y_n+r(y_n- x_n)\}$, if $FP(Y)>FP(X)$

4. Uniform mutation. One parent is selected and, then, randomly chosen position "*k*" of chromosome is mutated in such the way that its value is changed by the value chosen from the entire range - see eqs (4, 5). Selection of the position in chromosome and choice of the value is performed using uniform distribution.

5. Non-uniform mutation. This operator differs from the previous one since the value of parameter $x[k]$ is chosen from the range given by:

$<x[k]-\Delta, x[k]+\Delta>$. Parameter Δ is defined by the formula:

$$\Delta= (x^U - x^L)*(1-r^{(1-n/NPOK)*B}) \quad (11)$$

where: *n*- current number of generation, *r* - random number from the range <0,1>, *B* - constant parameter.

It is important to note that "Δ" is the function of number of populations generated to the moment and "Δ" increases with an increase of this number. In consequence, range of values for parameter "*k*" diminishes in course of optimisation.

6. Local mutation. Randomly selected position $x[k]$ from also randomly chosen individual is changed according to: $p[k]=x[k]\pm\Delta$, where: $\Delta=(x^U-x^L)/C$, C – operator's parameter.

7. Range limit mutation. Randomly chosen position $x[k]$ of individual's chromosome is given upper (x^U) or lower (x^L) limiting value with uniform distribution. The operator may have significant effect in case where optimum values of some variables are at their range limit.

3. EXAMPLES OF APPLICATIONS

At present the optimisation method is in course of testing procedure. The aim is to test its robustness and computational efficiency for a wide variety of optimisation problems that can be met in chemical and process engineering. Also, we intend to find possibly narrow ranges of values for control parameters. The results will be published in forthcoming work. Some general guidelines are given in summary section. In this paper we present results for two problems from chemical engineering.

3.1. Chemical reaction equilibrium

The problem was first given in [4] and considered also in [5-7]. This is minimisation of Gibbs free energy for chemical reaction system, i.e. determination of reaction equilibrium composition. For N species, temperature T and pressure P the free energy function is approximated by equation (12) according to [4]:

$$\frac{G_M}{RT} = \sum_{i=1}^{N} x_i \left(\frac{G_i^o}{RT} + ln\,P + ln \frac{x_i}{\sum_{i=1}^{N} x_i} \right) \quad (12)$$

where: G_i^o – standard free energy of specie i at temperature T, i – denotes specie, x_i – moles number of specie i, P – pressure, G_M –Gibbs free energy of a system.

Constraints of material balance have to be added, such that:

$$\sum_i a_{ij} x_i = b_j \quad j=1, \ldots, \text{number of atom types in the system} \tag{13}$$

where: a_{ij} – number of type „j" atoms in specie „i" after reaction, x_i –moles number of specie „i", b_j – number of type „j" atoms

We consider here literature example from [4] - calculation of the composition of gases after combustion of stoichiometric mixture of hydrazine and oxygen at 3500 K and 750 kPa. Ten species can potentially exist in a system after reaction: (i=1,...,10): H, H_2, H_2O, N, N_2, NH, NO, O, O_2, OH (H, O are radicals). There are three (3) types of atoms: (j = 1, ..., 3, j = 1 denotes H, j = 2 denotes N and j = 3 denotes O).

The optimisation model for hydrazine combustion is given in the following (symbol c_i denotes parameters (G_i^o/RT+ln$P$) in eq. (12)). Values of c_i were taken from [4] .

$$min \sum_{i=1}^{10} x_i \left(c_i + ln \frac{x_i}{x_1 + \ldots + x_{10}} \right) \tag{14}$$

subject to:

$$x_1 + 2x_2 + 2x_3 + x_6 + x_{10} = 2 \tag{15}$$

$$x_3 + x_7 + x_8 + 2x_9 + x_{10} = 1 \tag{16}$$

$$x_4 + 2x_5 + x_6 + x_7 = 1 \tag{17}$$

vector of parameters c_i:

$\boldsymbol{c}$=[-6.089 -17.164, -34.054 -5.914 -24.721 -14.986 -24.100 -10.708 -26.662 -22.179]

Optimal solution according to [7] is:

$\boldsymbol{x}^*$ = [0.04034785 0.15386976 0.77497089 0.00167479 0.48468539 0.00068965 0.02826479 0.01849179 0.03849563 0.10128126],

$f(\boldsymbol{x}^*)$ = - 47.760765

The problem has seven degrees of freedom since three equality constraints can be used to eliminate three variables. We solved the problem in this way and obtained the global optimum $f(\boldsymbol{x}^*)$ =-47.7602 using 6 members in population, 5000 populations and with modification ratio *u_mod*=0.95. The genetic operators were given the following probabilities: simple crossover – 0.1, arithmetic crossover – 0.1, heuristic crossover – 0.2, uniform mutation – 0.05, non-uniform mutation – 0.25, local mutation – 0.25, range limit mutation – 0.05.

3.2. Design of a Multi-product Batch Plant

The plant consists of a sequence of M batch processing stages which are used to manufacture N different products. In each stage j, R_j units operate independently in parallel and all the units within a given stage j have the same size V_j. The time required to process one batch of product i in stage j is given by t_{ij}, where $t_{ij} \geq 0$.

The required unit size, V_{ij}, for processing product i in stage j is given by

$$V_{ij} \geq S_{ij} B_i , \quad i=1,\ldots,N, \; j=1,\ldots,M \tag{18}$$

where B_i (kg) is the batch size for product i, S_{ij} is a constant. The unit sizes V_j must then be chosen to satisfy

$$V_j \geq V_{ij} , \quad i=1,\ldots, N, \; j=1,\ldots, M \tag{19}$$

and they are available in a continuous range of sizes

$$V_j^L \le V_j \le V_j^U \,,\ j=1,\ldots, M \tag{20}$$

where V_j^L, V_j^U are given limits.

The plant operates in a steady cyclic condition, and no auxiliary storage is available, so each product batch, once started, must be processed through all stages without any waiting time. Over a given period of operation H (h), the number of batches, n_i, of each product, and their sizes B_i, must be chosen to achieve the required production Q_i (kg).

$$Q_i = n_i B_i \tag{21}$$

The number of units in each stage must be chosen so that all the batches can be processed. The resulting sequencing and capacity constraints are complex, and require the introduction of a large number of auxiliary zero-one variables. However, a much simpler constraint, which gives good sub-optimal solutions was obtained in [9] by the following reasoning.

One average, the time taken to process the n_i batches of product i in stage j will be $(n_i t_{ij}/R_j)$, and clearly we must have

$$H \ge \sum_{i=1}^{N} n_i t_{ij}/N_j \,,\quad j=1,\ldots, M \tag{22}$$

The sequencing constraints prevent the continuous use of all units in all stages, so that equality cannot in general be obtained for all j in (22). On the other hand, it is clear that the scheduling can always be done if the period H is long enough to allow the maximum cycling time, T_{Li}, given by

$$T_{Li} = \max_{j=1,\ldots,M} (t_{ij}/N_j) \,,\quad j=1,\ldots, N \tag{23}$$

in every stage. This leads to the constraint

$$H \ge \sum_{i=1}^{N} n_i T_{Li} \,, \tag{24}$$

The true optimum lies between the limits (22) and (24) and if this difference is large it might be worthwhile to consider the general sequencing constraints, but here we are using (23) and (24) following other authors.

The design problem is thus to choose the B_i, V_j, and R_j to minimize the capital cost C of the plant, given by

$$C = \sum_{j=1}^{M} \alpha_j R_j V_j^{\beta_j} \tag{25}$$

It is clear that the number of batches (n_i) treated in a given arbitrary period H need not be integer-value, but the number of units (R_j) in each stage must of course be positive integers so the problem is a mixed integer nonlinear program (MINLP). This class of problem is very difficult to solve.

By elimination of the intermediate variables, this relaxed problem may be formulated as follows. Chose the B_i, T_{Li}, V_j, R_j to minimize (25) subject to:

$$\sum_{i=1}^{N} \frac{Q_i \cdot T_{Li}}{B_i} \le H \tag{26}$$

$$V_j \geq S_{ij} B_i \; ; \quad R_j \cdot T_{Li} \geq t_{ij} \; , \quad i=1,..., N, \; j=1,..., M \tag{27}$$

Problem has been solved for two sets of data that differs largely as for scale of combinatorial complexity:

- N=2 products in M=3 stages what is equivalent to 27 combinations of discrete variables with 13 inequalities
- N=5 products in M=6 stages what is equivalent to 4096 combinations of discrete variables with 61 inequalities.

Two formulations of the optimisation problem has been applied, original one as described above that requires solution of MINLP problem and modified one developed by the authors which requires solution of NLP problem only.

The global optima according to [8] are:
for data set (i):

C=38499.8; R_j[1 1 1]; V_j[480 720 960]; B_i[240 120]; T_{Li}[20 16].

for data set (ii):

C=285510; R_j[2 2 3 2 1 1]; V_j[3000 1891.64 1974.683 2619.195 2328.100 2109.797]; B_i[379.7467 770.3054 727.5089 638.2978 525.4531]; T_{Li}[3.2 3.4 6.2 3.4 3.7].

This problem is difficult for GA methods. At first it has many continuous variables and relatively few discrete ones, hence, it is not of highly combinatorial nature. As it was mentioned such problems are rather seldom solved in chemical engineering using GA methods. At second, the problem is ill-defined in regards to constraints at the global optimum. The analysis showed that changes of decision variables of order 0.01% around optimum values (in both directions) cause that the solution becomes infeasible. It can be considered that many constraints are practically active. Such optimisation problems are extremely difficult for GA since the method isn't able to ensure high precision for continuous variables.

Optimisation of this multi-product batch plant has been considered in several works and researchers attempted to solve it using both deterministic as well as stochastic optimisation methods. Authors [9] successfully solved this problem but only for data set (i) applying branch and bound approach. Advanced General Benders Decomposition approach, the same as used in well known commercial solver DICOPT from GAMS [10] was employed by authors [8]. It was found that solutions obtained depend on starting point and only linearisation by logarithmic transformation ensured the global optimum independent on initialisation.

Stochastic strategy from adaptive random search (ARS) class was applied in work [11]. It gave sufficient reliability only for data set (i). At last, authors [12] applied simulating annealing (SA) strategy. Also in this case sufficient reliability was reached for data set (i).

The authors developed on the basis of problem analysis a modification that allowed to eliminate discrete variables R_j and continuous ones V_j. Additionally inequality constraints were eliminated, too. In result, the MINLP problem was simplified to NLP one with reduced number of continuous variables and number of inequality constraints as well.

The reasoning which leads to the modification is as follows.

It can be concluded from the analysis of the goal function that variables N_j and V_j (j=1,...,M) have to reach admissible minimal values that meet constraints (27), which, in turn limit the variables from the lower bounds. For each j-th stage at least one of the constraints on products i=1,...,N must be active in the optimal solution. Since lower bounds on N_j and V_j determined by (27) depend only on B_i and T_{Li} , hence, the latter should be chosen as decision (independent) variables in optimization. Other variables become dependent ones and can be determined from active constraints (27), which, after transformation, become equations (28,29).

$$N_j = \max_i \left[int\left(\frac{t_{ij}}{T_{Li}} \right) \right], \quad \text{for } i=1,...,N,\ j=1,...,M \tag{28}$$

$$V_j = \max_i \left(S_{ij} B_i \right), \quad \text{for } i=1,...,N,\ j=1,...,M \tag{29}$$

where operator int(x) transform real x to integer one such, that: int(x)>x, function max[B] returns the element from set B of maximal value.

Thus, the original problem with both continuous and discrete variables defined as MINLP has been reformulated as NLP one with significantly reduced number of decision variables and, also, inequality constraints. It is of importance that such reformulation is possible only in frames of stochastic approaches, such as GA, where one can make direct use of computer programming language applied to code the optimisation method.

Using this NLP formulation it was possible to reach significantly better results even for data set (ii). Table 1 summarises results of our computations for data set (i) and table 2 for data set (ii).

Table 1.

Results of calculations for data set (i)

Optimisation model type	Goal function values	Total no. of population	Population size	Number of function evaluations
MINLP	38557.5	8000	28	224000
NLP	38499.5	5000	16	80000

Table 2.

Results of calculations for data set (ii)

Optimisation model type	Goal function values	Total no. of population	Population size	Number of function evaluations
MINLP	312386.3	20000	24	480000
NLP	285787.3	10000	56	560000

As one can expect better reliability was achieved for NLP formulation. For both data sets the global optimum was achieved with moderate number of goal function evaluations. In case of MINLP formulation the method located the global optimum for data set (i). For the second data set (ii) the results differ from global optimum but

this is negligible difference. Additionally, it is worth noting that our results are close to those obtained with application of other stochastic approaches as ARS from [11] or SA from [12]. The optimal rate of evolution was reached with modification ratio *u_mod* from range 0.15-0.30. The probabilities of using operators that we consider proper for the problem are of order: simple crossover – 0.2, arithmetic crossover – 0.12, heuristic crossover – 0.5, uniform mutation – 0.02, non-uniform mutation – 0.1, local mutation – 0.02, range limit mutation –0.04.

4. SUMMARY

The GA based optimisation method has been developed. The approach has a novel feature that was developed to decrease an effect of premature degeneration which prevents locating global optimum. In our method an intermediate population is created that is a superset of parent population and genetically modified sub-population. The latter consists of modified individuals created by genetic operators applied to randomly selected members of parent population. The size of sub-population is smaller than that of parent one and determined by control parameter *u_mod*. Members of intermediate population compete with each others during selection to the next generation. It was proved in our tests that addition of such the sub-population prevents premature degeneration. The algorithm of optimisation approach is given in the paper as well as description of seven genetic operators used in the method.

Application of the developed method for two chemical engineering problems is reported. The first problem consists in minimisation of Gibbs free energy of chemically reacting system – see also papers [4-7]. This is NLP task with seven degrees of freedom. The second problem is of MINLP type. This is structural and parametric optimisation of multi-product batch plant considered also in [8,9,11,12]. For second data set it is very difficult for solution to global optimum for deterministic and stochastic optimisation approaches.

For both problems global optimum solution has been obtained with our method. It is worthwhile noting that less number of goal function evaluations were needed in comparison with other stochastic approaches as e.g. simulating annealing from [12] or adaptive random search of authors [11].

The GA method has been also successfully applied to solve complex heat exchanger network retrofit design problem [13] as well as to smaller MINLP tasks from process engineering. The optimisation method was also tested using some typical problems for stochastic optimisation. The approach showed sufficient robustness and can be recommended for solving typical NLP problems.

It can be concluded that the developed optimisation approach is robust technique for solving MINLP problems of chemical and process engineering. We are in course of investigations aimed at finding good values of control parameters. Here, we limit ourselves to some general guidelines:

- number of members (*NPOP*) should 4 to 10 times higher than number of variables
- parameter *u_mod* should be of order 0.5-0.55
- probabilities of the genetic operators should be higher than 0.0 (i.e. we should use all the operators available). However, the influence of their values is complex and problem dependent.

SYMBOLS

CK	sum of penalty terms in augmented goal function
$\boldsymbol{D}_j$	set of values for "j-th" discrete variable
FC	original goal function in optimisation
FP	fitness function
g	inequality constraint
h	equality constraint
MINLP	Mixed Integer Non-Linear Programming
NLP	Non-Linear Programming
x/***x***	continuous variable / vector of continuous variables
y/***y***	discrete variable / vector of discrete variables

Subscripts

L	refers to lower limit
U	refers to upper limit

REFERENCES

1. C. Azzaro-Pantel, L. Bernal-Haro, P. Baudet, S. Domenech, L. Pibouleau, *Comput. Chem. Engng,* **1998**, *22*, 1461-1481.
2. D.J. Greeff, C. Aldrich, *Comput. Chem. Engng,* **1998**, *22*, 995-1005.
3. D.A. Manolas, G.A. Efthimeros, D.T. Tsahalis, *Int. Conference CHISA'98*, Prague, Czech Republic **1998**.
4. W.B. White, S.M. Johnson, G.B. Dantzig, *J. Chem. Phys.*, **1958**, *5*, 751-755.
5. M.W. Heuckroth, J.L. Gaddy, L.D. Gaines, *AIChE Journal*, **1976**, *22*, 744-750.
6. G.P. Rangaiah, *Comput. Chem. Engng*, **1985**, *9*, 395-400.
7. Z. Michalewicz, "Genetic Algorithms + Data Structures = Evolution Programs", Springer-Verlag, 1996.
8. G.R. Kocis, I.E. Grossmann, *Ind. Eng. Chem. Res.*, **1988**, *27*, 1407-1421.
9. Grossmann, I.E., Sargent, R.W.H., *Ind. Eng. Chem. Process Des. Dev.*, **1979**, *18*, 343-348.
10. A. Brooke, P. Kendrick, A. Meeraus, "GAMS. A users guide. Release 2.25", The Scientific Press Series 1992.
11. R.L. Salcedo, *Ind. Eng. Chem. Res.*, **1992**, *31*, 262-273.
12. M.F. Cardoso, R.L. Salcedo, S.F. Azevedo, D. Barbosa, *Comput. Chem. Engng*, **1997**, *21*, 1349-1364.
13. R. Bochenek, Optimal retrofit design of heat exchanger networks by genetic algorithms, Ph D Thesis, Rzeszow University of Technology, Poland (supervisor J. Jezowski, in Polish language) 2003

STUDIA UNIVERSITATIS BABEŞ-BOLYAI, CHEMIA, L, 2, 2005

E-LEARNING IN PROCESS AND CHEMICAL ENGINEERING EDUCATION: STUDENTS AND FACULTY MEMBER POINT OF VIEW

LAUREANO JIMÉNEZ ESTELLER

Department of Chemical Engineering and Metallurgy, Faculty of Chemistry, University of Barcelona, c/ Martí i Franquès 1-11, 08028-Barcelona, Spain.
Tel: +34-93-4034889. Fax: +34-93-4021291. E-mail: Laure.Jimenez@ub.edu

ABSTRACT. The aim of this work is to discuss the results of two surveys on e-learning carried out at eight chemical engineering faculties from seven European countries. The first survey was conducted with students, the second with faculty members. The focus of the survey was on aspects such as computer and network facilities, on-line use, personal skills in several computer applications, and use of computer-based learning materials. Similarities and contrasts regarding e-learning were analysed within the group of students as well as between students and faculty members. For the students, differences considering gender, faculty, and region were studied using both, descriptive and multivariate statistical techniques. Results show that the differences in computer use were stronger between different faculties than between women and men. The use of information and communication technologies is still evolving and all stakeholders (organisation, students and staff) are still exploring the best procedure to reach the maximum potential of these tools. Students' attitudes towards e-learning are rather conservative and the driving force depends mainly on the faculty members, who have a slightly more positive attitude to distance-learning initiatives. This positive attitude promotes a large number of e-learning activities. Efforts range from single personal initiatives to cooperative projects on regional, national or international level. The *EuPaCe.net* consortium (www.eupace.net) challenge consists in building a community that bundles some of these efforts, providing a platform to create an international online community.

Keywords: e-learning, chemical engineering, comparative study.

1. INTRODUCTION

This work presents the results of a study on e-learning in higher education in Europe that was conducted within the European Network for E-Learning in Process and Chemical Engineering (*EuPaCE.net*). Most analyses about the e-learning situation show that, independently of the domain, most initiatives, after a time of pioneering and expansion, lead to insufficient transfer of know-how and lack of sustainability of the applications developed. Still, e-learning initiatives in higher education are often "*lone ranger*" approaches (Bates, 2000) with high development costs and low pedagogic (not to mention economic) benefit. Harmonization, standards and communication about best practices is needed to achieve synergies. The central issue of the study consisted in the identification of trends, challenges, and open questions about e-learning in process and chemical engineering. Therefore, the study comprised two surveys that addressed the two most important groups in chemical engineering higher education: the first survey was conducted with students, the second with faculty members. This allows to draw conclusions about the e-learning market in European higher education for chemical engineering, comparing "*vendors*" (faculty members) and "*customers*" (students).

Both surveys were carried out with different questionnaires. While the student questionnaire consisted of rating questions, the faculty members questionnaire focused more on open questions for qualitative analysis. In addition, the questionnaires of students and faculty members contained some identical or comparable rating items on attitudes towards the use of new information and communication technologies, so that similarities and contrasts of students' and faculty members' opinions and preconceptions about e-learning could be analysed.

Moreover, to get a more detailed picture of the students' situation, classical statistical methods and multivariate statistical techniques (cluster analysis, linear principal component analysis and linear discriminant analysis; Montgomery and Runger, 1998; Ross, 1999) were applied to study similarities, differences and relationships among student variables like gender, faculty affiliation, and region. The advantages of these techniques is that results are shown in easily interpretable graphical plots. In particular, facing the high importance that is currently being put on the issue of gender mainstreaming by national and European authorities, the analysis of gender differences in the population of chemical engineering students was of interest.

The results of the study provide the empirical basis for guidelines for e-learning in process and chemical engineering, that are being developed by the EuPaCE.net consortium. At the open internet platform (available at www.eupace.net), a cooperative work space is provided for the discussion of the guidelines among the chemical engineering community.

This paper is organised as follows: in section 2, methodology and results of the students survey are presented. Section 3 is dedicated to the faculty members survey. In section 4, both surveys are compared to discuss similarities and contrasts of students' and faculty members' preconceptions. Section 5 provides the conclusions.

2. STUDENTS SURVEY

The student survey was carried out with a questionnaire comprising 54 items, divided into four aspects: (1) personal data, (2) computer experience, (3) attitudes towards computer based learning, and (4) motivation for studying. The following questions were addressed:

- What is the current state of private access, computer use, and computer experience of the students?
- How do students judge the use of computers at their faculty?
- To what extend are students knowing and using computer-based applications for learning that are offered by their faculty?

491 students at Bachelor and Master level participated in the study (Table 1). The sample sizes differed considerably at the different faculties, and therefore comparison between the different faculties can only be made in an explorative manner and conclusions have to be drawn with caution. In view of the historical and general economic situation, we distinguish for the analysis of regional differences between *EU-15* (represented by Barcelona, Berlin, Lappeenranta, Manchester, Oxford and St-Etienne) and *East-EU*, (represented by Bucharest and Cracow). In average, participants were 23 years old. 45% of the total sample were women, but only 27% of the *EU-15* sample. 80% of the subjects stated to have advanced English language skills (90% in *EU-15* vs. 65% in *East-EU*).

Table 1

Description of the sample.

University	Faculty/Department	n
Ecole Nat. Supérieure des Mines de St-Etienne (EMSE, France)	Sciences, Information et Tech. pour l'Environnement	101
Jagiellonian University of Cracow (JUC, Poland)	Chemistry	7
Lappeenranta University of Technology (LUT, Finland)	Chemical Technology	53
Technische Universitaet Berlin (TUB, Germany)	Process Dynamics and Operation	42
Univ. of Barcelona (UB, Spain)	Chem. Eng. and Metallurgy	22
University of Manchester (UMIST, England)	Process Integration	21
Univ. of Oxford (UOX, England)	Engineering Science	25
University Politehnica of Bucharest (UPB, Romania)	Chemical Engineering	220

2.1. PRIVATE ACCESS TO COMPUTERS AND THE INTERNET

At home, 87% of the total sample had access to a computer (96% in *EU-15* vs. 77% in *East-EU*), 75% had access to the internet (91% in *EU-15* vs. 56% in *East-EU*). Table 2 shows the distribution of Internet connection speed. While almost half of the connections in *EU-15* are high-speed, this is the case for only about one third in the *East-EU* sample.

In the total sample, there are gender differences concerning computer access at home (81% of women vs. 91% of men), internet access at home (66% of women vs. 82% of men), and speed of internet connection (37% of women vs. 50% of men have high speed connection). These results are caused by the situation in the *East-EU* sample.

Table 2

Speed of private internet connections (% of total).

		Slow < 56k	Medium	Fast > 768k	Total
EU-15	Men	17 %	28 %	46 %	91 %
	Women	17 %	22 %	58 %	97 %
East-EU	Men	20 %	17 %	33 %	70 %
	Women	18 %	28 %	10 %	56 %

2.2. COMPUTER USE

In average, the students use a computer for 25 hours per week (range 0 to 170, standard deviation, SD = 21), thereof 15 hrs/week online (range 0 to 104, SD = 16). For studying, they use computers for 12 hrs/week (range 0 to 105, SD = 12), thereof 6 hrs/week for studying online (range 0 to 80, SD = 8). There is a considerable variation in the intensity of computer use between subjects. Most students use computers to a relatively low extent, while a minority seem to spend most of their daytime with computers. There is a substantial difference in the average time between the different faculties: for total computer time ranging from an average of 19 hrs/week (TUB) to 43 hrs/week (UMIST), or for online time for studying ranging from an average of 2 hours (TUB, UB) to 11 hours (UMIST). Computer use time is strongly related to computer and internet access at home (Figure 1).

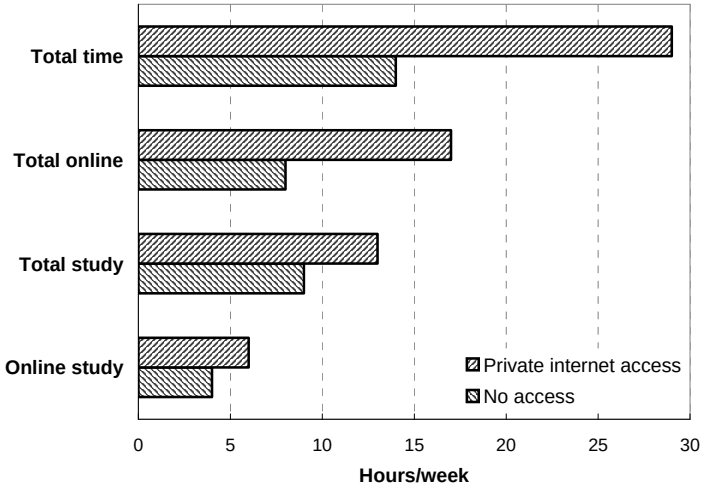

Figure 1. Computer use time for students: influence of private internet connection.

Students without private internet access only spent about half of the time than their fellows with private internet access. For computer use time related to their study, this difference is smaller. Despite the gap in computer and internet access at home, differences in computer use time between *EU-15* and *East-EU* are rather small.

The analysis of gender differences show a considerable difference in total time (women 19 vs. men 30 hrs/week). However, gender differences in computer use for studying were much smaller (women 11 vs. men 14 hrs/week). Concerning the effect of gender on computer use, a notable difference between *EU-15* and *East-EU* was found. In the *East-EU* sample, gender difference in total computer time is stronger (*East-EU*: women 16 vs. men 33 hrs/week; *EU-15*: women 24 vs. men 29 hrs/week). In the *EU-15* sample, women spend more time for studying with the computer than men (15 vs. 14 hrs/week), while in the *East-EU* sample the situation is reverse (9 vs. 14 hrs/week).

2.3. COMPUTER SKILLS

Students were asked to rate their skills from 0 (no skills) to 3 (expert). According to their answers, they can be grouped into:

(1) Basic skills (word processing, internet use, e-mail, spread sheet): average = 2.0, "*no skills*" < 10%.

(2) Domain specific skills (simulators, graphics software, programming languages): average = 1.0, "*no skills*" < 50%.

(3) Extra skills (web design, database systems): average = 0, "*no skills*" > 50%.

There are considerable differences in the self-ratings of computer skills in relation to internet access at home. In all categories of skills, students without private internet access rate their skills lower than students with private access. Also, regional and gender differences in the self ratings could be identified (Figure 2). In all categories, women from the *East-EU* sample gave the lowest self-rating.

2.4. ATTITUDES TOWARD LEARNING WITH COMPUTERS

Table 3 shows the ratings for six statements about learning with computers (0 = ”*completely disagree*”, 3 = ”*completely agree*”). Most students agree that computers should play a bigger role in their studies, that the quality of materials should be improved, and would like to have a wider choice of learning materials. However, they mostly also agree that the current extent of computer use is adequate, and they do not want traditional lectures to be replaced by learning with computers. From the students' point of view, higher quality, better integration, and variety of computer applications are rather needed than higher quantity of computer use. Overall, the students' attitudes toward learning with computers can be characterised as moderate to slightly positive, but not enthusiastic.

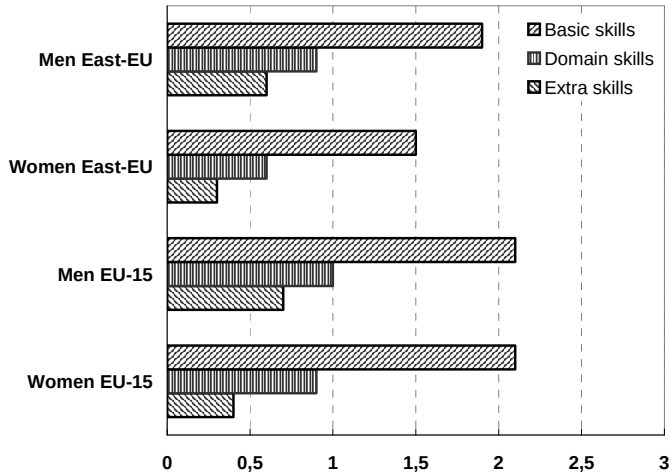

Figure 2. Regional and gender differences in self rating of computer skills.

Table 3

General attitudes toward learning with computers.

	Mean	SD
“I prefer learning with computer based learning software to attending a lecture“	1.4	0.9
“Learning with computers should play a bigger role in my studies“	1.9	0.9
“I would like to have a wider choice of computer based learning materials for my studies“	2.0	0.8
“Currently, the extent of computer use in my studies is adequate“	1.8	0.8
“The quality of computer based learning materials for my studies should be improved“	2.0	0.8
“We are already using computers too often in my studies”	1.2	0.9

2.5. PERCEPTION OF OFFERS AND USE OF APPLICATIONS

In the total sample, download of course materials is the best-known application (63% of the students perceive that downloads are offered by their faculty), followed by electronic communication (49%), online learning modules (33%), and virtual courses (14%). There are substantial differences in the perception of offers related to internet access at home.

The perception of offers is also related to the speed of the internet connection: students with a faster internet connection perceive more offers, while students without private access tend to ignore some of the e-learning applications offered. Also, the region is related to the perception of offers. *East-EU* faculties seem to offer less e-learning applications to their students than *EU-15* faculties. The patterns of the offers is reflected in the percentage of actual use of the different applications (Figure 3).

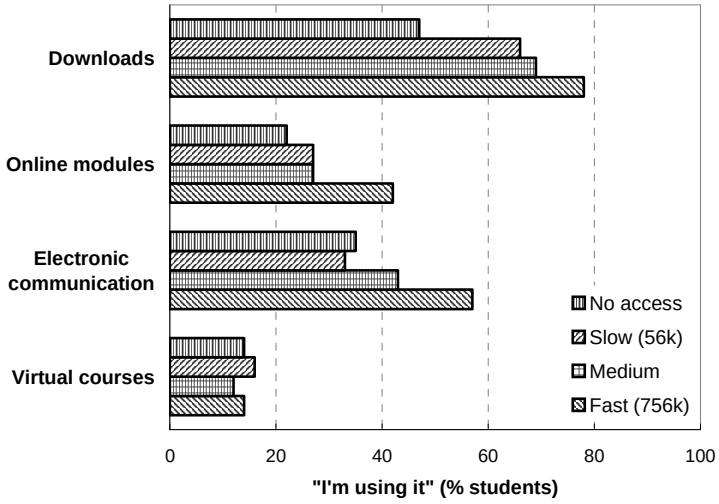

Figure 3. Relations between internet connection at home and use of applications.

2.6. MULTIVARIATE ANALYSIS

All variables group in a very predictable way. Just four linear principal components explain 75% of the variability of the original data: the key aspect is the use of computer (it is not very important if it is online or offline, at the university or at home). Also, the differences of gender behaviour can be neglected.

The linear discriminant analysis performed to find differences among students coming from different locations just includes five variables (a variable is not included because their behaviour is random or because their variability is already considered in another variable already included): use of computer at the university, gender, cost of the internet connection, e-mails related to study and time devoted to online study at home. Using this 5 variables, we can predict with a probability of 44 % to which University the student attends, while random probability is 16 % (Figure 4):

- Ecole Nationale Supérieure des Mines St-Etienne (EMSE): 41 %.
- Lappeenranta University of Technology (LUT): 25 %.
- University of Manchester (UMIST): 70 %.
- Technische Universitaet Berlin (TUB): 78 %.
- University of Barcelona (UB): 72 %.
- University of Oxford (UOX): 48 %.

3. FACULTY MEMBER SURVEY

The faculty member survey was conducted in two rounds. In the first round, a questionnaire was applied, containing 13 questions. About half of the questions were ratings, while the rest had open answers with free text (e. g., "What are the major advantages of e-learning in your opinion?"). In the second round, the results of the questionnaires were subject to a group discussion during a meeting of the EuPaCE.net project. On average, the 18 participating faculty members were 41 years old and had a teaching experience of 13 years. Faculty members were from the same departments than the students, and members of the EuPaCE.net consortium (Table 1).

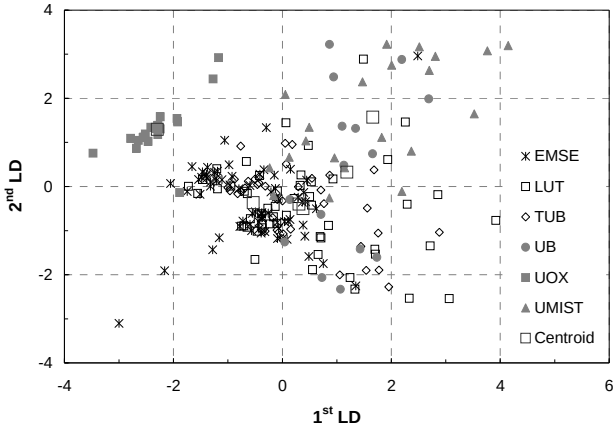

Figure 4. Linear discriminant analysis of the *EU-15* students.

The most important results of the faculty members survey are summarised in the following. The general observation of "*continuity and diversity*" for the introduction of e-learning into academic education (Lepori *et al.*, 2003) also applies to the present chemical engineering sample. Instead of provoking revolutionary changes, the integration of e-learning applications into the curricula is a slow, incremental process. At the moment, only one of the partners offers complete online courses, the others are still traditional campus universities. The most widely used information and communication technology (ICT) application is offering learning materials for download, and commu-nication via e-mail. Web-based interactive learning modules and virtual courses are still rare. Accordingly, the rationale behind the introduction of e-learning is in most cases the enrichment of face-to-face learning scenarios to improve the quality of learning. The survey revealed a considerable diversity in the use of e-learning within and between different chemical engineering faculties. For a staff member's engagement in e-learning, individual preferences are more important than organisational (not to mention national) culture. Table 4 summarizes some of the positive and negative comments and feedback received. As major challenges for e-learning in chemical engineering, the following issues were identified through qualitative content analysis of open questions and the group discussion:

- How can we integrate technology and pedagogical requirements?
- We need reliable tools for rapid development of e-learning materials.
- How can we keep our e-learning materials constantly updated?
- How can we develop and implement interactive process simulators, close to real industrial processes.

- How can we produce modules to achieve deep understanding and avoid superficial playing with e-learning applications?
- How can we integrate theory with online modelling, simulation and experiments?
- What about licence problems, authentication and intellectual property rights?

Table 4

Advantages and disadvantages of computer-based learning.

Advantages	Disadvantages
Visualization/Illustration/Animation: relations of input-output variables	Students' loss of motivation: no clear objectives and no evaluation criteria
Available anytime, anyplace	Lack of personal contact → abstraction
Enhance motivation	Superficial learning
Fast access to new releases	Which is the cost/benefit ratio?
To archive and provide course material	Never do with technology what could be done better without it
To prepare fast/interactive questions and answers tests	Initiative valuable for a few percentage of students that are deeply interested in learning ("They will learn anyway")
Student motivation	

4. COMPARISON OF SURVEYS

Overall, the results of both surveys match quite well, and there seems to be a "*mainstream*" of experiences, opinions, and preconceptions about e-learning that is shared by students and faculty members. Nonetheless, there are also some notable differences between the two groups of the surveys. Comparison of attitudes towards e-learning shows that the relations between the different items are similar in both groups, e.g. students as well as faculty members tend to agree that the quality of e-learning applications should be improved, and tend to disagree that computers are already being used too often for learning. But for all items, the tendency of the ratings of the faculty members can be interpreted as somewhat more in favour of e-learning than the students' ratings (Figure 5). The average staff members' attitude score on a scale from 0 (very negative) to 3 (very positive) was slightly more positive than the students' attitude score (2.0 vs. 1.6).

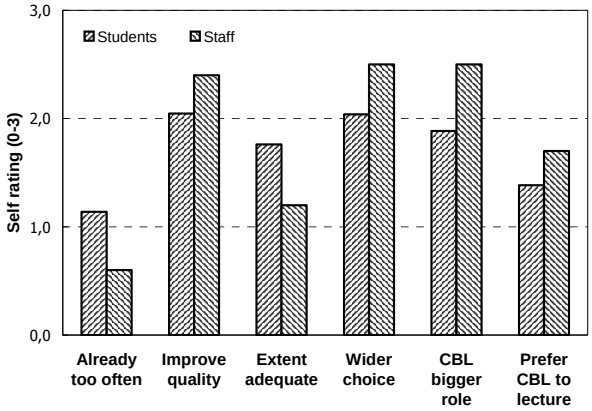

Figure 5. Attitudes towards computer base-learning (CBL).

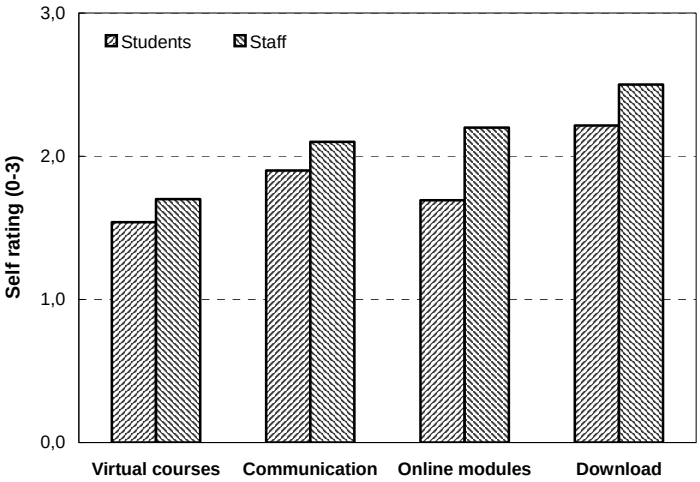

Figure 6. Attitudes towards different e-learning applications.

Today's most prevalent e-learning application is download of course materials, followed by electronic communication and online learning modules. Virtual courses are still rare. For both groups, prevalence is reflected by the judgment of the importance of different applications (Figure 6). Once more, faculty members show a general tendency to rate e-learning applications as more important than the students do, regardless of the type of application.

5. CONCLUSIONS

Summing up, the results of the study show that the use of information and communication technologies in chemical engineering education is still evolving. The vast majority of the students are already using computers in their daily life and for their studies. Students' attitudes towards e-learning are rather moderate, and there seems to be no urgent demand for new applications from their part. So, the driving force for innovations are the faculty members, who have a slightly more positive attitude towards e-learning and often act as "lone rangers" in experimenting with novel e-learning solutions. The situation on the higher education market for e-learning is characterised by "*customers*" that are generally open for new solutions, but have to be convinced by high quality offers. At least campus-based students are not very much interested in becoming completely virtual, nor are the faculty members planning tovirtualise chemical engineering higher education completely. Blended learning is the future.

Analysis shows that there is no substantial gender effect in computer use for chemical engineering students, i.e. the differences were stronger between different faculties than between women and men. Therefore, in *EU-15*, gender mainstreaming actions for chemical engineering higher education should primarily focus on attracting more women to increase their presence in engineering, instead of developing computer literacy programs for women that are already dedicated to chemical engineering. The most important precondition for perception and use of e-learning

offers, as well as for developing advanced computer skill, seems to be private computer and internet access. While in *EU-15*, women (at least if they are studying chemical engineering) have equal private access than men, women in *East-EU* have considerably less private access than their male fellows. Here, gender mainstreaming could consist in financing private computer access for women. On the other hand, in *EU-15*, the vast majority of chemical engineering faculty members are men, and the support of academic careers for women in engineering could be an appropriate measure.

Above gender issues, the great challenge on the European level consists in building a community that bundles the efforts and makes sure that the "lone rangers" of e-learning do not get annihilated in the academic wilderness. The *EuPaCE.net* project is an attempt to integrate and harmonize the currently existing activities in the field of e-learning in process and chemical engineering through an international dialogue, and the development of guidelines. We aim to achieve an international cooperative network with participants from various backgrounds. All interested actors in the field of process and chemical engineering education are welcome to register at the open internet portal www.eupace.net and become part of the *EuPaCE.net* online community.

ACKNOWLEDGMENTS

The *EuPaCE.net* is funded by the European Commission (2003-4828/001-001).

REFERENCES

1. W. Bates, *"Managing technological change",* Jossey-Bass, San Francisco, USA, 2000.
2. Lepori, L. Cantoni, C. Succi, C. *The introduction of eLearning in European universities: models and strategies*, GMW 2003, accessed March 2005: http://www.newmine.org/newmine_edum_lepori_alii_article_gmw03.pdf (2003).
3. D. Montgomery, G. Runger, "*Applied Statistics and Probability for Engineers",* John Wiley and Sons, New York, USA, 1998.
4. S. M. Ross, "*Introduction to Probability and Statistics for Engineers and Scientists"*, John Wiley and Sons, New York, USA, 1999.
5. www.eupace.net (accessed March 2005).

STUDIA UNIVERSITATIS BABEŞ-BOLYAI, CHEMIA, L, 2, 2005

INTEGRATED E-LEARNING PLATFORM FOR CHEMICAL ENGINEERING EDUCATION

ANA MARIA JOSCEANU[1], RALUCA ISOPESCU[1], VALENTIN PLESU[1], STEFAN MORCOV[2]

[1] *University 'Politehnica' of Bucharest, Centre for Technology Transfer in the Process Industries, Gheorghe Polizu, Building A, Room A056, Sector 1, RO-011061, Bucharest, Romania, phone/fax: +40-21-2125125, email: v_plesu@chim.upb.ro*
[2] *S.C. SIVECO Romania S.A., 8-10, Maresal Averescu Blvd., RO-011455, Bucharest, Romania, Phone: +40-21- 224 25 31, fax : +40 (21) 224 41 08, email : stefan.morcov@siveco.ro*

ABSTRACT. This contribution presents a running e-learning system for higher education in chemical engineering. The platform is structured in an administrative module and a teaching and evaluation module. Administratively, the faculty consists of several departments, organizing the student professional specializations. Special requests for the communication system are in place. The system is designed to allow further development towards large scale distance and continuous learning.
The main educational characteristic is complemented by the faculty organizational management. This refers to: academic records, timetable for students and academic staff, students examination and periodical assessment.
The strategy of developing specific chemical applications relayed on the conclusions of a large survey on the computer skills and attitude towards information technology assisted education. The survey was made within the academic staff and student population as well. Pilot topics were chosen to set up lectures and tutorials using the integrated e-learning platform.

Keywords: Chemical engineering education, e-learning, integrated platform, education management.

1. INTRODUCTION

Learning nowadays is a continuous and active process performed with a specified goal and applied to real life situations. Traditionally, the main criteria in selecting a higher education institution were connected with its prestige and location criteria. The location criteria are mainly connected to the life standards, and in Romania it played an important role. On the other hand, the prestige criterion brought many foreign students to the Romanian Universities. The globalisation process, reflected also in education, tends to amplify both criteria and a true education market has been created. Because of this, many academic institutions, find themselves in a situation of loosing some of their students in favour of other institutions, located at larger distances, but better anchored in the education market.

In Romania, development of infrastructure, communications and information systems and services represents a crucial condition for general economic development, as well as for integration in the European Union. Developing an education system through information and communication technology (ICT) could be the main approach to improve engineering education and to avoid the so-called "digital divide": people with low computer literacy are likely to have lower accessibility to information on the web than those with higher computer literacy. This would cause

a serious discrimination in the information society, as Internet is already a major source of knowledge and information in everyday life.

The industrial chemistry curriculum has a certain characteristic that makes it different from other technical courses: the higher amount of shared knowledge between different disciplines. By nature, an e-learning system allows modules from different disciplines to interact and complete one another (Kartan et al, 2002, Wanks, 1995, McCowan, 2002). For all these reasons, the faculty of Industrial Chemistry is the first higher education institution in Romania that developed an integrated e-learning system.

The e–learning platform in the Faculty of Industrial Chemistry was created during a joint project, involving University 'Politehnica' of Bucharest and SIVECO S.A.. This platform resulted from the adaptation of the Siveco commercial product, AEL, currently running in about 2000 high schools in Romania (Siveco).

Within this context we started our project of implementing an integrated e-learning system, with the specific objectives of

- developing the existing software environment – SeLFT,
- delivering straightforward procedures for SeLFT exploitation, addressing both student and academic users;
- content creation for teaching purposes.

This paper concentrates on the main characteristics of the e-learning system initiated in the Faculty of Industrial Chemistry, and the results obtained so far.

2. THE BASIC SYSTEM

Very often confusion is made between "e–learning" and "distance–learning". Distance learning can use the Internet, but also other teaching materials delivered by postal service. By e–learning it is generally understood a learning activity where ITC resources such as hardware resources (computers, video projectors, acquisition cards, etc) and/or software resources (simulators, interactive multimedia applications, e–books, etc) are involved. The use of Internet is not compulsory.

Computer aided education system may be focused on three different types of professor-student relationship:

1. "distance learning" model, where the education process is Internet supported. Although there is the advantage of a great flexibility in managing the students' time and material resources, there is the danger of depersonalising the educational process. Essential information may be lost in the feedback process when applying only a distance-learning type education model.
2. "face–to–face learning" model, assisted by ITC resources, characterised by extremely low flexibility and full social contact.
3. "combined" model, maximising the advantages of the previous two. It has a "face–to–face" component, since the professor participates physically in the classes, and a "distance" component supposing personal learning sessions outside the academic teaching schedule, and even in other locations. For the "distance" component the Internet, LANs, and CD-ROMs can be used as support.

Our e-learning system is based on the "combined" model. Therefore the platform is to be used by the students in the presence of the academic staff, in the virtual classroom (for lectures, certain laboratory activities and during the evaluation processes), and in their own time, to scroll through the applications available in the platform library.

The system offering both synchronous and asynchronous studying possibilities shows a series of features, such as:

- friendly, easily adaptable and differentiated upon roles interface,
- differentiated access of users depending on groups and roles, together with access privileges easy to manage.

The platform is based on several standards currently in use in the computer aided education community, such as the MathML, SCORM and IMS standards. During the development process Siveco has voted for portability and easy maintenance: they use a standard web–browser client application and an application server, based on the Java platform. High standard technologies are used (JDBC, JSP, Applets, XML). The content reusability concept is based on packaging description formats (in XML there are elements critical for importing and exporting according to the current standards in the field).

Actually the platform consists of three tiers:

- Database tier, offering all data managements services;
- Business tier (or LOGICAL tier), running the functional components (modules) and offering the users access to applications via local area networks or wide area networks.
- Thin clients tier, where several users access same application through a multithread process, while the application server runs the corresponding application and the database server provides the necessary data management services.

In terms of security such architecture offers certain advantages: an efficient management of users and groups of users (regarding mostly access rights to information/educational content for users or groups of users, according to files system principle) and well–defined access rights to functions (as they can be group upon roles and even the roles are configurable)

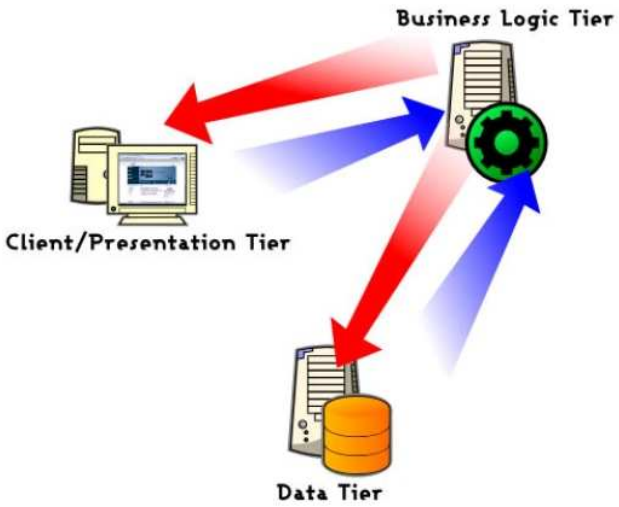

Figure 1. System Architecture

With its three tiers structure the system becomes extensible, scalable and distributed. The platform can be considered extensible since addition of new functions without disturbing those already in use and reorganizing the system data. Scalability should be understood in the sense that one dimension increase is accompanied by the automatic increase of the remaining dimensions (to ensure global compatibility). The scaling process may occur horizontally, as new machines are added and/or vertically, as new servers are added. The database and application servers allow connection of several instances running on different machines in the load balancing mode. Using one or several central databases servers, the platform shows its distributed character, as access is restricted by the administrator through the security module

3. THE MANAGEMENT SUBSYSTEM

The system architecture, benefiting from the features mentioned before, consists of a two-element system architecture: educational process management and content delivery. Both present similar importance for a faculty, training more than 1000 students for the technical field.

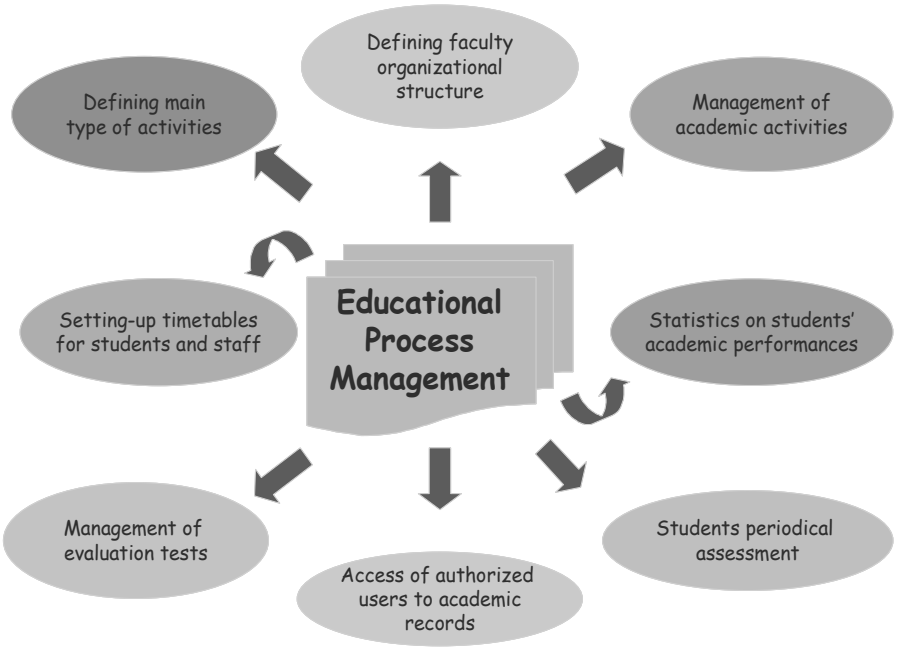

Figure 2. Administrative function of the e-learning system

The management features are briefly described in the figure 2. All aspects mentioned are fully covered by the platform, allowing students as well as faculty management to gain easy and instant access to academic records (figure 3), timetable (figure 4) or faculty structure (figure 5).

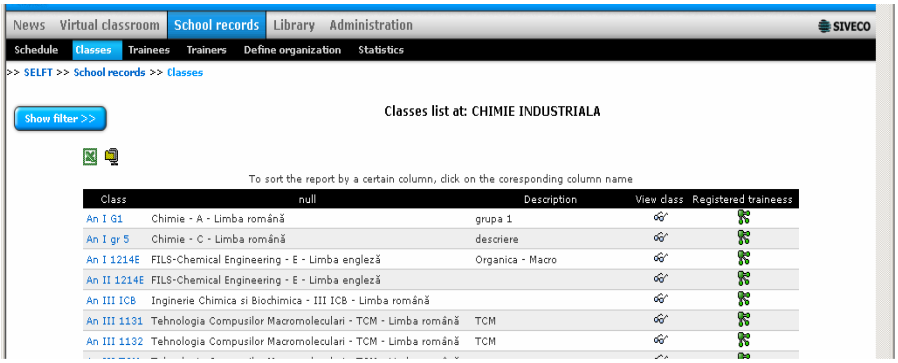

Figure 3. Access gate to full academic records of registered students

The database keeps full records on every evaluation test ever run with aid of the platform, offering the desired degree of transparency and fairness.

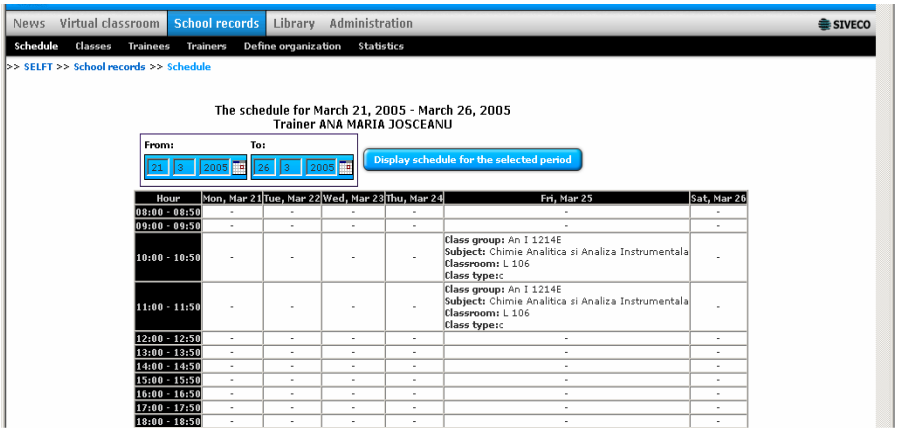

Figure 4. Timetable setting for the participants in the educational process.

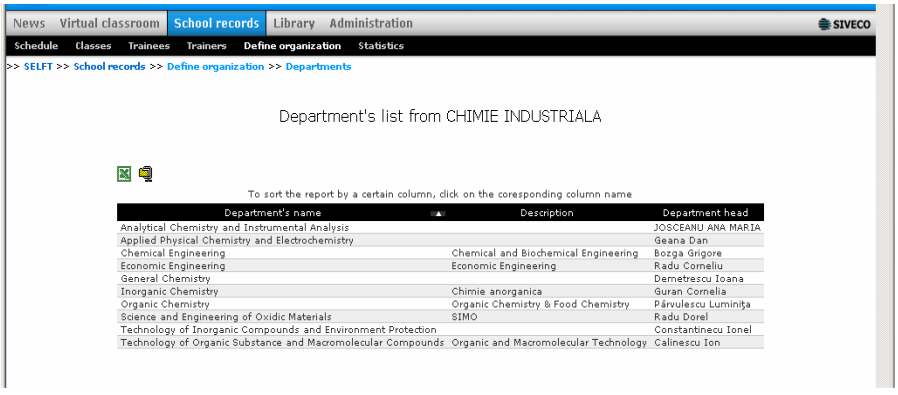

Figure 5. Faculty structure

4. CONTENT DELIVERY SUBSYSTEM

The content delivery subsystem consists of modules with a variable degree of interactivity as shown in figure 6. The virtual classroom is characterized by the largest degree of interactivity, thou many application for self study may show interactivity elements as well.

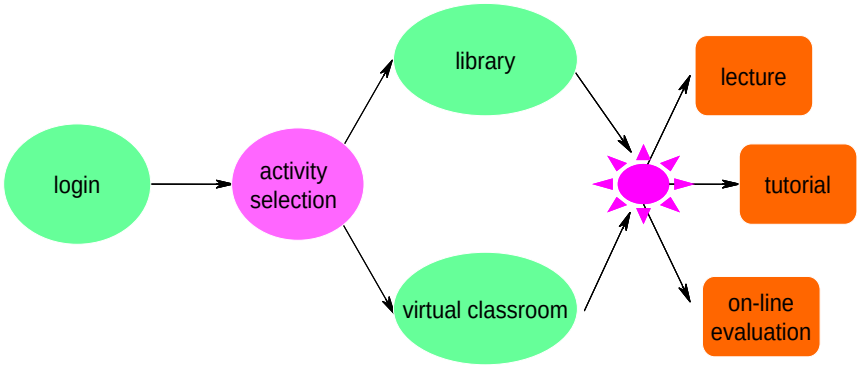

Figure 6. Choices in the content delivery subsystem.

Developing educational content is a tremendous challenge in front of the academic community. The content development team has adopted a special working policy: depending on each department's needs, the content managers develop general rules for content modules, while a small team with more expertise in Macromedia Authorware and other software develop complex procedures (Plesu et al, 2002, 2004). A library has been set up to solve two problems: a) efficient distribution of all activities between people, considering their experience level; b) avoiding redundancy in the content developing activity.

The following content modules have been defined for the e-learning integrated system:

- Assisted course–type modules

They are the most important modules, representing the basis of the content library as they have the important role to create fundamental knowledge as required by the curriculum. They are used in lecture theatres and locations designated for these activities (e–learning laboratories). These modules are accessible only during lectures, under academic staff supervision. The content delivery system is meant to be developed in Macromedia Authorware, especially for basic disciplines which are taught to a larger number of students.

Power Point presentations are also used for lecture type modules, mainly for special topics that are characterised by a high rate of content up-dating. These lectures are taught in the specialization years, for a smaller number of students, and often are optional courses. Figure 7 presents a possible selection from the "chemical

engineering" lecture packages, a lecture type module for "Technical thermodynamics". When selecting a lecture the user can also see some details, such as the name of the professor who created the application, the date, a brief description of the lecture, etc (see the window in the left upper corner of figure 7).

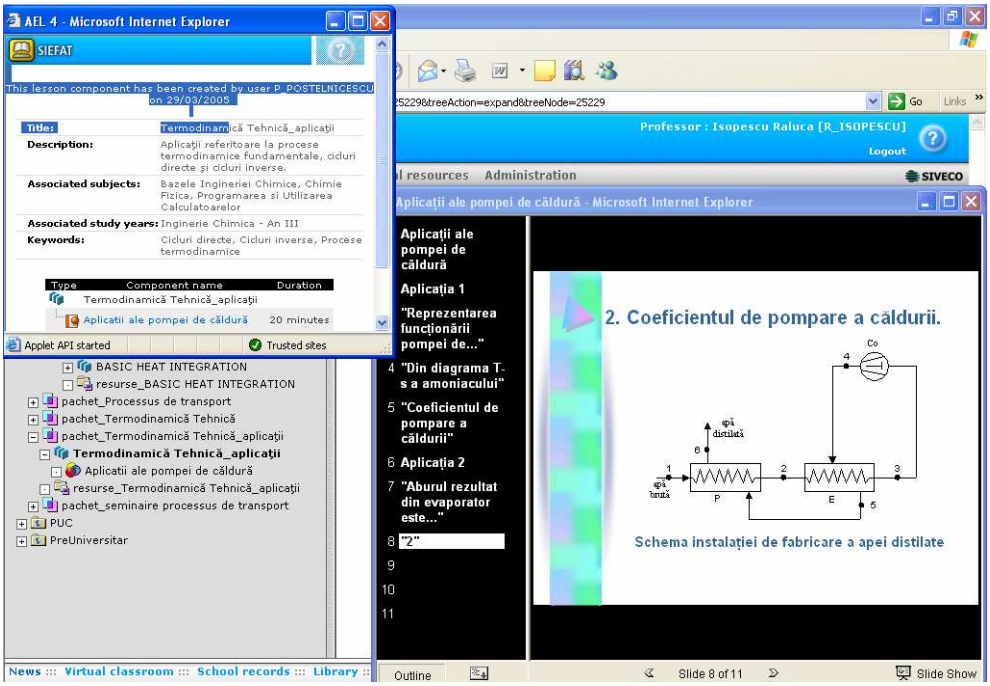

Figure 7. Assisted course type lecture in "Technical Thermodynamics"

- *Non–assisted course–type modules* follow the scenario of the assisted course modules, but are used for individual training. They include a large number of explanatory paragraphs, being available through the Internet, and other media (CD-ROM, floppy disk, etc.).

-*Tutorial-type modules* contain problems and applications and may be used both in classrooms (tutorials) and e–learning laboratories, as well as for individual study. Figure 8 presents a tutorial type module for technical thermodynamics. The application is an active simulation for a refrigeration system, which allows to choose automatically the parameters of the refrigerant using an interactive diagram.

- *Evaluation type modules* allow tracking the students' performances by the academic staff, as well as self–evaluations during the individual training stage (figure 9).

So far, we have implemented assisted course-type modules and seminar-type modules for basic topics as programming languages, analytical chemistry, numerical methods, applied thermodynamics, transport processes, unit operations and process simulation.

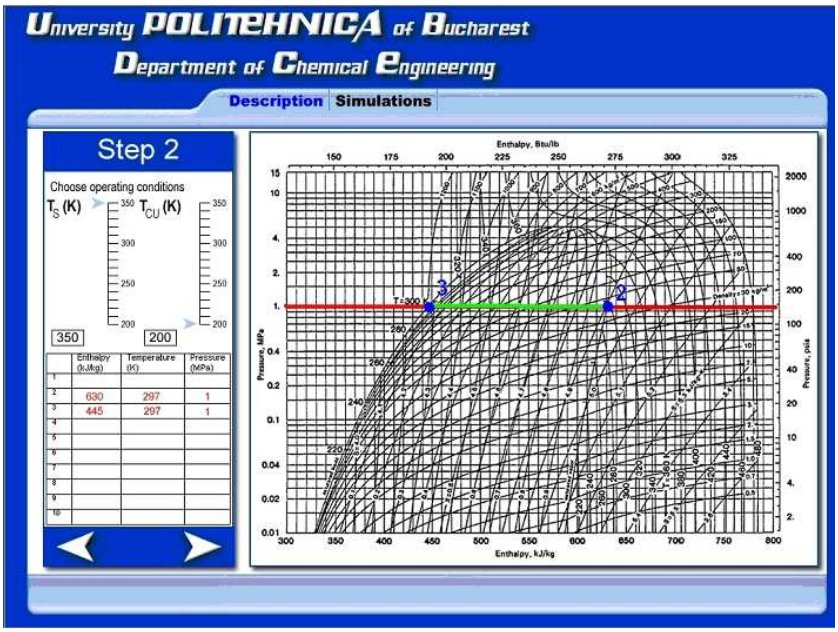

Figure 8. Interactive application for the description and simulationof a refrigerating system

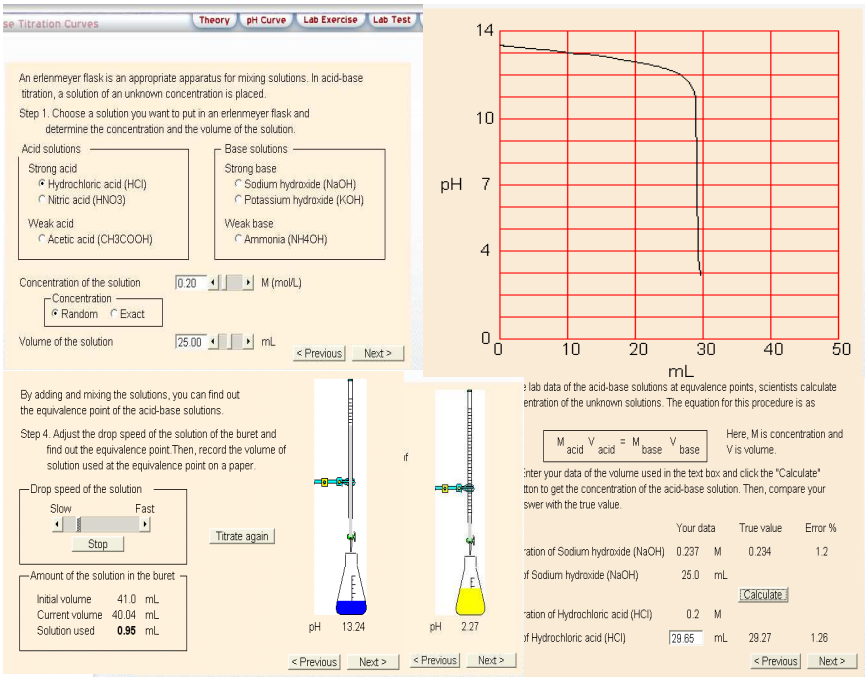

Figure 9. Interactive application for self evaluation in Analytical Chemistry.

5. STUDENT AND ACADEMIC STAFF FEEDBACK

Immediately after implementing the system, we launched a feedback questionnaire to the students directly involved in the "virtual classrooms". 70 % of the students declared their enthusiasm and appreciation for being able to gain instant access to test results, in terms of general score and selection of adequate answers. The rest of the students questioned either were not impressed (5 %) or found the on–line evaluation stressing (25 %). The last category included students with low computer literacy and interest. Most academics in our faculty (around 60 %) are still reluctant in changing significantly their teaching style, especially if they consider the time required to prepare an interactive lesson and to learn to use the e-learning platform. The team involved in this project is putting more and more effort in promoting the advantages of computer assisted education, being convinced that the new platform will fully demonstrate its value only if it is used extensively. Using such modern educational tools will give important opportunities to our faculty to promote efficient "life-long learning" and "distance learning" systems which became necessary in engineering education.

6. CONCLUSIONS

We have presented an already in use e-learning platform for a technical faculty that has administrative and educational functions. The system is still under development, and new features, according essentially to SCORM standards, were recently added. The complete system implementation will facilitate both educational process and the faculty management.

ACKNOWLEDGEMENTS

This work was performed in the frame of the Romanian National Research Programme INFOSOC, project no. 78/2002, and project no. 100B/2004.

REFERENCES

1. KARTAN N. and K. AL-RESHAID. Design and Implementation of a Web-based Multimedia Techniques for Construction Education. In *Int. J. Eng. Ed*. 2002, 682-691.
2. MC.COWAN J. An Integrated and Comprehensive Approach to Engineering
3. Curricula Part Two: Techniques. in *Int. J. Eng. Ed*. 2002, 638-644.
4. PLESU V., R. ONOFREI, A. BITA, G. DUCA and M. MATEI 2002, Using IT Methodologies for Training in Process Engineering, in PRES 2002 15th International Congress of Chemical and Process Engineering, CHISA 2002-PRES 2002. Prague, 2002, 263.
5. PLESU V., ISOPESCU R., ONOFREI R., JOSCEANU A.M., DIMA R., MORCOV S. 2004, 'Development of an e-Learning System for Chemical Engineering Education', ICEER 2004, Olomouc, Czeck Republic, 27-30 June 2004.
6. WANKS S., 1995, *Curriculum design*. *From an art towards a science.* Berlin: Tempus Publications, 1995.
7. SIVECO website, http://www.siveco.ro/products_ael.jsp

STUDIA UNIVERSITATIS. BABEŞ-BOLYAI, CHEMIA, L, 2, 2005

ADHESIVE ASSEMBLIES OPTIMIZATION

NEMES, O.[*], LACHAUD, F.[**], MOJTABI, A.[***]

[*] *Technical University of Cluj-Napoca*
[**] *ENSICA Toulouse*
[***] *"Paul Sabatier" University Toulouse*

ABSTRACT. This work presents a theoretical model of calculation of stuck cylindrical assemblies, based on an energy method. After the determination of the acceptable field of constraints, according to the applied load, a variational calculus on the expression of elastic potential energy makes it possible to lead to the complete expression of the stress field in the whole assembly. A first parametric analysis (geometrical and physical parameters) is carried out on an assembly of tubes and makes it possible to deduce the optimal length and the thickness of joining.

Keywords: Adhesion and adhesives; Energy methods; Variational calculus.

INTRODUCTION

Joining is a powerful technique of assembling which makes it possible more and more to replace or to supplement the other traditional methods of assembly (welding, riveting or the bolting). However, the optimization of this type of assembly passes by the determination of the constraints in the adhesive and the substrates; stresses are strongly influenced by the geometrical and physical parameters of the assembly.

The mechanical performance of an adhesive bonded joint is related to the distribution of the stresses in the adhesive film [1]. Consequently it is essential to know this distribution which, because of its complexity makes prediction of fracture difficult.

The first studies are developed on plane assemblies with simple covering loaded in traction. The work of Volkersen [2] developed into 1944 leads to a false evaluation of the maximum level of constraint because the effects of inflection of the supports are not taken into account.

Compared to the number of recent scientific publications concerning plane joints, with simple or double lap [3, 4], there are only a few theoretical publications concerning the study of the mechanical behavior in adhesive bonded joints, with symmetry of revolution, subjected to traction [5, 6].

The first theoretical studies concerning the cylindrical adhesive bonded joints are due to Lubkin [7] and Volkersen [8]. They suppose that the supports do not become deformed.

Therekhova and Skorkyi, [9], considered the influence of the pressures which are exerted inside and outside the tubes.

Kukovyankin and Skorkyi, [10], were interested in the action of the moments and the axisymmetric forces which make it possible to introduce the inflection into the tubes. In this work the orthoradiale constraints are not taken into account.

The most recent work, concerning the type of assembly considered, is by Shi and Cheng, [6]. They build a first stress field using the equilibrium equations

and the conditions of continuity of the stresses at the interfaces using an equation of compatibility. They then calculated the potential energy associated with this field and using the theorem of the minimal complementary energy, they obtain a system of differential equations whose solutions allow the determination of the optimal stress field.

However, if the field of the constraints obtained checks well a part of the equations of compatibility, this does not check therefore the totality of the equations of compatibility.

The treated numerical examples propose the zones of constraints which appear at the ends of the joints. The others also provide an outline of the consequence of the variations of the various geometrical and physical parameters on the distribution and the intensity of shear stresses in the adhesive.

All the developed techniques, based on the resolution of the associated differential equations, encounter a not overcome difficulty which is the taking into account of the boundary conditions at the ends of the joint. The damage declaring itself in these zones, it is thus important to model the effects edge.

Armengaud, [11] and Nemes [12] used a technique based on the minimization of the potential energy. The first stage consists in building a statically acceptable stress field, i.e. checking the boundary conditions and the equilibrium equations. The second stage consists in calculating the potential energy generated by such a stress field. In the third stage the use of the second theorem of the potential energy results in minimizing this energy, in order to determine the stress distributions.

The analytical approaches which relate to the cylindrical stuck interfaces are applicable at the time of estimated calculations, therefore for preparatory project, but there is not any doubt that, under complexes loading, the digital simulation is a stage impossible to circumvent if we want to optimize an adhesive assembly.

RESULTS

Analytical formulation

All works showed some difficulties encountered in modeling the stress field in the vicinity of the ends of the join.

The method used to obtain the optimal field for this type of assembly consists of:

- the construction of a statically acceptable field,
- the calculation of the potential energy associated to this stress field,
- the minimization of this energy by variational calculus,
- the resolution of the differential equation obtained.

Definition of the statically acceptable field

In this work we consider an assembly of stuck tubes subjected to a tensile load whose geometrical definitions are represented in fig. 1. The parameters of the assembly are: E_{it}, E_{il} - Transversal and longitudinal Young's modulus, v_{tli} - Poisson's ratio, r_i - Internal radius of the inner tube, r_{ic} - External radius of the inner tube, r_{ec} - Internal radius of the external tube, r_e - External radius of the external tube, L - Joining length, f - Tensile stress following z axis on the inner tube, q - Tensile stress following z axis on the external tube.

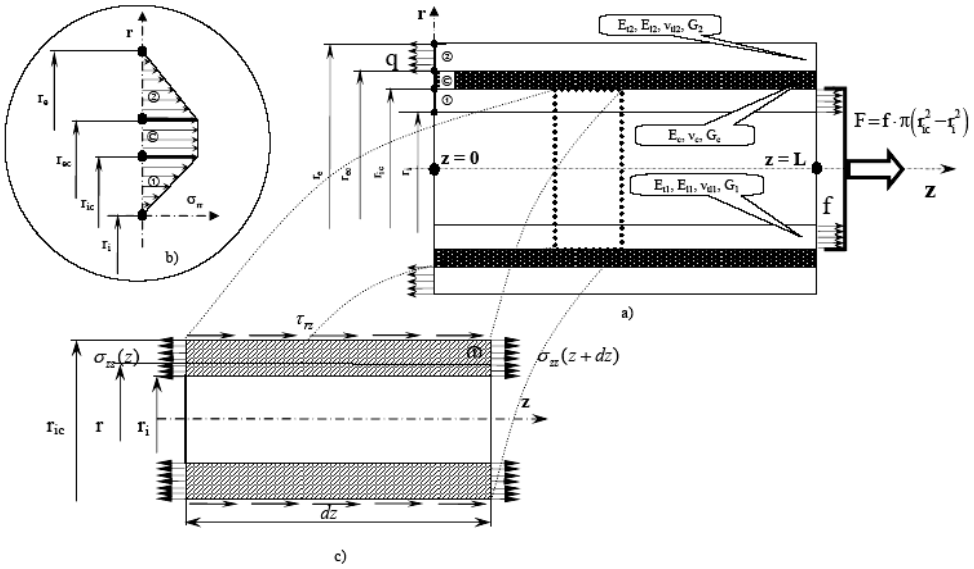

Figure 1. Cylindrical assemblies:

a) Diagram of the adhesive bonded joint;

b) σ_{rr} distribution in the cylindrical assembly;

c) Equilibrium of an elementary section of the inner tube, $r \in \left[r_i, r_{ic}\right]$.

The stresses in various materials will be located by the index (i), (i = ① for the inner tube, © for the adhesive and ② for the external tube).

To build the statically acceptable field, we will adopt the following hypothesis:

- the symmetry of revolution imposes that the shear stresses are nulls:

$$\tau_{r\theta} = \tau_{z\theta} = 0 \tag{1}$$

- the normal stress in the adhesive will be neglected:

$$\sigma_{zz}^{(©)} = 0 \tag{2}$$

- the axial stress will be a function only of variable z.

The stress field is reduced to the following components:

- for the inner tube (①):

$$\sigma_{zz}^{(1)}(z),\ \tau_{rz}^{(1)}(r,z),\ \sigma_{\theta\theta}^{(1)}(r,z),\ \sigma_{rr}^{(1)}(r) \tag{3}$$

- for the adhesive (©):

$$\sigma_{\theta\theta}^{(©)}(z),\ \tau_{rz}^{(©)}(r,z),\ \sigma_{rr}^{(©)} = \text{cst.} \tag{4}$$

- for the external tube (②):

$$\sigma_{zz}^{(2)}(z),\ \tau_{rz}^{(2)}(r,z),\ \sigma_{\theta\theta}^{(2)}(r,z),\ \sigma_{rr}^{(2)}(r) \tag{5}$$

Table 1 shows the components of the stress field developed in the references. We can notice that only the formulations of Armengaud [11] and Nemes [12] do not take into account the radial stress, by supposing them null.

Table 1

Comparative table of the stress fields.

References	zones	σ_{zz}	$\sigma_{\theta\theta}$	σ_{rr}	τ_{rz}	$\tau_{\theta z}$
Armengaud [11] Nemes [12]	Adhesive	/	$\sigma_{\theta\theta}(r,z)$	/	$\tau_{rz}(r,z)$	/
	Substrates	$\sigma_{zz}(z)$	$\sigma_{\theta\theta}(r,z)$	/	$\tau_{rz}(r,z)$	/
Shi and Cheng [6]	Adhesive	/	$\sigma_{\theta\theta}(r,z)$	$\sigma_{rr}(r,z)$	$\tau_{rz}(r,z)$	/
	Substrates	$\sigma_{zz}(r,z)$	$\sigma_{\theta\theta}(r,z)$	$\sigma_{rr}(z)$	$\tau_{rz}(r,z)$	/
Lubkin and Reissner [7]	Adhesive	/	/	$\sigma_{rr}(z)$	$\tau_{rz}(z)$	/
	Substrates	$\sigma_{zz}(z)$	/	$\sigma_{rr}(z)$	$\tau_{rz}(z)$	/
This study	Adhesive	/	$\sigma_{\theta\theta}(z)$	$\sigma_{rr}(z)$	$\tau_{rz}(z)$	/
	Substrates	$\sigma_{zz}(z)$	$\sigma_{\theta\theta}(r,z)$	$\sigma_{rr}(r,z)$	$\tau_{rz}(z)$	/

The equilibrium equations of an elementary volume of adhesive bonded joint length dz are:

$$\frac{\partial}{\partial r}[r\sigma_{rr}] + \frac{\partial}{\partial z}[r\tau_{rz}] = \sigma_{\theta\theta} \tag{6}$$

$$\frac{\partial}{\partial r}[r\tau_{rz}] + \frac{\partial}{\partial z}[r\sigma_{zz}] = 0 \tag{7}$$

The radial stress field (Fig. 1) is supposed equal to:

$$\sigma_{rr}^{(1)} = \alpha_1[r - r_i]\,;\ \sigma_{rr}^{(c)} = \beta_c = \text{cst.}\,;\ \sigma_{rr}^{(2)} = \alpha_2[r - r_e] \tag{8}$$

The continuity of σ_{rr} makes it possible to write:

$$r = r_{ic} \ \rightarrow\ \beta_c = \alpha_1[r_{ic} - r_i] \tag{9}$$

$$r = r_{ec} \rightarrow\ \beta_c = \alpha_2[r_{ec} - r_e] \tag{10}$$

$$\beta_c = \alpha_1[r_{ic} - r_i] = \alpha_2[r_{ec} - r_e] \tag{11}$$

Expressions of the stresses in the adhesive bonded joint

In the inner tube (①):

The equilibrium of an elementary section of the tube enables us to express the shear stress $\tau_{rz}^{(1)}$:

$$\tau_{rz}^{(1)}(r,z) = \frac{\left(r_i^2 - r^2\right)}{2r}\frac{d\sigma_{zz}^{(1)}}{dz} \tag{12}$$

From expression (12) and equilibrium equation (6), we express directly the orthoradial stress in the inner tube ①:

$$\sigma_{\theta\theta}^{(1)}(r,z)=\frac{r_i^2-r^2}{2}\frac{d^2\sigma_{zz}^{(1)}}{dz^2}+\alpha_1[2r-r_i] \tag{13}$$

In the adhesive ©:

Using the equilibrium equation:

$$\frac{\partial\tau_{rz}}{\partial r}+\frac{1}{r}\tau_{rz}+\frac{\partial\sigma_{zz}}{\partial z}=0 \tag{14}$$

and the continuity condition of the shear stress for $r = r_{ic}$, enable us to obtain the expression for the shear stress $\tau_{rz}^{(c)}$:

$$\tau_{rz}^{(c)}(r,z)=\frac{\left(r_i^2-r_{ic}^{\ 2}\right)}{2r}\frac{d\sigma_{zz}^{(1)}}{dz} \tag{15}$$

The expression of the orthoradial stress in the adhesive is obtained by the same manner like for the inner tube ①:

$$\sigma_{\theta\theta}^{(c)}(z)=\frac{r_i^2-r_{ic}^{\ 2}}{2}\frac{d^2\sigma_{zz}^{(1)}}{dz^2}+\alpha_1[r_{ic}-r_i] \tag{16}$$

In the external tube (②):

The expression of the normal stress $\sigma_{zz}^{(2)}$ can be given starting from the equation:

$$\left(r_{ic}^2-r_i^2\right)\sigma_{zz}^{(1)}+\left(r_{ec}^2-r_{ic}^2\right)\underbrace{\sigma_{zz}^{(C)}}_{=0}+\left(r_e^2-r_{ec}^2\right)\sigma_{zz}^{(2)}=\left(r_{ic}^2-r_i^2\right)f=\left(r_e^2-r_{ec}^2\right)q \tag{17}$$

that is to say:

$$\sigma_{zz}^{(2)}(r,z)=\left(\frac{r_{ic}^2-r_i^2}{r_e^2-r_{ec}^2}\right)\left(f-\sigma_{zz}^{(1)}\right) \tag{18}$$

The expression of the shear stress in the external tube can be given in two ways, either by considering the equilibrium of a section of tube, or using the equilibrium equation (7) and the condition of continuity of the same constraint at the interface with the adhesive.

These two methods lead to the same expression:

$$\tau_{rz}^{(2)}(r,z)=\frac{\left(r_e^2-r^2\right)\left(r_{ic}^2-r_i^2\right)}{2r(r_{ec}^2-r_e^{\ 2})}\frac{d\sigma_{zz}^{(1)}}{dz} \tag{19}$$

The orthoradial stress is obtained immediately and is written:

$$\sigma_{\theta\theta}^{(2)}(r,z)=\frac{(r_e^2-r^2)(r_{ic}^2-r_i^2)}{2(r_{ec}^2-r_e^2)}\frac{d^2\sigma_{zz}^{(1)}}{dz^2}+\underbrace{\alpha_1\frac{r_{ic}-r_i}{r_{ec}-r_e}}_{\alpha_2}[2r-r_e] \tag{20}$$

The field is entirely determined and its components are written according to the axial stress in the inner tube ($\sigma_{zz}^{(1)}$).

Expression of the deformation energy

The expression of the deformation energy is:

$$\xi_P = \pi\int_0^L\int_{r_i}^{r_{ic}}\left[\frac{\sigma_{\theta\theta}^{(1)2}}{E_{1t}}+\frac{\sigma_{zz}^{(1)2}}{E_{1l}}-\frac{2\nu_{tl1}}{E_{1t}}\sigma_{zz}^{(1)}\sigma_{\theta\theta}^{(1)}+\frac{\tau_{rz}^{(1)2}}{G_1}\right]rdrdz+$$
$$+\pi\int_0^L\int_{r_{ic}}^{r_{ec}}\left[\frac{\sigma_{\theta\theta}^{(c)2}}{E_c}+\frac{2(1+\nu_c)}{E_c}\tau_{rz}^{(c)2}\right]rdrdz+ \quad (21)$$
$$+\pi\int_0^L\int_{r_{ec}}^{r_e}\left[\frac{\sigma_{\theta\theta}^{(2)2}}{E_{2t}}+\frac{\sigma_{zz}^{(1)2}}{E_{2l}}-\frac{2\nu_{tl2}}{E_{2t}}\sigma_{zz}^{(2)}\sigma_{\theta\theta}^{(2)}+\frac{\tau_{rz}^{(2)2}}{G_2}\right]rdrdz$$

The expressions of the stresses given by the equations (12) to (20) makes it possible to simply write the deformation energy according to $\sigma_{zz}^{(1)}$:

$$\xi_P = \pi\int_0^L \underbrace{\left[A\sigma_{zz}^{(1)2}+B\sigma_{zz}^{(1)}\frac{d^2\sigma_{zz}^{(1)}}{dz^2}+C\left(\frac{d\sigma_{zz}^{(1)}}{dz}\right)^2+\tilde{D}\sigma_{zz}^{(1)}+E\left(\frac{d^2\sigma_{zz}^{(1)}}{dz^2}\right)^2+\tilde{F}\frac{d^2\sigma_{zz}^{(1)}}{dz^2}+\tilde{K}\right]}_{\Gamma}dz \quad (22)$$

where: $\tilde{D} = D + \alpha_1 k$, $\tilde{F} = F + \alpha_1 h$, $\tilde{K} = K + \alpha_1^2 m$ (23)

The A, B, C, D, E, F, K constants (the same ones as those obtained for the case $\sigma_{rr} = 0$) and k, h, m are depending on the load and on the dimensional and mechanical specifications of the two tubes and adhesive [8].

The constant α_1 is given by the equation (24):

$$2m\alpha_1 L + \int_0^L\left[k\sigma_{zz}^{(1)}+h\frac{d^2\sigma_{zz}^{(1)}}{dz^2}\right]dz = 0 \quad (24)$$

and with the boundary conditions in z = 0 and z = L we have:

$$2m\alpha_1 L + \int_0^L k\sigma_{zz}^{(1)}dz + h\underbrace{\left[\frac{d\sigma_{zz}^{(1)}}{dz}\right]_0^L}_{=0} = 0 \quad (25)$$

By carrying out a variational calculus on the expression of the potential energy (21) and using the boundary conditions in z = 0 and z = L, we obtain that the complementary energy is minimal when $\sigma_{zz}^{(1)}(z)$ is the solution of the following differential equation:

$$E\frac{d^4\sigma_{zz}^{(1)}(z)}{dz^4}+(B-C)\frac{d^2\sigma_{zz}^{(1)}(z)}{dz^2}+A\sigma_{zz}^{(1)}(z)+\frac{D}{2}+\frac{\alpha_1 k}{2} = 0 \quad (26)$$

Parametric study of the adhesive bonded joints

The numerical application developed in this work is presented in the following way: we use the configuration presented in table 2, and the load presented figure 1, figure2 showing the stress distribution in the assembly.

Table 2

Analyzed assembly configuration

Tube 1	Adhesive	Tube 2	r_i [mm]	r_{ic} [mm]	r_{ec} [mm]	r_e [mm]	L [mm]	f [MPa]
Glass/Epoxy +/- 45° E_x = 14470 MPa E_y = 14470 MPa G_{xy} = 12140 MPa υ = 0.508	Araldite Redux 312 E_c = 2500 MPa G_c = 1000 MPa u_c = 0.35	Carbon/Epoxy +/- 45° E_x = 17090 MPa E_y = 17090 MPa G_{xy} = 36380 MPa υ = 0.781	10	12	12.2	15.2	50	1000

Following, we present an analysis of the influence of various parameters affecting the intensity and the stress distribution. This analysis will be reduced to the study of the influence of the following parameters: the adhesive thickness, the length of adhesive cover, the Young's modulus of the adhesive and the relative rigidity of tubes E_2/E_1.

PARAMETRIC STUDY

Stress distribution

Figure 2 shows the stress distributions in the adhesive for the first analyzed configuration, that is to say the distributions of the orthoradial and shear stresses.

We notice that:

- for $\sigma_{\theta\theta}$, the maximum values are obtained on the free edges (z = 0, z = L). These values are about 60 % of the pressure applied. They are localized at the edges, however, the maximum stress $\sigma_{\theta\theta\ max}$ is obtained in compression,
- for τ_{rz}, we have two peaks of stresses located at equal distance of the two free edges (≈ 6,5 mm). The maximum value is about 12 % of the applied effort.

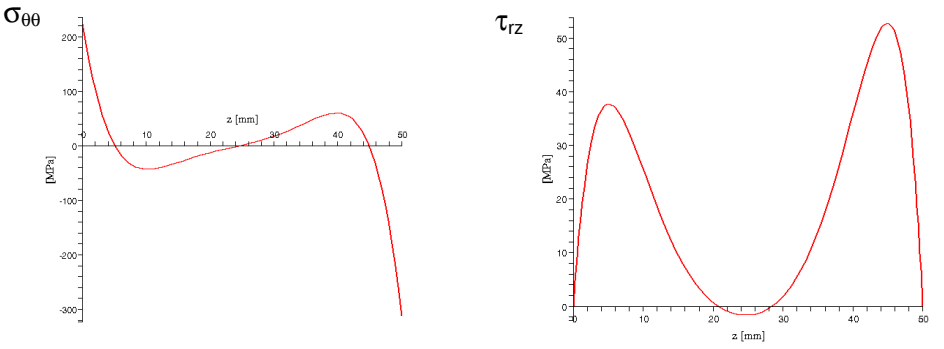

a) b)

Figure 2. Stress distributions in the adhesive (f = 1000 MPa, L = 50 mm).
a) The orthoradial stress ($\sigma_{\theta\theta}$); b) The shear stress (τ_{rz}).

The peaks do not have the same intensity because of the difference of rigidities of the two stuck tubes. We can note that the orthoradial stresses are more important than shear stresses. The use of an fracture criterion of the adhesive bonded joint must take into account not only the shear stress τ_{rz} but also the orthoradial stress $\sigma_{\theta\theta}$.

Influence of covering length

Figure 3 shows the influence of covering length on the shear stresses distribution. We note thus that when the length of covering exceeds 50 mm, a part of this one is not requested any more. This makes it possible to determine a useful maximum length of joining.

We can observe that for low lengths of covering we have a distribution with only one peak (fig. 3). Two peaks of constraint appear starting from approximately 30 mm. By increasing the covering length gradually we observed:

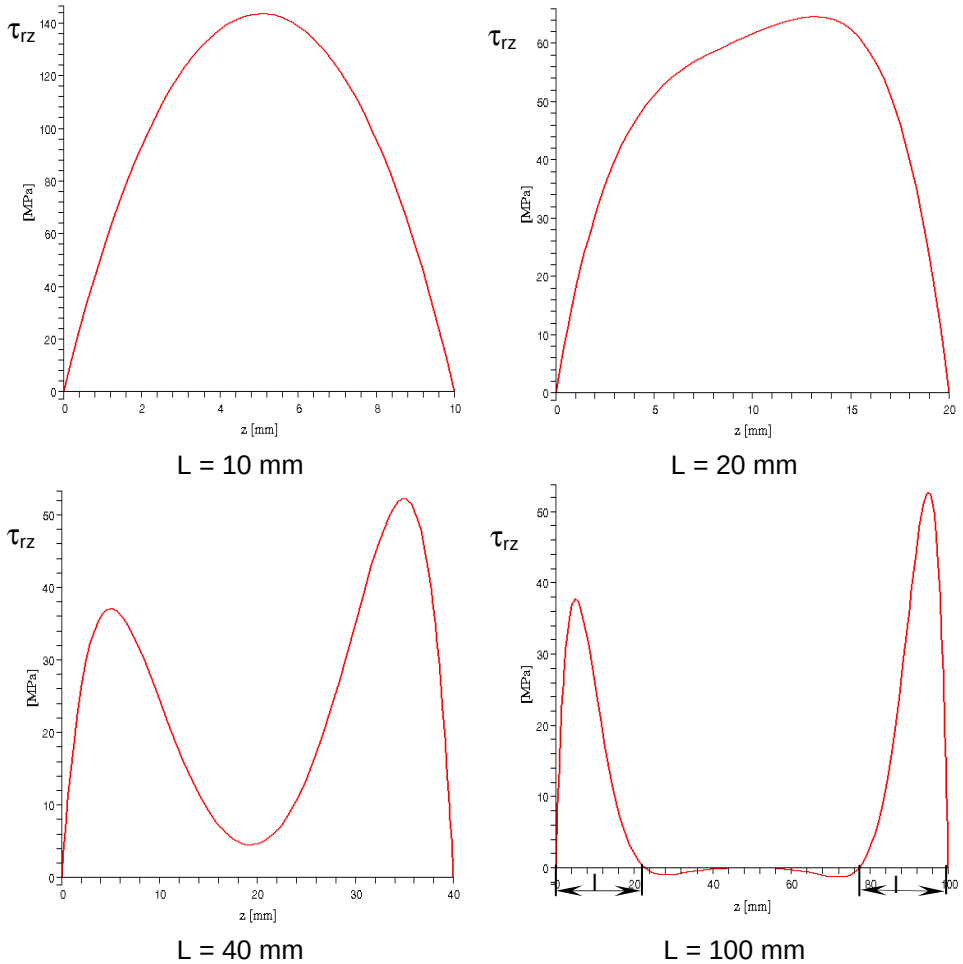

Figure 3. Shear stress (τ_{rz}) distribution according with the covering length (f = 1000 MPa).

- the reduction of the values of the shear stress in the medium of the joint,
- the displacement of the peaks of constraints towards the free edges.

We notice that there is an optimal length beyond which the maximum constraints do not evolve any more.

Influence of adhesive thickness

The adhesive thickness influence on the intensity and distribution of shear stresses is shown in figure 4. We can notice that more we increases the thickness of adhesive, the more the values of the constraints decrease on the level of the free edges. The distribution tends to being uniform.

CONCLUSIONS

A theoretical model to calculate the cylindrical assemblies is proposed. This model is based on the variational calculus applied on the potential energy in the assembly.

After having determined all the components of the stress field according to the effort $\sigma_{zz}^{(1)}(z)$ in the first tube, by considering the equilibrium of an elementary volume, the use of variational calculus enabled us to obtain the solution of the defined model.

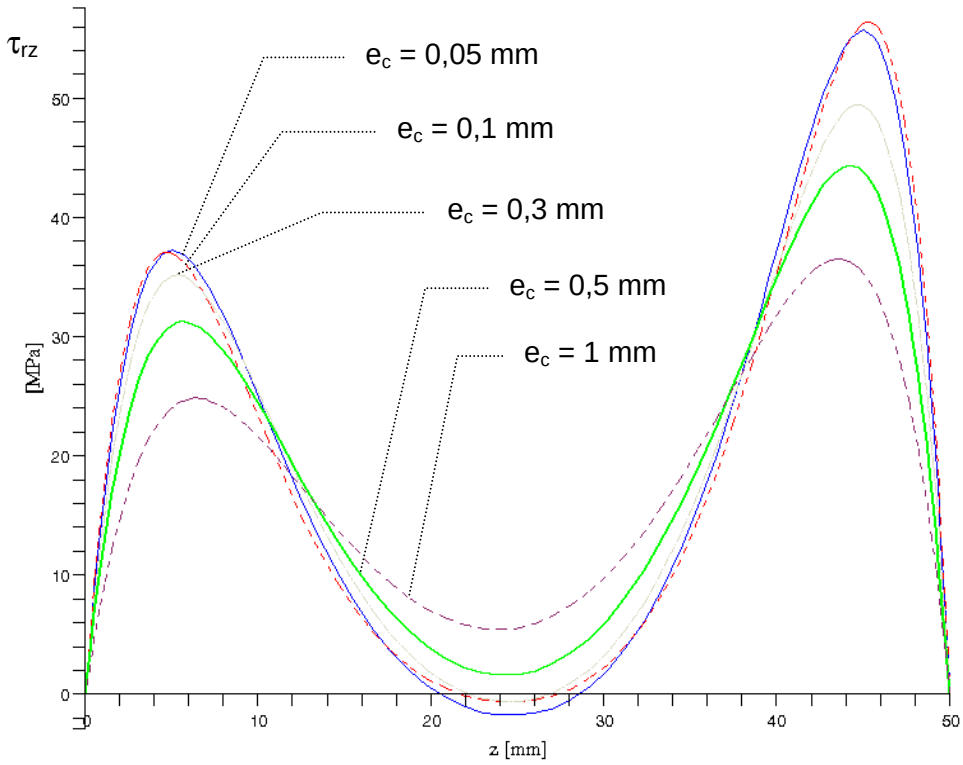

Figure 4. Shear stress (τ_{rz}) variation according with the adhesive thickness (f = 1000 MPa, L = 50 mm).

It comes out from this study the following points: the maximum values of $\sigma_{\theta\theta}$ are obtained on the free edges and the maximum values are about 60 % of the applied effort, moreover they are localized at the edges; concerning τ_{rz}, we have two peaks of constraints located at equal distance of the two free edges ($\approx$ 6,5 mm). The maximum value is approximately 12 % of the applied effort. The taking into account in the model of the σ_{rr} stress influences only the distribution of the $\sigma_{\theta\theta}$ stress, the orthoradiale stresses are more important than shear stresses. There exists an optimal length beyond which the maximum constraints do not evolve any more; the intensities of the peaks are influenced by the difference of rigidities of the two stuck tubes. Te maximum peaks increase slightly when the elastic module grows.

The shear stress in the adhesive increases with the increase of the relative rigidity of the tubes, more we increases the adhesive thickness, plus the values of the constraints decrease on the level of the free edges and the distribution tends to being uniform. The taking into account in the model of the σ_{rr} stress influences only the distribution of the $\sigma_{\theta\theta}$ stress.

REFERENCES

1. Konate, M., “Etude expérimentale du comportement mécanique à la rupture par cisaillement de films d'adhésif”, Revue Française de Mécanique, **1990**, N°4.
2. Volkersen, O., “Die Nietkraftverteilung in zugbeanspruchten nietverbendungen mit konstanten laschenquerschnitten, Luftfahrtforschung”, **1938**, Vol. 15, pp. 41-47.
3. Tsai, M.Y., Oplinger, D.W., Morton, J., “Improved theoretical solutions for adhesive lap joints”, Int. J. Solid Structures, Vol. 35, No. 12, **1998**, pp. 1163-1185.
4. Mortensen, F., Thomsen, O.T., “Analysis of adhesive bonded joints: a unified approach”, Composite Science and Technology, Vol. 62, **2002**, pp. 1011-1031.
5. Adams, R.D., Peppiatt, N.A., “Stress analysis of adhesive bonded tubular lap joints, Journal of Adhesion”, Vol. 9, **1977**, pp. 1-18.
6. Shi, Y.P., Cheng, S., “Analysis of adhesive-bonded cylindrical lap joints subjected to axial load”, Journal of Engineering Mechanics, Vol. 119, **1993**, pp. 584-602.
7. Lubkin, L., Reissner, E., “Stress distribution and design data for adhesive lap joints between circular tubes”, Trans. Of ASME, Journal of Applied Mechanics, Vol. 78, **1956**, pp. 1213-1221.
8. Volkersen, O., “Recherche sur la théorie des assemblages collés”, Construction métallique, n°4, **1965**, pp. 3-13.
9. Therekhova, L.P., Skorkyi, I.A., “Stresses in bonded joints of thin cylindrical shells”, Strength of materials, Vol. 4, N°10, **1971**, pp. 1271-1274.
10. Kukovyankin, A., Skorkyi, I.A., Stresses in cylindrical joints, Russian Engineering Journal, N°4, **1972**, pp. 40-43.
11. Armengaud, G., “Calcul explicite (analytique et numérique) des champs de contraintes dans des structures élancées homogènes et composites à l'aide de méthodes énergétiques”, PhD. Thesis, ”Paul Sabatier” University Toulouse III, Toulouse, France, **1996**.
12. Nemeş, O., “Contribution à l'étude des assemblages collés cylindriques et plans”, PhD. Thesis, INSA Toulouse, France, **2004**.

STUDIA UNIVERSITATIS. BABEŞ-BOLYAI, CHEMIA, L, 2, 2005

FIRST PRINCIPLES MODELING AND NONLINEAR OPTIMIZATION BASED ESTIMATION AND CONTROL OF A FLUID CATALYTIC CRACKING UNIT

ZOLTAN K. NAGY[1,2*], RALUCA ROMAN[1], SERBAN P. AGACHI[1], FRANK ALLGÖWER[2]

[1] Department of Chemical Engineering, "Babes-Bolyai" University, 11 Arany J., Cluj-Napoca, 3400, Romania, {romanr, znagy,sagachi}@chem.ubbcluj.ro
[2] Institute for Systems Theory in Engineering,University of Stuttgart, 9 Pfaffenwaldring, 70550, Stuttgart, Germany, allgower@ist.uni-stuttgart.de
**Corresponding author. University of Stuttgart, Pfaffenwaldring 9, 70550, Stuttgart, Germany, Phone: +49-711-6857742; Fax:+49-711-6857735; Email: nagy@ist.uni-stuttgart.de*

ABSTRACT. In this paper the output feedback NMPC approach is illustrated on a simulated fluid catalytic cracking unit (FCCU). This approach considers the most important features of a real-time control algorithm, which are often overlooked in simulation studies, contouring thus a framework for practical NMPC implementation. The most important features considered in the approach are: state and parameter estimation, efficient solution of the optimization, and computational delay. In the output feedback NMPC approach used in this paper, only measurements that are available in practice are considered, whereas the rest of the states are estimated together with uncertain model parameters using a moving horizon estimation (MHE) technique. The importance of taking this computational delay into account will also be assessed and a real-time formulation of the control approach is describes that includes the computational delay in the NMPC approach. The advantages of the proposed real-time approach are assessed through the simulated industrial FCCU application.

Keywords: Fluid catalytic cracking unit (FCCU), nonlinear model predictive control, moving horizon estimation, real-time control, multiple shooting, interior point algorithm.

1. INTRODUCTION

The fluid catalytic cracking unit (FCCU) is an important processing unit in an oil refinery. This process converts high molecular-weight gas oils into significantly more valuable, lighter hydrocarbon products. Any improvement, whether in design, operation or control, can result in dramatic economic benefits. The process is multivariable, strongly nonlinear, highly interactive, and is subject to many operational, safety and environmental constraints, posing challenging control problems. The competitive nature of the petrochemical industries drives the constant technological development of FCC processes, with the clear economic objective of improving productivity, while maintaining safety and environmental regulations. Due to its complexity, the modeling and control of FCCU poses important challenges (McFarlane et al., 1993). FCCU has become in the last decades the testing bench for many modern refinery control systems. This chemical process has been traditionally controlled by using algorithms on a linear time-invariant approximate process model, the most common being step and impulse response models derived from the convolution integral account (Qin and Badgewell,

2003). Linear model predictive control has proved its benefits in the petrochemical industries in the past two decades, however nonlinear model predictive control (NMPC) has the potential to achieve higher productivity by exploiting the advantages of taking process nonlinearities explicitly into Nonlinear model predictive control (NMPC) is a good candidate for the control of the FCCU, because of its ability to explicitly handle most of the aforementioned problems. First-principles model based NMPC requires full state information for the prediction, which is usually not available in practical applications. In the output feedback NMPC approach used in this paper, only measurements that are available in practice are considered, whereas the rest of the states are estimated together with uncertain model parameters using a moving horizon estimation (MHE) technique. The goal of state estimation is to reconstruct the state of a system from process measurements and a model. The state estimation is used to reconstruct the states and time-varying parameter for a process from a set of measurements. The concepts of observability and detectability provide conditions for state estimation to converge to the true value of the state and parameters (Russo et al, 1999). State estimators for physical processes often must address many different challenges, including nonlinear dynamics, state (e.g nonnegative concentrations, temperatures) and local optima, subject to hard constraints (Haseltine and Rawlings, 2003).

Industrial applications of model predictive control commonly use a constant additive disturbance model to compensate for model error. However, the use of a constant additive disturbance model may result in a poor or even unstable behaviour when there are significant unmodeled process dynamics or the plant is open-loop unstable. State estimation provides the mechanism to use more appropriate disturbance models (Russo et al, 1999). As a result, state and parameter estimation are a persistent topic for the research academy.

The paper is structured as follows: Section two presents the description of the plant. Section three and section four give an overview to the areas of moving horizon estimation and nonlinear model predictive control that have both attracted considerable industrial and academic interest over recent years.

2. DYNAMIC MODELING OF THE FCCU

The schematic diagram of the FCCU, for which the mathematical model was developed and the assessment of the NMPC has been performed is presented on Figure 1.

In the FCCU raw material is mixed with the regenerated catalyst in the reactor riser. The cracking reactions and coke formation occur in the riser and the products (gasoline, diesel, slurry) are separated in a fractionator. The deactivated catalyst due to coke deposition is regenerated in the regenerator.

The developed dynamic simulator consists of detailed models of: the feed and preheat system, reactor stripper, riser, regenerator, air blower, wet gas compressor, catalyst circulation lines and main fractionator. Based on the assumption given in Dupain at al. (2003) a five lump kinetic model (schematically shown on Figure 2) that predicts the yields of valuable products is proposed and included in the simulator. The resulted global model of the FCCU is described by a complex system of partial-differential- equations, which was solved by discretizing the kinetic models in the riser

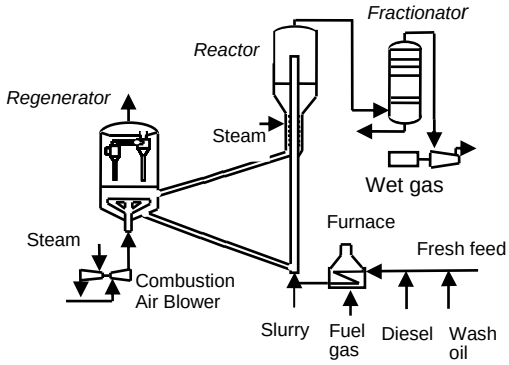

Figure 1. FCCU plant

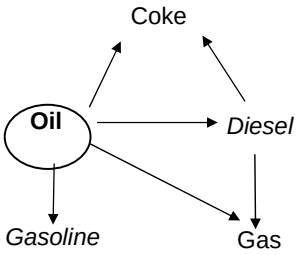

Figure 2. Five lump model for the catalytic cracking

and regenerator on a fixed grid along the height of the units, using finite differences. The resulted model is a very high order DAE, with 2143 ODEs (143 from material and energy balances and 2000 resulted from the discretization of the kinetic models). The model was implemented in C programming language for efficient solution and was used first to study the dynamics of the process and then in the NMPC controller.

3. MHE ALGORITHM

In a typical industrial application (FCCU) there is a need to reconstruct unmeasured states using a limited number of available measurements. A moving horizon estimator is employed for states estimation. The benefits arise because MHE incorporate physical state constraints into an optimization, accurately uses the nonlinear model, and optimize over a trajectory of states and measurements (Haseltine and Rawlings, 2003). The MHE estimator express as a nonlinear programming techniques (NLP) problem is as follows:

Problem P1:

$$\min_{x_{k-N},\theta_e} J_{MHE} = \sum_{j=k-N+1}^{k} \left\| y_i - y_i^{meas} \right\|_W^2 + \left\| \theta_e - \theta_e^{ref} \right\|_Z^2 \tag{1}$$

subject to: $x_i = f(x_{j-1}, u_{j-1}, \theta),\ j = k-N+1,...,k$ (2)

$$y_i = g(x_j, \theta),\ j = k-N+1,...,k \tag{3}$$

$$\theta_{e,\min} \le \theta \le \theta_{e,\max} \tag{4}$$

where N is the estimation horizon, W, Z are weighting matrices and θ_e is a subset of model parameters selected for on-line adjustment. θ_e^{ref} is a set of reference values and $\theta_{e,\min}, \theta_{e,\max}$ are specified lower and upper bounds for the adjustment parameters; y_i denotes the output at discrete time j, and y_i^{meas} its corresponding measurement.

The second term in (1) penalize parameter moves away from reference values, while constraint ensure that parameter estimates stay within reasonable physical rages. In problem *P1* the inputs u_j, $j = k-N,...,k-1$ are known, applied inputs to system. The solution of problem *P1* results in $\hat{x}$ which is used to calculate an estimate of the controlled variable when this last quantity is not measured.

Figure 3 present comparatively, the simulation results of the model of the plant and simulation results using MHE algorithm in the presence of disturbance in the coke factor (*Kc*). The disturbance have an influence on the reactor temperature (T_r) and regenerator temperature (T_{reg}), on coke concentration on spent and regenerated catalyst (*csc* and *crgc*), on the regenerator and reactor catalyst inventory (W_{reg} and W_r), on the catalyst inventory on spent circulation lines (W_{sp}). The disturbance have also an influence also on the carbon inventory (W_c) deposited on the catalyst in regenerator and on the moles of carbon in regenerator (*n*). Coke factor has a small influence on the speed of catalyst in spent circulation line (*vsc*) and regenerated circulation line (*vrgc*). A small influence of the disturbance can be observed on the pressures of the system: combustion air blower sunction pressure (p_1), combustion air blower discharge pressure (p_2), reactor-fractionator pressure (p_5), regenerator pressure (p_6), wer gas compressor sunction pressure (p_7).

The goal of MHE is to reconstruct the state of a system from process measurements and estimate the unknown model parameter *Kc*. Figure 3 also presents the evolution of the states of the FCCU model using eleven measurements: T_r, T_{reg}, *vrgc, vsc* and the pressures in the system (p_1, p_2, p_5, p_6, p_7), considering errors in the initial states of the model. As can be seen from the Figure 3, a few states are unobservable: W_{reg}, W_r, W_c, W_{sp} and *n,* however the estimator achieves excellent performance in estimating the unknown model parameter.

4. NONLINEAR MODEL PREDICTIVE CONTROL

4.1 Formulation of the algorithm

NMPC is typically implemented as a two-step algorithm: state estimation and prediction to minimize a specified control objective function. An NMPC algorithm must also be formulated must also be formulated to ensure integral action in the feedback path. We consider the following general differential- algebraic optimization problem, as the starting point for the development of state estimation and predictive control algorithms:

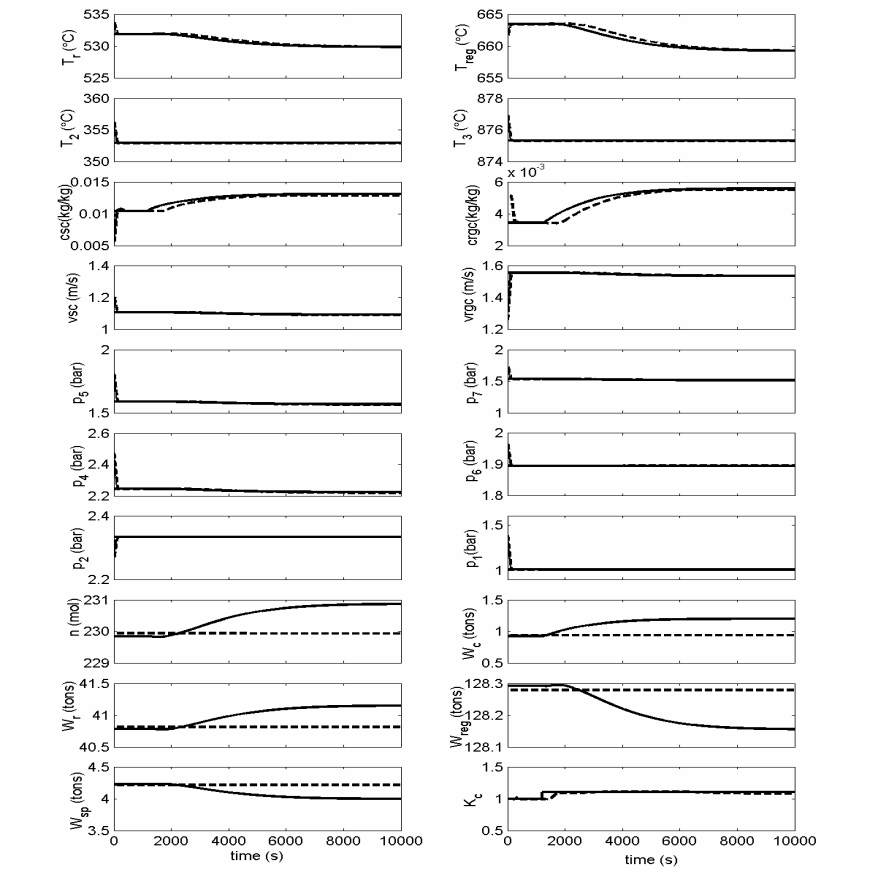

Figure 3. Performance of the MHE in the case of errors in the initial states and disturbance in K_c (10 % increase at t= 20 min) plant data modeling results (solid line); MHE results (dotted line)

Problem P2:

$$\text{Minimize } J = \phi(x(t_f), t_f + \int_{t_0}^{t_f} L[x(t), u(t), t]dt \tag{5}$$

$$\text{subject to: } \dot{x}(t) = f(x(t), u(t)) \tag{6}$$

$$G(x(t), u(t)) = 0 \tag{7}$$

$$H(x(t), u(t)) \leq 0 \tag{8}$$

where J is the state estimation or predictive control objective function, $x(t)$ and $u(t)$ are the state and input vectors, respectively, and F and G represent the mechanistic system model, a coupled set of ordinary differential and algebraic equations. H represents bounds on system variables or other linear or nonlinear constraints.

4.2. Efficient solution of the NMPC optimization via multiple shooting

Problem P2 can neither be solved by typical nonlinear programming (NLP) techniques nor by optimal control methods. In general, NLP methods cannot optimize continuous systems while optimal control methods do not handle algebraic constraints for G and H. Considering the discrete nature of the online control problem, a convenient approach to solving Problem 2 is to formulate discrete approximation to it that can be handled by conventional NLP solvers. An alternate formulation for discrete approximation of the problem for nonlinear model predictive control is adopted for its generality (*Problem P3*). The prediction horizon $[0, t_f]$ is divided into p equally spaced time intervals, Δt, with discrete time $k+i$ representing $t = i\Delta t$, $i = 0,1...p$.

Problem P3:

$$\min_{u_{k/k}, u_{k+1/k} \ldots, u_{k+m-1/k}} J_{NLMPC} = \sum_{j=k+1}^{k+p} \left\| y^c_{j/k} - d_k - y^{ref}_j \right\|^2_Q + \sum_{j=k}^{k+p} \left\| u_{j/k} - u^{ref}_j \right\|^2_R + \left\| \Delta u_{j/k} \right\|^2_S \quad (9)$$

subject to: $x_{j/k} = f(x_{j-1/k}, u_{j-1/k}, \theta)$, $j = k+1, \ldots, k+p$ (10)

$$y^c_{j/k} = g(x_{j/k}, \theta), \; j = k+1, \ldots, k+p \quad (11)$$

$$y^c_{\min} \le y^c_{j/k} \le y^c_{\max}, \; j = k+1, \ldots, k+p \quad (12)$$

$$u_{\min} \le u_{j/k} \le u_{\max}, \; j = k, \ldots, k+m-1 \quad (13)$$

$$\Delta u_{\min} \le \Delta u_{j/k} \le \Delta u_{\max}, \; j = k, \ldots, k+m-1 \quad (14)$$

$$u_{j/k} = u_{j-1/k}, \; j = k+m-1, \ldots, k+p-1 \quad (15)$$

where p is the predicted horizon, m is the control horizon, $u_{j/k}$ is the process input and $y^c_{j/k}$ is the controlled output variable at discrete time j calculated from information available up to discrete time, k. $\Delta u_{j/k} = u_{j/k} - u_{j-1/k}$, $j = k, \ldots k+m$, are present in the objective function to allow excessive input moves to be penalized and const rained if necessary, d_k is an estimate of unmeasured disturbance at time k, and is required in the control formulation to ensure offset free operation of the controller.

At each control interval, the entire *Problem P3* is solved but only the input $u_k = u_{k/k}$ is implemented. Q, R, S are the weighting matrices and θ is a vector of model parameters. The trajectories of target, y^{ref}, u^{ref} are obtained from the solution of an off-line dynamic optimization problem.

A very efficient solution technique for the problem (9)-(15) is based on the multiple shooting approach (Diehl, 2001; Franke and Arnold). This procedure consists of dividing up the time interval $t \in [t_0, t_f]$ into a series of grid points $[t_0, t_1, t_2, \ldots, t_f]$. Note that the grid points do not necessary correspond to the discretization points in the definition of problem *P*2. Using a local control parameterizations a shooting method is performed between successive grid points (see Figure 4). The differential equations and cost on these intervals are integrated independently during each optimization iteration, based on the current guess of the control. The continuity/consistency of the final state trajectory at the end of the optimization is enforced by adding consistency constraints to the nonlinear programming problem. A set of starting values for the state and adjoint vectors is required at each grid point in time, and continuity conditions for the solution trajectory introduce additional interior boundary conditions, which are incorporated into one large zero-finding problem to be solved. The solution of Problem *P2* is performed using an NMPC tool (Nagy *et al.*, 2004) based on the sequential-quadratic-programming (SQP) type optimizer HQP, which is used in conjunction with the implicit differential-algebraic-equation (DAE) solver, DASPK, for robust and fast solution of the model equations.

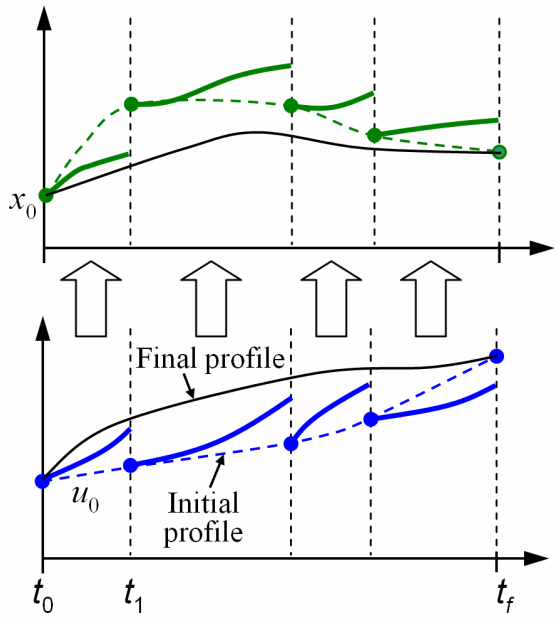

Figure 4. Ilustration of the multiple shooting approach.

4.3 Real-time NMPC algorithm

The solution of problem *P2* requires a certain, usually not negligible, amount of computation time d_k, while the system will evolve to a different state. In

this case the optimal feedback control $u^{\star}(t_k) = [u_{0|t_k}, u_{1|t_k}, \mathrm{K}, u_{N_p|t_k}]$ computed in moment t_k corresponding to the information available up to this moment, will no longer be optimal. Computational delay d_k has to be taken into consideration in real-time applications. In the approach used here, in moment t_k, first the control input from the second stage of the previous optimization problem $u_{1|t_{k-1}}$ (which corresponds to the first stage of the current optimization) is injected into the process, and then the solution of the current optimization problem is started, with fixed $u_{0|t_k} = u_{1|t_{k-1}}$. After completion, the optimization idles for the remaining period of $t \in (t_k + d_k, t_{k+1})$, and then at the beginning of the next stage, at moment $t_{k+1} = t_k + \Delta t$, $u_{1|t_k}$ is introduced into the process, and the algorithm is repeated. This approach requires real-time feasibility for the solution of each open-loop optimization problems ($d_k \leq \Delta t$).

4.4. MHE-NMPC of the FCCU

Simulation results of a combined NLMPC-MHE algorithm are shown in Figure 5 together with the open loop simulation in the case of 5% decrease in the coke formation factor. The controlled variables: the temperatures in the reactor and regenerator are shown in Figure 6, whereas the control inputs are the input flow rate in the reactor riser and the valve position on the regenerated catalyst pipe. In the simulation a sampling time of 2 minutes and a control horizon of one sampling time were used. The prediction horizon for the NMPC is 50 sampling periods, whereas the horizon of the MHE is 30 sampling instances in the past. It can be seen that the MHE is able to estimate unmeasured states and the model parameters very well. Although some of the states are not estimated they are kept within the boundaries of physical limits due to one of the major advantages of MHE, i.e., bounds on the estimated states can be incorporated in the optimization problem easily. The overall performance of the MHE-NMPC is very good; the temperatures are kept within a narrow band of variation compared to the open loop response of the process. It can be seen that the unknown model parameter is estimated with no offset in about one hour, and the disturbance is rejected in about two hours by the NMPC.

The CPU times corresponding to the MHE and NMPC calculations are presented in Figure 7. The dimension of the optimization for the NMPC is only two since a control horizon of only one sampling time, whereas the dimension of the optimization problems from the MHE is 19 (18 states plus one model parameter), leading to a significantly higher computational burden. Figure 6 demonstrates that the computational time scales only linearly with dimension of the optimization problem due to the efficient multiple shooting approach used, and the maximum total computational time (approximately 20*s*) is well bellow the sampling time (120*s*). The results demonstrate that efficient optimization algorithms can guarantee the real-time feasibility of the MHE-NMPC implementation even when a model with 2143 ODEs is used.

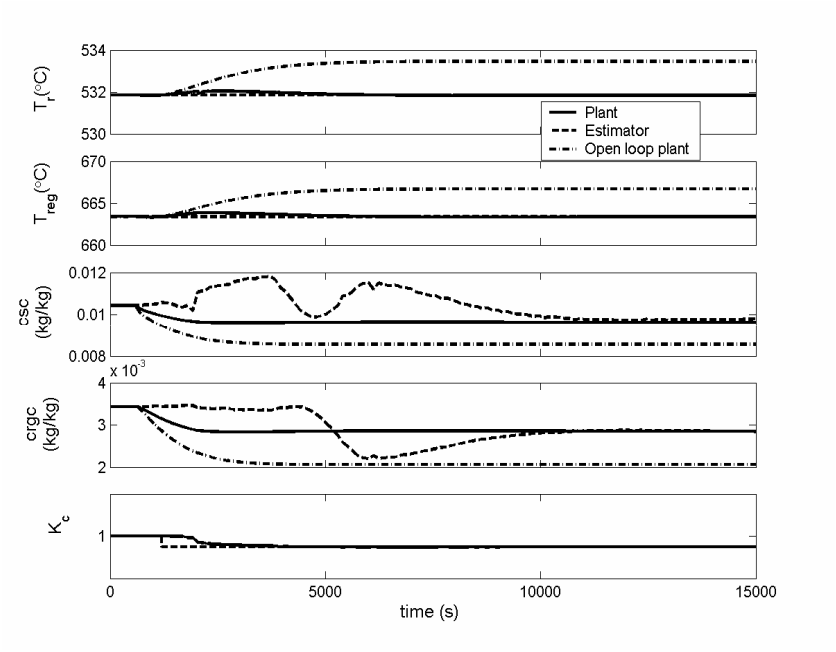

Figure 5. Simulation results of the MHE-NMPC of the FCCU

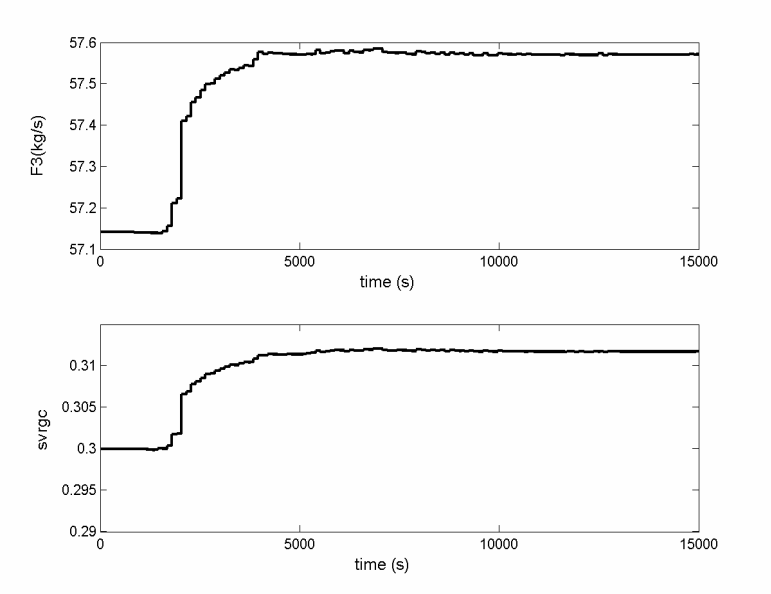

Figure 6. The controlled variables of the MHE-NMPC of the FCCU

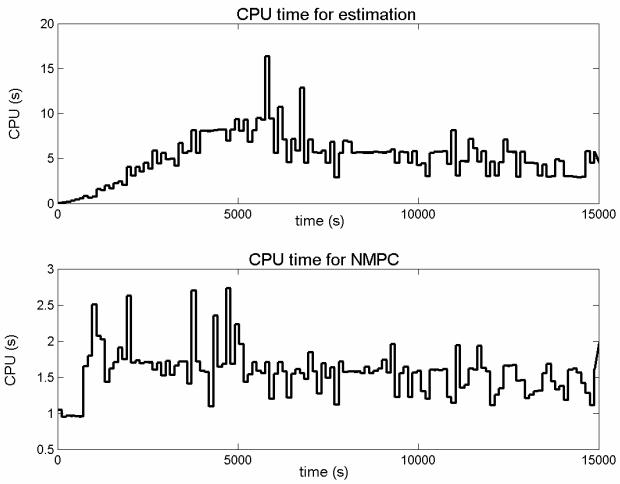

Figure 7. CPU times required for the optimization problems from the MHE and NMPC

5. CONCLUSIONS

The paper assesses the performance of a moving horizon estimation based nonlinear model predictive control approach in the case of a highly complex industrially relevant process the FCCU. The estimation of model states and parameters is critical to the success of model based process monitoring and control applications. Simulation results demonstrate that using state-of-the-art optimization algorithms and software advanced control and estimation strategies can implemented on complex industrially relevant problems.

Acknowledgements

This work was supported by the Marie Curie fellowship HPMT-CT-2001-00278.

REFERENCES

1. F. Allgoewer, T.A. Badgwell, J.S. Quin, J.B. Rawlings, S.J. Wright, 'Nonlinear predictive control and moving horizon estimation-An introductory overview', In P.M. Frank (editor), *Advances in Control*, 1999, 391-449.
2. Diehl M., 'Real-Time Optimization for Large Scale Nonlinear Processes', PhD Thesis, University of Heidelberg, 2001.
3. R.C McFarlane, R.C. Rieneman, J.F. Bartee and C. Georgakis, 'Dynamic simulator for a model IV Fluid Catalytic Cracking Unit', *Computers Chem. Engng*, 1993,*17*, 275-300.

4. X. Dupain, E. D. Gamas, R. Madon, C.P. Kelkar, M. Makkee, J.A. Moulijin, 'Aromatic gas oil cracking under realistic FCC conditions in a microriser reactor', *Fuel*, 2003,*82*, 1559-1668.
5. P. L. Russo, R. E. Young, 'Moving-Horizon State Estimation applied to an Industrial polymerization process', *Proceeding of the American Control Conference*, 1999.
6. R. Franke, E. Arnold, H. Linke, ,HQP: A solver for nonlinearly constrained large-scale optimization', http://hqp.sourceforge.net.
7. L.E. Haseltine, J.B. Rawlings, 'A critical evaluation of Extenden Kalman Filtering and Moving Horizon Estimation', Technical report, 2003.
8. Z.K.Nagy, F. Allgower, R. Franke, A. Frick and B. Mahn, ' Efficient tool for nonlinear model predictive control of batch processes', *Proc. of the 12th Mediterranean Conf. on Cont. and Aut. (MED'04)*, Kusadasi, Turkey,2004.

STUDIA UNIVERSITATIS BABEŞ-BOLYAI, CHEMIA, L, 2, 2005

TRAINING SYSTEM FOR DISTRIBUTED CONTROL SYSTEMS

CRISTIAN PĂTRĂŞCIOIU*

* *Petroleum – Gas University of Ploieşti*

ABSTRACT. This paper presents the efforts and achievements of members of the research center *Advanced chemical process control* from Petroleum-Gas University of Ploiesti, in the creation of a training laboratory for TDC3000 distributed control systems operation. It is presented the training system's structure, the training software DSS-100 produced by Simtronics Corporation and training hardware component developed by *Advanced chemical process control* research center. It is also presented the experience within the training program dedicated to operators from the S.C Petrom – Petrobrazi Subsidiary.

1. INTRODUCTION

The distributed control system represents a current tool in controlling chemical plants from modern refineries. In the last years, the distributed control systems were distinguished as leading technology in control system structures for chemical and petrochemical plants of Romanian refineries. After implementing these control systems, it took place a change in the structure of plants operating staff. Thereby, the operators that worked on instrument panel were transformed in distributed control system operators. If in the past a panel operator used to be responsible for a certain sector of the plant, usually of 20 control loops, in the present a distributed control system operator takes care of the entire plant. This radical change of operating tasks needed an advanced degree of knowledge, both in the construction and functioning of the distributed control system and in controlling the entire operating process.

In this context, one of the higher education tasks must be the creation of a flexible structure that enables the requalification of the operating personnel of chemical plants and assures an ongoing training. Till recently, there was not such a structure that enables in an organized and professionally manner, an ongoing training in the distributed control systems field.

The present paper presents the joint efforts of Petroleum - Gas University of Ploieşti, SC Petrom – Petrobrazi Subsidiary and SC Honeywell representatives in order to build up a training system in the distributed control system field.

2. THE TRAINING SYSTEM

The training system is composed of the following subsystems: a laboratory room dedicated to training and research, software simulators of some distributed control systems, devices for studying the real distributed control systems, as shown in Figure 1.

The laboratory room has a 45 m^2 area, being arranged at the current standard level in the computer aided training field. The lab has 6 training stations and a server

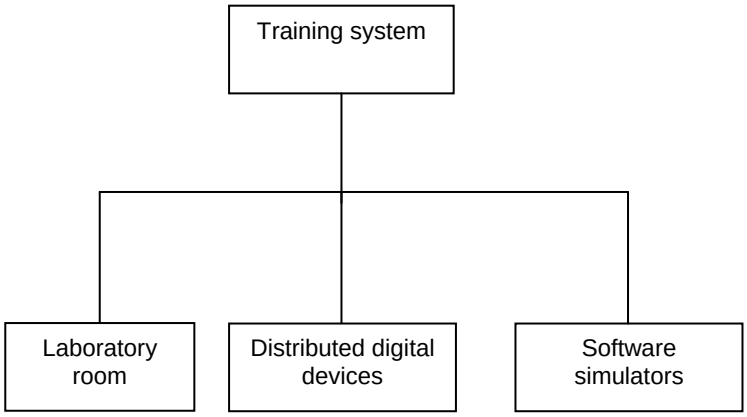

Figure 1. The training system structure.

dedicated to training and multimedia presentation of the courses, as shown in Figure 2. The numerical training devices are composed from a distributed control equipment HC900 (Honeywell), a server and a process control computer (ASTI). The software simulators are programs that simulate the distributed control with TDC3000 of some process units and chemical plants.

3. THE SOFTWARE SIMULATORS

The software simulators are dedicated to training the operating personnel, process engineers, foremen and operators from chemical plants. The training simulators are program systems that numerically simulate both the dynamic functioning of a process unit and the functioning of a certain distributed control device.

The simulated process units are: mixing fluids, heat exchangers, distillation column, air-blown cooler, tubular furnace, centrifugal compressor, overheating steam boiler, batch reactor, perfect stirring continuous reactor, and tubular reactor.

The simulated petrochemical plants have enhanced complexity and the available simulated plants are: fluidized catalytic cracking unit, atmospheric-vacuum distillation unit, gas processing unit, coker (delayed) gas desulphurizing unit.

The simulated distributed control systems available in the training program systems are: Honeywell TDC3000, Yokogawa Centrum, Fisher-Rosemount, Bailey, Foxboro, ABB.

In the training system framework from Petroleum - Gas University of Ploieşti were developed two software products specific to the distributed control system TDC3000*. The two simulators are provided by Star Simulation (2000 variant) and Simtronics Corporation (2005 variant).

The Simtronics Corporation product DSS-100 is a software tool dedicated to real-time simulation of dynamic processes. DSS-100 includes a series of algebraic

Figure 2. Image from training laboratory.

and differential equations that mathematically describe in dynamic regime the operating process or a control device. These differential equations are expressed related to time and are solved at regularly spaced time periods. At the end of each integration step, the numerical values and the graphical evolutions are updated, indicating the system state at a particular moment in time. DSS-100 is equipped with display and control system of industrial processes. The controls and displays presented by this software are typical for the TDC3000 used in industrial processes, Figure 3.

DSS-100 is composed by two software modules: System module and Process simulation module.

The system module has the following components:

– Various numerical displays and graphics that indicate the status of the particular simulated process that allow the user to interact with the process by changing various operating parameters. Using a database, these displays can be easily configured in the case of the simulated process.

– The graphical facilities allow the user to see the way in which any variable of the simulated process evolves in time. These displays are automatic and the sampling period is easy to tune.

– The simulation of typical elements such as on/off switches and PID controllers. The controllers are easy to tune for the simulated process.

– Programming tools and subroutines that allow various developments of process simulations.

– Post-simulation tools that allow the simulation analysis for process analysis or operator evaluation and certification.

The process simulation module consists in a mathematical model of a particular industrial process. These process simulations can be easily interchanged. A library for standard process simulation is available for base, medium and advanced training levels.

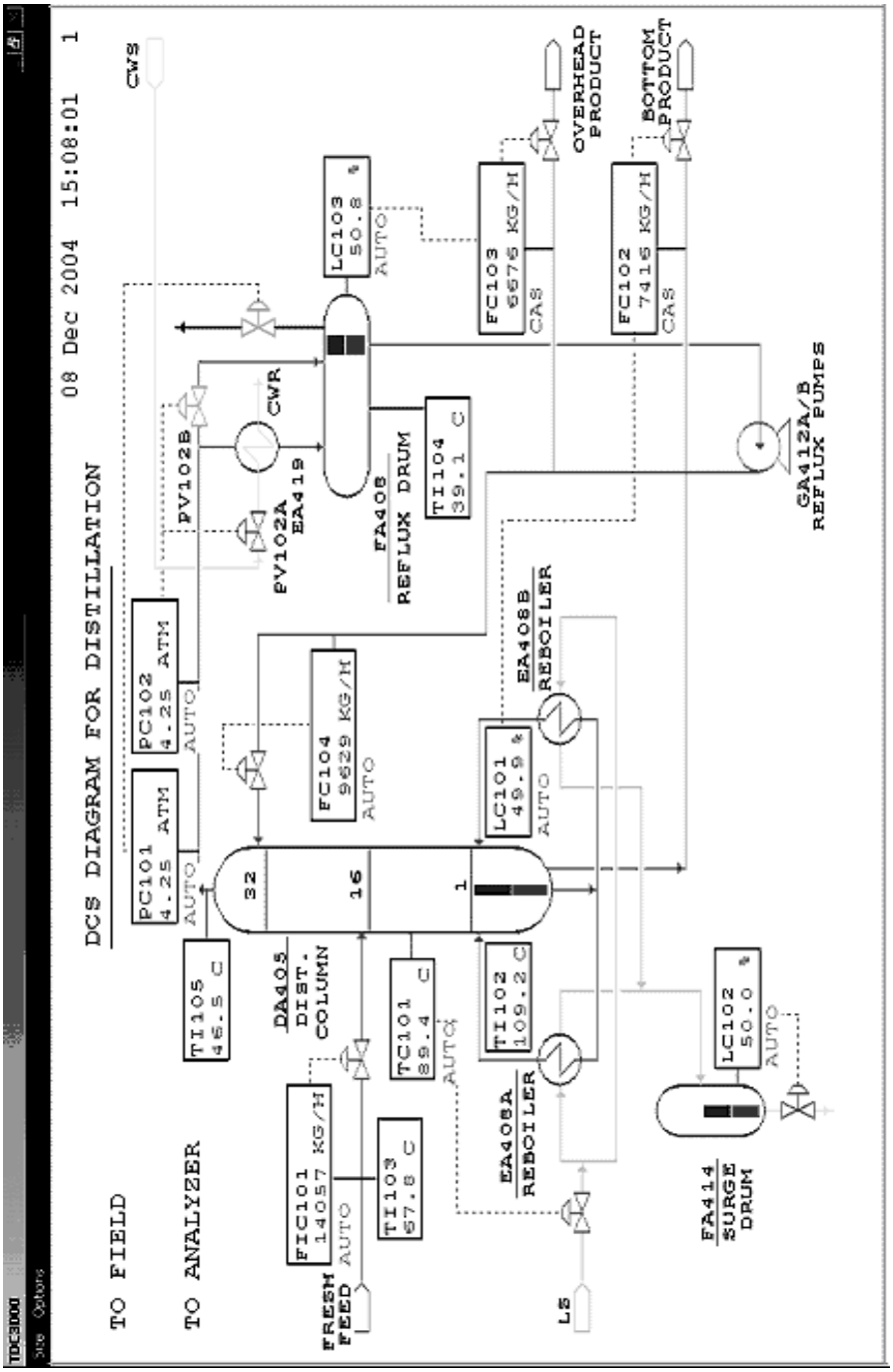

Figure 3. The training system for a distillation column

DSS-100 is composed of three modules: SPM-Series (Standard Process Models), PSU-100 (Performance Evaluation Software) and NSS-10 (Network Simulator System).

SPM is a Standard Process Module library, that contains the fundamental models of the processes such as tubular furnaces, pumping systems, intermediary models such as distillation, compressor, co-boiler and advanced model such as fixed bed reactor or perfect stirring reactor.

PSU-100 is a post-simulating tool that quantifies the performance of each trainee, for each process model and for each exercise corresponding to the desired standards. PSU-100 realizes a 0-100% evaluation by six performance criteria.

NSS-100 is the network system files administrator for network simulation. With NSS-100 a trainer can configure the exercises from a single station and can send those exercises to the other training stations. The trainer can find the results of the numerous training sessions and can interpret the results.

The software simulator also contains an industrial keyboard, which is a specific device of the emulated distributed control system. In the case of the distributed control system TDC3000 a personalized keyboard KBD-100 is used, which allows the replacement of the QWERTY keyboard with another one that resembles the main popular DCS operating interfaces. Using keyboard patterns, KBD-100 allows the training of the operators with an interface that resemble the real life control room without the necessary hardware costs for control room.

4. DIGITAL DISTRIBUTED EQUIPMENTS

The real distributed control system can be studied using small digital devices dedicated for this purpose. The real distributed control system is composed by a process computer, that simulates some technological processes, field lines of 4-20 mA, a minisystem of distributed control HC900 and a server, Figure 4.

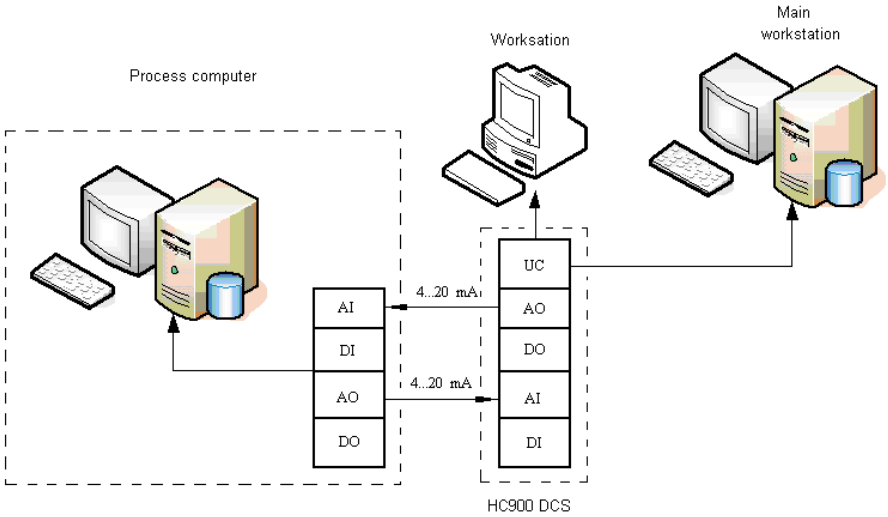

Figure 4. The distributed control system structure.

The process computer is equipped with analogical/digital input output interfaces and serial communication interfaces RS 485. The main features of these interfaces are presented in Table 1.

In the process computer there are simulated process units and more complex processes. The measurable variables of these processes are converted in 4-20 mA unified signals and sent as acquired measures to the distributed minisystem HC900.

Table 1

Interface	Input/Output signals	Number of channels
Analog Input	4-20 mA dc	16
Analog Output	4-20 mA dc	4
Digital input	24 V dc	16
Digital Output	24 V dc	16
RS-485	-	8

The commands to the controlled process, also 4-20 mA signals, generated by the distributed minisystem HC900, are acquired by process computer using analogical inputs interfaces.

The real control system is configured for the simulated process characteristics using the process computer. The ditributed control minisystem accomplishes the specific functions of a distributed control system: data acquisition, monitoring, database updating, control etc. The main features of the miniDCS are presented in Table 2. A picture of HC900 device is shown in figure 5.

Figure 5. HC900 distributed system (Honeywell).

Table 2

Module	Input/Output signals	Number of channels
Analog Input	4-20 mA dc	16
Analog Output	4-20 mA dc	4
Digital input	24 V dc	16
Digital Output	24 V dc	16

5. The training course

The training course lasts for a week and contains 40 hours of courses and applications. The courses are taught exclusively by didactic staff from Petroleum - Gas University of Ploieşti. The topics are:

1. Computer functioning and architecture.
2. Distributed control structure concepts.
3. Presenting the distributed system TDC3000.
4. The startup, normal operating procedures and shutdown of distillation process using TDC3000 emulator.
5. Classical and advanced control algorithms
6. Process control devices
7. Total Plant Solution system presentation
8. Control structures for distillation processes
9. Simulation programs of distillation process

The courses are oriented to the specific of the operating process or chemical plant. Until now there were realized training courses in the field of operating distillation processes with DCS, courses named *distillation module*. In the future the training will be extended to operating catalytic cracking unit and atmospheric-vacuum distillation unit with DCS.

The courses manuals are distributed to each trainee, at the beginning of the training. The actual size of these manuals is about 250 pages that include every training course. The number of trainees in a training group is 6, being limited by the training stations. Until now, the training course was granted for two series of operators, from SNP PETROM, Petrobrazi Subsidiary.

6. Performance criteria

There are 6 performance criteria in the postsimulation PSU-100 tool. In the following are presented the senses and significances of each criterion.

1. *The duration* measures the time needed to fill the exercises. A well trained operator must be able to quickly and efficiently solve the problems.
2. *The procedure* analyzes the event operator file in order to verify if the operator really followed the established operating procedures.
3. *The safety* measures the time interval while the operator has exceeded alarm limits and the magnitude of this deviation. In correcting this problem, remaining in safety parameters is of great importance.
4. *The alarms* calculate the final number of alarm when an exercise is finished. This is a measure of the operator ability to correctly solve the problem.

5. *The deviation* measures the time and magnitude of the deviation in operating from the design conditions. This is a measure of operator ability to maintain product quality in unfavorable conditions.

6. *The quality* measures the amplitude of the deviations from setpoints when an exercise is completed. This is a measure of final product quality.

7. Conclusions

The paper presents the efforts and achievements regarding the creation of a training laboratory for distributed control systems operation. The training system was materialized through creation of a laboratory, implementation of a program training system for TDC3000 distributed control system and also numerical equipment integration used for investigation of a distributed control minisystem. The training system was completed with training textbooks specific to the fractionating process and to the TDC3000 distributed control system. The members of the research center *Advanced chemical process control* from Petroleum-Gas University of Ploiesti have gained experience within the training program dedicated to operators from the S.C Petrom – Petrobrazi Subsidiary.

BIBLIOGRAPHY

1. * * * Training Simulators and e-Learning for the Process Industries, Simtronics Corporation, Little Silver, New York, 2004.
2. * * * Dynamic Process Training Simulator, Star Simulation, Houston, 2000.
3. * * * Sistem de instruire a personalului tehnolog in vederea operarii sistemelor de conducere distribuite, Universitatea Petrol-Gaze din Ploiesti, 2004.
4. * * * HC900 Hybrid Controller Documentation, Honeywell International Inc., 2002.

STUDIA UNIVERSITATIS BABEŞ-BOLYAI, CHEMIA, L, 2, 2005

GENERAL FRAMEWORK FOR MATLAB IMPLEMENTATION OF STATE-SPACE MODELING (SSM) APPROACH USED FOR THE INVESTIGATION OF THE REACTION MECHANISMS AT ELECTRODES

VALENTINA TASOTI, SERBAN AGACHI

"Babes-Bolyai" University, Faculty of Chemistry and Chemical Engineering,
11 Arrany Janos Street, Cluj-Napoca, Romania, tel: +40 (264) 593833,
email: vtasoti@chem.ubbcluj.ro, sagachi@chem.ubbcluj.ro

ABSTRACT. An approach focusing on the identification of the reaction mechanisms at electrochemical interfaces will be further described. It is based on state-space modeling (SSM) which is an approach used in control theory for the simulation of coupled differential equations. In this case, the state-space modeling approach consists of a combination of modeling, simulations, and experiments.

1. INTRODUCTION

The kinetics of the processes at the electrodes go trough is very important for a better understanding and also for an improvement of the performance of electrodes processes. We proposed the steady-space modeling approach for the identification of the reaction mechanisms at electrodes. This is based on the experimental results but also modeling and simulations, using the impedance spectroscopy technique, which is widely used in electrochemistry.

The method is based on transient numerical simulations of the elementary kinetics [1]. Imposing a harmonically varying overpotential leads to a periodic response of the system from which the impedance is obtained.

Impedance measurements used in electrochemistry must be performed at a system in steady state simulation. Normally, impedance measurements are performed under potential control with a steady state current. A small potential disturbance is applied and the current response is measured as it is schematically shown in figure 1. Every system subjected to a perturbation x(t) will determine a response y(t). The system can be described by the following differential equation:

$$a_0 x(t) + a_1 \frac{dx(t)}{dt} + a_2 \frac{d^2x}{dt^2} + ... = b_0 y(t) + b_1 \frac{dy(t)}{dt} + a_2 \frac{d^2y}{dt^2} + ... \qquad (1.1)$$

The impedance is only defined for a linear system i.e. a system with only first order response to the applied potential. However, the current response of a system is not linear as it can be seen in figure 1, which shows a part of the polarization curve. But if the applied disturbance is small the system can be approximated by a linear system.

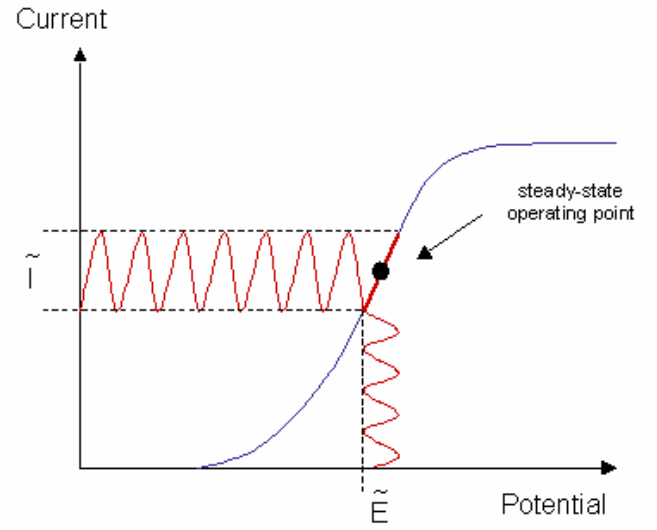

Figure 1. The application of a potential disturbance and its current response

The applied disturbance x(t) has a sine wave form: $x(t)=E_m\sin(\omega t)$ and the response $y(t)=I_m\sin(\omega t+\Phi)$, where *t* is the time, E_m and I_m the amplitudes, ω the angular frequency, Φ the phase difference between the voltage and the current.

The impedance, Z is then defined as:

$$Z(\omega)=\frac{\Delta E(\omega,t)}{\Delta j(\omega,t)}=\frac{E_m}{I_m}\cdot e^{i\Phi} \tag{1.2}$$

Using the Euler relation:

$$e^{i\Phi}=\cos\Phi+i\sin\Phi \tag{1.3}$$

the impedance becomes:

$$Z(\omega)=Z'(\omega)+iZ''(\omega) \tag{1.4}$$

where:

$$Z'(\omega)=\text{real}(Z)=|Z|\cos\Phi \tag{1.5}$$

$$Z''(\omega)=\text{imag}(Z)=|Z|\sin\Phi \tag{1.6}$$

$$|Z|=\frac{E_m}{I_m}=\sqrt{Z'+Z''} \tag{1.7}$$

$$\tan\Phi=\frac{Z''(\omega)}{Z'(\omega)} \tag{1.8}$$

The method represents a numerical experiment of impedance measurements using frequency response analysers. It allows the calculation of impedance spectra based on elementary electrochemistry without the necessity of applying equivalent circuit models [2,3]. By fitting simulated spectra to experimental data, kinetic parameters (exchange current density, reaction rate constant) are obtained directly.

2. CHARACTERISTIC PARAMETERS

Impedance spectra can be plotted in two ways: in the Nyquist representation where the negative imaginary part of the impedance, Z'', is plotted vs. the real part of the impedance, Z' (Fig.3) or in the Bode representation where the absolute impedance, |Z|, as well as the phase shift, Φ, are plotted vs. the angular frequency ω (Fig.2).

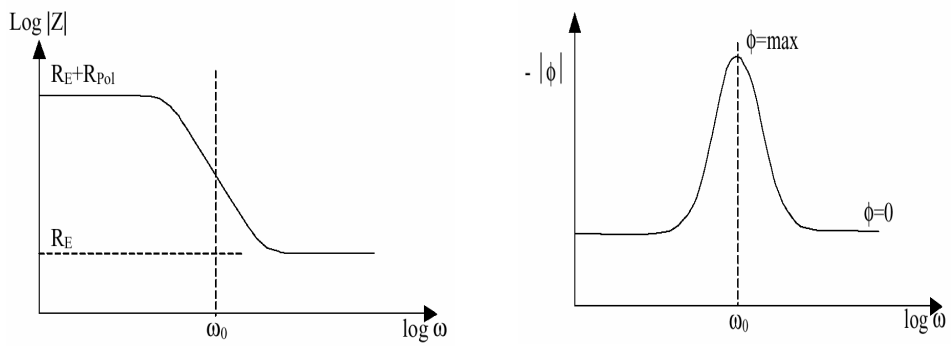

Figure 2: Bode plot

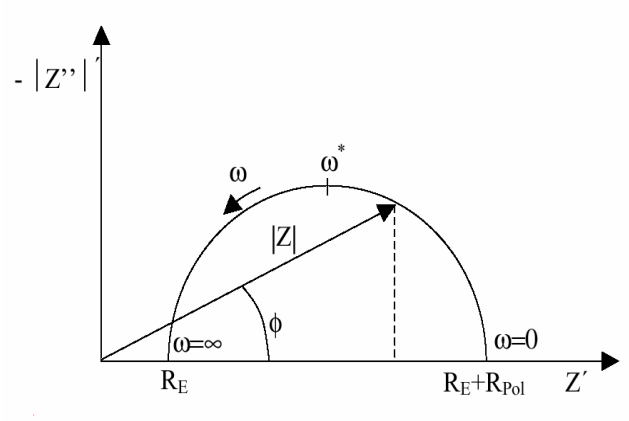

Figure 3. Nyquist plot

Both representations contain, in principle, the same information and can be transformed into each other. However, depending on the data, one or the other representation is preferred because specific details can be resolved more precisely. Hence, in impedance analyses, both representations must always be considered. The following characteristic parameters are obtained from the impedance data:

- the *polarization resistanc*e, R_{pol}, which is the purely ohmic part of the electrode resistance. It can be determined from both Nyquist as well as from Bode plot (Fig.2, Fig.3)
- the *electrolyte resistanc*e, R_e, which is caused by a certain contribution of the electrolyte. It can be determined from the high frequency part of Nyquist plot at the intersection of the impedance data with the real axis (Fig. 3).
- the *relaxation frequenc*y, ω*, which is defined as the frequency at the maximum imaginary impedance value. In the case of several relaxation processes, there are several relaxation frequencies, which can be identified as local maxima in the Nyquist plot [4,5,6]

3. MODELING

There are two different models possible for interpreting EIS measurements:

a. electrical equivalent circuit models - interpretation of the electrical models in terms of the fundamental physical or chemical parameters is often difficult [7,8]

b. elementary kinetic models - represents a more fundamental description of the involved physicochemical processes

For the identification of the reaction mechanisms at electrodes was used the state-space modeling approach that is based on a combination of experiments, modelling and simulations.

Data from surface science literature were used for the prediction of the main reaction steps that might take place at the electrochemically active interface. The electrochemical model consists of a set of possible chemical and electrochemical reactions that are derived from the relevant surface science literature.

The chemical and the electrochemical equations of the model can be formulated as mass and charge balances.

The kinetic constants of the chemical and electrochemical reactions will first be estimated for our particular model with the help of literature data and afterwards by an optimization procedure using an electrochemical impedance measurement under well-defined operating conditions.

The state-space model is believed to be the most reliable linear time-dependent model to use for computer analysis [9,10]. The general state-space representation is: $\dot{x}(t,p) = \frac{dx(t,p)}{dt} = f[x(t,p),u(t),t,p]$ where x(t,p) represents the vector of the state-variables depending on the time t, and the vector of unknown parameters, p. The vector u(t) signifies the input variables that can be varied in the experiments and in the simulations.

In addition to the differential equations, the state-space description contains the observation function y(t,p), which denotes the observed quantities and is referred to as the model output. $y(t,p) = g[x(t,p),p]$

The variables in the general state-space model can be directly interpreted in terms of the kinetic variables used in the electrochemical model. The vector of state-variables, x(t,p), represents the surface concentrations of the different adsorbed species. The concentration of the adsorbed species is a function of the time, t, and the vector of unknown parameters, p, i.e. the reaction rate constants and the surface coverage values. The vector u(t) signifies the overpotential, η ,and the model output, y(t,p), can be interpreted as the Faraday current, I_F .

The simulation algorithm is the following: in a first step, the electrochemical model is linearized. Afterwards, a Laplace transformation is used in order to transfer the system into the frequency domain. Third step-the impedance is calculated.

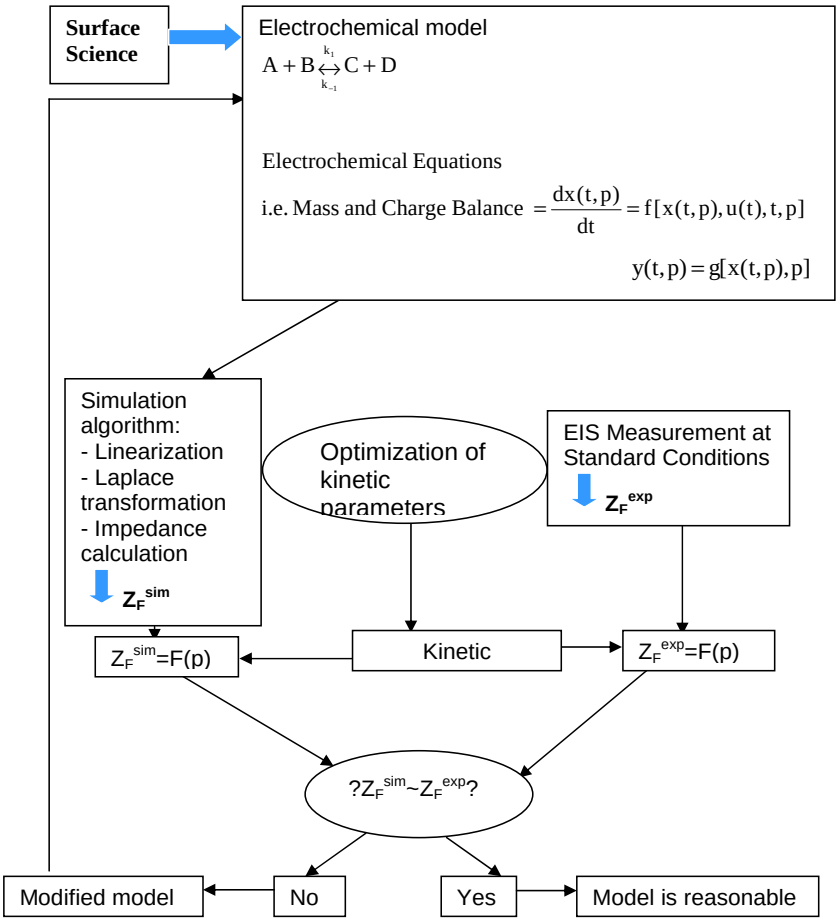

Figure 4. State-Space Modeling (SSM) approach for the investigation of the reaction mechanisms at electrodes

An electrochemical impedance spectrum will then be simulated directly from the electrochemical model [11]. The model spectrum as well as simulations under varying parameters will be compared to experimental data under the same conditions in order to prove the validity of the chosen model.

The electrochemical model consists of a set of possible chemical and electrochemical reactions that are derived from the relevant surface science literature. These reactions are of the following form:

$$A + B \underset{k_{-1}}{\overset{k_1}{\rightleftharpoons}} C + D \tag{3.1}$$

where *A*, *B*, *C*, and *D* are gas phase species, surface species, adsorption sites, or electrons; k_1 and k_{-1} are the reaction rate constants for the forward and the backward reaction, respectively. In order to establish an electrochemical model, which describes the entire system, several assumptions have to be taken into consideration.

For instance, the number and the kind of surface species, their diffusion and their reaction behavior have to be estimated. As many of the kinetic constants are not known from the literature, it is necessary to estimate the unknown kinetic constants.

The chemical and the electrochemical equations of the electrochemical model can be formulated as mass and charge balance.

The mass balance concerning the time-dependent surface species *C* in eq. 3.1 is given as:

$$\dot{[C]} = \frac{d[C]}{dt} = k_1[A][B] - k_{-1}[C][D] \tag{3.2}$$

In the case of several parallel and consecutive reactions as well as several surface species, a whole system of coupled differential equations results. The system becomes very complex and cannot be solved analytically anymore. For a numerical solution, the electrochemical model must be written in a form that can be used for computer analysis.

4. SIMULATIONS

Having established an electrochemical model for the system, it is now required to implement the system into the computer. An impedance spectrum, $Z_{F\,sim}$, can then be simulated and can be compared to the experimental EIS data, $Z_{F\,exp}$. The simulations are carried out using the computer program MATLAB® with the graphical programming extension SIMULINK that is used in control theory for simulations of dynamic systems [12,13,14,15].

SIMULINK is designed as a unit construction system. The mathematical equations are built from construction blocks given in the program. An illustrative example is shown in Fig. 5. There the computer implementation for the calculation of the surface concentration *C* according to Eq. 3.2 is illustrated. The concentrations *A*, *B*, and *D* are assumed to be constant and are illustrated as boxes in Fig. 5. The triangles containing k_1 and k_{-1} represent multiplications, whereas the program element 1/s stands for the integration of a Laplace transformed variable.

The output is shown in the display box and represents, in this example, the concentration of the surface species *C*.

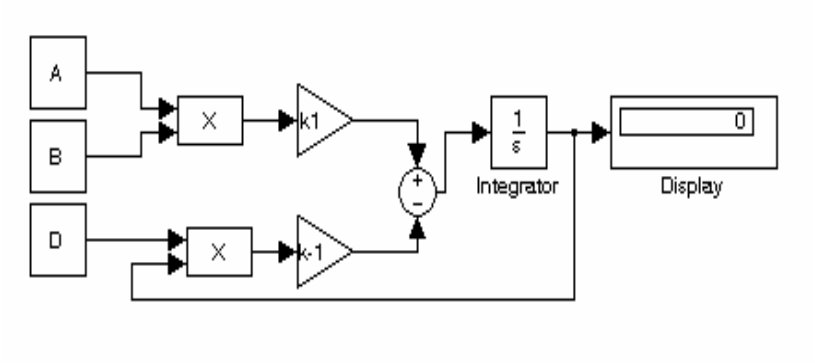

Figure 5. Simulink block diagram

5. CONCLUSIONS

The concept of the present study was presented by investigating the reaction mechanism.

An electrochemical impedance spectrum will then be simulated directly from the electrochemical model. The model spectrum as well as simulations under varying parameters will be compared to experimental data under the same conditions in order to prove the validity of the chosen model.

Steady-space modeling approach and implementation of this in Matlab that we proposed, make easier the work of solving a set of equations, permits determination of the kinetic parameters and could give us a explanation of the chemical processes that are happening to the electrode. The electrical equivalent circuit models for a complex process could not do this explanation so why this approach is recommended.

State-space models can accommodate any degree of complexity, the need for testing the structural proprieties demands rather than simple equations. A case study using SSM approach will be presented in the next article as application at this general framework paper.

REFERENCES

1. MacDonald - Impedance spectroscopy. Emphasizing solid materials and systems, John Wiley&Sons, New York, 1987
2. J. R. Scully, D. C. Silverman, M. W. Kendig - Electrochemical Impedance: analysis and interpretation, ASTM, Philadelphia, 1993
3. K. Darowicki, P. Slepski - Dynamic electrochemical impedance spectroscopy of the first order electrode reaction, Journal of Electroanalytical Chemistry 547, 1-8, 2003

4. M.Bojinov, G.Fabricius, T. Laitinen, K. Makela, T. Saario, G. Sundholm -Coulpling between ionic defect structure and electronic conduction in passive films on iron, chromium and iron-chromium alloys, Electrochimica Acta 45, 2029-2048, 2000
5. R. Antano-Lopez, M.Keddam, H. Takenouti - A new experimental approach to the time-constants of electrochemical impedance: frequency response of the double layer capacitance, Electrochimica Acta 46, 3611-3617, 2001
6. M.Bojinov, T.Laitinen, K.Makela, T. Saario - Conduction Mechanism of the passive film on iron based on contact electric impedance and resistance measurements, The Journal of the Electrochemical Society, 148(6), B234-B250, 2001
7. N.T.C. Oliveira, S.R. Biaggio, S. Piazza, C.Sunseri, F. Di Quatro - Photo-electrochemical and impedance investigations of passive layers grown anodically on titanium alloys, Electrochimica Acta 49, 4563-4576, 2004
8. M. Metikos-Hukovic, Z. Grubac - The growth kinetics of thin anodic WO_3 films investigated by electrochemical impedance spectroscopy, Journal of Electroanalytical Chemistry 556, 167-178, 2003
9. T. Kailath, Linear systems, Prentice-Hall, New York, NY, USA, 1980
10. G. F. Franklin, J. D. Powell, A. E. Naeini, Feedback Control of Dynamic Systems, Addison - Wesley, Reading, MA, USA, 1994
11. P. H. Rieger-Electrochemistry, Prentice-Hall, Inc., 128-134, 1987
12. ***, MATLAB Users Guide, The MathWorks Inc, 1999
13. Ghinea M., Fireteanu V., MATLAB - Calcul numeric ~ Grafică ~ Aplicații, Ed. Teora, 1997
14. ***, SIMULINK, Dynamic System Simulation for MATLAB - Using Simulink, MathWorks Inc., chapter 3 - 5, 1999
15. D.J. Higham, N.J. Higham - Matlab Guide, SIAM, 2005

STUDIA UNIVERSITATIS BABEŞ-BOLYAI, CHEMIA, L, 2, 2005

MONITORING SYSTEM WITH WIRELESS COMPONENTS FOR AIR POLLUTION GENERATED BY INDUSTRIAL PLANTS

Ş.P. AGACHI[*], I. STOIAN[**], E. STÂNCEL[**], M. CRISTEA[*], S. DRĂGAN[*], O. GHIRAN[**], D. CĂPĂŢÂNĂ[**], A. IMRE[*], A. GHIRIŞAN[*], ŞT. HEGHEDUŞ[**], C. POSTEUCĂ

[*] *Department of Chemical Engineering, Faculty of Chemistry and Chemical Engineering, Univ. Babeş-Bolyai Cluj-Napoca*

[**] *S.C. IPA S.A. Bucharest, Research, development and technological ransfer center (CIFATT) Cluj-Napoca,*

Developed under *The National Research and Development Program in Informatics* (**PNCDI**) – **INFOSOC** Program (*INFOrmational SOCiety*)

ABSTRACT. This paper presents *WIPOL*, a monitoring system for air pollution generated by industrial plants with wireless components. The system is developed to supervise the air pollution generated by industrial plants, especially dust. Two industrial plants are monitored using a hierarchical system of sensors and computers including wireless components.

1. INTRODUCTION

In nowadays the environment protection is one of the most important problems. The pollution of the air with dust, particles, smoke and vapor gas is a complex problem due to the variety of the pollutants from industry, agriculture, transport, and energy production.

The environment quality at a specific moment depends on the quality of the air, water and soil, the health of the population and deficit of the plants and animals species in the analyzed area. All of these factors are expressed by some indicators of the quality with specifically limits [1]. For example, the natural, unpolluted air has the next composition: 78 % N_2, 21 % O_2, 0.03 % CO, 0.93 % Ar and 0.04 % CH_4.

The main pollutants for the air are: CO, $(SO)_x$, $(NO)_x$, H_2S and dust. The air quality management of the air could be solved by: determination of the distribution of the pollutants and by determination of the correlation between the quality of the air and the distribution of the pollutants.

The estimation of the pollution produced by a chemical plant or equipment (apparatus) represents a requirement in the design step of the plant (ISO norms, ISO 14000 in EU area). Beginning December 1995 in Romania it is applied a new law for the environment protection (Law 137/1995). The disposal 184/1997 contains the means and procedures to carry out the balance of the pollutants. The disposal 756/1997 contains the rules for the estimation of the pollution of the water, air and soil. HG. 34/2002 contains the rules to prevent, reduce and control the pollution and the limitation of the CO, SO_x, NO_x, dust in suspension (PM_{10}) and ($PM_{2,5}$), Pb, benzene and O_3 in the environment.

2. CHARACTERIZATION OF THE INDUSTRIAL POLLUTANTS

The **WIPOL** monitoring system was developed to trace the pollutants from two main industrial sites: **S.C. CASIROM S.A. Turda** and **S.C. SOMEŞUL S.A. Dej** companies.

S.C. CASIROM S.A. Turda is the only plant in our country, which produces refractory products necessary in the metallurgical, glass and coke industry. From 1985 the plant **S.C. CASIROM S.A. Turda** produces abrasive materials too.

The pollutants from **S.C. CASIROM S.A. Turda** are from the department of refractory products and from the department of CSi.

– ***dust*** from technological process: grinding and milling of the quartz, sand and lime, transport of the row materials, sorting out of materials on the vibrator sieves, drying of the refractory products;

– ***gases*** from the combustion in the furnace Mendheim as *CO, NO_x, SO_2;*

– ***volatile organic compounds*** *(VOC)* from the chemical reaction.

The dust is formed from particles, 70 % from this particle have the diameter between 0.5–2 mm. This means that the particles will settle in the near proximity of the department (inside the plant).

The gaseous products are: SO_2 – in the process of CSi production due to the presence of the S (0.6–6 %) in coke (2 g/m^3), and SO_x, NO_x, CO, NO_x, and VOC from oxidation, combustion and reaction.

The evacuation of the pollutants could be made in two different ways: a) systematically through pipes and ventilation outlets in known and controlled concentrations and flows; b) unsystematically through orifices and areas with unknown flows and concentrations.

At **S.C. CASIROM S.A. Turda** the evacuation of the gases from the combustion is made through the dust funnel (with H = 10 m and D = 0.9 m), with a flow of 150 m^3/h.

The balance of the pollutants in this area shows that the environment is very strongly affected. The monitoring of the pollutants and the application of the control for preventing the pollution is a necessity in this area.

S.C. SOMEŞUL S.A. Dej is a cellulose and paper plant. In the paper and cellulose preparation at **S.C. SOMEŞUL S.A. Dej** the main pollutants are: dust with particles and smoke and gas pollutants (CO, CO_2, NO_x, C, H_2S, Cl, and ClO_2) from the spinning of the wood, from the combustion and from the fabrication of the cellulose.

3. MEASUREMENT PRINCIPLES FOR FLOW RATE COMPUTATION

The methods to determine the concentration limits of the pollutants (dust, particles, smoke or/and vapor gases) in the outlet flow of the industrial plants, applied at the present in Romania, are regulated by the disposal 462/1993.

In agreement with this disposal, the measurement principle consists in the iso-kinetic sampling of a representative outlet flow. The measurement has to be made in the outlet flow having a homogenous concentration and with the highest concentration of the pollutants. The duration and the place of the measurement are variable. The norms of the environmental pollution suggest at least 3 individual measurements.

The outlet flow to be measured must be collected without perturbations. This means that it is necessary to have a linear length equivalent to 3–5 hydraulic diameters d_e in the upstream of the measurement point, where the hydraulic diameters d_e is formulated as:

$$d_e = \frac{4 \cdot A}{P_u}$$

The total flow rate will be calculated as a function of the flow, temperature and pressure [2]. The local velocity of the outlet flow determined with a Pitot-Prandl device is:

$$v = \sqrt{\frac{2 \cdot \Delta P}{\rho}}$$

The average velocity is calculated using the following equation:

$$\bar{v} = \frac{\sum_{i=1}^{n} v_i}{n}$$

The volumetric flow V (m^3/s) is defined as: $V = \bar{v} \cdot A$

Other possibilities to measure the flow are the orifice plates coupled with differential pressure manometers. With the orifice plate the flow can be calculated with the equation:

$V = K \cdot \sqrt{\frac{2 \cdot \Delta P}{\rho}}$, where K is the flow coefficient.

The outlet concentration of the pollutant can be determined using direct methods with special reactants or Dragger pump.

For the dust analysis a device with outside filter can be used. The diameter (cm) of the analyzer pipe is:

$$d = 3{,}6 \sqrt{\frac{4 \cdot V_{(t_0 + t_{efluent})}}{\pi \cdot v_{\max(p_0 + p_s in \sec.)}}}$$

The measurement device must be mounted in vertical position.

4. SENSORS

For the present application a specialized in-situ, continuous emission-measuring device performs the dust concentration detection.

The measuring instrumentation is based on the principle of scattering light in the forward direction, as shown in figure 1.

The Laser Diode sends a collimated and modulated light beam that is scattered by the dust particles present in the measuring zone. The scattered light is collected and then sent to a receiver diode by means of an optical fiber. An electronic circuit processes the received light beam and transforms it in an electrical signal. In order to provide independence on the disturbances, two light beams are used:

one for reference and one for measuring. The device is designed such as the velocity and electrical charge of the dust particles do not affect the measuring signal. The measuring device may be programmed via its interactive control display or with a PC via bus interface. The installation is executed on the exhaust channel using a single mounting flange. Gravimetric calibration for dust concentration in mg/l is performed at commissioning [3]. The measuring signal is sent, as an analog output current signal, to the wireless module for remote transfer.

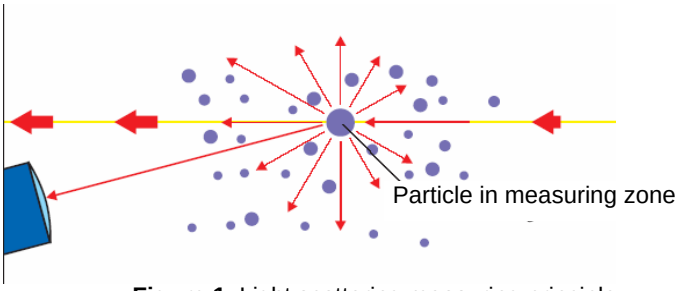

Figure 1. Light scattering measuring principle.

The measuring system may be extended, on request, with a multi component monitoring system for different gas components: NO_x, CO, CO_2 and SO_2. The measuring principle is based on the infrared absorption in the λ=2.5-8 μm wavelength range. The photometer may measure from 1 to 4 components with 1 or 2 beam paths and 1 or 2 receivers in each beam path. The measurement system includes the following parts: analyzer with the central unit, gas sampling unit and sample conditioning unit. The sample conditioning unit incorporates: heated sampling lines, filters, gas pump, gas cooler, condense separator, flow monitor, electric actuated calibration gas valves and calibration gas vessels, all enclosed in a special designed cabinet. Analog output current signals are generated for each of the measured components.

5. DISPERSION SIMULATION

The software module for simulation of the dispersion is based on a Gaussian dispersion based model named SLAB. This computer model was developed by the Lawrence Livermore National Laboratory (USA) in the mid ‘80s and it’s used to model the atmospheric dispersion of denser than air releases. Based on the description of the model presented in the literature [4, 5] a simulation module was developed. This module allows real time prediction, based on meteorological data (the direction and speed of the wind, external temperature, the presence and the rate of precipitations, the degree of cloud coverage) and data about the effluent (rate and temperature of gases that emerge from the source, concentrations in pollutant – gases or dust) by taking into account the shape and height of the source, the concentration gradient at the ground level in the area of the source. These concentration curves allow the prediction of the effects of pollution on humans and also to prevent them in the case of pollutant concentration exceeding the allowed limits. In figure 2 is presented a 3D representation of NO_2 concentration in the vicinity of a source.

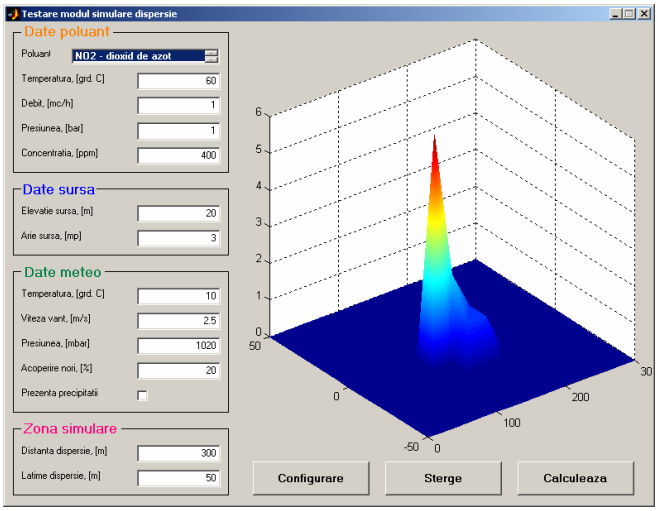

Figure 2. A 3D representation of NO_2 concentration based on the prediction module.

6. GENERAL PRESENTATION OF THE SOFTWARE

The developed software product is referred as a distributed remote measurement system dedicated for monitoring the pollutant emissions from industrial plants using the resources of a programmable automaton, data concentrator computers, data transmitting equipments with specific transducers and wireless communication techniques. The monitoring system has a distributed architecture that includes:

- **Local level** is the level used to communicate and interface with transducers and sensors for pollutant emissions by an acquisition station with programmable automaton. The local stations communicate at this level with a data concentrator computer. In these two units the following functions are implemented:
  - acquisition and concentration of data;
  - modeling of pollutant dispersion;
  - transmission of data to the higher level;
- **Central level** is an automated system for data surveillance and data processing located in the dispatcher unit where the information is received from the local level. At this level event reports and environment balances are synthesized for the monitored locations. In emergency situations the simulation of pollutant dispersion is made and the obtained results are compared with the measured ones. The dispersion simulation takes into account the current local meteorological data.

The coupling between these two functional levels is performed in real time using a dedicated telephone line with high speed modem data transmission equipment.

The monitoring system allows configuring the data acquisition station for larger variety of pollutants and extending the number of data acquisition channels. The systems are extensible also from the hardware or software point of view, allowing additional measurement devices to be easily integrated in the architecture of the system.

7. THE ARCHITECTURE OF THE WIPOL SYSTEM

The software products developed in the frame of this project has the aim to oversee potential industrial air pollutants.

The application includes a series of executable modules that communicate each other in order to achieve the goal of the project.

The architecture selected for this project is based on client-server architecture (figure 3).

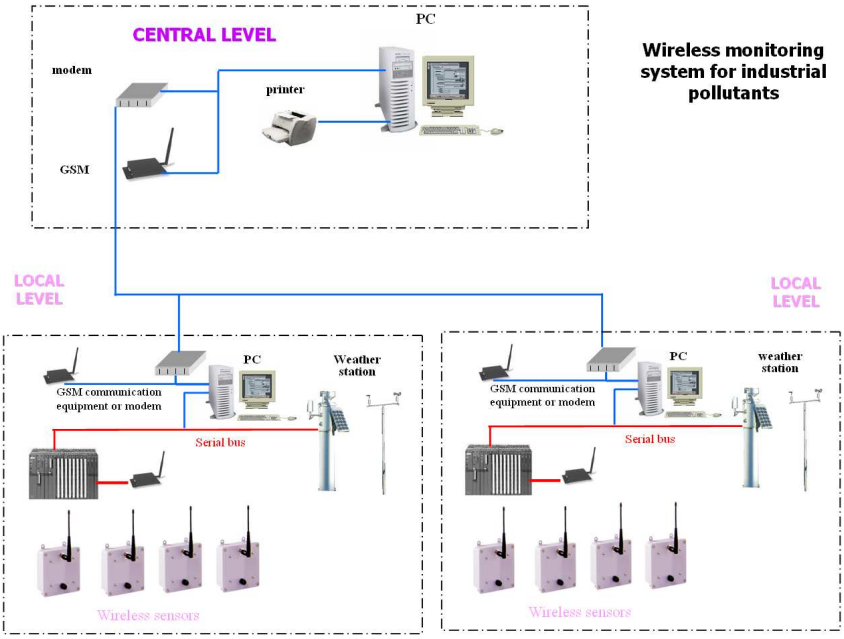

Figure 3. The architecture of the **WIPOL** system.

8. THE WIPOL SOFTWARE APPLICATION

The software application is resident on the computers situated on both hierarchical levels of the tele-assistence system. The **WIPOL** system includes the following executable programs:

- achizsenz – program for data acquisition from sensors – runs on the level of programmable automaton and performs the acquisition of data in engineering units using a configuration table for each sensor attached to it.
- Local dispatcher program consists of two modules:
  i. Module for sensors supervision - supravsenz - for data acquisition from the programmable automaton; the data are introduced into the database and the evolution of these parameters are represented under numerical or graphical form on the operator console;
  ii. Local dispatcher program - displocal - for primary data processing, generates acquisition reports and graphical representations of data, events report and dispersion maps for the monitored pollutants.

- Central dispatcher program which includes:

i. supravagent - program for supervision of the potentially polluted industrial plant by using a telephone line connection with the economic agent, at preset time intervals or in the case of alarm, uploading the data on the central dispatcher computer for further processing;

ii. central dispatcher program - dispcentral - for processing the acquired data, conditioning the acquisition reports, graphics with the evolution of the parameters, events report and dispersion maps for the monitored pollutants.

The description of the local level programs

The functions of the supervision program at the local dispatcher level are implemented in the application program having two main components:

- application manager - program package at the local dispatcher computer level (figure 4);
- specific program for communication between the local dispatcher computer and the programmable automaton or a wireless RTU (including data packing for transmission, scaling and communication drivers).

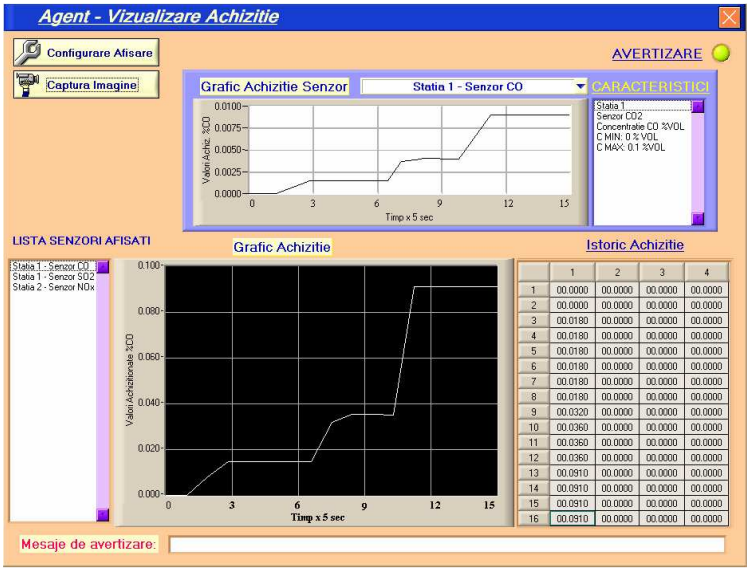

Figure 4. Screen shoot of the manager application at the local dispatcher level.

The program on the local dispatcher level is developed on the principle of virtual instrumentation under the LabWindows CVI (National Instruments) programming environment using the database, statistics and network connectivity components (Enterprise Connectivity Tools) and includes the following functions:

- monitoring of the sensors and transducers network distributed in the location of polluting plants; the monitoring takes place consulting each sensors configuration table and using preset sampling times;

- graphical or tabular acquisition of monitored and calculated parameters; transformation of acquired data in physical units (concentrations, flow rates etc.) according to the associated calibration charts;
- generation of the event reports, recording the moment of time when the event appears and the source of the event;
- application and measurement channels configuration, measurement domain limits setup for sensors and transducers;
- assuring only authorized access to critical operations by a hierarchical system of passwords;
- supervision of alarm limits, the state of the communication with the programmable automaton, the operations made by the exploit personnel determining the alert of the operator by:

i. acoustic signal – by voice – using the multimedia component of the system;
ii. visual signal – using overlapping windows techniques that block any other access of the operator until the confirmation of the pop-up message window.

The data transfer to the central level

The transfer is made by modem using a dedicated line introducing the appropriate telephone number in the Connection phone number labeled textbox, with visual indication of the connection status with the central dispatcher computer. The program transfers the files using a modem based communication protocol with data correction algorithm, thus eliminating the transfer errors (figure 5).

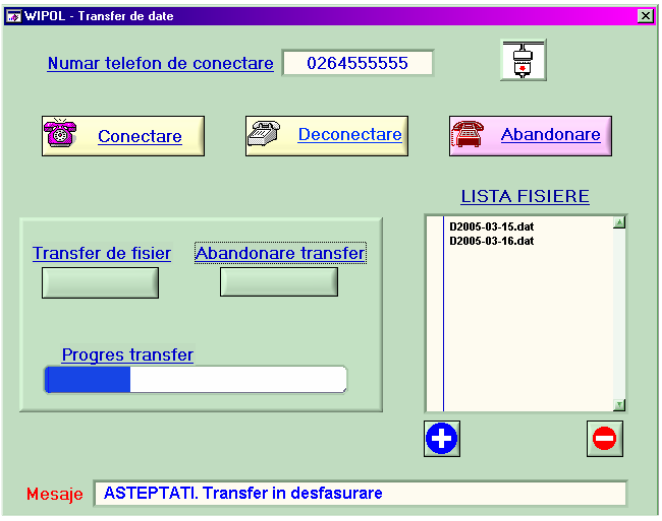

Figure 5. The Data transfer window at the central dispatcher computer.

The functional description of the central level program

In the established geographical area, the local monitoring points are located in the vicinity or on the platform of the potential pollutant industrial plant.

The monitoring equipments, located in the local centre, communicate in real time with the local dispatcher computer (figure 6).

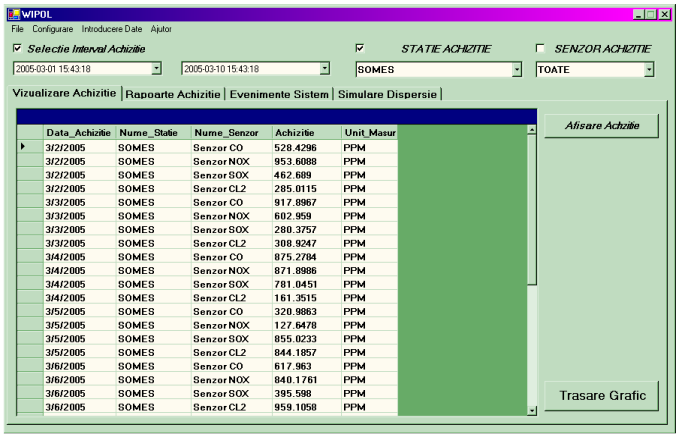

Data_Achizitie	Nume_Statie	Nume_Senzor	Achizitie	Unit_Masur
3/2/2005	SOMES	Senzor CO	528.4296	PPM
3/2/2005	SOMES	Senzor NOX	953.6088	PPM
3/2/2005	SOMES	Senzor SOX	462.689	PPM
3/2/2005	SOMES	Senzor CL2	285.0115	PPM
3/3/2005	SOMES	Senzor CO	917.8967	PPM
3/3/2005	SOMES	Senzor NOX	602.959	PPM
3/3/2005	SOMES	Senzor SOX	280.3757	PPM
3/3/2005	SOMES	Senzor CL2	308.9247	PPM
3/4/2005	SOMES	Senzor CO	875.2784	PPM
3/4/2005	SOMES	Senzor NOX	871.8986	PPM
3/4/2005	SOMES	Senzor SOX	781.0451	PPM
3/4/2005	SOMES	Senzor CL2	161.3515	PPM
3/5/2005	SOMES	Senzor CO	320.9863	PPM
3/5/2005	SOMES	Senzor NOX	127.6478	PPM
3/5/2005	SOMES	Senzor SOX	855.0233	PPM
3/5/2005	SOMES	Senzor CL2	844.1857	PPM
3/6/2005	SOMES	Senzor CO	617.963	PPM
3/6/2005	SOMES	Senzor NOX	840.1761	PPM
3/6/2005	SOMES	Senzor SOX	395.598	PPM
3/6/2005	SOMES	Senzor CL2	959.1058	PPM

Figure 6. Central dispatcher.

The functions of the central level monitoring system are:

- Monitoring of the locally distributed measurement points of the network by uploading the data to the local dispatcher stations at user preset sampling time;
- Generation of the measurement databases by including the acquired measurement data of the local dispatcher stations;
- Generation of graphical representations showing the pollutant concentration and the affected geographical area using the data from measurements and from simulations that are based on the dispersion models and measured meteorological data;
- Presentation in graphical or tabular forms of the acquired and calculated data (figure 7);

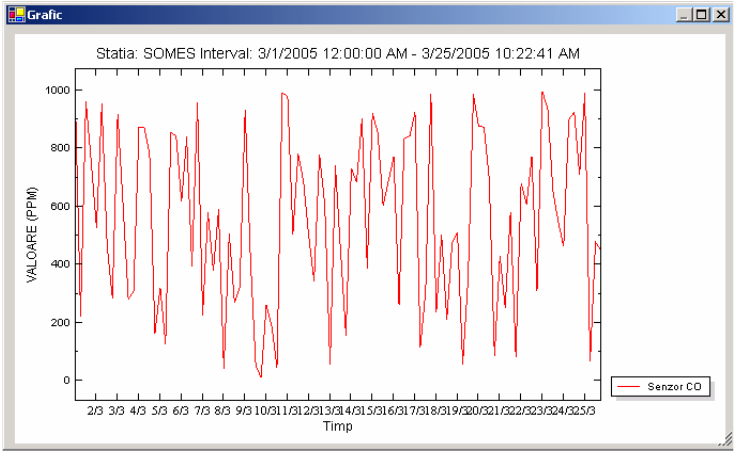

Figure 7. The graphical representation of the CO sensor at the central dispatcher.

- Generation of event and alarm reports, including the moment of time, source and value of the parameters that triggered the event;

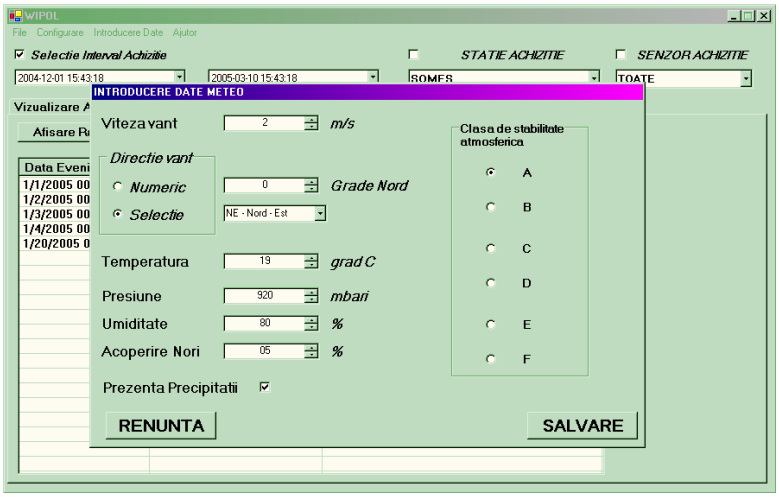

Figure 8. Meteorological data.

- Application configuration, local monitoring station configuration, establishing the risk limits and propagation distances for monitored data taking into account the real meteorological conditions;

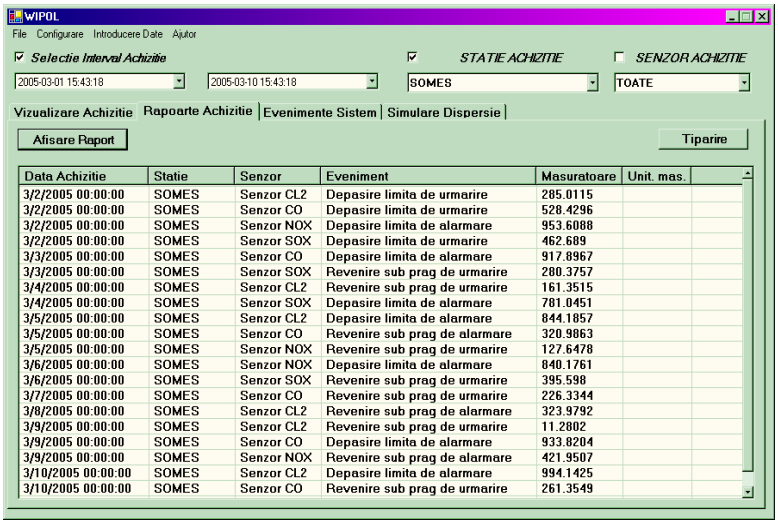

Data Achizitie	Statie	Senzor	Eveniment	Masuratoare	Unit. mas.
3/2/2005 00:00:00	SOMES	Senzor CL2	Depasire limita de urmarire	285.0115	
3/2/2005 00:00:00	SOMES	Senzor CO	Depasire limita de urmarire	528.4296	
3/2/2005 00:00:00	SOMES	Senzor NOX	Depasire limita de alarmare	953.6088	
3/2/2005 00:00:00	SOMES	Senzor SOX	Depasire limita de urmarire	462.689	
3/3/2005 00:00:00	SOMES	Senzor CO	Depasire limita de alarmare	917.8967	
3/3/2005 00:00:00	SOMES	Senzor SOX	Revenire sub prag de urmarire	280.3757	
3/4/2005 00:00:00	SOMES	Senzor CL2	Revenire sub prag de urmarire	161.3515	
3/4/2005 00:00:00	SOMES	Senzor SOX	Depasire limita de alarmare	781.0451	
3/5/2005 00:00:00	SOMES	Senzor CL2	Depasire limita de alarmare	844.1857	
3/5/2005 00:00:00	SOMES	Senzor CO	Revenire sub prag de alarmare	320.9863	
3/5/2005 00:00:00	SOMES	Senzor NOX	Revenire sub prag de urmarire	127.6478	
3/6/2005 00:00:00	SOMES	Senzor NOX	Depasire limita de alarmare	840.1761	
3/6/2005 00:00:00	SOMES	Senzor SOX	Revenire sub prag de urmarire	395.598	
3/7/2005 00:00:00	SOMES	Senzor CO	Revenire sub prag de urmarire	226.3344	
3/8/2005 00:00:00	SOMES	Senzor CL2	Revenire sub prag de alarmare	323.9792	
3/9/2005 00:00:00	SOMES	Senzor CL2	Revenire sub prag de urmarire	11.2802	
3/9/2005 00:00:00	SOMES	Senzor CO	Depasire limita de alarmare	933.8204	
3/9/2005 00:00:00	SOMES	Senzor NOX	Revenire sub prag de alarmare	421.9507	
3/10/2005 00:00:00	SOMES	Senzor CL2	Depasire limita de alarmare	994.1425	
3/10/2005 00:00:00	SOMES	Senzor CO	Revenire sub prag de urmarire	261.3549	

Figure 9. Report window at the central dispatcher.

- Assuring the authorized access to the critical operations by a hierarchical system of passwords;
- Supervision of alarm limits, of the state of the communication with the local monitoring systems, the maneuvers made by the dispatcher personnel, determining an acoustic or visual warning signal generation (figure 9).

9. CONCLUSIONS

Using wireless components a monitoring system for air pollution generated by industrial plants was developed. The main modules of the system are:

- Data acquisition module – using sensors for gases and dust– based on the programmable automaton;
- Concentration prediction module – based on simulation using a mathematical model for dispersion of gases and dust;
- Weather station – to measure the meteorological parameters;
- Client-server system organized on two levels – a local level in charge with: data acquisition, data management and a central level for monitoring multiple pollution sources simultaneously;
- Data transfer module – to transfer the data between the two levels of the system.

The **WIPOL** system is extensible, allowing inclusion of up to 256 monitoring sites. The system is useful in supervising multiple industrial plants releasing pollutant effluents in the air.

REFERENCES

1. *** *Acte Normative privind poluarea mediului* (Legea 137/1995, Ordinul 756/1997, HG 34/2002)
2. R. Z. Tudose, *Ingineria proceselor fizice din industria chimica*, *Vol. I Fenomene de transfer*, Ed. Academiei Romane, Bucuresti, 2000
3. *** DURAG D-R 800 Dust Concentration Monitor, DURAG Industrie Elektronik GmbH & Co KG, Germany
4. D. L. Ermak, *User's manual for SLAB: An atmospheric dispersion model for denser-than-air releases*, Lawrence Livermore National Laboratory, USA, 1990
5. S. Coldea, *Diffusion and dispersion of pollutants in geofluids* (in romanian), Presa Universitară Clujeană, Cluj-Napoca, Romania, 2002

STUDIA UNIVERSITATIS BABEŞ-BOLYAI, CHEMIA, L, 2, 2005

A QUANTUM CHEMICAL STUDY ON BORON NITRIDE AND CARBON NITRIDE NANOTUBES

SIMONA RADA[1], IOAN SILAGHI DUMITRESCU[1]

[1]*Departament of Chemistry, "Babeş-Bolyai"University, Cluj-Napoca, Ro-400084, Romania*

ABSTRACT. In order to use tubes for constructing electronic nanodevices we determined the energetic and electronic properties of the boron nitride and carbon nitride nanotubes.

Keywords: carbon-nitrogen and boron nitride nanotubes, semiempirical calculations, electronic properties, nanodevices.

INTRODUCTION

The discovery of carbon nanotubes [1] bring about unprecedented opportunities for obtaining materials with nanoscale structures. Recently, classes of tubes originating in compounds hexagonal tessellation: BN, CN_x have been synthesized [2-4]. Carbon and boron nitride nanotubes are promising systems for manufacturing of electronic devices, such as transistors, actuators and logic circuits [5-10]. These devices require precise control of the electronic properties. The fact that the electronic properties of the carbon nanotubes depend upon their chirality and diameter makes them unsuitable for some electronic devices.

The effect of chirality on energetic and electronic properties of zigzag boron nitride and carbon nitride nanotubes with 1:1 stoechiometry have been considered in this contribution.

METHOD OF CALCULATION

Carbon-nitrogen and boron nitride nanotubes with zigzag geometry have been considered theoretically by performing *PM3-RHF* [11] type semiempirical molecular orbital calculations by using Spartan '02 package [12].

The densities of states (*DOS*) have been calculated by the extended Hückel tight-binding method using BICON-CEDIT package [13].

RESULTS AND DISCUSSION

A) Thermodynamic stability

In the present work we have calculated the enthalpies of formation (ΔH) for (n,0)CN nanotubes with n=5, 6,….,12 depending on the chiral vector, n of the tube and compared them with the corresponding results for boron nitride nanotubes, **figure 1**.

Accordingly, the PM3 results show that both BN and CN nanotubes are thermodynamically stabilized with increasing of the chiral vector, n. All BN nanotubes are more stable than their carbon nitride analogues. This might explain the synthesis of carbon nitride nanotubes containing no more than 13% nitrogen [14].

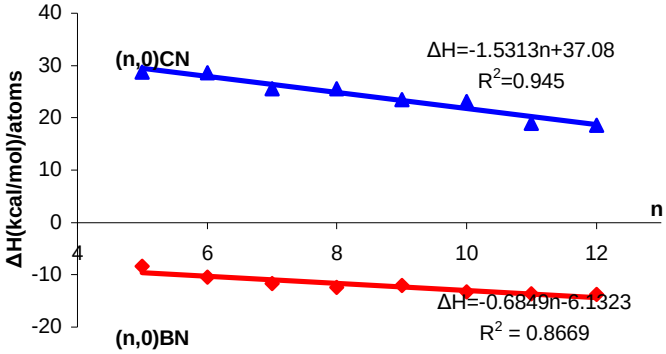

Figure 1. Enthalpies of formation (per atom) of the (n,0)CN/BN tubes as a function of chiral parameter (n).

B) Polarizability (α)

One of the current research topics in this area is the influence of different chiralities of the tubes on polarizabilities for possible applications on nanodevices. Polarizability measures the ability of an atom or molecule to deform the electric cloud in the presence of an electric field.

The calculated data have been plotted on graph in **figure 2**. This finding suggests that the polarizabilities of these tubes increases almost linearly with the chiral vector, n [15]. It is also important to notice that the polarizabilities of the CN nanotubes are higher than that of the BN analogues due to the higher polarizability of the carbon relative to boron.

C) Density of states (DOS)

The electronic properties of the nanotubes are examined using the information provided by density of states. The total DOS, IDOS (integrated DOS) and the N(2s, 2p), B(2s, 2p) contributions for (10,0)BN tube (with the 1:1 stoechiometry) are given in **figure 3**.

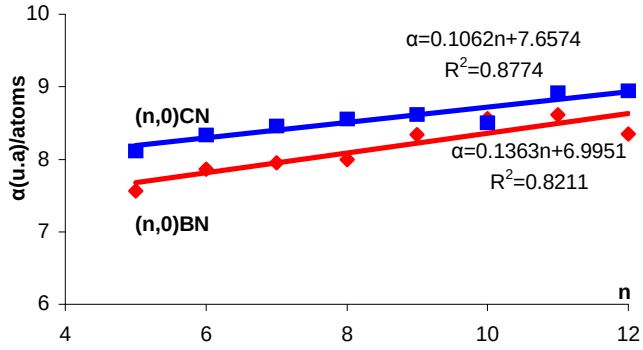

Figure 2. Polarizability (per atom) of the nanotubes as a function of chiral vector, n.

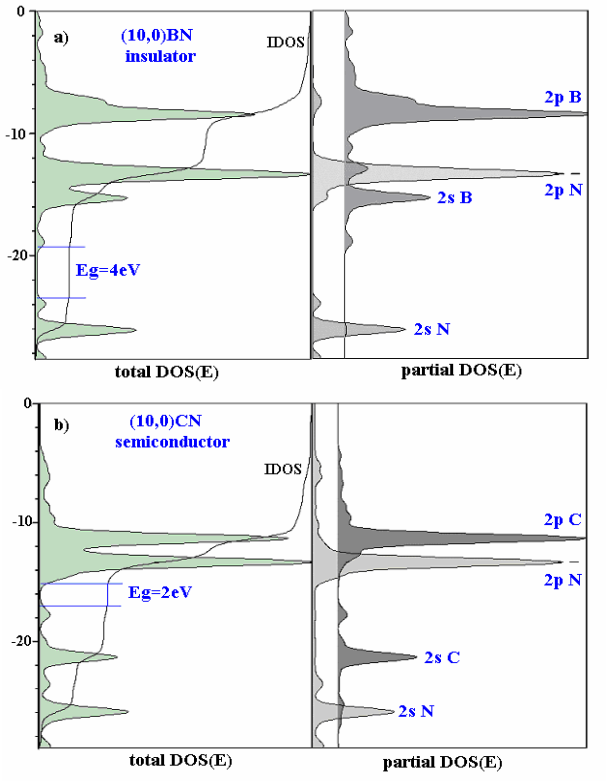

Figure 3. The total, partial *DOS* and *IDOS* diagrams for (10,0)BN and (10,0)CN tube.

The partial DOS(E) plot shows that the lowest band is derived from N(2s) orbitals and conduction bands are composed of 2s orbitals of the boron mixed with the 2p orbitals of the nitrogen and boron respectively. Since the gap between the valence and conduction bands (4eV) is greater than 3eV [16], indicates that the BN nanotube is an insulator. This finding is in agreement with the resultants published by Blasé [17] (tube is an insulator with a gap of 5,5eV).

From the DOS(E) plot indicates in **figure 3b** it is evident that the lowest bands (valence bands) are composed of N(2s), C(2s) derived states while the conduction bands are consisted of N(2p) and C(2p) derived states. Similar results indicates the DOS diagrams of the (n,0)BN and (n,0)CN with n=5, 6, 7, 8, 9, 11, 12. So that, all BN nanotubes are insulators while the CN nanotubes exhibit semiconductor properties, with constant gap independent of their chiral vector, n.

CONCLUSION

The carbon nitride nanotubes are thermodynamically stabilized with the increasing of the chiral vector, n. A higher polarizability and a semiconductor behaviour suggests that the carbon nitride nanotubes are good candidate for possible applications in nanodevices.

REFERENCES

1. S. Iijima, *Nature,* **1991***, 354*, 56.
2. N. G. Chopra, R. J. Luyken, K. Cherrey, V. H. Crespi, M. L. Cohen, S. G. Louie, A. Zettl, *Science,* **1995***, 269*, 966.
3. A. Loiseau, F. Willaime, N. Demoncy, G. Hug, H. Pascard, *Phys. Rev. Lett.,* **1996***, 76*, 4737.
4. Z. Weng-Sieh, K. Cherrey, N. G. Chopra, X. Blasé, Y. Miyamoto, A. Rubio, M. L. Cohen, S. G. Louie, A. Zettl, R. Gronsky, *Phys. Rev. Lett.,* **1995***, 51*, 11229.
5. S. J. Tans, A. Verschueren, C. Dekker, *Nature,* **1998***, 393*, 6680.
6. R. Martel, T. Schmidth, H. R. Shea, T. Hertel, Ph. Avouris, *Appl. Phys. Lett.,* **1998***, 73*, 2447.
7. H. W. C. Postma, T. Teepen, Z. Yoa, M. Grifoni, C. Dekker, *Science***, 2001***, 293*, 76.
8. V. Derycke, R. Martel, J. Appenzeller, Ph. Avouris, *Nano Lett.,* **2001***, 1*, 453.
9. K. H. Baughman, C. Cui, A. A. Zakhidov, Z. Iqbal, J.N. Baricsi, G. M. Spinks, G. G. Wallace, A. Mazzoldi, D. De Rosi, A. G. Rinzler, O. Jaschinski, S. Roth, M. Kertesz, *Science,* **1999***, 284*, 1340.
10. A. Bachtold, P. Hadley, T. Nakanishi, C. Dekker, *Science,* **2001***, 294*, 1317.
11. J. J. P. Stewart, *J. Comput. Chem,* **1989***, 10*,209.
12. Spartan '02, Wavefunction, Inc., Irvine, C. A.
13. M. Brandle, R. Rytz, G. Calzaferri, *BICON-CEDIT – manual*, University of Bern, **1997**.
14. S. Trasobares, C. Stephan, C. Colliex, W. K. Hsu, D. R. M. Walton, H. W. Kroto, *Eur. Phys. J.,* **2001***, 22B*, 117.
15. S. Rada, *Teza doctorat*, **2004**.
16. N. C. Greenham, R. H. Friend, *Solid State Physics, Advances in Research and Application*, edited by H. Ehrenreich and F. Spaepen , **1995**, *49*, 1, Academic Press, New York.
17. X. Blasé, A. Rubio, S. G. Louie, M. L. Cohen, *Europhys. Lett.,* **1994**, *28*, 335.

STUDIA UNIVERSITATIS BABEŞ-BOLYAI, CHEMIA, L, 2, 2005

THEORETICAL MODELING AND EXPERIMENTAL STUDY OF INTRAMOLECULAR HYDROGEN-BOND IN TETRAMETHYL 3,7-DIHYDROXYBICYCLO[3.3.1]NONA-2,6-DIENE-2,4,6,8-TETRACARBOXYLATE

N. TOSA[1], A. BENDE[2], I. BRATU[2], I. GROSU[1]

[1] *Organic Chemistry Department, Babes-Bolyai University, 11 Arany Janos, RO 400028 Cluj-Napoca, Romania,*

[2] *National Institute for R&D of Isotopic and Molecular Technologies, 71-103 Donath, RO 400293 Cluj-Napoca, Romania*

ABSTRACT. Theoretical study on *tetramethyl 3,7-dihydroxybicyclo [3.3.1]nona-2,6-diene-2,4,6,8-tetracarboxylate* is performed by using density functional theory (DFT) considering 6-31G basis sets. The results are compared with different experimental data obtained by using FT-IR spectroscopy in liquid state, using solvents of various polarities. Two hypothetical structures have been considered for the analysed compound: (i) one having intramolecular hydrogen bonding between OH enolic group and carbonylic oxygen from carboxylate group and (ii) the other with intramolecular hydrogen bonding between OH enolic group and methoxy oxygen from carboxylate group. The energy difference between these two possible forms is very low, suggesting a fast inter-conversion between each other. Our study was focused on the bands at 1600-1850 cm^{-1}, and 2900-3200 cm^{-1} of spectrum. A reasonable agreement between theoretical and experimental data in liquid phase has been found.

Keywords : intramolecular hydrogen bond, energetics, conformations, IR spectroscopy, DFT.

INTRODUCTION

Molecules have the tendency to develop the stongest interactions possible under the given conditions. The hydrogen bonds, especially the intramolecular ones, as weak interactions, play an important role because they add up and thus generate very strong molecules conformations.

The secondary, tertiary and quaternary structure of proteins, the double helix of DNA, the membrane structures and complex intracellular particles like ribosomes are all maintained by weak interactions[1]. They give a deep insight into peptides and protein chemistry. Classically, a hydrogen bond is formed when the hydrogen atom attached to an electronegative atom (X) as a donor, interacts with a lone pair electron of another electronegative atom (Y), as an acceptor, that is X-H...Y interactions[2,3]. One of the most suitable tools to investigate the nature of these hydrogen bonds is the FT-IR spectroscopy technique in liquide phase. The solvents play an important role in the spectra's shape establisment, the increase of the solvent polarity could generate a considerable line enlargement and frequency shift[4-6]. The enolisable β-keto esters exhibit the phenomenon of conjugate chelation, through the intramolecular hydrogen bonds, similar effects being observed in case of the corresponding diketones. The frequency shifts of chelated esters have been used to measure the double-bond character in a few series of compounds. The enolisable β-keto esters show absorption near 1718 cm^{-1} and 1735 cm^{-1} corresponding to the ketonic and ester carbonyl groups, respectively, and at 1618 cm^{-1} and 1656 cm^{-1}, which must arise from the chelate structure of enol form. The first of these two bands is associated with the carbon double-bond absorption and the second

with the chelated carbonyl absorption[7]. Presence of the intramolecular hydrogen bond and the solvent effects exhibit a significant influence on the normal vibrational mode of C=O and C=C bonds in the spectral domain of 1600 – 1850 cm^{-1}.

The aim of our work is to give an accurate description of these intramolecular hydrogen bonds in tetramethyl 3,7-dihydroxybicyclo[3.3.1]nona-2,6-diene-2,4,6,8-tetracarboxylate, a potential macrocycles precursor, and solvent effects using theoretical molecular modeling and experimental IR spectroscopy study.

RESULTS AND DISCUSSIONS

The experimental study consisted of the registration of the IR spectra in liquid state for *tetramethyl 3,7-dihydroxybicyclo[3.3.1]nona-2,6-diene-2,4,6,8-tetracarboxylate*[8]. Several 20% concentrated solutions were prepared, using six solvents situated in 2.25 - 4.8 polarity values range (tetracarbon chloride, benzene, dichloromethane, ethylic ether, tetrahydrofurane, 1,4-dioxane). All these selected solvents are "transparent" on 1600 – 1850 cm^{-1} and 2800 – 3100 cm^{-1} spectral range and allow C=O and intramolecular hydrogen bonds study. Infrared spectroscopic analyses were performed on a UR20 Carl Zeiss spectrophotometer, with a spectral resolution of 0.6 cm^{-1}, in 650-4000 cm^{-1} spectral range have been prepared. Cells with CaF_2 windows and 0.1 mm thickness of the layer, have been used. The appropriate solvent for each investigated solution has been filled in the reference cell.

Theoretical calculations were carried out by DFT method at the B3LYP exchange-correlations functional, using 6-31G Pople's basis sets implemented in GAMESS[9] quantum chemical program package under Linux.

Two hypotetical structures for the investigated β-ketoester[10] were considered: the one with intramolecular hydrogen bonds being formed between the the enol hydrogen and the carbonyl oxygen atom (Fig. 1a), and respectively methoxy oxygen atom, both belonging to the methoxycarbonyl group (Fig. 1b). The strength of the hydrogen bond shows a steady increase of the stability of β-ketoester chelate, which through such of intramolecular weak interactions closes a stable six-membered ring.

The strength of the hydrogen bond is a little bit different within these two conformations. Both conformers exhibit an identical orientation of the molecular backbone. The C=O···H-O distance in conformer A is 1.6895 Å, while the H_3C-O···H-O distance in conformer B is 1.6788 Å, shorter than the other conformer (Table 1.).

Table 1

Conf_A		Conf_B	
Coord.	Values	Coord.	Values
Bond lenghts (Å)			
O3-H3	1.0060	O3-H3	0.9949
H3···O5	1.6895	H3···O4	1.6788
O5-C6	1.2649	O4-C6	1.4107
C6-O4	1.3683	C6-O5	1.2399
C6-C5	1.4492	C5-C6	1.4554
C5-C4	1.3717	C5-C4	1.3686
C4-O3	1.3567	C4-O3	1.3606
Angles (Deg.)			
H3···O5-C6	100.794	H3···O4-C6	106.278
O5-C6-O4	120.675	O4-C6-O5	119.636
O5-C6-C5	125.097	O4-C6-C5	114.151
C6-C5-C4	117.839	C6-C5-C4	123.124
C5-C4-O3	123.603	C5-C4-O3	124.904
C4-O3-H3	109.562	C4-O3-H3	110.091

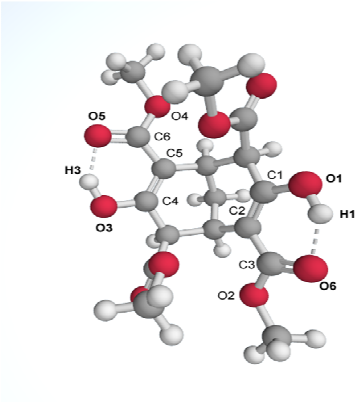

Figure 1. a) Conformation A

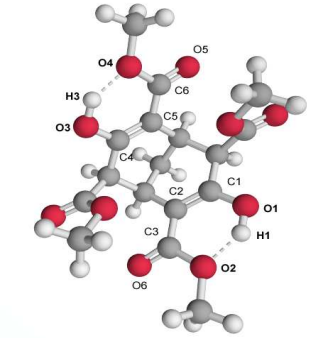

Figure 1. b) Conformation B

The selected molecular parameters of conf_A and conf_B calculated by DFT method using B3LYP exchange-correlation function with 6-31G basis set.

These two conformations were found to have an energetical barrier of only 0.2204 eV, that suggests a very fast interconversion between each other. Considering a transition state for this conformational equilibrium, the minima (the relative energies) calculated for the matching conformers were 3.047 eV for conf_A and 2.827 eV for conf_B (Fig. 2).

The IR spectra in the O-H region, C=O and C=C stretching vibrations, respectively, have been studied in a wide range of solvents solutions of 20% concentration. Taking into account that the O-H stretching band depends on the solvent polarity and on eventual intramolecular hydrogen bonds, this band is situated around 2900 cm^{-1}.

It can be observed (Fig. 3 a.-f.) that, increasing the solvent polarity (from tetracarbon chloride to 1,4-dioxane), the origin of experimental absorption band is blue shifted and the band shape becomes larger.

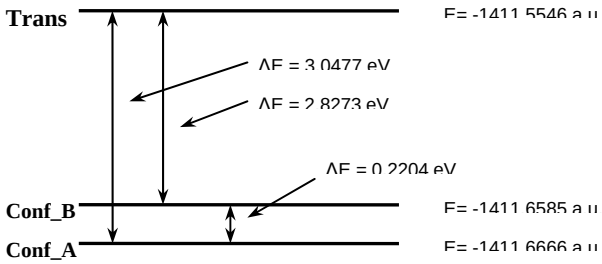

Figure 2. The optimised energetical diagram for the transition state, respectively for both conformations of the *tetramethyl 3,7-dihydroxybicyclo[3.3.1]nona-2,6-diene-2,4,6,8-tetracarboxylate*

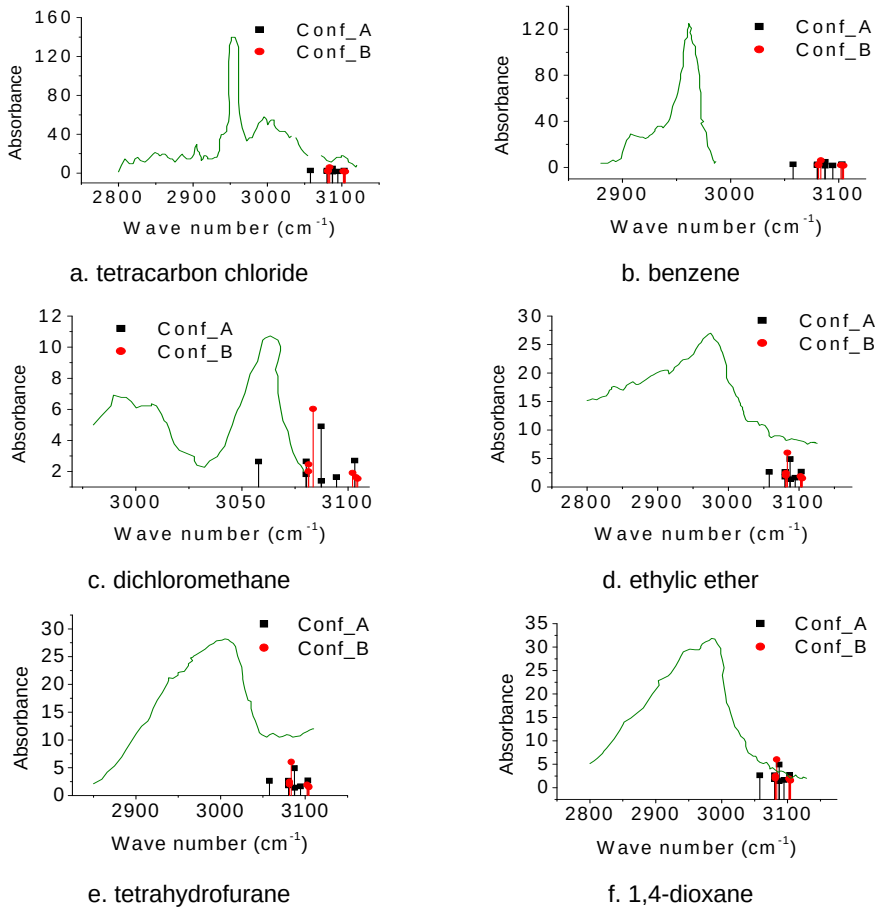

Figure 3. Theoretical and experimental IR spectra (2800 – 3200 cm-1) in the C-H and O-H stretching region, using solvents with various polarities.

A good agreement between the theoretical frequency values and the experimental ones has been found in 1600-1850 cm^{-1} spectral region, especially for the lines belonging to conf_B structure (Fig. 4 a.-f.). In these normal modes, two characteristic bond stretching (C=C and C=O) and C-O-H angle bending, are involved. The corresponding frequencies of C=O belong to the carbonyl group involved in intramolecular hydrogen bond formation (1639.1 cm^{-1} for conf_A, and 1699.3 cm^{-1} for conf_B) and to carbonyl included in the ester group, which exists as a nonbonded group (1730.6 cm^{-1} and 1731.4 cm^{-1} for conf_A, 1733.1 cm^{-1} and 1734.5 cm^{-1} for confB). The corresponding frequencies for C=C bond stretching are 1665.1 cm^{-1} and 1658.9 cm^{-1} for conf_A, 1660.8 cm^{-1} and 1668.2 cm^{-1} for conf_B. The C-O-H angle bending are coupled with bonded C=O in case of conf_A and with C=C in case of conf_B, having 50 cm^{-1} frequency shift between them. This frequency shift suggests that conf_B spectral shape is closer to the experimental spectra and its geometry structure is more realistic than that of conf_A.

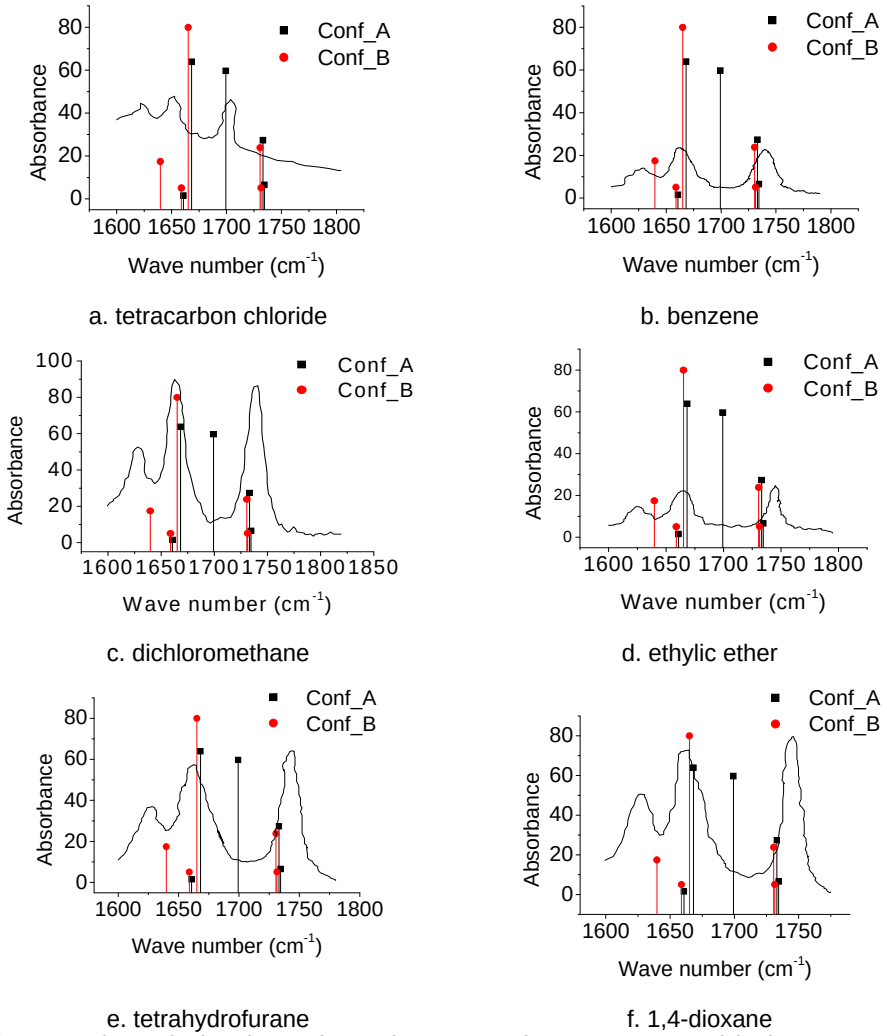

Figure 4. Theoretical and experimental IR spectra (1600 – 1800 cm-1) in the C=O and C=C stretching region, using solvents with various polarities.

CONCLUSIONS

Two possible conformations of the *tetramethyl 3,7-dihydroxybicyclo[3.3.1] nona-2,6-diene-2,4,6,8-tetracarboxylate*, both of them involving the formation of intramolecular hydrogen bond have been modeled. The energy difference between the two forms is very low (ΔE=0.2204 eV), suggesting a fast inter-conversion between each other, passing through a transition state. The IR spectroscopy study in liquid phase, in conjunction with DFT revealed the existence of intramolecular hydrogen bonds in the analysed compound. The calculated and experimental IR spectra are in good agreement, especially in the 1600 – 1850 cm^{-1} spectral region, meanwhile

in the 2800 – 3100 cm^{-1} spectral region it has been registered blue shift of the calculated frequency due to the solvents polarity and the chelatization *via* intramolecular hydrogen bond effects. The characteristic line for *bonded* C=O at 1700 cm^{-1} of the theoretical spectrum of conf_A has no correspondence in the experimental spectra. As a consequence of the increase of the solvent polarity, a considerable line enlargement and frequency shift of the C-H, and the associated O-H enol stretching bands, has been observed. Summarizing the results, it can be concluded that the geometry of the conf_B structure is in better agreement with the experimental data than that of the conf_A structure.

REFERENCES

1. Ch. P Rao, P Balaram and C. N. R. Rao, *Biopolymers,* **1983** *22(9)* 2091-2104.
2. *(a)* S. Scheiner, "Hydrogen Bonding",Oxford University Press, New York, 1997. *(b)* G. A. Jeffrey, "An Introduction to Hydrogen Bond", Oxford University Press, New York, 1997. *(c)* G. Desiraju, T. Steiner, "The Weak Hydrogen Bond", Oxford University Press, New York, **1999**.
3. L. Pauling, *J. Am. Chem. Soc.*, **1992**, *55*, 459.
4. J.Abraham, E. J. Chambers, and W. A. Thomas, *J. Chem. Soc., Perkin Trans. 2*, **1993**, 1061.
5. C. J. Cramer, and D. Truhlar, *J. Am. Chem. Soc*., **1993** *115*, 5745, *ibid*, **1994**, *116*, 3892.
6. A. Klamt and G. Schürmann, *J. Chem. Soc., Perkin Trans. 2*, **1993** 799.
7. L. J. Bellamy, "The Infra-red Spectra of Complex Molecules", Methuen & Co. LTD, London, **1956**, 157-158.
8. Bertz SH, Dabbagh G, *Angew. Chem, Int. Ed. Engl.* **1983**, *21*, 303; (b) Sands RD, *J. Org. Chem.* **1983**, *48*, 3362.
9. Program GAMESS: M. W. Schmidt, K. K. Baldridge, J. A. Boatz, S. T. Elbert, M. S. Gordon, J. J. Jensen, S. Koseki, N. Matsunaga, K. A. Nguyen, S. Su, T. L. Windus, M. Dupuis,and J. A. Montgomery, *J. Comput. Chem.* **1993**, *14*, 1347.
10. N. Tosa, A. Bende, S. Cîntă Pînzaru, I. Grosu, and E. Surducan, *Studia Univ. Babes-Bolyai, Physica*, **2004**, 44(3), 289-292.

STUDIA UNIVERSITATIS BABEŞ-BOLYAI, CHEMIA, L, 2, 2005

COMPOSITE OPERATIONS ON MAPS

MONICA ŞTEFU,[1*] MIRCEA V. DIUDEA,[a] AND PETER E. JOHN,[2]

[1] *Faculty of Chemistry and Chemical Engineering, "Babeş-Bolyai" University 400028, Cluj, Romania*
[2] *Technical University Ilmenau, Institute of Mathematics, PSF 100565, D-98684 Ilmenau, Germany*

ABSTRACT. A map *M* is a combinatorial representation of a closed surface. Convex polyhedra, starting from the Platonic solids and going to spherical fullerenes, can be generated by applying some operations on maps. Three composite map operations: leapfrog, chamfering and capra, play a central role in the fullerenes construction and their electronic properties. Generalization of the above operations leads to series of transformations, characterized by distinct, successive pairs in the Goldberg multiplication formula *m*(*a*,*b*). Parents and products of most representative operations are illustrated.

INTRODUCTION

A map *M* is a combinatorial representation of a (closed) surface.[1,2] Let: *v, e, f* – be the number of vertices, edges, faces, *d* – the vertex degree and *s* – the face size, in the map. A subscript "0" will mark the corresponding parameters in the parent map.

Some basic relations in a map, have been discovered by Euler:[3,4]

$$\sum d\, v_d = 2e \tag{1}$$

$$\sum s\, f_s = 2e \tag{2}$$

where v_d and f_s are the number of vertices of degree *d* and number of *s*-gonal faces, respectively and ($d, s \geq 3$). The two relations are joined in the famous formula:

$$v - e + f = 2(1 - g) \tag{3}$$

with *g* the genus[5] of a graph (*i.e.*, the number of holes performed on a plastic sphere to make it homeomorphic to the surface on which the given graph is embedded; $g = 0$ for a planar graph and 1 for a toroidal graph).

The nuclearity of fullerene polyhedra can be counted by the Goldberg's[6] relation:

$$m = (a^2 + ab + b^2);\ a \geq b;\ a + b > 0 \tag{4}$$

which predicts the multiplication factor $m = v/v_0$ in a 3-valent map transformed by a given operation (see below). The *m* factor is related to the formula giving the volume of truncated pyramid, of height *h*: $V = mh/3$, coming from the ancient Egypt.

This paper is organized as follows: the second section presents some classical composite operations, with definitions given in terms of simple map operations; the third section deals with generalized operations, inspired from the Goldberg's representation of polyhedra in the (*a*,*b*) "inclined coordinates"; the forth section presents some molecular realization of these composite operations. The last two sections give a summary of the paper and references, respectively.

CLASSICAL COMPOSITE OPERATIONS

We limit here to the most important composite operations, meaning the basic, simple operations, such as: Dual, Medial, Stellation, Truncation, Snub, etc., are known. The reader can consult some already published papers.[1,2,7]

Leapfrog *Le* (*tripling*) operation[8-12] can be written as:

$$Le(M) = Du(P_3(M)) = Tr(Du(M)) \quad (5)$$

where P_3 is a particular case of the *Polygonal* P_s *capping* (s = 3, 4, 5), realizable[13,14] by (i) adding a new vertex in the center of the face, (ii) putting s-3 points on the boundary edges and (iii) connecting the central point with one vertex (the end points included) on each edge. In this way the parent face is covered by trigons (s = 3), tetragons (s = 4) and pentagons (s = 5). The P_3 operation is also called *stellation* or (centered) *triangulation*.

A sequence of stellation-dualization rotates the parent s-gonal faces by π/s. Leapfrog operation is illustrated, for a pentagonal face, in Figure 1.

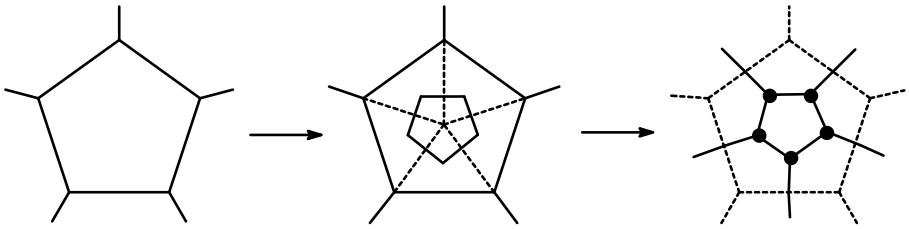

Figure 1. Leapfrogging a pentagonal face of a trivalent map

A bounding polygon, of size $2d_0$, is formed around each original vertex. In the most frequent cases of 4- and 3-valent maps, the bounding polygon is an octagon and a hexagon, respectively.

The complete transformed parameters are:

$$Le(M): \quad v = s_0 f_0 = d_0 v_0 \; ; \; e = 3e_0 \; ; \; f = v_0 + f_0 \; ; m(1,1) = 3 \quad (6)$$

In trivalent maps d_0 = 3, so that *Le*(*M*) is also called the *tripling* operation. Note that the vertex degree in *Le*(*M*) is *always* 3, as a consequence of the dualization of a triangulation.

A nice example of using *Le* operation is: *Le*(Dodecahedron) = Fullerene C_{60}. The leapfrog operation can be used to insulate the parent faces by surrounding bounding polygons.

Chamfering (*quadrupling*) *Q* is another composite operation, achieved by the sequence:[6,13,14]

$$Q(M) = E_{-}(Tr_{P_3}(P_3(M))) \quad (7)$$

where E_{-} means the (old) edge deletion in the truncation Tr_{P3} of the new, face centered, vertices introduced by the P_3 capping (Figure 2). The old vertices are preserved.

The complete transformed parameters are:

$$Q(M): \quad v = (d_0 + 1)v_0;\ e = 4e_0;\ f = f_0 + e_0;\ m(2,0) = 4 \tag{8}$$

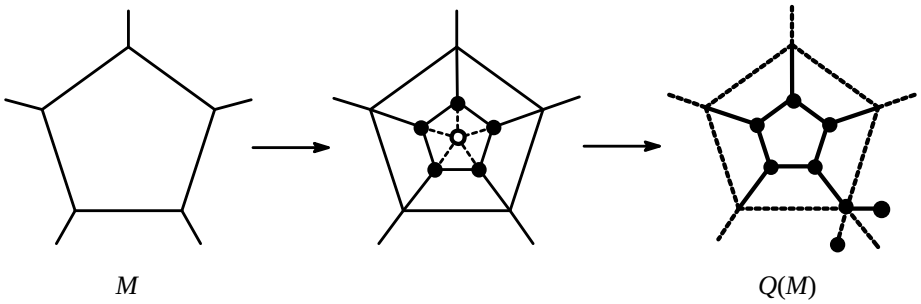

Figure 2. Quadrupling a pentagonal face of a 3-valent map.

Q operation leaves unchanged the initial orientation of the polygonal faces. Note that, the chamfering of a 4-valent map is not a regular graph anymore (because of mixing the new trivalent vertices with the parent 4-valent ones). Only a 3-valent map is chamfered to a 3-regular graph.

Q insulates the parent faces always by hexagons. An example of this operation is: *Q* (Dodecahedron) = Fullerene C_{80}.

The "chamfering" (edge chamfering being equivalent to vertex truncation)[6] is most often called "quadrupling", by the vertex multiplication $m = 4$, in trivalent maps.

Capra *Ca* (*septupling*) - the goat, is the Romanian corresponding of the *leapfrog* English children game. It is a composite operation,[15] necessarily coming third, by the Goldberg's multiplying factor $m(2,1) = 7$.[14]

The transformation can be written as:

$$Ca(M) = Tr_{P_5}(P_5(M)) \tag{9}$$

with Tr_{P5} meaning the truncation of new, face centered, vertices introduced by the P_5 capping (Figure 3). Note that, P_5 involves an E_2 (*i.e.*, edge trisection) operation. *Ca* insulates any face of *M* by its own hexagons, which are not shared with any old face (in contrast to *Le* or *Q*).

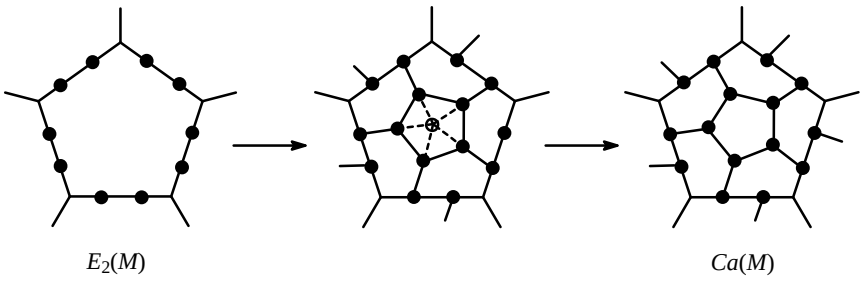

Figure 3. Capring a pentagonal face of a 3-valent map.

Table 1 lists the net parameters in Capra transforms,[15] either in simple or iterative application on finite objects.

According to the *m*-value in trivalent maps, Capra is the *septupling* S_1 operation. A second septupling operation S_2 was defined in ref. 13.

Only a 3-valent regular map leads to a regular 3-valent graph by Capra; clearly, maps/graphs of degree greater than 3 will not be regular anymore.

Table 1.

The transformed parameters by the iterative *Ca* operation

Operation	Parameter
$Ca(M)$	$v_1 = v_0 + 2e_0 + s_0 f_0 = (2d_0 + 1)v_0$
	$e_1 = 7e_0$
	$f_1 = s_0 f_0 + f_0$
$Ca_2(M)$	$v_2 = v_1 + 2e_1 + \sum s f_{1,s} = (16d_0 + 1)v_0$
	$e_2 = 7^2 e_0$
	$f_2 = \sum s f_{1,s} + f_0 = 8s_0 f_0 + f_0$
$Ca_n(M)$	case $d_0 > 3$
	$v_n = 8v_{n-1} - 7v_{n-2}$; $n \geq 2$

GENERALIZED OPERATIONS

One of us (P. E. J.) has proposed a generalization of operations on maps, inspired from the work of Goldberg,[6] and its representation of polyhedra in the (*a*,*b*) "inclined coordinates" (60^o between axes). The nuclearity multiplicity factor *m* for trivalent maps is given by eq. (4).

Figures 4 and 5 illustrate the method on the hexagonal face. The points of the "master" hexagon must lie either in the center of a lattice hexagon or on a lattice vertex, so that in the center of the parent hexagon must be a new hexagon. The edge length of the parent hexagon is counted by the primitive lattice vectors (*x*,*y*).

A similar procedure was used by Coxeter,[16] who built up icosahedral polyhedra/fullerenes as dual master triangular patches, represented by pairs of integers.

For the (3,2) Cut operation - Figure 5 b, the central face and first connected atoms were cut off.

Some of the generalized composite operations, corresponding to non-prime *m*, can be expressed as operation sequences, as shown in Table 2. It is obvious that (*a*,*a*) and (*a*,0) operations provide achiral products (*e.g.*, fullerenes of the full I_h point group symmetry) while (*a*,*b*), $a \neq b$, result in chiral transformed maps (*e.g.*, fullerenes of therotational *I* point group symmetry) . The (*a*,0) operations produce non-rotated maps. The above generalized operations, as implemented in the software package CageVersatile,[17] work on any face and vertex-degree type maps.

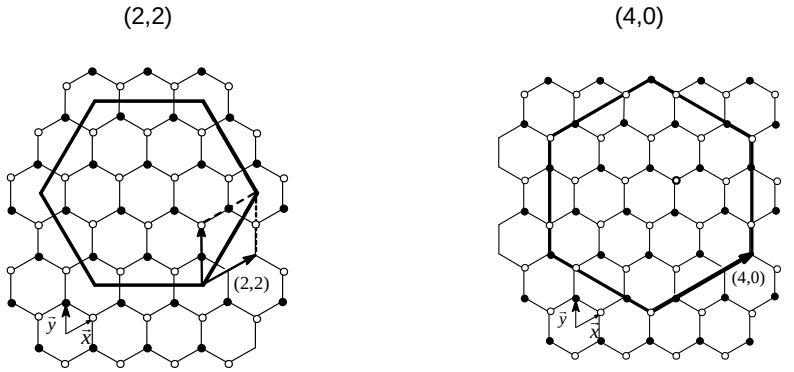

Figure 4. Generalized (*a*, *a*) and (*a*, 0) operations

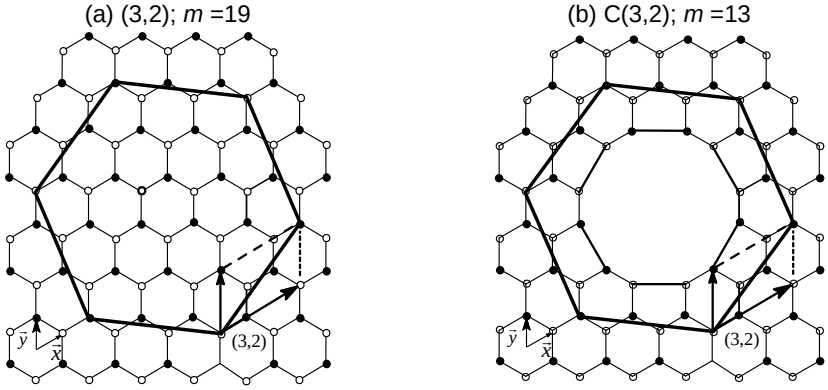

Figure 5. Generalized (*a*, *b*) operation: *a* = *b* + 1 (5a) and (central face and first connected atoms) "cut" C(*a*,*b*)
(5b),the last one corresponding to *m*(3,1) =13 factor.

In case of trivalent regular maps, relations (1) and (2) can be rewritten as:

$$3 \cdot v_0 = 2 \cdot e_0 = s_0 \cdot f_0 \tag{10}$$

Keeping in mind the multiplication factor *m* (see (4)), the number of vertices in the transformed map is:

$$v_1 = m \cdot v_0 \tag{11}$$

Eq 10 leads to:

$$3 \cdot v_1 = 3 \cdot m \cdot v_0 = 2 \cdot e_1 \tag{12}$$

$$e_1 = \frac{3}{2} \cdot m \cdot v_0 = \frac{3}{2} \cdot m \cdot \frac{2}{3} e_0 = m \cdot e_0 \tag{13}$$

Table 2.

Inclined coordinates (*a*, *b*), multiplication factor $m = (a^2 + ab + b^2)$, number of atoms *N* and operation symbols (running on the dodecahedral C_{20} fullerene)

	(*a*, *b*)	*m*	*N*	Operation	Obs.
1	(1, 0)	1	20	*I*	Identity
2	(1, 1)	3	60	$Le_{1,1}$	Rotated by π / s; achiral
3	(2, 0)	4	80	$Q_{2,0}$	Non-rotated; achiral
4	(2, 1)	7	140	$Ca_{2,1}$	Rotated by $\pi / 2s$; chiral
5	(2, 2)	12	240	$Le_{1,1}$, $Q_{2,0}$	Rotated by π / s; achiral
6	(3, 0)	9	180	$Le_{1,1}$, $Le_{1,1}$	Non-rotated; achiral
7	(3, 1)	13	260	-	Rotated; chiral
8	(3, 2)	19	380	-	Rotated; chiral
8'	C(3, 2)	13	260	-	Rotated; chiral
9	(3, 3)	27	540	$Le_{1,1}$, $Le_{1,1}$, $Le_{1,1}$	Rotated by π / s; achiral
10	(4, 0)	16	320	$Q_{2,0}$, $Q_{2,0}$	Non-rotated; achiral
11	(4, 1)	21	420	$Le_{1,1}$, $Ca_{2,1}$	Rotated; chiral*
12	(4, 2)	28	560	$Q_{2,0}$, $Ca_{2,1}$	Rotated by $\pi / 2s$; chiral
13	(4, 3)	37	740	-	Rotated; chiral
14	(4, 4)	48	960	$Le_{1,1}$, $Q_{2,0}$, $Q_{2,0}$	Rotated by π / s; achiral
15	(5, 0)	25	500	-	Non-rotated; achiral
16	(5, 1)	31	620	-	Rotated; chiral
17	(5, 2)	39	780	-	Rotated; chiral
18	(5, 3)	49	980	$Ca_{2,1}$, $Ca_{2,1}$	Chiral/ achiral*
19	(5, 4)	61	1220	-	Rotated; chiral
20	(5, 5)	75	1500	-	Rotated; achiral

***** achiral, when the sequence *CaR*(*CaS*(*M*)) is used.

The above operations introduce new hexagons, keeping the original faces. Thus, the number of faces of any size *s* in M_1 is:

$$f_{1,s} = f_{1,6} + f_0 \tag{14}$$

Relation (10) becomes:

$$2 \cdot e_1 = \sum s \cdot f_{1,s} = 6 \cdot f_{1,6} + s_0 \cdot f_0 \tag{15}$$

Substitution of e_1 in (15) leads to:

$$f_{1,6} = \frac{m-1}{6} \cdot s_0 \cdot f_0 \tag{16}$$

$$f_{1,s} = \frac{m-1}{6} \cdot s_0 \cdot f_0 + f_0 \tag{17}$$

For the n^{th} iterative operation, one deduces:

$$v_n = m^n \cdot v_0 \tag{18}$$

$$e_n = m^n \cdot e_0 \tag{19}$$

$$f_{n,s} = \frac{m^n - 1}{6} \cdot s_0 \cdot f_0 + f_0 \qquad (20)$$

Relations (18) to (20) hold for all the presented operations running on a trivalent regular M_0. In other words, the above relations are true for the 3-valent Platonic solids: tetrahedron *T*, cube *C* and dodecahedron *D*.

For other degree maps, in case of *Le*, *Q* and *Ca* operations, some relations are above presented.

We stress here that, in contrast to the Coxeter[16] procedure our method operates on the original graph (not its dual) which enables the embedding on any kind of close or open surface. Moreover, extensions by "cutting" the master faces have not been explored in the cited literature. Thus, a large palette of polyhedral structures, useful in modeling nanostructures, is available.

MOLECULAR REALIZATION

This section illustrates the “molecular” realization or, in other words, the transformation of molecules (such as graphitoids) by the mathematical operations.

It is well-established that *Le* operating on fullerenes provides Clar fullerenes.[2] The *Q* and *Ca* operations are more related to each other.

Recall that, according to the Clar theory, any polyhedral map may be looked for a perfect Clar structure[2,18] PCS (Figure 6), which is a disjoint set of faces (built up on all vertices in *M*) whose boundaries form a 2-factor. A *k*-factor is a regular *k*-valent spanning subgraph. A PCS is complementary to a Fries structure,[19] which is a Kekulé structure having the maximum possible number of benzenoid (alternating single-double edge) faces. A Kekulé structure is a set of pairwise disjoint edges/bonds of the molecule (over all its atoms) that coincides with a perfect matching and a 1-factor in Graph Theory. A trivalent polyhedral graph, like that of fullerenes, has a PCS if and only if it has a Fries structure.[2] Such structures represent *total resonant sextet* TRS benzenoid molecules and it is expected to be extremely stable, in the valence bond theory.[2,20] Leapfrog *Le* is the only operation that provides PCS transforms.

By extension, Diudea[13] proposed a corannulenic system (Figure 7). A perfect corannulenic structure PCorS is a *disjoint set* of (supra) faces covering all vertices in the molecular graph. The associated Fries-like structure is defined as above but its construction will avoid the corannulenic core vertices.

Among the above three classical composite operations: *Le*, *Q* and *Ca*, none is able to provide a PCorS. It is, however, possible by the operation sequence *Le*(*Q*(*M*)) or *Q*(*Le*(*M*)), as shown in Figure 7. This sequence is equivalent to the generalized (2,2) operation.

The PCorS superimposes over PCS. Thus, any PCorS is necessarily a PCS. The supra-organized corannulenic units are expected to contribute to the stability of the whole molecule.

As above mentioned, operations (*a*,*b*), $a \neq b$, provide chiral transformed maps. It is, however, possible that the horizontal edge of the parent hexagon be inclined either to the right or to the left, thus resulting pair operations and enantiomeric products (see Figure 5).

(3,0)(C_{20}) = *Le*(*Le*(C_{20})) = C_{180}
PCS

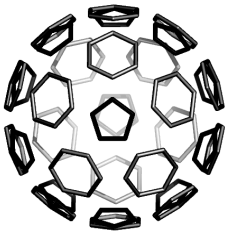

(3,0)(C_{20}) = C_{180}
Fries structure

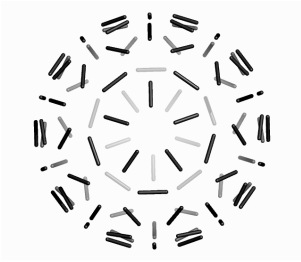

Figure 6. The transform of dodecahedron - C_{20}, by generalized operation (3,0), leading to perfect Clar PCS structure.

(2,2)(C_{20}) = *Q*(*Le*(C_{20})) = C_{240} PCorS

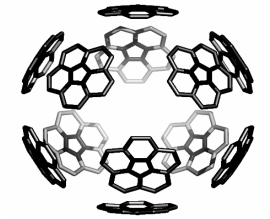

(2,2)(C_{20}) = C_{240}

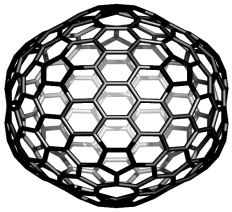

Figure 7. The transform of dodecahedron - C_{20}, by generalized operation (2,2), leading to and perfect corannulenic PCorS structure.

Since pentangulation (2,1) of a face can be done either clockwise or counter-clockwise, it results in an enantiomeric pair of objects: *CaS*(*M*) and *CaR*(*M*), in terms of the sinister/rectus stereochemical isomers.[15] Figure 8 illustrates of such a pair derived from the Dodecahedron.

CaS (C_{20}) non-optimized

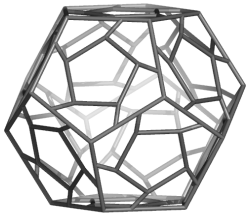

CaR (C_{20}) non-optimized

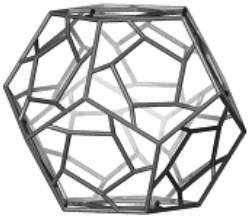

Figure 8. Enantiomeric pair of the (2,1) Capra transforms of C_{20}

If a composite operation includes an even repetition of a pro-chiral operation, the sequence of one kind pro-chiral operation will lead to either a chiral transform or an achiral object, the last one in case of 1:1 ratio of pro-enantiomeric operations (see Figure 9).

(5,3)(*C*) = *CaS*(*CaS*(*C*)); *m* = 49; *N* = 392
(Rotated; chiral)

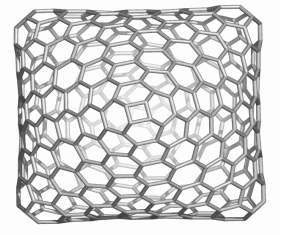

(7,0)(*C*) = *CaR*(*CaS*(*C*)); *m* = 49; *N* = 392
(Non-rotated; achiral)

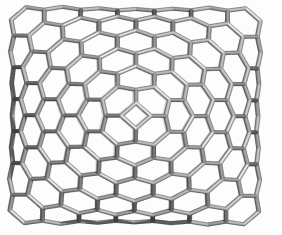

Figure 9. Pair of Capra transforms of the Cube

Other pro-chiral operations are further illustrated: the (3,2) and C(3,2) cut operations working on the dodecahedron (Figure 10). For the procedure working on a hexagonal face see Figure 5.

(3,2)(*D*); *m* =19; *N* =380

C(3,2)(*D*); *m* =13; *N* =260

(a)

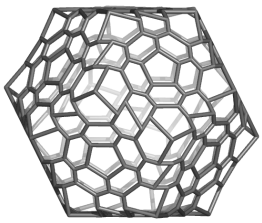

(b)

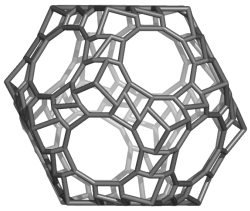

(c)

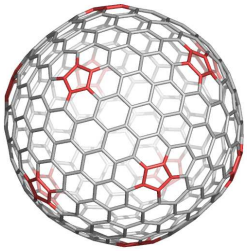

(d)

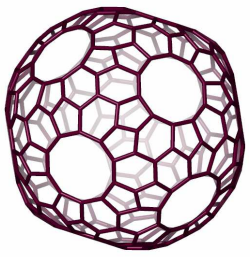

Figure 10. (3,2) and C(3,2) operations performed on the Dodecahedron, non-optimized (a, b) and optimized (c, d).

CONCLUSIONS

Convex polyhedra, starting from the Platonic solids and going to spherical fullerenes, can be generated by map operations.

Three composite map operations: leapfrog, chamfering and capra have been analyzed with respect to their lattice elements.

Generalization of the above operations provided a series of transformations, characterized by distinct, successive pairs in the Goldberg multiplication formula *m*(*a*,*b*).

Parents and products of most representative operations have been illustrated, for finite cages.

REFERENCES

1. T. Pisanski and M. Randić, in: C. A. Gorini, Ed., *Geometry at Work*, (Ed.,) *Math*. *Assoc*. *Amer*. **2000**, *53*, 174-194.
2. P. W. Fowler and T. Pisanski, *J*. *Chem*. *Soc*. *Faraday Trans*. **1994**, *90*, 2865-2871.
3. L. Euler, *Comment. Acad. Sci. I. Petropolitanae* **1736**, *8*,128-140.
4. L. Euler, *Novi Comment*. *Acad*. *Sci*. *I*. *Petropolitanae*, **1758**, *4*, 109-160.
5. F. Harary, *Graph Theory*, Addison-Wesley, Reading, MA, **1969**.
6. M. Goldberg, *Tohoku Math*. *J*. **1937**, *43*, 104-108.
7. M. V. Diudea, P. E. John, A. Graovac, M. Primorac, and T. Pisanski, *Croat*. *Chem*. *Acta*, **2003**, *76*, 153-159.
8. P. W. Fowler, *Phys*. *Lett*. **1986**, *131*, 444-450.
9. P. W. Fowler and J. I. Steer, *J*. *Chem*. *Soc*., *Chem*. *Commun*. **1987**, 1403-1405.
10. P. W. Fowler and K.M.Rogers, *J*. *Chem*. *Soc*., *Faraday Trans*. **1998**, *94*, 1019-1027.
11. P. W. Fowler and K.M.Rogers, *J*. *Chem*. *Soc*., *Faraday Trans*. **1998**, *94*, 2509-2514.
12. M. V. Diudea and P. E. John, *MATCH*, *Commun*. *Math*. *Comput*. *Chem*. **2001**, *44*, 103-116.
13. M. V. Diudea, *Forma* (submitted).
14. M. V. Diudea, in: M. V. Diudea, Ed., *Nanostructures-Novel Architecture*, NOVA, New York, **2004** (submitted).
15. M. V. Diudea, *Studia Univ*. *"Babes-Bolyai"* **2003**, *48(2)*, 3-16.
16. H. S. M. Coxeter, *Regular polytopes*, 3rd Ed., Dover Pubs, Dover, **1973**.
17. M. Stefu and M. V. Diudea, *CageVersatile* 1.3, "Babes-Bolyai" University, **2003**.
18. E. Clar, *The Aromatic Sextet*, Wiley, New York, **1972**.
19. K. Fries, *J*. *Liebigs Ann*. *Chem*. **1927**, *454*, 121-324.
20. J. R. Dias, *J*. *Chem*. *Inf*. *Comput*. *Sci*. **1999**, *39*, 144-150.

STUDIA UNIVERSITATIS BABEŞ-BOLYAI, CHEMIA, L, 2, 2005

3D MOLECULAR SIMILARITY; METHOD AND ALGORITHMS

OLEG URSU*, MIRCEA V. DIUDEA*

* *Faculty of Chemistry and Chemical Engineering*
Babes-Bolyai University, 400028 Cluj, Romania

ABSTRACT. This study presents a method and algorithms for calculation of 3D similarity between pairs of chemical structures represented as 3D molecular graphs. Similarity searching in chemical databases is widely used for virtual screening, lead discovery and optimization, and most recently protein amino-acid sequences studies to discover and determine the functionality of a new isolated protein. This method has obvious advantages over other known methods due to the following: (*i*) the superposition method does not depend on the preliminary alignments of the chemical structures; (*ii*) entire conformational space is searched without generation of each conformer; (*iii*) excellent discrimination between geometrical isomers. Although it is a computationally demanding method, recent implementation of maximum clique algorithm and bound smoothing algorithm made possible the optimization of this method and application to similarity searching in chemical databases of non trivial size.

INTRODUCTION

The investigation of molecular structure involves research on its constitution – the number and chemical identity of atoms and bonds joining them along with the configuration in 3D space. Molecular similarity has been studied from two different major view points: (i) topological similarity defined in connectivity and constitutional terms and (ii) geometrical similarity, when geometrical aspects of the molecular structure are taken into account.

Similarity searching in databases of 2D chemical structures is widely used for virtual screening and lead discovery. A similarity measure, that quantifies the degree of structural resemblance between the target structure and each of the database structure, is based on fingerprint or molecular descriptor encoding of the molecular structure with similarity between pairs of such representations being computed using the *Tanimoto* coefficient. Another topological similarity measure of increasing interest (although more computationally demanding) is detection of 2D maximum common subgraphs (MCS).[1,2] The binding affinity of the ligand to the receptor site, which usually express the biological activity, is related to a single geometrical configuration of the ligand.

The procedures and algorithms used in detection of the MCS can be extended to 3D similarity searching, with several modifications, the most important being conformational flexibility in the matching algorithm. This study presents a complete implementation of such an algorithm. The effectiveness of the proposed method in classifying chemical structures with respect to a given bioactive leader is evaluated.

SIMILARITY METHODOLOGY

Chemical graphs. All molecular structures can be represented as simple, undirected graphs. In a 3D chemical graph, the vertices denote atoms but edges here can indicate the geometric distance or a range of distances between pair of atoms (vertices). The main difference between these two representations is that 3D chemical graph is usually weighted by geometrical distance (see figure 1).

(a) 2D chemical graph (b) 3D chemical graph

Figure 1. Acetic acid chemical graphs representations

Distance geometry. In ligand-receptor interaction mechanism, ligand usually exhibits some degree of flexibility and thus the distances between atoms are not fixed.

One approach to cope with this drawback is to generate several conformations of low energy for each structure under consideration and then to compare all possible pairs of the resulting conformations. This approach is, however, computationally demanding, if exhaustive sampling of the molecules' conformational space is to be achieved and still cannot guarantee that the optimal similarity has been identified.

Distance geometry, herein considered, encodes the molecules' conformational flexibility within a single graphical representation.[3] Specifically, each edge of a 3D molecular graph is represented by a range of distances spanning the maximum and minimum allowable distance between two atoms. Distance ranges are imposed by some constrains, e.g., distance and chirality. The distance constrains are simply the lower and upper bounds of the interatomic distances; the chirality includes the handedness of the asymmetric centers in the molecule.

Covalent distance constrains. The local covalent structure of a molecule is easily defined by distance constrains. Unless one is dealing with a highly strained ring system, it is sufficiently to use the exact distance constrains in which the lower and upper bounds are equal. For example, the distances among covalently bonded pairs of atoms, are determined with high precision by the bond order and the types of atoms connected. Similarly, the bond angles can usually be determined from the covalent structure, while for fixed bond lengths there is a one-to-one relation between the bond angle and the geminal distance, so that these distances can also be determined. The relation between the geminal distances and the bond angle θ is given explicitly by the law of cosines:

$$\begin{aligned} d_{13}^2 &= d_{12}^2 + d_{23}^2 - 2d_{12}d_{23}\cos(\theta) \\ d_{13}^2 &= l_{13}^2 + (u_{13}^2 + l_{13}^2)\sin^2\left(\frac{\theta}{2}\right) \end{aligned} \tag{1}$$

where, $l_{13} = |d_{12} - d_{23}|$ and $u_{13} = d_{12} + d_{23}$ are called the *lower* and *upper* triangle inequality limits, respectively.

Vicinal distance constrains. Similarly, when the incident and geminal distances are held fixed, there is a one-to-one relation between the *absolute value* of the torsion angle φ and the vicinal distance, given by:

$$d_{14}^2 = l_{14}^2 + \left(u_{14}^2 - l_{14}^2\right)\sin^2\left(\frac{\varphi}{2}\right) \tag{2}$$

where l_{14} and u_{14} are *cis* and *trans* limits on the *1,4* distance.

Chirality constrains. The chirality χ_{1234} of an ordered quadruple of points numbered *1,2,3,4* is given in terms of their Cartesian coordinates by the sign of the following determinant:

$$\chi_{1234} = \mathrm{sgn}\left(\det\begin{bmatrix} 1 & 1 & 1 & 1 \\ x_1 & x_2 & x_3 & x_4 \\ y_1 & y_2 & y_3 & y_4 \\ z_1 & z_2 & z_3 & z_4 \end{bmatrix}\right) \tag{3}$$

Torsion angle constrains. As shown above, the absolute value of a torsion angle can be constrained to any range of values by means of suitable 1,4 distance constraints, including its *cis* and *trans* limits. Moreover, since the chirality χ_{1234} of a chain of four bonded atoms A_1-A_2-A_3-A_4 is equal to the sign of the torsion angle $\mathrm{sgn}(\varphi) = 0,\pm 1$ about the 2,3 bond, by a suitable combination of distance and chirality constraints we can obtain any range of values with a given sign. This is sufficient to specify the rotameric state (*gauche*$^+$, *gauche*$^-$ or *anti*) about the single bonds.

Steric distance constrains. Since two atoms cannot be in nearly the same place at the same time, in order to obtain reasonable conformations it is necessary to impose lower bound constraints on the distances between all pairs of atoms, separated by more than three bonds. For the sake of simplicity, these lower bounds are generally set to the sum of suitable *hard sphere radii* (van der Waals radii):

$$l_{ij} = r_i + r_j \tag{4}$$

After applying the preceding distance and chirality constrains, we ensure that the structures which satisfy them are not grossly unreasonably on energetic grounds. In order to get the correct conformation, it is necessary to impose constrains on interatomic distances for atoms that are separated by four or more bonds. Such constrains are determined by *bound smoothing* procedures: the *triangle bound smoothing* and *tetrangle bound smoothing*.

Triangle bound smoothing. Triangle inequality bound smoothing is based upon the well-known triangle inequality among the distances:

$$d_{ij} \le d_{ik} + d_{jk} \tag{5}$$

for all triples of atoms *i*, *j*, *k*. It follows that if $d_{ik} \le u_{ik}$ and $d_{jk} \le u_{jk}$ then:

$$d_{ij} \le d_{ik} + d_{jk} \le u_{ik} + u_{jk} \tag{6}$$

So, if $u_{ij} > u_{ik} + u_{jk}$, then $u_{ij} > d_{ij}$ and hence u_{ij} can be replaced by the upper limit u_{ik}+u_{jk} on d_{ij} without eliminating any conformation that satisfy the constrains $d_{ik} \le u_{ik}$ and $d_{jk} \le u_{jk}$ (see figure 2).

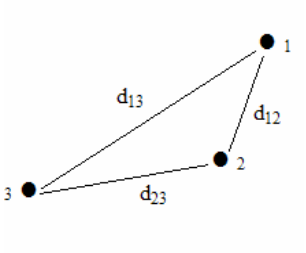

Figure 2. Triangle inequality

Tetrangle inequality bound smoothing. Unfortunately, the triangle inequality limits represent a rather poor approximation to the actual Euclidean limits, so that the triangle inequality bound smoothing is not a very effective approach to locating errors in the bounds. A somewhat more effective (although much more time-consuming) approach looks at four atoms at a time, rather than three. In this case, the algebraic form of the relations among the distances is far more complicated, so that the *tetrangle inequality limits* are best described pictorially as in Figure 3.

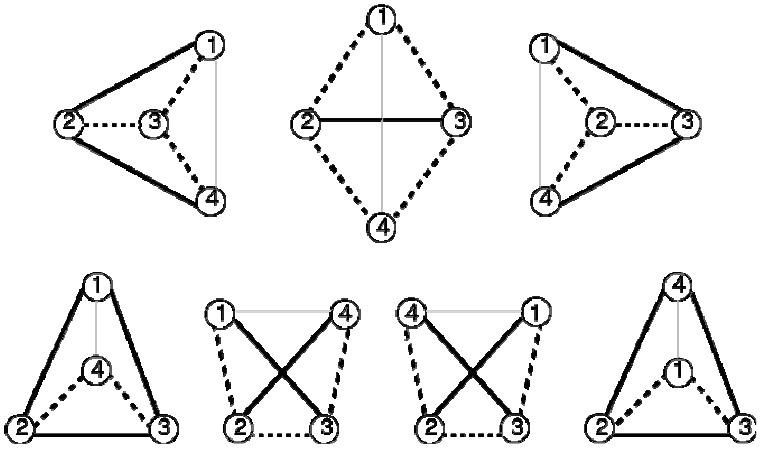

Figure 3. Tetrangle inequality limits

The mathematical form of this inequality can be expressed in terms of *Cayley-Menger* determinants:[4]

$$0 \le CM\left(d_{12},\ldots,d_{34}\right) = \det\begin{pmatrix} 0 & 1 & 1 & 1 & 1 \\ 1 & 0 & d_{12}^2 & d_{13}^2 & d_{14}^2 \\ 1 & d_{12}^2 & 0 & d_{23}^2 & d_{24}^2 \\ 1 & d_{13}^2 & d_{23}^2 & 0 & d_{34}^2 \\ 1 & d_{14}^2 & d_{24}^2 & d_{34}^2 & 0 \end{pmatrix} \tag{7}$$

Thus the corresponding mathematical forms of the above tetrangle inequalities are:

$$\begin{aligned} & 0 \le CM\left(l_{12},u_{13},u_{14},u_{23},u_{24},u_{34}\right), \\ \textit{or}\quad & 0 \le CM\left(u_{12},l_{13},l_{14},u_{23},u_{24},u_{34}\right), \\ \textit{or}\quad & 0 \le CM\left(u_{12},u_{13},u_{14},l_{23},l_{24},u_{34}\right), \end{aligned} \tag{8}$$

together with

$$\begin{aligned} & 0 \le CM\left(u_{12},u_{13},l_{14},l_{23},u_{24},l_{34}\right), \\ \textit{or}\quad & 0 \le CM\left(u_{12},l_{13},u_{14},u_{23},l_{24},l_{34}\right), \\ \textit{or}\quad & 0 \le CM\left(l_{12},l_{13},u_{14},l_{23},u_{24},l_{34}\right), \\ \textit{or}\quad & 0 \le CM\left(l_{12},u_{13},l_{14},u_{23},l_{24},l_{34}\right), \end{aligned} \tag{9}$$

Figure 4 illustrates a pair of structures and their corresponding 3D MCS; the initial coordinates are generated by *Hyperchem* molecular modeling package.

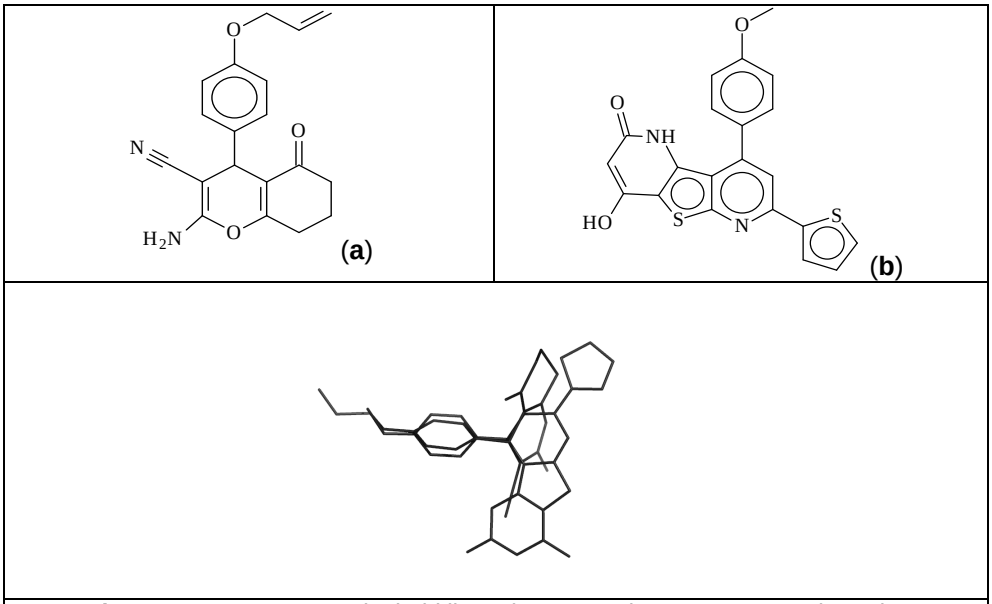

Figure 4. 3D MCS example, bold lines denote maximum common subgraphs

Upper and lower distance matrix for structure (**a**) Figure 4, before bound smoothing and after bound smoothing procedure is illustrated in Figure 5.

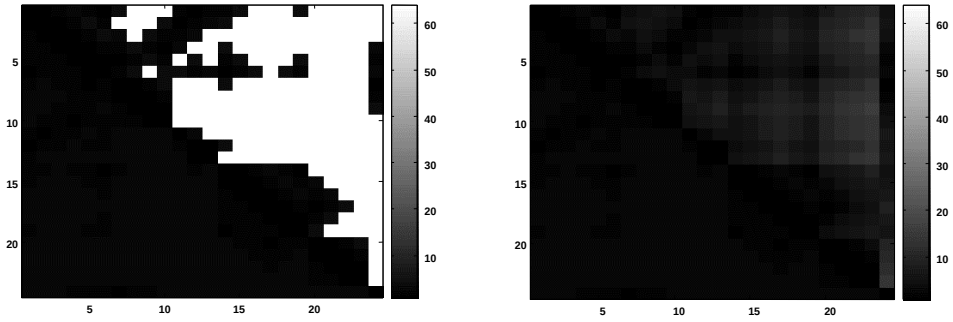

(**a**) Before bound smoothing (**b**) After bound smoothing

Figure 5. Distance bound smoothing example

A significant improvement in upper and lower bound is observed after applying distance geometry bound smoothing procedure (see Figure 5).

VALIDATION STUDIES

Validation studies were carried out on a set of 19 dopamine receptor antagonists. Dopamine receptors in the brain are important in modulating motor, endocrine, and emotional functions.[5,6] The antagonist affinity was measured at recombinant receptors selectively expressed in cloned cells (see Figure 6).

The test set used here was published by Brusniak;[7] it contains experimental data $\log(1/K_d)$, where K_d is the dissociation constant of the receptor-antagonist complex (see Table 1). For this simulation, the most active compound ((R) SKF82526) was used as a query; 18 pairwise comparisons were performed, with distance tolerance value ε = 0.1Å. Initial coordinates are obtained by *Hyperchem* program, followed by bound smoothing procedure. The 3D similarity threshold was set to 0.2 to prevent unnecessary pairwise comparisons. On a PC with 2.8 GHz Intel processor, 512 RAM, Windows XP, the computations for overall pairs comparisons took less then 2 s. The results are summarized in Table 1. It is noticeable the fact that receptor can discriminate between stereo-isomers (R)-SKF-82526 and (S)-SKF82526, although the difference is only one carbon atom configuration; the procedure is discriminative, giving appropriate similarity index.

The similarity index values were calculated using a weighing atom scheme. Thus the atoms that ensemble the active scaffold necessary for a structure to be active have a higher rank than the irrelevant atoms. All the active structures contain this scaffold, so that, after the overlapping procedure, it is easy to identify these atoms.

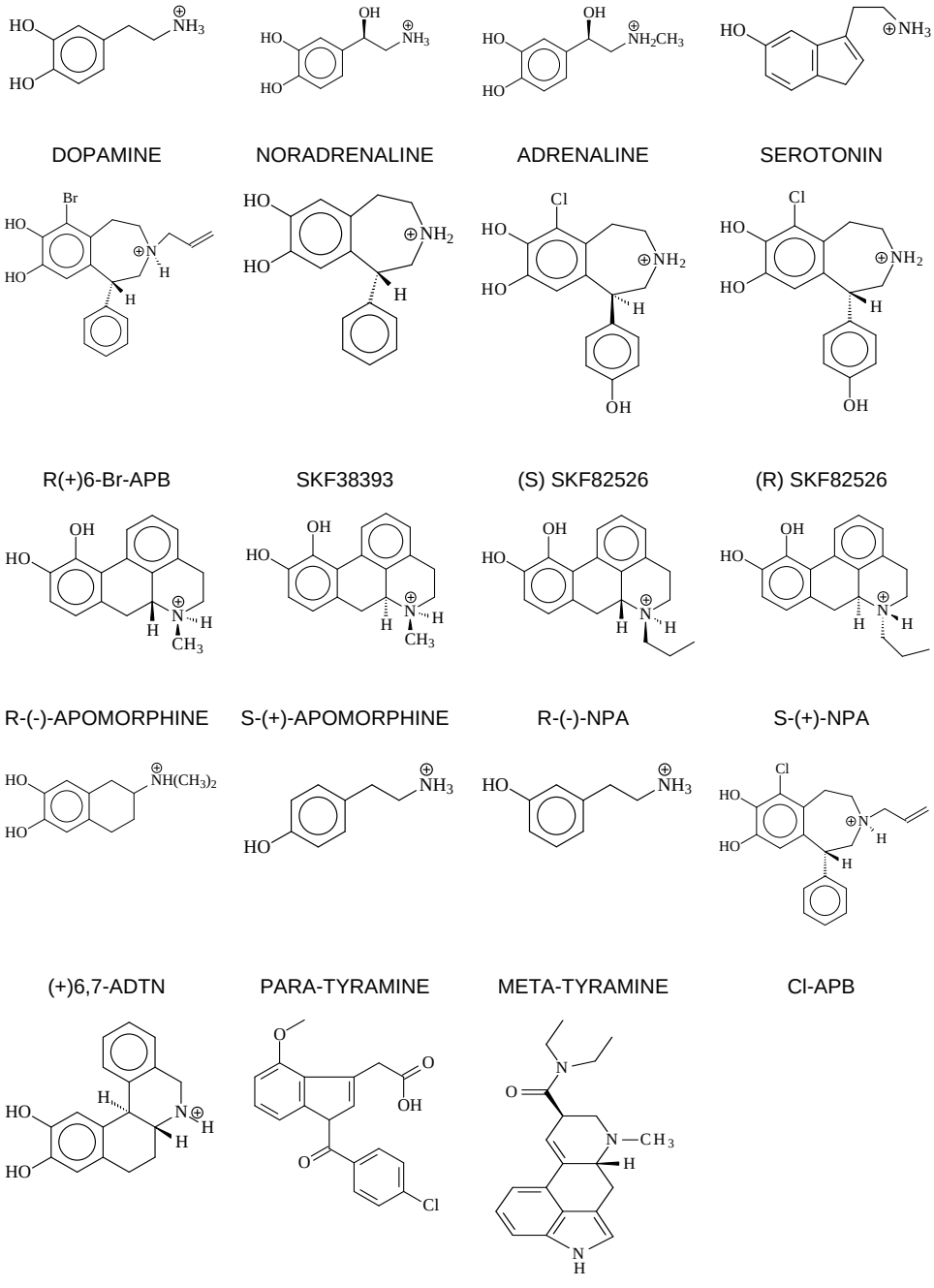

Figure 6. Structures of dopamine receptor antagonists

Table 1.

Drug affinities and similarity calculation results

molecule	$\log(1/K_d)$	Similarity
(+)-6,7-ADTN	-3.66	0.7500
adrenaline	-4.74	0.4444
Cl-APB	-1.92	0.9907
DHX	-3.08	0.8102
dopamine	-3.39	0.6759
m-tyramine	-4.68	0.5833
noradrenaline	-4.69	0.6759
p-tyramine	-5.59	0.5880
(R)-apomorfine	-2.83	0.7685
(R)-(-)-NPA	-3.26	0.7546
(R)-(+)-6-Br-APB	-2.58	0.9861
(S)-(+)-apomorfine	-3.08	0.7639
S-(+)-NPA	-3.72	0.7639
(S)-SKF82526	-3.26	0.7778
serotonin	-3.99	0.6806
SKF38393	-2.18	0.9861
(R)-SKF-82526*	-1.45	1.0000
INDOMETHACIN**	-3.53	0.7479
LSD**	-4.02	0.6818

*query structure
**estimate values for BA

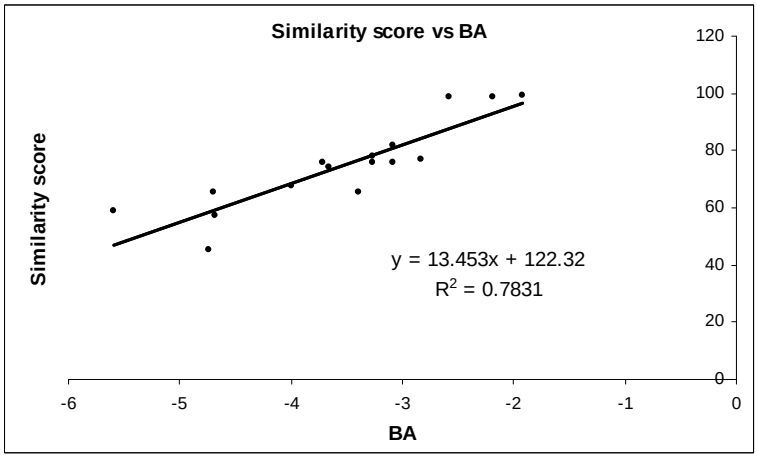

Figure 7. Linear dependence between Similarity scores and BA

Linear regression analysis showed good correlations between similarity score and BA. Thus an attempt to give estimative values of BA for two compounds of interest (INDOMETHACIN and LSD) was made. The predicted values (by using regression eq. in Figure 7) showed mild activity of these known antagonists.

Considering the simplicity of the used model, we can draw the conclusion that the similarity scores can classify correctly the unknowns, which is the most desirable feature (see Figure 7).

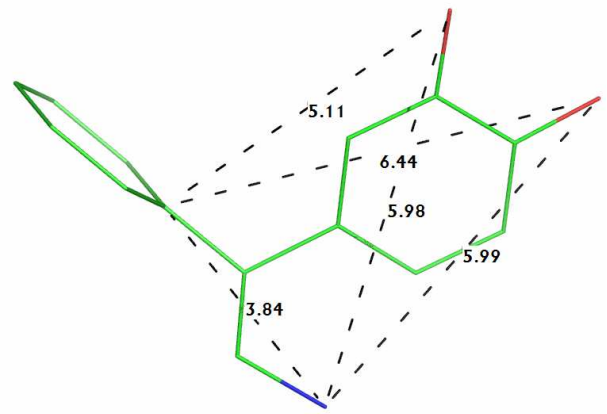

Figure 8. Pharmacophore map for dopamine receptor antagonists

The obtained results reveal the important structural features, *i.e*., the *pharmacophore*, of antagonists of the dopamine receptor (see Figure 8). In the high affinity compounds, the distance between the cationic nitrogen and the m-hydroxyl oxygen ranged from 6 to 6.45 Á with highest activity compound (R)-SKF-82526 having a distance of 6 Á. The distance between the cationic nitrogen and the first carbon in the second benzene cycle ranged from 3.78 to 3.81 Á; in the lowest activity compounds, this pharmacophore is missing.

CONCLUSIONS

In this paper we described an advanced method for the calculation of intermolecular structural similarity, useful in mining databases of 3D structures. This method takes a full account of the conformational flexibility, being in the mean time sufficiently rapid to allow search in databases of nontrivial size. Validation studies demonstrated that the method is more accurate than fingerprint screening, allowing discrimination even between stereo-chemical isomers. It would be also possible to use fingerprints screening procedure prior to graph matching in view of improving the overall efficiency. The method provides an effective extension to current approaches in virtual screening and lead optimization procedures.

REFERENCES

1. Raymond, J.; Gardiner, E.; Willett, P.; RASCAL: Calculation of Graph Similarity Using Maximum Common Edge Subgraphs, Comput. J., 2002, **45**, 631-644.
2. Raymond, J.; Gardiner, E.; Willett, P.; Heuristics for Rapid Similarity Searching of Chemical Graphs Using a Maximum Common Edge Subgraph Algorithm, J. Chem. Inf. Comput. Sci. 2002, **42**, 305-316.

3. Crippen, G.; Havel, T.; Distance Geometry and Molecular Conformation, Research Studies Press: **1988**.
4. Easthope, P.; Havel, T. F.; Computational Experience with an Algorithm for Tetrangle Inequality Bound Smoothing, Bull. Math. Biol., 1989, **51**, 173-194.
5. Strange, P. G.; Brain biochemistry and brain disorders; Oxford University Press: New York, **1993**.
6. Waddington, J.; D1:D2 Dopamine receptor interactions; Academic Press: New York, **1993**.